

ADVANCED STEEL CONSTRUCTION

An International Journal

Volume 15 Number 3

September 2019

CONTENTS

Technical Papers

Seismic Behavior of Precast Concrete Filled Dual Steel Tube Columns In Socket Foundations

Xian Li, Xiao-han Ma, Bei-Dou Ding Yu-wei Zhao and Feng Zhang

Flexural Strength of Weathered Granites Under Wetting - Drying Cycles: Implications To Steel Structures

Sarkar Noor-E-Khuda and Faris Albermani

Fatigue Repairing Craftsmanship of Deck-To-Vertical Stiffener Weld In The Steel Bridge Deck

Yi-xun Wang, Bo-hai Ji, Zhong-qiu Fu and Yue Yao

Resistance of Cold Formed High Strength Steel Angles

Anh Tuan Tran, Lars Bernspång, Milan Veljković, Carlos Rebelo and Luís Simões da Silva

Study on Load-Deflection Relationship Of Recycled Self-Compacting Concrete Filled Steel Tubular Columns Subjected To Eccentric Compression

Feng Yu, Long Chen, Yuan Fang, Jun-jie Jiang, Shi-long Wang and Zheng-yi Kong

A Review of Class 4 Slender Section Properties Calculation For Thin-Walled Steel Sections According To Ec3

Chi-King Lee and Sing-Ping Chiew

Finite Element Analysis for The Progressive Failure of Frp-Reinforced Steel Component Under Low-Velocity Impact

Qi-jian Wu, Xu-Dong Zhi and Meng-Hai Guo

Design Optimization of Tubular Lattice Girders

Tugrul Talaslioglu

Experimental Study of The Bearing Capacity of Long Span Profiled Steel Sheet Concrete Composite Slabs

Xiao-Xiang He, Guo-Chang Li and Zhi-jian Yang

Development and Application of A Mechanical Model of Beam-To-Column Connections of Steel Storage Racks

Nattawut Asawasongkram, Prakit Chomchuen and Prakit Premthamkorn

Copyright © 2019 by :

The Hong Kong Institute of Steel Construction

Website: <http://www.hkisc.org>

ISSN 1816-112X

Science Citation Index Expanded, Materials Science Citation Index and ISI Alerting

Cover: Macao Athletic Training and Development Centre

e-copy of IJASC is free to download at "www.scijournal.com" in internet and mobile apps.

ADVANCED STEEL CONSTRUCTION

VOL.15, NO.3 (2019)

ADVANCED STEEL CONSTRUCTION

an International Journal

ISSN 1816-112X

Volume 15 Number 3

September 2019



Editors-in-Chief

S.L. Chan, The Hong Kong Polytechnic University, Hong Kong

W.F. Chen, University of Hawaii at Manoa, USA

R. Zandonini, Trento University, Italy



ISSN 1816-112X

Science Citation Index Expanded,
Materials Science Citation Index
and ISI Alerting

EDITORS-IN-CHIEF

**Asian Pacific, African
and organizing Editor**
S.L. Chan
*The Hong Kong Polyt. Univ.,
Hong Kong*

American Editor
W.F. Chen
Univ. of Hawaii at Manoa, USA

European Editor
R. Zandonini
Trento Univ., Italy

ASSOCIATE EDITORS

Y.P. Liu
The Hong Kong Polyt. Univ., Hong Kong

S.W. Liu
Sun Yat-Sen Univ., China

INTERNATIONAL EDITORIAL BOARD

F.G. Albermani
Central Queensland Univ., Australia

I. Burgess
Univ. of Sheffield, UK

F.S.K. Bijlaard
Delft Univ. of Technology, The Netherlands

R. Bjorhovde
The Bjorhovde Group, USA

M.A. Bradford
The Univ. of New South Wales, Australia

D. Camotim
Technical Univ. of Lisbon, Portugal

C.M. Chan
Hong Kong Univ. of Science & Technology, Hong Kong, China

T.H.T. Chan
Queensland Univ. of Technology, Australia

T.M. Chan
The Hong Kong Polyt. Univ., Hong Kong, China

Z.H. Chen
Tianjin Univ., China

S.P. Chiew
Nanyang Technological Univ., Singapore

W.K. Chow
The Hong Kong Polyt. Univ., Hong Kong, China

G.G. Deierlein
Stanford Univ., California, USA

L. Dezi
Univ. of Ancona, Italy

D. Dubina
The Politehnica Univ. of Timisoara, Romania

R. Greiner
Technical Univ. of Graz, Austria

L. Gardner
Imperial College of Science, Technology and Medicine, UK

Y. Goto
Nagoya Institute of Technology, Japan

L.H. Han
Tsinghua Univ. China

S. Herion
University of Karlsruhe, Germany

G.W.M. Ho
Ove Arup & Partners Hong Kong Ltd., Hong Kong

B.A. Izzuddin
*Imperial College of Science, Technology and
Medicine, UK*

J.P. Jaspart
Univ. of Liege, Belgium

S. A. Jayachandran
IIT Madras, Chennai, India

S.E. Kim
Sejong Univ., South Korea

S. Kitipornchai
The Univ., of Queensland, Australia

D. Lam
Univ. of Bradford, UK

H.F. Lam
City Univ. of Hong Kong, Hong Kong, China

G.Q. Li
Tongji Univ., China

J.Y.R. Liew
National Univ. of Singapore, Singapore

E.M. Lui
Syracuse Univ., USA

Y.L. Mo
Univ. of Houston, USA

J.P. Muzeau
CUST, Clermont Ferrand, France

D.A. Nethercot
*Imperial College of Science, Technology and
Medicine, UK*

Y.Q. Ni
The Hong Kong Polyt. Univ., Hong Kong, China

D.J. Oehlers
The Univ. of Adelaide, Australia

J.L. Peng
Yunlin Uni. of Science & Technology, Taiwan, China

K. Rasmussen
The Univ. of Sydney, Australia

J.M. Rotter
The Univ. of Edinburgh, UK

C. Scawthorn
Scawthorn Porter Associates, USA

P. Schaumann
Univ. of Hannover, Germany

Y.J. Shi
Tsinghua Univ., China

G.P. Shu
Southeast Univ. China

L. Simões da Silva
*Department of Civil Engineering, University of
Coimbra, Portugal*

J.G. Teng
The Hong Kong Polyt. Univ., Hong Kong, China

G.S. Tong
Zhejiang Univ., China

K.C. Tsai
National Taiwan Univ., Taiwan, China

C.M. Uang
Univ. of California, USA

B. Uy
University of Western Sydney, Australia

M. Veljkovic
Univ. of Lulea, Sweden

F. Wald
Czech Technical Univ. in Prague, Czech

Y.C. Wang
The Univ. of Manchester, UK

Y.L. Xu
The Hong Kong Polyt. Univ., Hong Kong, China

D. White
Georgia Institute of Technology, USA

E. Yamaguchi
Kyushu Institute of Technology, Japan

Y.B. Yang
National Taiwan Univ., Taiwan, China

Y.Y. Yang
China Academy of Building Research, Beijing, China

B. Young
The Univ. of Hong Kong, Hong Kong, China

X.L. Zhao
Monash Univ., Australia

X.H. Zhou
Chongqing University, China

Z.H. Zhou
The Hong Kong Polyt. Univ., Hong Kong, China

S.Y. Zhu
The Hong Kong Polyt. Univ., Hong Kong, China

R.D. Ziemian
Bucknell Univ., USA

Cover: Macao Athletic Training and Development Centre

e-copy of IJASC is free to download at "www.ascjournal.com" in internet and mobile apps.

General Information

Advanced Steel Construction, an international journal

Aims and scope

The International Journal of Advanced Steel Construction provides a platform for the publication and rapid dissemination of original and up-to-date research and technological developments in steel construction, design and analysis. Scope of research papers published in this journal includes but is not limited to theoretical and experimental research on elements, assemblages, systems, material, design philosophy and codification, standards, fabrication, projects of innovative nature and computer techniques. The journal is specifically tailored to channel the exchange of technological know-how between researchers and practitioners. Contributions from all aspects related to the recent developments of advanced steel construction are welcome.

Disclaimer. No responsibility is assumed for any injury and / or damage to persons or property as a matter of products liability, negligence or otherwise, or from any use or operation of any methods, products, instructions or ideas contained in the material herein.

Subscription inquiries and change of address. Address all subscription inquiries and correspondence to Member Records, IJASC. Notify an address change as soon as possible. All communications should include both old and new addresses with zip codes and be accompanied by a mailing label from a recent issue. Allow six weeks for all changes to become effective.

The Hong Kong Institute of Steel Construction

HKISC

c/o Department of Civil and Environmental Engineering,
The Hong Kong Polytechnic University,
Hungghom, Kowloon, Hong Kong, China.

Tel: 852- 2766 6047 Fax: 852- 2334 6389

Email: ceslchan@polyu.edu.hk Website: <http://www.hkisc.org/>

ISSN 1816-112X

Science Citation Index Expanded, Materials Science Citation Index and ISI Alerting

Copyright © 2019 by:

The Hong Kong Institute of Steel Construction.



ISSN 1816-112X

Science Citation Index Expanded,
Materials Science Citation Index and
ISI Alerting

EDITORS-IN-CHIEF

Asian Pacific, African and organizing Editor

S.L. Chan

*The Hong Kong Polyt. Univ.,
Hong Kong*

Email: ceslchan@polyu.edu.hk

American Editor

W.F. Chen

Univ. of Hawaii at Manoa, USA

Email: waifah@hawaii.edu

European Editor

R. Zandonini

Trento Univ., Italy

Email: riccardo.zandonini@ing.unitn.it

Advanced Steel Construction

an international journal

VOLUME 15 NUMBER 3

September 2019

Technical Papers

Seismic Behavior of Precast Concrete Filled Dual Steel Tube Columns In Socket Foundations 215

Xian Li, Xiao-han Ma, Bei-Dou Ding, Yu-wei Zhao and Peng Zhang*

Flexural Strength of Weathered Granites Under Wetting – Drying Cycles: Implications To Steel Structures 225

Sarkar Noor-E-Khuda and Faris Albermani*

Fatigue Repairing Craftsmanship of Deck-To-Vertical Stiffener Weld In The Steel Bridge Deck 232

Yi-xun Wang, Bo-hai Ji, Zhong-qiu Fu and Yue Yao

Resistance of Cold Formed High Strength Steel Angles 242

Anh Tuan Tran, Lars Bernspång, Milan Veljkovic, Carlos Rebelo and Luís Simões da Silva*

Study on Load-Deflection Relationship Of Recycled Self-Compacting Concrete Filled Steel Tubular Columns Subjected To Eccentric Compression 252

Feng Yu, Long Chen, Yuan Fang, Jun-jie Jiang, Shi-long Wang and Zheng-yi Kong*

A Review of Class 4 Slender Section Properties Calculation For Thin-Walled Steel Sections According To Ec3 259

Chi-King Lee and Sing-Ping Chiew

Finite Element Analysis for The Progressive Failure of Frp-Reinforced Steel Component Under Low-Velocity Impact 267

Qi-Jian Wu, Xu-Dong Zhi and Meng-Hui Guo*

Design Optimization of Tubular Lattice Girders 274

Tugrul Talaslioglu

Experimental Study of The Bearing Capacity of Long Span Profiled Steel Sheet Concrete Composite Slabs 288

Xiao-Xiang He, Guo-Chang Li and Zhi-Jian Yang*

Development and Application of A Mechanical Model of Beam-To-Column Connections of Steel Storage Racks 297

Nattawut Asawasongkram, Prakrit Chomchuen and Prakrit Premthamkorn*

SEISMIC BEHAVIOR OF PRECAST CONCRETE FILLED DUAL STEEL TUBE COLUMNS IN SOCKET FOUNDATIONS

Xian Li^{*1,2,3}, Xiao-han Ma¹, Bei-Dou Ding^{1,2}, Yu-wei Zhao^{1,3} and Peng Zhang¹

¹ Jiangsu Key Laboratory of Environmental Impact and Structural Safety in Civil Engineering, China University of Mining and Technology, Xuzhou, 221116, Jiangsu, China

² State Key Laboratory for Geomechanics & Deep Underground Engineering, China University of Mining and Technology, Xuzhou, 221116, Jiangsu, China

³ Jiangsu Collaborative Innovation Center for Building Energy Saving and Construction Technology, Jiangsu Vocational Institute of Architectural Technology, Xuzhou, 221116, Jiangsu, China

* (Corresponding author: Xian Li; E-mail: lixian@cumt.edu.cn)

ABSTRACT

This paper presents an experimental study on the seismic behavior of precast concrete filled dual steel tube (CFDST) columns in socket foundations. The type of socket foundation is a good choice to accelerate the construction of precast CFDST structures, which involves embedding the precast CFDST column portion into a cavity within the precast footing and then filling the cavity with cast-in-place concrete or grout. In this study, five precast CFDST columns with various column base details were tested under simulated seismic loads until failure, and the effects of embedment depths and details of column bases on the seismic behavior were evaluated. The test results indicate that all precast CFDST columns with an embedment depth into the socket foundations larger than $1.0D$ (D is the outer diameter of the column) achieved a desirable plastic hinge failure at the column base. The further increase of the embedment depth larger than $1.0D$ and the use of CFRP wraps to confine the column base had no significant improvement on the seismic behavior of the specimens. However, the use of steel rings and the un-bond region left in the column base significantly improved the deformation capacity, ductility and energy-dissipation capacity of the specimens.

ARTICLE HISTORY

Received: 6 July 2018
Revised: 14 October 2018
Accepted: 14 October 2018

KEYWORDS

Concrete filled dual steel tube column;
Seismic behavior;
Plastic hinge;
Precast footing;
Socket connections

Copyright © 2019 by The Hong Kong Institute of Steel Construction. All rights reserved.

1. Introduction

Extensive studies have been conducted on concrete filled steel tubes (CFTs) over the past two decades, and the structural and constructional merits of CFTs are well recognized. Concrete filled dual steel tubes (CFDSTs), which consist of double concentric steel tubes with concrete sandwiched between them, can be recognized as a new type of CFT construction and have shown a great potential to be used in the construction of offshore platforms, bridge piers and high-rise buildings in recent years. Due to the existence of inner steel tubes, CFDST members exhibit some superior performance such as lighter weight, higher bending stiffness, and better earthquake- and fire-resistance behavior when compared with CFTs. To better understand the behavior of CFDSTs, previous investigations have been carried out on CFDST columns [1-9], beams [10] and beam-columns [11-12] under monotonic or cyclic loadings. However, the issues related to the behavior of CFDST column to concrete footing connections have not been fully addressed to date. The gravity and seismic loads resisted by the columns must be properly transferred down to the soil/rock through the concrete footings. Thus, the proper evaluation of the behavior of CFDST columns, particularly precast columns, in foundations is quite important for reliable CFDST construction.

In this study, the seismic behavior of precast CFDST columns in socket foundations are intended to be studied. The use of precast CFDST structures is a good choice to reduce the construction time and construction-related disruption to society. Nowadays the existing column base connections mainly includes exposed base-plate column base connections, embedded column base connections, concrete-encased column base connections and socket column base connections [13-14]. Among these column base connections, the type of socket connections is relatively most suitable for precast structures. The socket connection is usually constructed by embedding a precast CFDST column portion into a cavity within a precast concrete footing, and then the space between the cavity and the column is filled with cast-in-place concrete or grout. Lehman et al. [13] conducted experimental studies on the seismic behavior of CFT columns in socket foundations and developed design procedure for socket connections. Canha et al. [15] carried out theoretical and experimental studies on socket foundations for precast concrete structures. To date, however, the seismic behavior of precast CFDST columns in socket foundations have not been well studied yet, even the required embedment depth of CFDST columns into footings to develop a column plastic hinge failure is still not clear. In China, the required embedment depths varied from $1.0D$ to $2.5D$ (D is the diameter of the column) in the different codes and standards for CFT structures due to the lack of efficient experimental studies in this field. Therefore, this paper presents an experimental study to determine the required embedment depths of CFDST

columns into concrete footings, and the effects of embedment depths and details of column bases on the seismic behavior are also to be evaluated.

2. Experiment program

2.1. Specimen design

Five precast CFDST columns in socket foundations were constructed and tested under simulated seismic loads, as shown in Fig. 1 and Table 1. The CFDST columns for all specimens had an identical cross section and a height of 1360mm from the load point to the top surface of the precast footing. The inner and outer seamless steel tubes had a thickness of 7mm and were made of Q235 steel with a nominal yield strength of 235MPa. The inner and outer steel tubes had an outer diameter of 168mm and 273mm, respectively. Thus, the hollow ratio of the CFDST columns, which is defined as the ratio between the outside diameter of the inner steel tube and the inside diameter of the outer steel tube by Tao et al. [16], is 0.65. Concrete was sandwiched between these two steel tubes and the inner tube was partially filled with concrete from the bottom of the tube to a height of 410mm above the top surface of the concrete footing. An end annular ring with a thickness of 14mm and a width of 159mm was welded onto the column to transfer loads from the steel tubes and in-filled concrete to the concrete footing. The flange of the end ring projected out from the tube a distance equal to 9 times the wall thickness of the outer tube. All of the precast concrete footing had an identical dimension of 1250mm×1250mm in plan and 600mm in depth. Each concrete footing was longitudinally and transversely reinforced at both the bottom and the top with 18mm-diameter HRB400 deformed bars (hot-rolled ribbed bar $\Phi 18$ with a nominal yield strength of 400MPa) averagely spaced at 125mm. The top longitudinal bars intersecting with CFDST columns were bent downwards with a length of 200mm to avoid passing through the columns. Vertical reinforcement with a diameter of 8mm was used to strengthen the areas of the footings with the holes for bolts. The thickness of concrete cover was 50mm.

The intended test variables were the embedment depths of the CFDST columns into concrete footings and the details of column bases. The CFDST columns for specimens CFDST1 and CFDST2 had an embedment depth of 273mm, which is equal to the outer diameter of the column D , while the CFDST columns for other three specimens had an embedment depth L_e of 410mm, which is equal to 1.5 times the outer diameter of the column D . The cavity for the column was located at the center of the precast footing and formed by the corrugated pipe with a diameter of 500mm and a thickness of 2mm. To control the local buckling of the column base and enhance the ductility of the specimens, steel rings and CFRP wraps were used to confine the column base in the region

200mm above the footing in specimens CFDST2 ~ CFDST5. The concept of using steel and CFRP sheets to confine the CFT column base was firstly proposed by Choi et al. [17] and the efficiency of the confinement was validated by their experiments. In specimen CFDST2, two steel rings with a 299mm-

outer-diameter, a 10mm- thickness and a 100mm-height were used to confine the potential plastic hinge at the column base. Therefore, a 3mm-wide gap was left between the steel rings

Table 1

Details of test specimens

Specimen number	Footing size (mm ³)	Embedment depth L_e (mm)	Column base details
CFDST1	1250×1250×600	273 (1.0D)	Reference specimen
CFDST2	1250×1250×600	273 (1.0D)	The column base was confined by two steel rings with a gap.
CFDST3	1250×1250×600	410 (1.5D)	The column base was confined by two layers of CFRP wraps with a 2mm-wide gap.
CFDST4	1250×1250×600	410 (1.5D)	The column base was confined by two layers of CFRP wraps directly glued onto it.
CFDST5	1250×1250×600	410 (1.5D)	The region from 137mm lower than the top surface of the footing to 200mm above the footing was confined by two layers of CFRP wraps with a 2mm-wide gap.

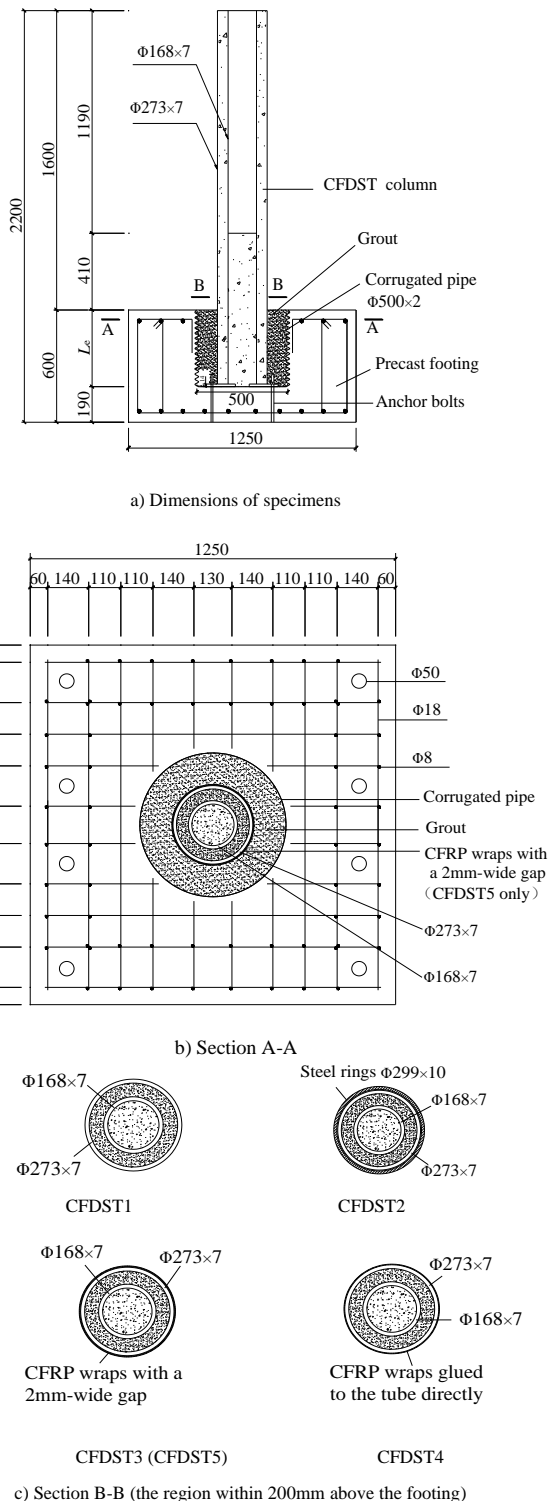


Fig. 1 Details of test specimens

and the column steel tube. In specimens CFDST3~CFDST5, two layers of CFRP sheets with a nominal thickness of 0.167mm were employed to confine the column base in the region of 200mm above the top of the footing, but the confinement methods were different in these specimens. In specimen CFDST3 and CFDST5, a gap between the steel tube and the CFRP confinement was left and the gap was made by 2mm-thick soft foam tapes affixed on the surface of the steel tube to provide a cushioning effect. Such cushioning effect was designed to delay the participation of the CFRP wraps for possibly maximizing the deformability while minimizing the unnecessary strength enhancement. In specimen CFDST5, the CFRP confinement extended down into the footing with a height of 137mm. Therefore, the column had a un-bond length of 137mm left in the concrete footing and the un-bond region left herein was intended to prevent the serious buckling of column by the concrete of the footing and then enlarge the plastic hinge zone of the column. In specimen CFDST4, the CFRP sheets were directly glued onto the outer steel tube.

All of the specimens were constructed according to the following steps. The CFDST columns and the reinforced concrete footings were firstly precast, and the column bases were confined by CFRP sheets or steel according to the design. Then the columns were set in the excavation, plumbed and anchored to the footings using four Grade 4.6 anchors with a diameter of 14mm. The voids between the columns and the corrugated pipes were lastly filled using cast-in-place grout.

2.2. Material properties

The measured yield strength f_y and the tensile strength f_u of both the steel tubes and the steel bars are shown in Table 2. The concrete cubic strength f_{cu} was obtained by compression tests of 150 mm concrete cubes as per the Chinese standard. The concrete cubes were cured at room temperature the same to the test specimens, and the average compressive strengths f_{cu} of the concrete for footings and columns at the time of testing were 53.4MPa and 55.2MPa, respectively. The cylinder strength f_c can be calculated as 0.8 times the cubic strength f_{cu} . The grout used to fill the void in the corrugated pipes had a compressive strength of 80MPa. The unidirectional CFRP sheets used to confine column bases had a width of 200mm and a nominal thickness of 0.167mm. As provided by the manufacturer, the tensile rupture strength, average rupture strain and elastic modulus were 3062MPa, 0.0172 and 214GPa, respectively. The tensile strength and elastic modulus of the structural adhesive used in this test were about 42MPa and 3.1GPa, respectively.

Table 2

Material properties of steel components

Components	Details	f_y (MPa)	f_u (MPa)
Outer steel tube	$t=7\text{mm}$	307	436
Inner steel tube	$t=7\text{mm}$	276	398
Steel rings	$t=10\text{mm}$	426	565
Steel reinforcement	HPB300Φ8	374	508
Steel reinforcement	HRB400Φ18	415	627

2.3. Test methods

The experimental setup for all tests is presented in Fig. 2. The experimental setup was designed to apply lateral cyclic loadings using a horizontally positioned 500kN capacity hydraulic actuator to the CFDST columns in a condition of vertical cantilever. The precast concrete footings were tied to the strong floor by eight high-strength bolts and the potential slipping of the concrete footing was prevented by four hydraulic jacks. The axial load was applied to the top of

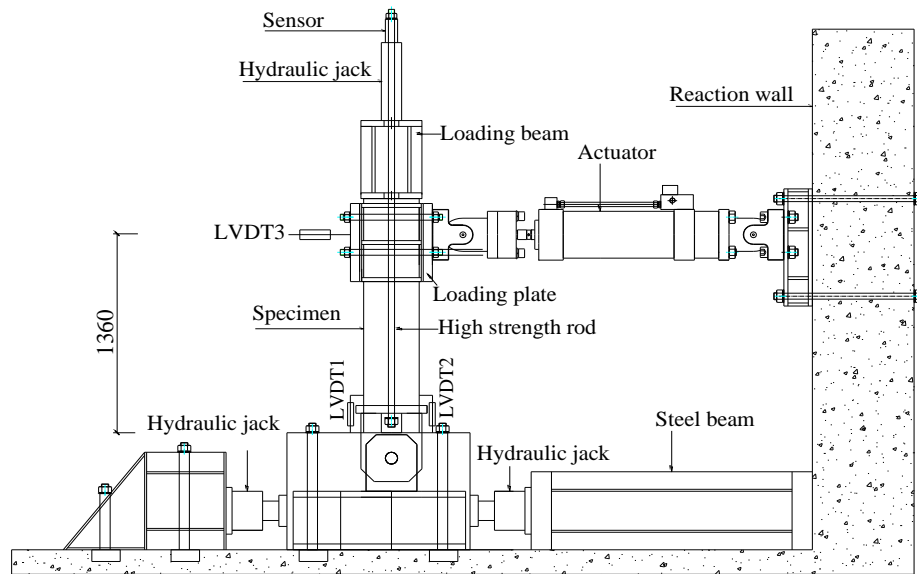


Fig. 2 Experimental setup (unit: mm)

the CFST columns using a steel beam posttensioned by two vertical 50-mm-diameter high-strength steel rods. The forces of the steel rods were applied by two 1000kN capacity hydraulic hollow jacks and were monitored by two calibrated load cells. A specially designed pin device was connected to the bottom end of each posttensioned steel rod to eliminate the bending of the rods during the lateral loading cycles. The imposed lateral displacement at the loading point was monitored by both a separate linear potentiometer and the displacement transducer of the actuator. The curvatures of the column bases were monitored by two linear potentiometers. The corresponding lateral force was recorded by the load cell of the actuator, as shown in Fig. 2. The strain responses of the outer and inner steel tubes as well as the steel bars of the precast footing were measured by electrical resistance strain gauges.

During the testing, the axial load was maintained constantly to 650kN, whereas the lateral loading sequences were controlled by the drift ratios of the columns at the shear force application point. The drift ratio herein was defined as the ratio of the applied displacement (Δ) to the height ($H=1360$ mm) from the loading point to the top surface of the concrete footing. One complete loading cycle for each peak lateral drift ratio was applied corresponding to an increment of peak drift ratio of $\Delta/H=0.25\%$, until $\Delta/H=1\%$ was reached. Subsequent loading was carried out with three complete cycles corresponding to each of the peak drift ratios of Δ/H equal to 1%, 1.5%, 2%, 3%, 4% and then with two complete cycles corresponding to Δ/H equal to 5%, 6%, 7% and 8%, until physical fracture of the specimens occurred.

3. Experimental results and discussions

3.1. Experimental observations and failure modes

All of the tested specimens with a column embedment depth of $1.0D$ or $1.5D$ successfully formed a plastic hinge at the column base, indicating that the column embedment depth larger than $1.0D$ is adequate for socket connections.

However, the specimens with a smaller embedment depth suffered more serious damage of the infilled grout at the footings. For specimen CFST1, cracks initiated at the column-footing interface at approximately 0.75% drift ratio and these cracks remained small and local within the corrugated pipe with increasing lateral deformation until 3% drift ratio. After that, the cracks extended out the corrugated pipe and the cracking around the corrugated pipe occurred at the third cycle of 4% drift ratio. The outer steel tube of the column started to buckle at the lateral drift ratio of 7% and was fractured at a drift ratio of 11%. For specimen CFST2 with confinement provided by two steel rings at the column base, the buckling of the steel tube was successfully prohibited and the outer steel tube was fractured at the column bottom due to too large inelastic deformation at the drift ratio of 13%. The grout in the corrugated pipe suffered more serious damage due to the slight increase of the loading capacity of the specimen.

For specimens CFST3~CFST5 with an embedment depth of $1.5D$, the cracking of the footing became slighter. The fibers of CFRP sheets were gradually fractured due to the serious buckling of the steel tubes at the large drift ratios larger than 5%. The use of sponge between the CFRP sheets and steel tubes slightly delayed the fracture of the CFRP fibers but had no significant effect on the deformation capacity of the specimens. Both the specimens CFST3 and CFST4 failed at a drift ratio of 11% due to the fracture of steel tubes. In specimen CFST5, the un-bond region left in the footing significantly delayed the fracture of both CFRP sheets and the outer steel tube. The initial yielding of the outer steel tube occurred in the un-bond region; however, with the increase of the applied displacements, the outer steel tube gradually buckled at the region above the footing and it was finally torn off during a drift ratio of 15%. According to the strain measurement, the steel bars in all precast concrete footings did not yield at the failure conditions of the testing. The final failure modes of the tested specimens are presented in Fig. 3.



a) CFST1



b) CFST2



c) CFST3

Fig. 3 Failure modes of tested specimens



d) CFDST4



e) CFDST5

Fig. 3 Continued

3.2. Load-deformation responses

Fig. 4 presents the measured lateral load-deformation relationship curves of the tested specimens CFDST1~ CFDST5. The yield loads P_y and the peak loads P_{max} of the specimens are included in Table 4. As shown in Fig. 4, all of the tested specimens exhibited stable spindle-type hysteretic loops. The strength of the specimens did not significantly deteriorate prior to the fracture of outer steel tubes. The comparison of the hysteretic loops of the specimens with embedment depths of $1.0D$ and $1.5D$ indicated that the embedment depth of $1.0D$ is adequate to develop the full plastic flexural strength of the columns. Specimens CFDST1 and CFDST3 had the same deformation capacity equal to 11% drift ratio and the loading capacity of specimen CFDST3 was only 5.5% higher than that of specimen CFDST1. For the specimens CFDST1 and CFDST2 with an embedment depth of $1.0D$, the use of steel rings to confine the potential plastic hinge in specimen CFDST2 significantly increased the deformation and loading capacities. The deformation capacity of this specimen was approximately 19.0% higher than that of specimen CFDST1, and the specimen achieved an average loading capacity of 349.75kN in the positive and negative loading directions, which was 13% higher than that of specimen CFDST1. The strength deterioration rate of specimen CFDST2 was also found to be slow due to the good confinement of the column base. Specimens CFDST3 and CFDST4 exhibited almost the same hysteretic behavior with similar load and deformation capacities. This is because the buckling of outer steel tubes resulted in uneven stress distribution in the CFRP sheets and then the CFRP fibers were ruptured one by one due to the limited ultimate deformability. For specimen CFDST5, the loading capacity and ultimate displacement were 338kN and 204mm, respectively, which were 3.4% and 36.36% higher than the corresponding values of specimen CFDST3. That is to say, the un-bond region left in the column-footing interface had no significant effect on the loading capacity but significantly improved the deformation capacity of the specimen. The improvement of the deformation capacity was attributed to that the plastic deformation initially occurred in the un-bond region; however, with the increase of the applied loads, the further plastic deformation in the un-bond region were prohibited by the concrete footing and then the plastic deformation was enlarged to the region above the top surface of the footing. Thus, the un-bond region left in the column-footing interface is a good detail for the column base connection to enlarge the plastic zone of CFDST columns.

3.3 Moment-curvature responses

The average curvature Φ of the plastic hinge was measured using LVDTs and then calculated as follows.

$$\phi = \frac{\Delta_1 - \Delta_2}{b_l l_i} \quad (1)$$

where Δ_1 and Δ_2 are the vertical displacements of LVDT1 and LVDT2 shown in Fig. 2; b_l is the distance between the two LVDTs; and l_i is the measured length of the LVDTs, equal to 200mm herein.

The relationship curves between the moments at the column-footing interfaces and the average curvatures of the plastic hinges are presented in Fig. 5. It can be found that, with the increase of the column embedment depth, the plastic deformation at the column bases developed more fully and thus the moment-curvature curves became flatter. The use of steel rings in specimen

CFDST2 was effective to confine the potential plastic hinge and resulted in much larger and more stable hysteretic loops. Specimen CFDST4 with a confinement of the column base using CFRP sheets glued on the steel tube directly exhibited slight improvement of the plastic deformation at the plastic hinge when compared with specimen CFDST3. For specimen CFDST5, though the specimen exhibited the most favorable deformation capacity, its moment-curvature curve at the column base was much thinner. The results further verified the fact that serious plastic deformation of the column developed at the un-bond region in the concrete footing.

3.4 Stiffness and stiffness degradation

In this study, both the peak-to-peak stiffness and normalized stiffness, as shown in Fig. 6, were adopted to evaluate the stiffness characteristics of the tested specimens. The peak-to-peak stiffness is defined as the ratio of the peak shear load at the first cycle of each deformation level to their corresponding displacement, while the normalized stiffness is obtained by the peak-to-peak stiffness divided by the initial stiffness. The normalized stiffness can reflect the stiffness degradation rate of each specimen and it is plotted in Fig. 6b. As shown in Fig. 6, the initial stiffness of all of the tested specimens varied between 9.64kN/mm and 11.13kN/mm, and with increasing applied drift ratios, the stiffness degraded gradually. Specimens CFDST1 and CFDST3 had almost identical peak-to-peak at different drift ratios and stiffness degradation rates, indicating again that the embedment depth of $1.0D$ is adequate for the socket connections for CFDST columns. The use of steel rings had no significant effect on the initial stiffness but resulted in relatively slow stiffness degradation. The use of CFRP sheets directly glued onto the steel tube slightly increased the initial stiffness of specimen CFDST4 but had no significant effect on the stiffness degradation rate due to gradual fracture of fibers at large drift ratios. Specimen CFDST5 with a un-bond region left in the concrete footing had a reduced initial stiffness since the gap between the column and the footing in the un-bond region increased the column height. However, the stiffness degradation became slow after the applied drift ratio of 5% due to the confinement at the column base provided by the concrete footing and CFRP sheets.

Table 4 shows the predicted and measured initial elastic stiffness of each specimen. The theoretically predicted elastic stiffness K_e of the tested specimens can be determined using the Eq. 2 for cantilever beams.

$$K_e = \frac{\pi EI}{L^3} \quad (2)$$

where EI is the elastic section flexural stiffness of a CFDST column; L is the length of an fixed column; for specimen CFDST5, the fixed end was assumed to be located at the section $0.5D$ lower than the top surface of the footing due to the existence of the gap. As for the elastic section flexural stiffness EI of the CFDST column, different codes give different calculation methods. In general, the total initial flexural stiffness (EI) of a CFDST column is a sum of the flexural stiffness (EJ_{si}) of the inner tube and the flexural stiffness (EI_{osc}) contributed by the outer tube together with the infilled concrete.

$$EI = EJ_{si} + EI_{osc} \quad (3)$$

-BS5400[18]

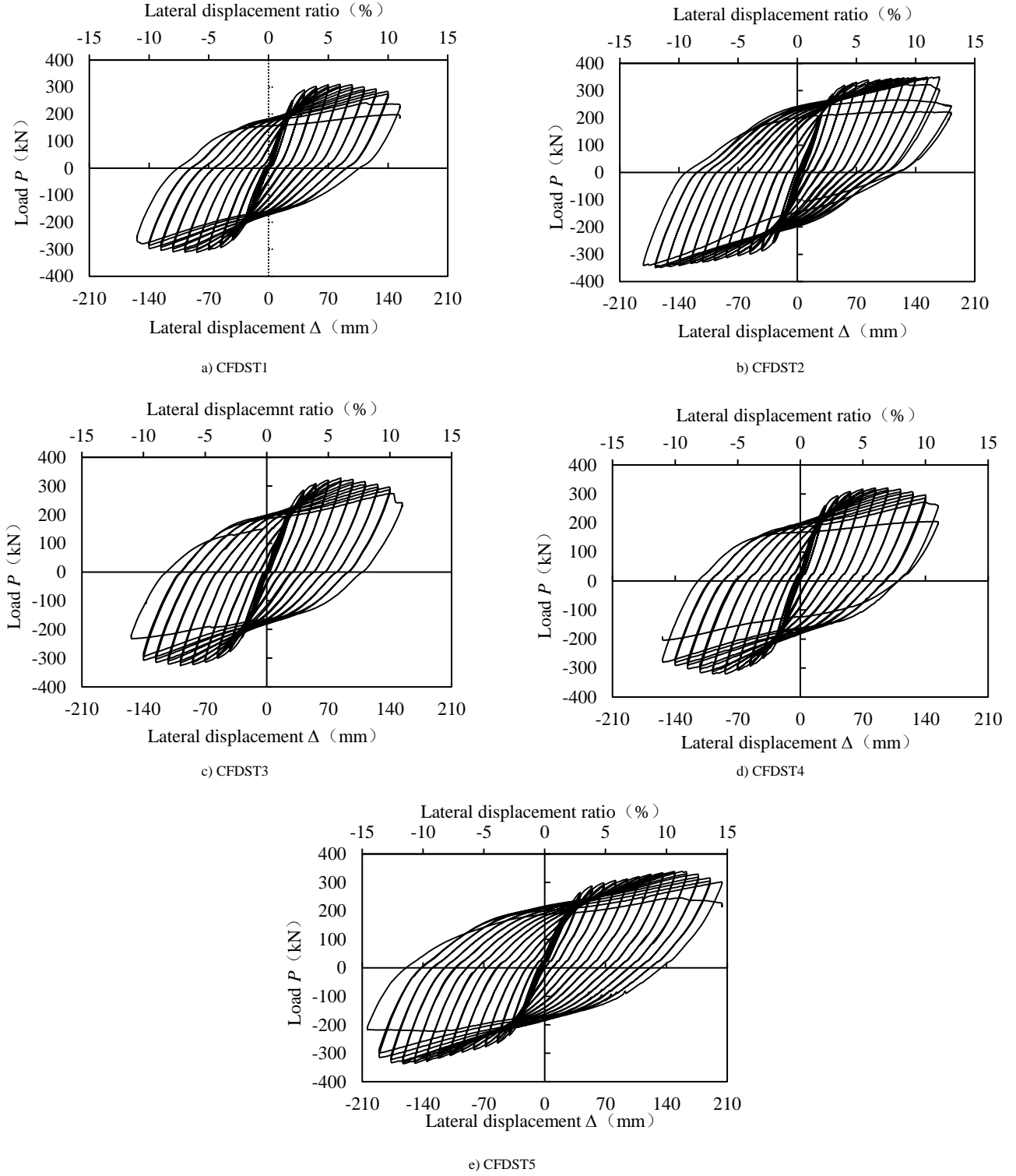


Fig. 4 Hysteretic curves of tested specimens

$$EI_{osc} = E_s I_{so} + E_c I_c \quad (4)$$

where $E_s=206000$ MPa and $E_c=450f_{cu}$ MPa are the elastic modulus of the steel tubes and infilled concrete, respectively. I_{so} and I_c are the moment of inertia for outer steel tube and the gross section of infilled concrete, respectively.

-AIJ [19]

$$EI_{osc} = E_s I_{so} + 0.2E_c I_c \quad (5)$$

where $E_s=205800$ MPa; $E_c = 21000\sqrt{f'_c/19.6}$ MPa, and f'_c is the cylinder compressive strength of concrete.

-AISC-LRFD[20]

$$EI_{osc} = E_s I_{so} + C_1 E_c I_c \quad (6a)$$

$$C_1 = 0.25 + 0.3A_s/A_g \leq 0.7 \quad (6b)$$

where $E_s=200000$ MPa; $E_c = 0.043w_c^{1.5}\sqrt{f'_c}$ MPa; w_c is the weight of infilled concrete per unit volume; A_s and A_g are the cross-sectional areas of steel section and gross section, respectively.

-Eurocode 4[21]

$$EI_{osc} = E_s I_{so} + 0.6E_c I_c \quad (7)$$

where $E_s=206000$ MPa; $E_c = 9500(f'_c + 8)^{1/3}$ MPa.

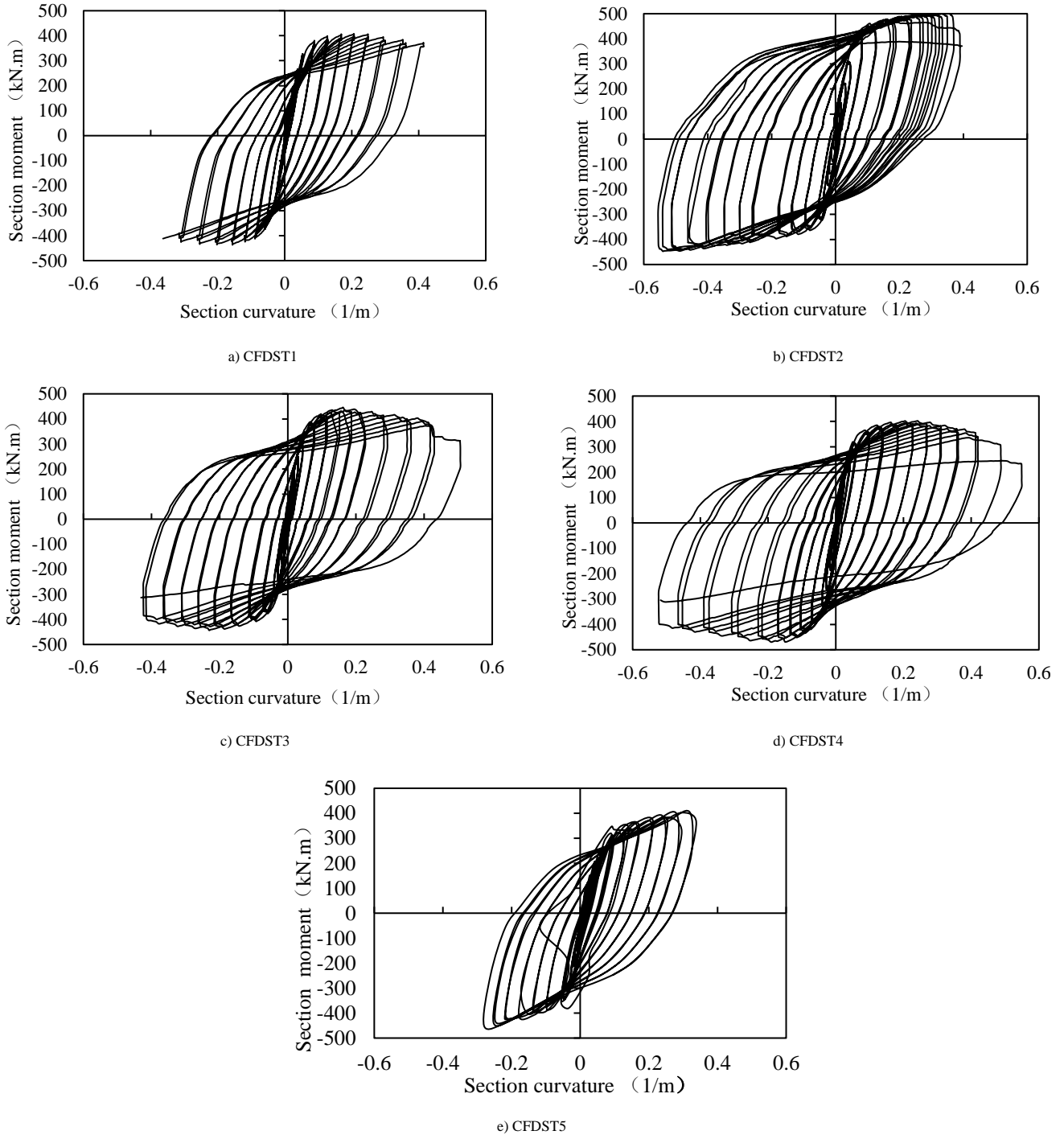


Fig. 5 Moment-curvature relationship curves of tested specimens

$$C_1 = 0.25 + 0.3A_s/A_g \leq 0.7 \quad (6b)$$

where $E_s = 200000 \text{ MPa}$; $E_c = 0.043w_c^{1.5}\sqrt{f'_c}$ MPa; w_c is the weight of infilled concrete per unit volume; A_s and A_g are the cross-sectional areas of steel section and gross section, respectively.

- Eurocode 4[21]

$$EI_{osc} = E_s I_{so} + 0.6E_c I_c \quad (7)$$

where $E_s = 206000 \text{ MPa}$; $E_c = 9500(f'_c + 8)^{1/3}$ MPa.

The comparisons of the measured initial stiffness K_i and the predicted values are presented in Table 3, where K_{e-B5} , K_{e-AIJ} , K_{e-AISC} and K_{e-EC4} were the predicted results based on the code provisions BS5400, AIJ, AISC-LRFD and Eurocode 4, respectively. It can be found that though all of the tested specimens

in socket foundations achieved a column plastic hinge failure, the measured initial stiffness of all specimens was lower than the predicted values. BS5400, AISC-LRFD and Eurocode 4 gave similar predicted results about 2 times the measured values, while the predicted stiffness by AIJ code was relatively close to the measured values with the ratios K_i/K_{e-AIJ} varying between 0.58 and 0.76. The overestimation of the flexural stiffness of CFDST columns in socket foundations is mainly due to the over-estimation of the rigidity of socket connections. The study conducted by Hsu *et al.* [22] indicated that it was too costly to achieve a rigid socket connection in construction projects, and a coefficient α should be employed to account for the effectiveness of the base connections. Since the coefficient α proposed by Hsu *et al.* [22] was obtained by testing of solid square CFT columns embedded into concrete footings, in this study the coefficient α was further modified using a factor I/I_{sq} to account for the differences between the solid square and the CFDST columns. Thus, the elastic stiffness K_{e-Hsu} can be calculated as follows for design purposes.

$$K_{e-Hsu} = \frac{\alpha EI}{L^3} \quad (8)$$

$$\alpha = \left[-0.4763 \left(\frac{L_e}{D} \right)^2 + 1.627 \left(\frac{L_e}{D} \right) + 1.4313 \right] \frac{I}{I_{sq}} \leq 3 \quad (9)$$

where I_{sq} is the moment of inertia for a solid square CFT column that has a square steel tube with the thickness and the width the same to the outer steel tube of CFDST section.

Table 3 also presents the predicted stiffness based on Eqs. (8) and (9). In these equations, the elastic section flexural stiffness EI of the CFDST column was taken according to AIJ code. It can be found from Table 3 that, except specimen CFDST5 with more complicated connection details, the tested specimens got reasonable predicted stiffness based on Eqs. (8) and (9) with the ratios K_t/K_{e-Hsu} varying between 0.95 and 1.04.

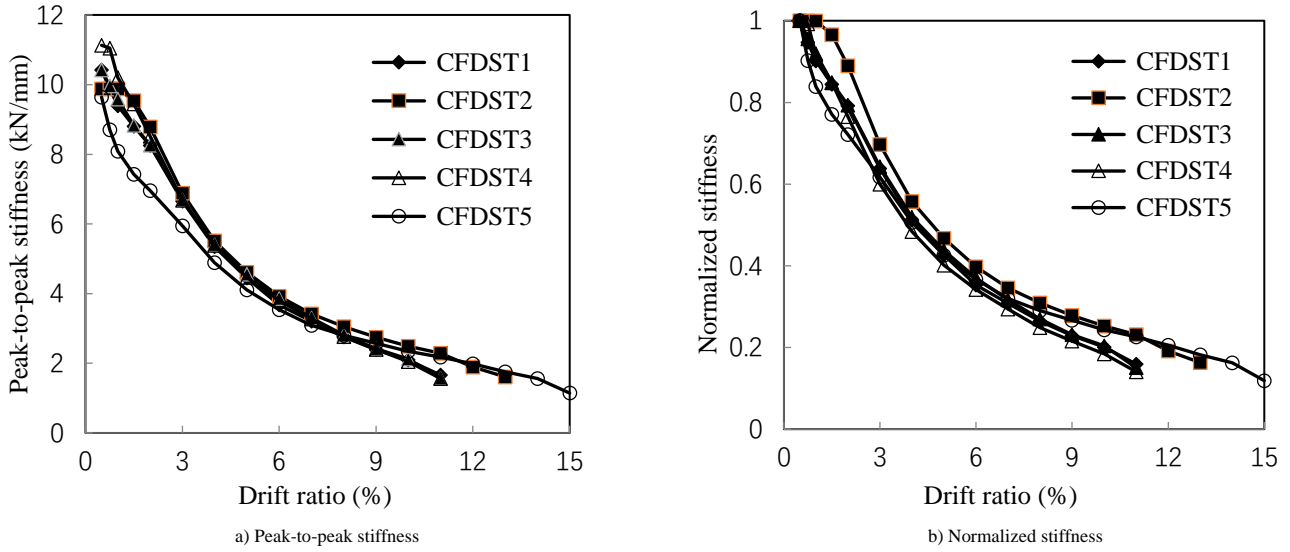


Fig. 6 Stiffness characteristics

Table 3
Comparisons between predicted initial stiffness and test results

Specimens	K_t	K_{e-Bs}	$\frac{K_t}{K_{e-Bs}}$	K_{e-AIJ}	$\frac{K_t}{K_{e-AIJ}}$	K_{e-AISC}	$\frac{K_t}{K_{e-AISC}}$	K_{e-EC4}	$\frac{K_t}{K_{e-EC4}}$	K_{e-Hsu}	$\frac{K_t}{K_{e-Hsu}}$
CFDST1	10.45	20.93	0.50	16.90	0.62	20.51	0.51	20.16	0.52	10.00	1.04
CFDST2	9.88	20.93	0.47	16.90	0.58	20.51	0.48	20.16	0.49	10.00	0.99
CFDST3	10.42	20.93	0.50	16.90	0.62	20.51	0.51	20.16	0.52	10.92	0.95
CFDST4	11.13	20.93	0.53	16.90	0.66	20.51	0.54	20.16	0.55	10.92	1.02
CFDST5	9.64	15.69	0.61	12.67	0.76	15.38	0.63	15.12	0.64	8.19	1.18

3.5 Ductility

The ductility of the tested specimens is presented in Table 4. The displacement ductility factor μ is defined as the ratio of the displacement at ultimate stage Δ_u and that at the yield stage Δ_y , where the former is obtained at 85% of the maximum capacity after reaching a peak load. The yield displacement is determined by the tangent method and the definition of the yield point can be found in Reference [11]. According to ASCE/SEI 41[23], the ductility capacity of the tested specimens can be classified as low if μ is less than 2; moderate if it is between 2 and 5, and high if μ is greater than 5.

As shown in Table 4, the tested specimens exhibited good ductility with the ductility factors varying between 3.97 and 5.09. The increase of the column embedment depth to be larger than $1.0D$ had no significant effect on the ductility of the specimens. The confinement of the potential plastic hinges using steel rings and CFRP sheets delayed the local plastic buckling of the tested specimens and thus improved the ductility of the specimens. The ductility factor of specimen CFDST2 was 33.4% larger than that of specimen CFDST1. The un-bond region left in the footing of specimen CFDST5 also resulted in an improved ductility factor equal to 5.09, which was 28.2% greater than that of specimen CFDST3.

3.6 Energy dissipation capacity

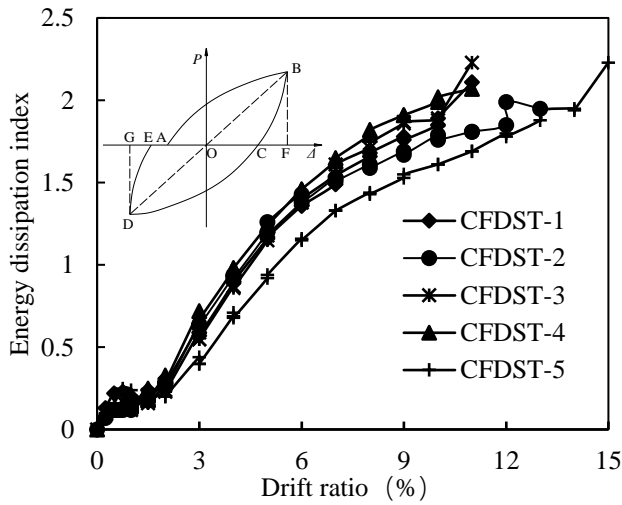
The energy dissipation capacity of the tested specimens under cyclic loadings was evaluated by two indices: energy dissipation index E_h and cumulative dissipated energy. The energy dissipation index E_h is defined as the ratio of total energy dissipation (area S_{ABCDE}) at the first cycle of each drift level to the corresponding elastic potential energy (areas $S_{OBF} + S_{ODG}$), as shown in Fig. 7a. The total energy dissipation is the area enclosed by the load-deformation

hysteresis loops of specimens. The specimens with a larger energy dissipation index E_h usually show a greater ability to dissipate energy.

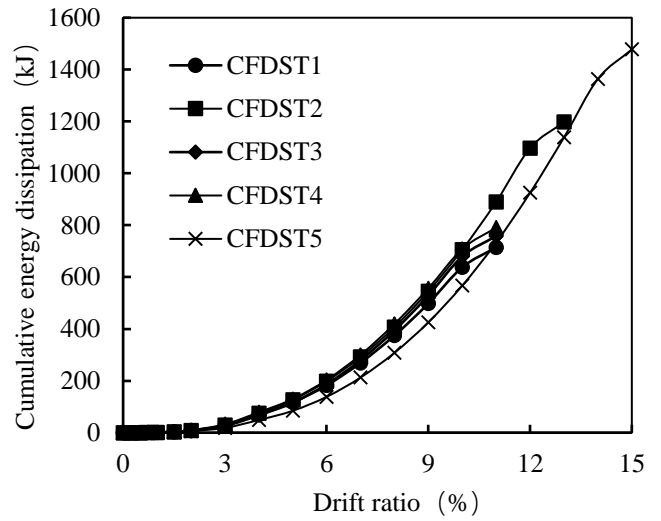
As seen from Fig. 7, when the lateral drift ratios were less than 2%, the tested specimens were almost elastic and the dissipated energy of the specimens was very small. When the applied drift ratios larger than 2%, both the energy dissipation index E_h and cumulative dissipated energy of each specimen increased obviously with the increase of the applied drift ratios, and the energy dissipation index did not show obvious degradation with the increase of the number of cycles at each lateral drift ratio. The comparison of specimens CFDST1 and CFDST2 showed that at the drift ratio less than 2.0%, these two specimens had the same energy dissipation index and cumulative dissipated energy due to the gap left between the steel rings and the column base in specimen CFDST2. However, at the large drift ratios, since the steel rings effectively delayed the local buckling of the column base, specimen CFDST2 achieved a cumulative energy dissipation capacity much better than specimen CFDST1. At the failure condition, the cumulative dissipated energy of CFDST2 was 1198 kJ, which was 1.68 times that of specimen CFDST1. However, the energy dissipation index of specimen CFDST2 was inferior to that of specimen CFDST1 due to the increase of the loading capacity and the elastic potential energy. The increase of the embedment depth and the use of CFRP sheets showed slight improvement in the energy dissipation capacities of the tested specimens, as evidenced by the test results of specimens CFDST1, CFDST3 and CFDST4. Specimen CFDST5 exhibited lower energy dissipation index and energy dissipation capacity when compared with other specimens at the small drift ratios; however, this specimen had the best deformation capacity and thus had the largest cumulative energy dissipation equal to 1478 kJ prior to failure. Thus, the detail using the un-bond region between the concrete footing and the column base is the simplest and the most effective method to enhance the energy dissipation capacity of the CFDST columns in socket foundations.

Table 4
Test results of specimens

Specimens	Loading direction	P_y (kN)	P_{max} (kN)	Δ_y (mm)	Δ_u (mm)	μ	Average μ
CFDST1	positive	262.48	310.03	31.1	136.12	4.38	3.98
	negative	-262.13	-311.54	-41.8	-149.56	3.58	
CFDST2	positive	277.87	350.51	36.2	163.21	4.51	5.31
	negative	-261.24	-348.99	-28.9	-176.78	6.12	
CFDST3	positive	262.11	327.71	34.2	136.12	3.98	3.97
	negative	-249.84	-326.08	-34.3	-136.12	3.97	
CFDST4	positive	258.38	320.71	26.1	136.23	5.22	4.40
	negative	-259.26	-320.36	-37.9	-135.98	3.59	
CFDST5	positive	221.14	338.56	30.0	190.41	6.35	5.09
	negative	-255.34	-336.79	-49.9	-190.41	3.82	



a) Energy dissipation index



b) Cumulative energy dissipation

Fig. 7 Energy dissipation of tested specimens

3.7 Strain responses

The monitoring of the strains of the steel tubes can reveal the stress distribution of the tested specimens under cyclic loads. The labels of the strain gauges on outer and inner steel tubes at the embedded regions and the plastic hinge zones are presented in Fig. 8 and the typical strain distributions of outer and inner steel tubes at the embedded regions are presented in Figs. 9 and 10. The steel bars in the concrete footings got the strain values lower than $1000\mu\epsilon$ even at the failure conditions of the tested specimens and thus the strain distribution of the steel bars were not shown herein. According to the material tests, the outer and inner steel tubes yielded when the strain values larger than $1490\mu\epsilon$ and $1340\mu\epsilon$, respectively. It can be found that both the strain values of the outer and inner steel tubes reduced with the increase of the distances to the top surfaces of the footings. The outer and inner steel tubes yielded at the regions within about $1.0D$ embedment depth when the applied drift ratios were larger than 2.0%, as evidenced by Fig. 9a. The comparison between the strain distribution of specimens CFDST1 and CFDST3 shown in Figs. 9b and 9c can be found that the strains of the inner steel tubes in the embedded region increased much more rapidly when the embedment depth of the column base increased. This result indicated that the increase of the embedment depth could more effectively motivate the contribution of inner steel tubes. As for the strain at the plastic hinge zones, the outer steel tubes for all specimens yielded at the measured zones 350mm above the footing surfaces. However, for the inner steel tubes, the strain distribution of the tested specimens showed significant difference due to the different connection details. As shown in Fig. 10, the use of steel rings and CFRP wraps resulted in larger strain values at the column-

footing surfaces, and the un-bond region left in specimen CFDST5 resulted in smaller strain value of the inner steel tube at the plastic hinge above the footing. It can be also found that at the drift ratios lower than 1%, the strain of inner steel tube was nearly zero, indicating that the contribution of inner steel tubes to the strength and initial stiffness cannot effectively motivated.

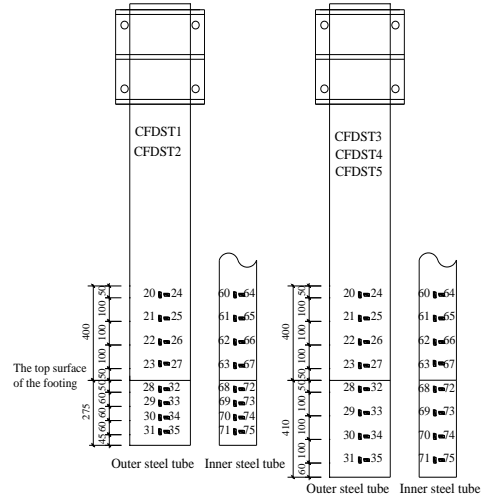


Fig. 8 Labels of strain gauges on outer and inner steel tubes

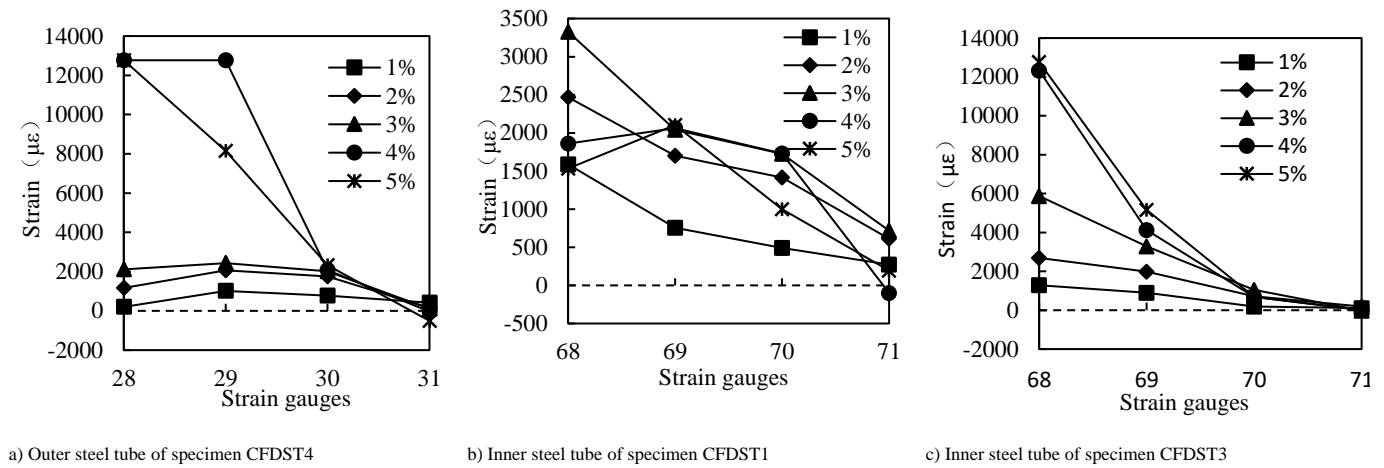


Fig. 9 Typical strain distributions of steel tubes at embedded regions

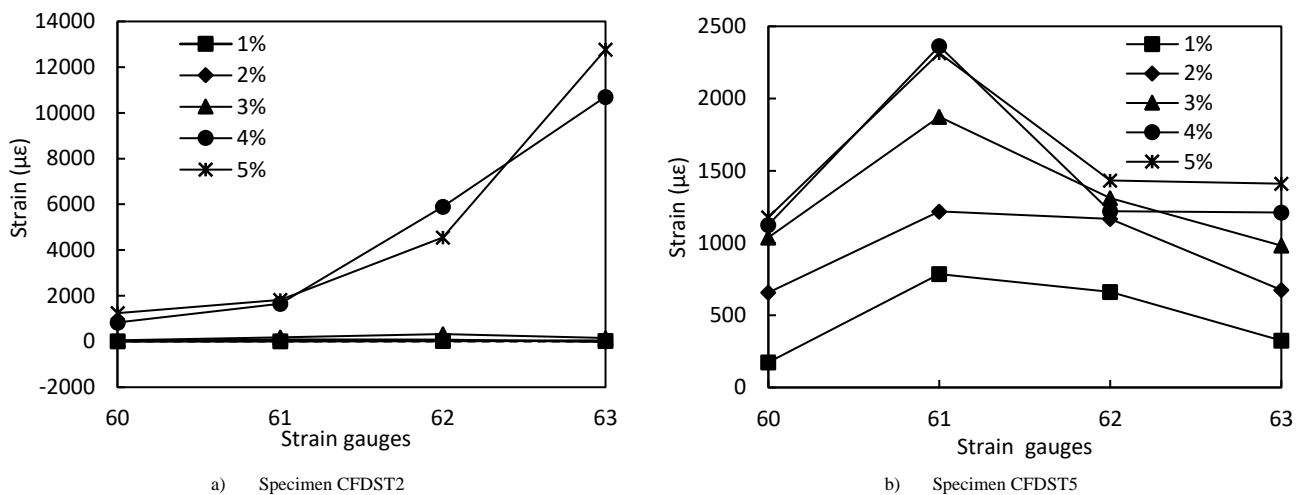


Fig. 10 Typical strain distributions of inner steel tubes at potential plastic hinge zones

4. Summary and conclusions

An experimental investigation on the seismic behavior of five precast concrete filled dual steel tube columns in socket foundations was conducted. The effects of the embedment depths and the details of column bases on the seismic behavior were evaluated. The following conclusions can be drawn from this study.

- The type of socket foundation is a viable choice for precast CFDST columns. The embedment depth of $1.0D$ is adequate to achieve the column plastic hinge failure and both the outer and the inner steel tubes of the tested specimens yielded in the embedded regions and the plastic hinge zones at the final conditions. The further increase of the embedment depth larger than $1.0D$ had no significant effect on the seismic behavior of the precast CFDST columns in socket foundations.
- The use of steel rings can effectively prevent the local elastic-plastic buckling of outer steel tubes, and thus can effectively improve the deformation capacity, ductility and energy-dissipation capacity of the specimens.
- The use of CFRP wraps had no significant effects on the load-deformation responses of the tested specimens due to the gradual fracture of the fibers but resulted in fatter and more stable moment-curvature relationship curves at the plastic hinges.
- The un-bond region left in the concrete footing can enlarge the plastic hinge zone at the column base and thus can significantly improve the deformation and the energy dissipation capacities of the specimen.
- All of the tested specimens in socket connections exhibited initial stiffness lower than the theoretical elastic values, and for design purposes a coefficient α should be taken to account for the effectiveness of the socket connections.

Acknowledgments

The authors would like to express their sincere appreciation for the financial support from the Fundamental Research Funds for the Central Universities (Grant number: 2017XKQY051). The experimental work described in this

paper was conducted at the Jiangsu Key Laboratory of Environmental Impact and Structural Safety in Civil Engineering in the China University of Mining and Technology, which is supported by a Project Funded by the Priority Academic Program Development of Jiangsu Higher Education Institutions (PAPD). Thanks are extended to the staffs and the students at the laboratory for their help during the test preparation and completion. The collaborative research was also facilitated by Jiangsu collaborative innovation center for building energy saving and construction technology.

References

- [1] Elchalakani M., Zhao X.L. and Grzebieta R., "Tests on concrete filled double-skin (CHS outer and SHS inner) composite short columns under axial compression", *Thin-Walled Structures*, 40(5), 415-441, 2002.
- [2] Zhao X.L., Tong L.W. and Wang X.Y., "CFDST stub columns subjected to large deformation axial loading", *Engineering Structures*, 32(3), 692-703, 2010.
- [3] Kim, J.K. Kwak H.G. and Kwak J.H., "Behavior of hybrid double skin concrete filled circular steel tube columns", *Steel & Composite Structures*, 14(14), 191-204, 2013.
- [4] Ho J.C.M. and Dong C.X., "Improving strength, stiffness and ductility of CFDST columns by external confinement", *Thin-Walled Structures*, 75(75), 18-29, 2014.
- [5] Ren Q.X., Hou C., Lam D. and Han L.H., "Experiments on the bearing capacity of tapered concrete filled double skin steel tubular (CFDST) stub columns", *Steel & Composite Structures*, 17(5), 667-686, 2014.
- [6] Essopjee Y. and Dundu M., "Performance of concrete-filled double-skin circular tubes in compression", *Composite Structures*, 133, 1276-1283, 2015.
- [7] Hassanein M.F., Kharoob O.F. and Gardner L., "Behaviour and design of square concrete-filled double skin tubular columns with inner circular tubes", *Engineering Structures*, 100, 410-424, 2015.
- [8] Hassanein M.F., Elchalakani M. and Patel V.I., "Overall buckling behaviour of circular concrete-filled dual steel tubular columns with stainless steel external tubes", *Thin-Walled Structures*, 115, 336-348, 2017.
- [9] Pons D., Espinós A., Albero V. and Romero M.L., "Numerical study on axially loaded ultra-high strength concrete-filled dual steel columns", *Steel & Composite Structures*, 26(6), DOI: 10.12989/scs.2018.26.6.705, 2018.
- [10] Han L.H., Yang Y.F., "Cyclic performance of concrete-filled steel CHS columns under flexural loading", *Journal of Constructional Steel Research*, 61(4), 423-452, 2005.
- [11] Han L.H., Huang H., Tao Z. and Zhao X.L., "Concrete-filled double skin steel tubular (CFDST) beam-columns subjected to cyclic bending", *Engineering Structures*, 28(12), 1698-1714, 2006.

- [12] Guerrini G., Restrepo J.I., Massari M. and Vervelidis A., "Seismic behavior of posttensioned self-centering precast concrete dual-shell steel columns", *Journal of Structural Engineering*, 141(4), 04014115, 2015.
- [13] Lehman D.E. and Roeder C.W., "Foundation connections for circular concrete-filled tubes", *Journal of Constructional Steel Research*, 78(11), 212-225, 2012.
- [14] Li X., Wu Y.P., Li X.Z., Xia J. and Lv H.L., "Punching shear strength of CFT bridge column to reinforced concrete four-pile cap connections", *Journal of Bridge Engineering*, 22(8), 04017036, 2017.
- [15] Canha R.M.F., Jr K.D.B. and Debs M.K.E., "Analysis of the behavior of transverse walls of socket base connections", *Engineering Structures*, 31(3), 788-798, 2009.
- [16] Tao Z., Han L.H. and Zhao X.L. "Behaviour of concrete-filled double skin (CHS inner and CHS outer) steel tubular stub columns and beam-columns", *Journal of Constructional Steel Research*, 60(8), 1129-1158, 2004.
- [17] Choi K., Xiao Y. and He W., "Confined concrete-filled tubular columns", *Journal of Structural Engineering*, 131(3), 488-497, 2005.
- [18] BS5400, "Concrete and Composite Bridges, Part 5", British Standard Institute, London, UK, 2006.
- [19] AIJ, "Recommendations for Design and Construction of Concrete Filled Steel Tubular Structures", Architectural Institute of Japan, 1997.
- [20] AISC-LRFD, "Load and Resistance Factor Design (LRFD) Specification for Structural Steel Buildings", Chicago: American Institute of Steel Construction, Inc. 2016.
- [21] Eurocode 4, "Design of Composite Steel and Concrete Structures, Part 1.1: General Rules and Rules for Buildings (Together with United Kingdom National Application Document), DD ENV 1994-1-1:1994", London: British Standards Institution, 2005.
- [22] Hsu H.L. and Lin H.W., "Improving seismic performance of concrete-filled tube to base connections", *Journal of Constructional Steel Research*, 62(12), 1333-1340, 2006.
- [23] ASCE/SEI 41, "Seismic Rehabilitation of Existing Buildings", Reston, VA., 2013.

FLEXURAL STRENGTH OF WEATHERED GRANITES UNDER WETTING – DRYING CYCLES: IMPLICATIONS TO STEEL STRUCTURES

Sarkar Noor-E-Khuda ^{1,*} and Faris Albermani ²

¹ School of Engineering and Technology, Central Queensland University, Perth, Australia

² School of Engineering and Technology, Central Queensland University, Mackay, Australia

* (Corresponding author: E-mail: s.noorekhuda@cqu.edu.au)

ABSTRACT

Deterioration of stone veneer cladding panels due to environmental weathering can lead to expensive restoration work, serious risks from falling debris and compromises the performance of high-rise steel and concrete structures. The influence of wetting – drying cycles (WDC) on the flexural tensile strength of thin granite cladding panels is investigated. Forty-five specimens of Imperial Black, Calca and Grandee type Australian granite panels were used in the experimental program. Total 15 specimens served as control reference, while 30 specimens were subjected to 100 WDC in two separate stages. The wetting cycles were conducted in contact with tapwater and acidified solution of pH \approx 4.5, while the drying cycles were conducted using a controlled drying chamber at 40 °C. Ultrasonic pulse velocity (UPV) and flexural tensile strength of the control, and weathered specimens were measured after the 50th and 100th weathering cycle of WDC. It was noticed that the thin granite cladding panels experienced limited flexural strength reduction accompanied by changes in UPV and weight loss. A correlation between flexural strength and UPV of the unweathered and weathered WDC specimens is proposed which can be useful in on-site assessment of granite cladding panels during the service life of the primary steel structure.

ARTICLE HISTORY

Received: 27 February 2018
Revised: 20 October 2018
Accepted: 25 October 2018

KEYWORDS

Ultrasonic pulse velocity;
Wetting – drying cycles;
Granite;
Flexural strength;
Weight loss

Copyright © 2019 by The Hong Kong Institute of Steel Construction. All rights reserved.

1. Introduction

With the advent of modern building technologies such as the skeletal steel frame system, bearing walls have given way to curtain walls, and thick stone walls are often replaced by thin stone structural veneer cladding panels while retaining the masonry appearance of the structure. Damage and deterioration of the stone veneer cladding panels due to environmental weathering (physical, chemical and biological) and improper design can lead to expensive restoration work as well as serious risks from falling debris [1]. Numerous incidents of façade/cladding failure due to deterioration of the stone cladding panels and collapse/corrosion of the supporting steel/aluminium anchorage system have been reported around the world [1-5]. With the recent fire safety concerns regarding aluminium sandwich panels cladding on tall buildings around the world, it is expected that a renewed interest will emerge in the use of thin granite veneer cladding as an alternative safe façade solution on existing and new high-rise buildings.

The veneer cladding system installed on a steel or concrete frame structure is usually a non-loadbearing system. Attention to detailing, anchor design and panel size selection is required to eliminate possible secondary stresses resulting from coupling between the primary structure and the cladding system. Two type of metal anchoring systems are usually utilised to attach thin granite veneers panels to the frame. These are; kerf anchors and rear fixed pin anchors. Kerf anchor requires attachment of a metal bracket to a slot cut into the edge of the granite panel. An inclined stainless steel pin is usually attached to the rear face of the panel when a rear fixed pin anchor is used [1].

Granite is the most preferred natural stone for thin structural veneer claddings (Pires et al. [4]). Being structurally superior over other stone veneers, granite received fewer research attention. As thin structural veneer claddings are usually installed on the exterior of buildings, they inevitably are subjected to environmental weathering [5]. It is therefore important to quantify the design strength of the granite veneer cladding panels and the effect of wetting–drying cycles on the strength. This will lead to better design and less failure incidents. Although granite veneer panels are used as a cladding, and seldom considered as a structural element, being thin panels raise concern over its flexural capacity under wind loading. Whether the flexural strength of thin granite veneer cladding panels is influenced by wetting–drying cycles (WDC) has not been widely addressed.

The anisotropic material properties of granite depend heavily on the general geology at the source, and the local geological features at the scale of fissures and cleavage planes which can alter due to weathering. Material characterisation of the thin granite panels through destructive testing such as four–point bending test (which is preferred in conventional engineering practice) can be impractical, considering the wide variety of granites available. Moreover, the results obtained through random samples from a particular batch may fail to represent the other available granite types, which means individual tests have to be

conducted on each variety/batch. Alternatively, a less costly investigation can be carried out using non-destructive testing (NDT) techniques. Among the NDT techniques the ultrasonic pulse velocity (UPV) has facilitated in detailed examination of civil structures [6], material characterisation and damage detection [7 – 10], and health monitoring [11,12]. Vasconcelos et al. [8] and Chen et al. [10] successfully assessed the strength, stiffness and fracture energy of granite, and estimated crack depth, direction and thickness of damaged surface layers, respectively using UPV.

A number of studies have reported of the variation in mechanical properties of thin structural stone veneers due to freezing/thawing [5], salt crystallisation [12], wetting/flooding [13], heating [14] and simulated acid rain [15]. Franzoni and Sassoni [15] tested several limestone, sandstone and marble specimens (of different microstructural characteristics) in a simulated acid rain test. It was shown that all the stone specimens experienced higher weight loss with increased acidity of the solution and exposure duration, which indicates possible alteration of the internal grain structure/fissure/micro-cracks and degradation of the mechanical strength properties. Vasconcelos et al. [8], from series of destructive and non-destructive tests, derived the direct tensile and compressive strength of granite specimens and proposed correlation between the strength parameters and UPV. It was shown that the direct tensile strength of granite increased exponentially and the compressive strength increased linearly, with UPV. Noor-E-Khuda et al. [5] proposed a linear relation between flexural strength and UPV for thin granite cladding panels subjected to accelerated freeze-thaw cycles (FTC). The study also showed that the commonly used Australian granite cladding panels suffered a considerable loss of flexural strength under FTC. This has prompted the current investigation to assess the influence of wetting – drying cycles on the flexural strength of the same types of Australian granite cladding panels.

Moisture change that occurs under cyclic wetting and drying can weaken the overlying rock by expansion and contraction. Water itself is a good solvent and is known to be the principal agent in physical/chemical weathering. It provides, a medium in which reactions can occur at a faster rate (reactions are usually faster in liquid phase than in solid phase) and a medium of transport to remove the reaction products and perpetuating a state of inequilibrium (promoting the forward reaction to take place). Hence, the duration of wetting exposure can have stronger influence on the mechanical properties of the stone veneers and will be different based on the geographic location and climatic condition. While the standard EN 13919:2002 [16] provides test method for intensive acid attack on stone, researchers used varied test procedures to simulate test environment appropriate for the prevalent local conditions. In-fact, [17], [15], [18] used 3 weeks; 1, 3, 7 and 14 days; and 5 days periodic wetting, respectively in their research. The periodic wetting does not truly reflect the situation experienced by the cladding panels in the real environment, as rainwater or cleaning water seldom deposits on the panel surface except as droplets due to localised imperfections on the panel surface. Instead rainwater

comes in-contact with the panel surface in frequent cycles and runoff from the surface, possibly transporting any deposit away from the surface. Different acid solution of pH = -1 ~ 5.6 were used to simulate the wetting acid solution, for example [15], [18] and [19] used acid solutions of pH value 5.6, 4.5 and, -1 and 3, respectively. It was also reported that distilled water with pH = 6.5 caused considerable material loss in calcareous stones [18]. Several researcher concluded that pH = 4 ~ 5 represent the environment of the major European [20] and Australian [21] cities. The accelerated WDC used in this research is an innovative method that suits the Australian conditions.

The effects of WDC on the flexural strength of three commonly used Australian granite cladding panels are investigated in this paper. This work compliments a previous investigation on the effect of FTC on the same three types of Australian granite [5]. The specimens were manually subjected to WDC, where the effect of wetting the samples in tapwater and acidified solution and drying is evaluated. The drying cycles were achieved through a controlled heating chamber. Based on the test results, the effect of WDC on strength is assessed and a correlation between UPV and strength of WDC weathered granite specimens is proposed.

2. Experimental Program

In this section WDC weathering, destructive and non-destructive tests of the thin granite cladding specimens are presented and discussed.

2.1. Material Description

Three common Australian granite types; Calca, Imperial Black (or Adelaide Black) and Grandee were used in this study. Petrographic description of the selected granite types is summarised in Table 1. Key features of these three stones are high compressive strength, hardness, durability, visible crystalline structure with interlocking crystals of medium to coarse grain and highly polished surfaces. The stones can be distinguished by their appearances as shown in Fig. 1.

2.2. Test Specimens and Accelerated Wetting-Drying Cycles (WDC)

Total 45 specimens, 15 for each granite type were randomly selected from a pile of granite coupons which were stacked outdoors under exposure to natural weather conditions. The nominal dimensions of a typical coupon is: 400 × 100 × 30 mm (length × width × thickness). Only one face (400 × 100 mm) of each coupon is polished. The specimens were grouped into three batches: tapwater, acidified and control groups. A total of 30 specimens (10 of each stone type, S1–S10) were subjected to the WDC while another 15 control specimens (5 of each stone type, C1–C5) were preserved as the unweathered reference. Each specimen was weighed and, their dimensions were carefully checked and recorded according to the flexural test requirements of ASTM C880/C880M [22]. The tapwater and acidified group specimens were then subjected to the WDC in two separate stages. Fig. 2 and Fig. 3 shows the WDC cycles used in the experimental program and the experimental setup, respectively.

Table 1
Petrographic description

Granite Type	Alternative Name	Quarry	Geological Classification	Primary Minerals	Appearance
Imperial Black	Adelaide Black	Black Mountain, 85 km North and North-East of Adelaide	Monzogabbro	Plagioclase feldspar Pyroxene K-feldspar	Dark black Highly polishable.
Calca	Calca Red Empire Red Dragon Red Autumn Brown	Calca, South Australia	Granite	Orthoclase feldspar Quartz	Pink/ light reddish
Grandee	Ashcroft Grandee	District of Mullandry, 38 km from Forbes in central-western NSW.	Quartz Monzogabbro Geologically Devonian quartz diorite	Plagioclase feldspar Pyroxene Quartz (low)	Dark color Highly polishable.



Fig. 1 Granite types (a) Calca; (b) Imperial Black; (c) Grandee [5]

Fig. 2 (a) shows Stage I of the weathering process that consisted of fifty WDC. In each wetting cycle as shown in Fig. 3(a), the specimens were grouped according to their granite type and were fully immersed in separate tanks of tap water for one hour in room temperature. This process was done manually with fresh tap water used to fill the tanks and was discarded at the end of each wetting cycle. In each drying cycle, the specimens were placed on shelves in a drying chamber as shown in Fig. 3b. Warm air was blown onto the specimens and the temperature in the chamber was maintained at 40 °C for three to six hours. At the end of the fiftieth cycle, the specimens were left to dry in open air for 48 hours, then weighed. Three specimens from each granite type were randomly selected for an interim UPV test.

Fig. 2 (b) shows Stage II of WDC. In Stage II, tap water was used in wetting cycles for 5 specimens of each granite type while for the remaining 5 specimens acidified water was used in the wetting cycle. Different tanks were used in Stage II for different granite types and groups (i.e., tap water and acidified groups).

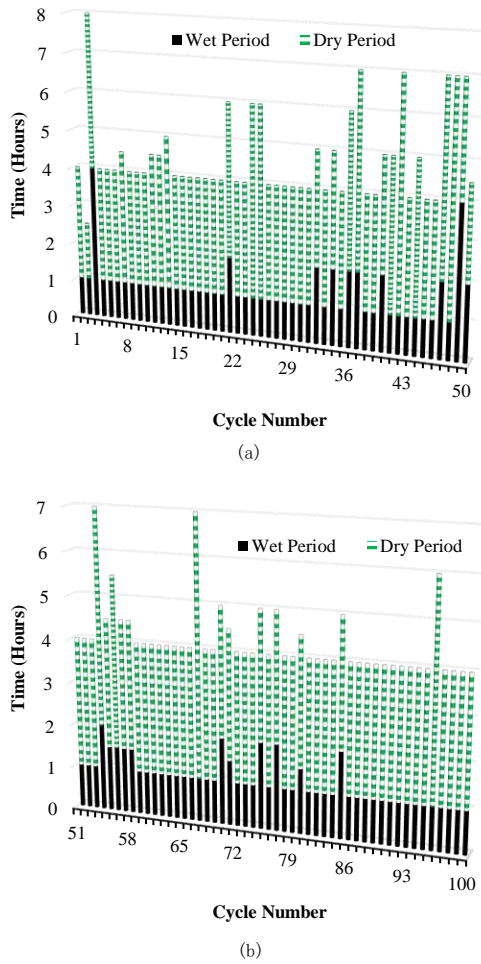


Fig. 2 Wetting – drying cycles (a) Stage – I; (b) Stage – II

The acidified solution in each tank was a mixture of tap water, HNO_3 and H_2SO_4 . Similar acid solution ($\text{H}_2\text{SO}_4 + \text{HNO}_3 + \text{H}_2\text{O}$) and ($\text{H}_2\text{SO}_3 + \text{HNO}_3 + \text{H}_2\text{O}$) were also used in [15] and [17], respectively while [18] and [23] adopted a sulphuric acid solution ($\text{H}_2\text{SO}_4 + \text{H}_2\text{O}$) and a nitric acid solution ($\text{HNO}_3 + \text{H}_2\text{O}$), respectively in their studies. It was further reported in [17] that the HNO_3 present in the acid solution acted as a catalyst of the H_2SO_3 reaction, while the presence of H_2SO_4 caused more damage [18]. The acidified solution used in each tank was a mixture of 40.5 mL of 1.0M, HNO_3 , 27 mL of 1.0 M, H_2SO_4 and 27 L of H_2O (tap water). The pH of this solution was measured using pH paper and was maintained at $\text{pH} \approx 4.5$ to simulate typical acid rain. The acidified solution was freshly mixed for each acidified wetting cycle and discarded at the end of each cycle. While researchers [15] and [17] adopted measures to maintain the pH level during periodic wetting, such measure was not required for the frequent wetting cycles. The ratio of HNO_3 to H_2SO_4 was based on the concentration of atmospheric $\text{SO}_2 : \text{NO}_x = 1 : 2$, that reflect the air quality in a typical Australian urban environment [21] where buildings with external granite cladding are likely to be found.

At the end of the one 100th cycle, the specimens were left to dry in open space for 48 hours then weighed. Full 100 °C periodic drying similar to those reported in [15, 17, 18] was avoided, as such high temperature is not an actual representation of the local outdoor climate conditions. Moreover, strong heating cycles [14] would potentially minimise the influence of the wetting cycles.

2.3. Ultrasonic Pulse Velocity (UPV) Testing

The UPV test setup consisted of a Panametrics 5077 PR pulser-receiver with two contact transducers and a Tektronix TDS210 LCD oscilloscope. UPV was measured by placing the transducers on the opposite parallel faces of the specimen. The resonance frequency of the transducers was checked against the UPV test requirements of ASTM D2845-05 [24]. The ultrasonic waves were transmitted through the test specimen by transducer-1: acting as the emitter and received by transducer-2: acting as the receiver. Trial UPV test was performed with the transducers coated with Vaseline and generic gel couplant (Sonotech Ultragel II). The generic gel couplant demonstrated improved connectivity with the test specimen which was used throughout the NDT program. UPV measurements were taken along the width and thickness of the specimen, and

the average of three independent readings in each direction was recorded.

2.4. Flexural Strength Testing

All 45 specimens, including those in the control group, were tested destructively to failure by flexure according to ASTM C880/C880M [22]. A four-point bending test rig placed in Instron 5500R/6027 testing machine was used as shown in Fig. 4. The 4-point bending test was performed on the specimens with a span length (L) of 320mm, which is 10 times the specimen's thickness. The overall length of each specimen was limited to 400mm. A rigid steel loading frame was used to facilitate the roller support arrangement; the two point loads ($W/2$ each) were placed 80mm ($L/4$) inward from each support and 160mm ($L/2$) apart from each other. All the specimens were tested with the polished face down, at a monotonic loading rate of 0.05 mm/min consistent with ASTM recommendation of 4.14MPa/min. The maximum applied load was measured from the load cell data, while the length, orientation and the average thickness at the failure plane were measured and recorded at the completion of each test.

The flexural tensile strength (f_t) of the specimen was calculated using eq 1, where, W is the maximum applied load on the specimen, L , b and t are the length, width and thickness dimensions of the specimen, respectively and l is the actual length of the inclined failure plane across the tension face.

$$f_t = \frac{3WLb}{4l^2t^2} \quad (1)$$

Equation 1 accounts for the fact that the failure plane is usually not perpendicular to the span, which was observed in all 45 granite specimens [5].

3. Test Results and Discussions

The test results of the 15 unweathered (control) and 30 weathered specimens are discussed in this section.



(a)



(b)

Fig. 3 Experimental setup (a) Wetting; (b) Drying

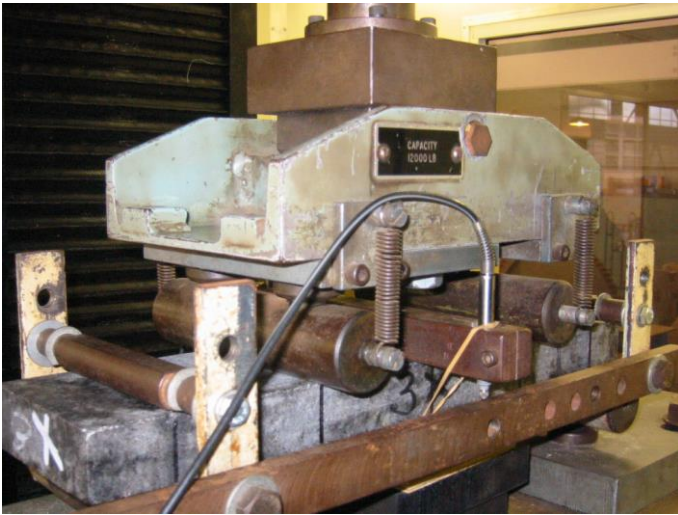


Fig. 4 Four-point bending test arrangement

3.1. Flexural Strength

Figs. 5 shows the average flexural strength, f_t of the unweathered and weathered granite specimens obtained from the four-point bending tests. The results demonstrate that f_t of the Imperial Black, Calca and Grandee control specimens was 16.18 MPa, 9.73 MPa and 15.11 MPa, respectively. For the weathered tap water group specimens, f_t was 14.25 MPa, 9.99 MPa and 15.43 MPa; while for the acidified group f_t was 14.55 MPa, 9.08 MPa and 15.2 MPa, respectively. No simple trend could be established to account for the effect of WDC by tapwater and acidified solution within each granite group. Based on the results shown in Fig. 5, it can be inferred that Imperial Black was the only granite type affected by the WDC. The Imperial Black tapwater group experienced the highest loss in flexural strength of 11.96%. There was a slight loss in flexural strength of Calca acidified group of 6.7%; although the tapwater group shows 2.6% increase in f_t . Flexural strength of the weathered tapwater and acidified groups of Grandee increased by 2.2% and 0.6%, respectively. Factors such as the highly polished surface, grain distribution and porosity of the stones and the accumulation of salts [17, 25] may have contributed towards this trend. The non-porous surface of Imperial Black and Grandee samples provided resistance against water and acids attack, whereas the semi-porous surface of Calca allowed deposition and accumulation of salts which may be present in tapwater.

3.2. Ultrasonic Pulse Velocity (UPV)

Figs. 6 (a) and (b) show the UPV values for all the Imperial Black specimens measured along the width and the thickness, respectively. UPV is measured at the unweathered state labelled as initial in Fig. 6, and weathered specimens after stage – I and stage – II WDC labelled as interim and tapwater/acidified, respectively. The average UPV of unweathered Imperial Black specimens measured along the width were 5992 ± 94.32 m/s which is consistent with the findings of [5]. It was noticed that the UPV measurements along the width of the specimen was higher than that along the thickness direction. UPV measured across the width of the Imperial Black specimens at the following stages; initial, interim, tapwater and acidified were 16.8%, 14.5%, 14.3% and 14.4% higher than that of the respective measurements taken across the thickness of the specimen. Variation in UPV due to WDC was insignificant, interestingly some of the weathered specimens showed slightly higher UPV value over their unweathered counterpart.

Fig. 7a-c show the average UPV values of the Imperial Black, Calca and Grandee specimens at different stages of weathering. The average UPV values measured along the width and thickness of the specimens are shown in Table 2. Larger standard deviation is observed among the UPV measurements across the thickness of the specimen, than that of the width. The UPV readings were the most consistent within Imperial Black specimens, while readings taken on Grandee specimens showed the highest variation. No difference was expected between the average UPV values of tapwater and acidified groups of each granite type in the initial and interim stages, as they were subjected to identical conditions. However, following Stage – II WDC, differences in UPV values emerged. The average UPV of the acidified group of Calca and Grandee specimens were 0.49% and 0.89% higher than that of the tapwater group, while it was 0.3% lower for the Imperial Black specimens.

3.3. Variations in Weight, UPV and f_t due to WDC

Fig. 8 (a) shows the variation in weight and UPV experienced by the granite specimens at different stages of the WDC, where the positive and negative variation represent the gain and loss in the parameters, respectively. Samples were weighed before the WDC and after the 50th and 100th cycle. The weight losses of the granite specimens were small. Only the Calca acidified group specimens experienced an average weight loss of 1.34% (equivalent to 47g of material). No definitive weight loss pattern could be established. It was also found that several specimens from all granite types experienced slight gain in weight (0.3 – 0.65%) which is consistent with those reported in [17, 26]. Many sources such as incomplete desiccation of samples, change in chemistry of the constituent minerals, accumulation of salt introduced from the immersion liquids during the wetting cycles could contribute to the increase in the weight of the granite specimens.

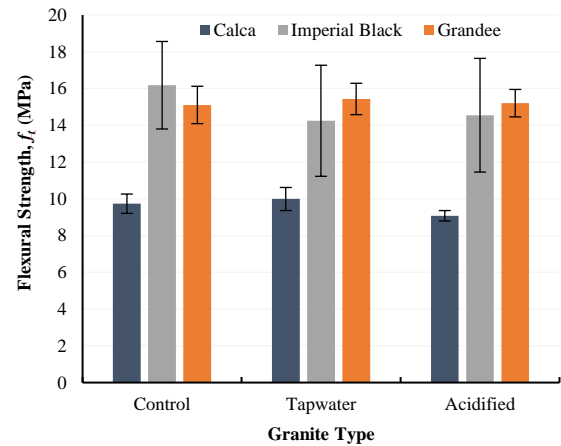
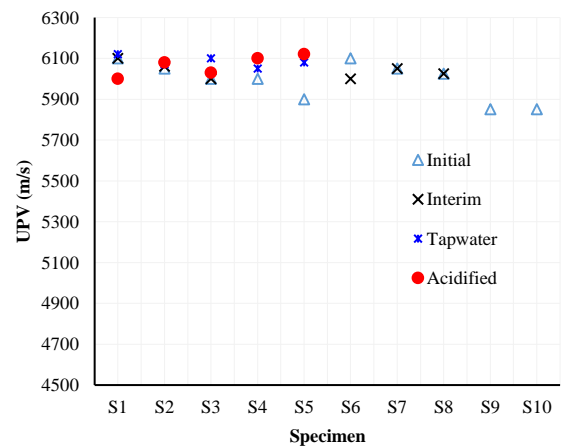
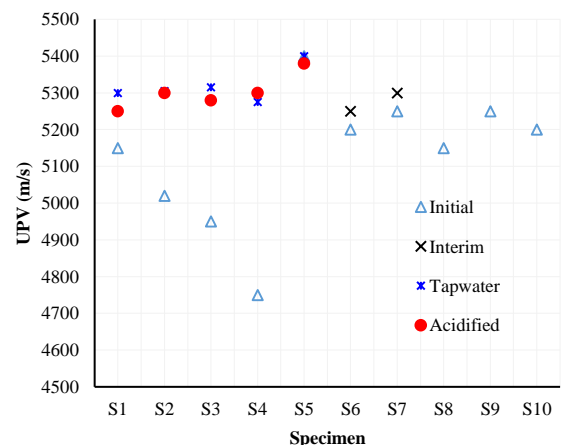


Fig. 5 Flexural strength of granite specimens



(a)



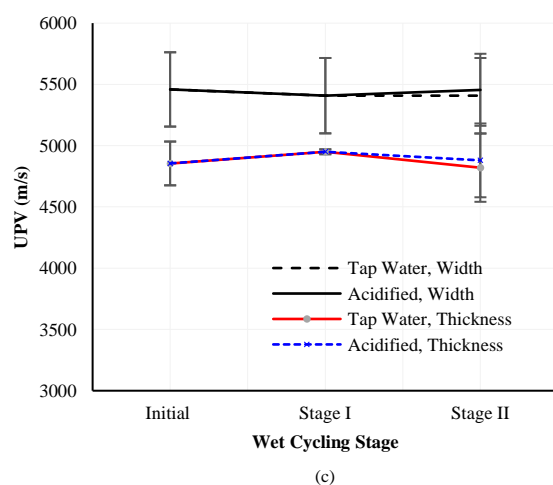
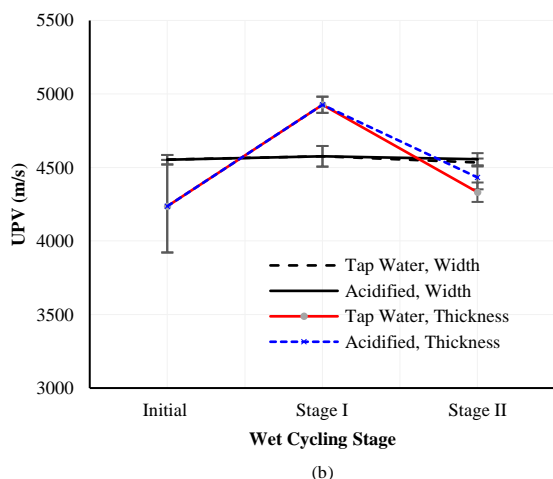
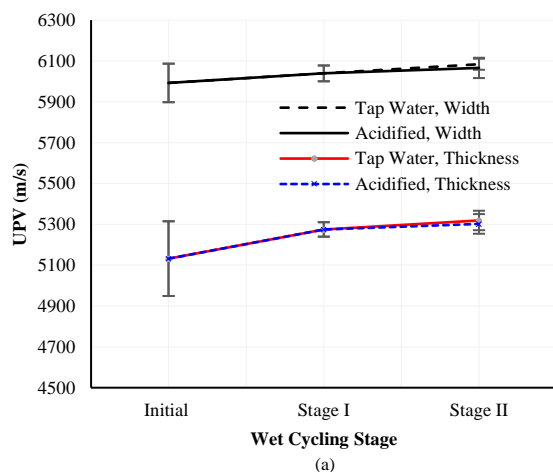
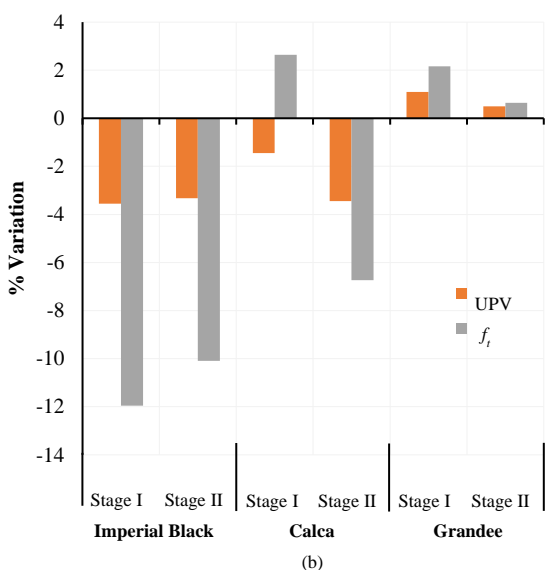
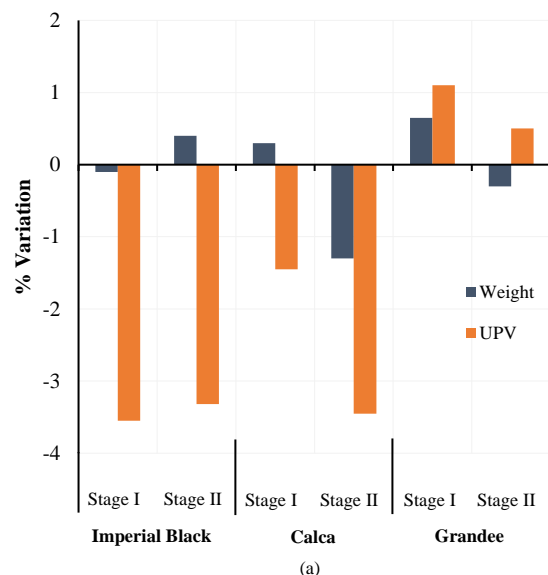
(b)

Fig. 6 UPV of Imperial Black specimens measured along (a) Width; (b) Thickness

Table 2

Average UPV of unweathered and weathered specimens

Granite Type	UPV _{Unweathered} (m/s)		UPV _{Interim} (m/s)		UPV _{Tapwater} (m/s)		UPV _{Acidified} (m/s)	
	Width	Thickness	Width	Thickness	Width	Thickness	Width	Thickness
Imperial Black	5992.5±94.3	5132±182.9	6039.18±38.8	5275±35.3	6084±27	5319±47.6	6066±49.8	5302±48.2
Calca	4553±32.3	4236.8±314.9	4576.25±70.3	4926.7±55.1	4534±27	4332±66.1	4556±41.7	4432±80.2
Grandee	5459±303.2	4885±178.65	5408±307.5	4950±20	5408±307.5	4820±278.4	5456±293.9	4880±301.2

**Fig. 7** Average UPV of unweathered and weathered specimens (a) Imperial Black; (b) Calca; (c) Grandee**Fig. 8** Percentage loss (a) Weight and UPV; (b) Flexural Strength and UPV

Loss in the UPV value in response to the WDC was more prominent than the loss in weight of the specimen. Although no consistent relation could be established between the losses in weight and the losses in UPV. The maximum loss in UPV was recorded for the Imperial Black specimens of 3.55%, after the stage – I weathering, while the acidified group of Calca specimens endured an average UPV loss of 3.45% after the WDC. On the contrary, the tapwater and acidified group Grandee specimens experienced an average UPV gain of 1.1% and 0.5%, respectively.

Fig. 8(b) shows losses in UPV and f_i experienced by the granite specimens at different stages of WDC. The loss in f_i under WDC is higher compared to the loss in UPV. The Imperial Black specimens after the stage – I weathering showed an average 11.96% loss in f_i . A similar trend between UPV and f_i is

observed for Imperial Black and the Grandee specimens unlike that for the Calca specimens. The tapwater group Calca and Grandee specimens experienced an average gain in f_t of 2.64% and 2.16%, respectively. According to Fig. 8(b) the Grandee specimens were the least affected by the WDC.

Fig. 9 shows the variation in f_t and UPV of the granite specimens following stage – I and – II WDC, and the same following FTC weathering reported in [5]. The Fig. shows that losses in f_t and UPV of the granite specimens was more pronounced under FTC than under WDC. The Imperial Black specimens experienced an average loss in f_t of 28.56% due to FTC, which is 2.39 times higher than the losses due to WDC.

3.4. Correlation between UPV in the Width and Thickness Directions

Linear correlation between UPV values measured along the width and the thickness direction of the granite specimens is shown in Fig. 10 and given by eq 2 with $R^2 = 0.709$. The developed relation in eq 2 can be used to predict the UPV value of granite panels along the width when measurement is only possible in the thickness direction.

$$UPV_{Width} = 1.103UPV_{Thickness} - 45.709 \quad (2)$$

3.5. Correlations between UPV and Tensile Strength

Fig. 11 shows the relation between $f_{t,WDC}$ obtained from destructive test and measured UPV along the width of all 45 unweathered and weathered (i.e., tapwater and acidified groups) granite specimens from the WDC testing. Based on the obtained results, a linear correlation is established as shown in Fig. 11 and eq 3 with $R^2 = 0.57$ that can be used to predict the on-site $f_{t,WDC}$ of the granite cladding panels by means of the measured pulse velocity.

$$f_{t,WDC} = 0.0041UPV_{mean} - 8.55 \quad (3)$$

Based on the FTC weathering results the correlation between $f_{t,FTC}$ and UPV of unweathered and weathered granite specimens was reported in [5] as,

$$f_{t,FTC} = 0.0041UPV_{mean} - 9.6345 \quad (4)$$

Performance of the proposed eq 3 for the flexural tensile strength $f_{t,WDC}$ is compared against eq 4 and those proposed by other researchers [8] for the direct tensile strength σ_t (eq 5). A range of UPV between 3000 m/s to 6500 m/s was selected for the comparison.

$$\sigma_t = 0.701e^{(0.00052UPV)} \quad (5)$$

Fig. 12 shows the predicted tensile strength ($f_{t,WDC}$, $f_{t,FTC}$ and σ_t) using Eqs (3), (4) and (5) against the corresponding UPV values, and the results seems reasonable.

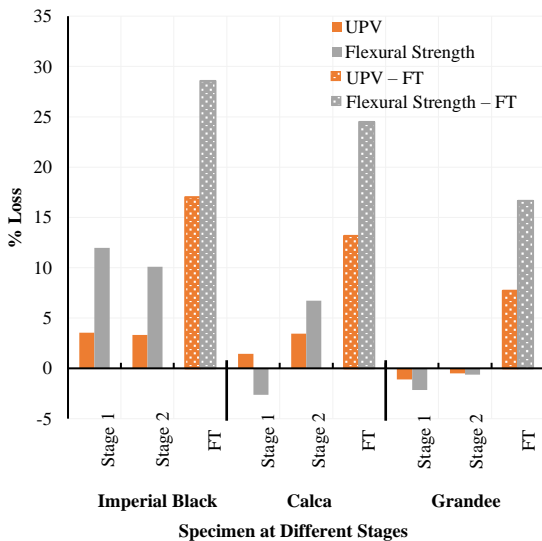


Fig. 9 Percentage loss due to WDC and FTC

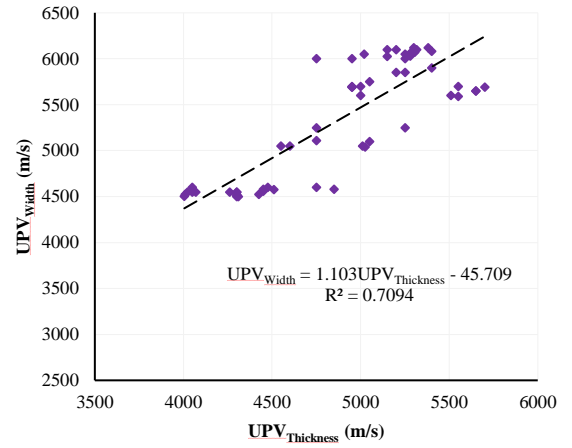


Fig. 10 Correlation between UPV along width and thickness of specimen

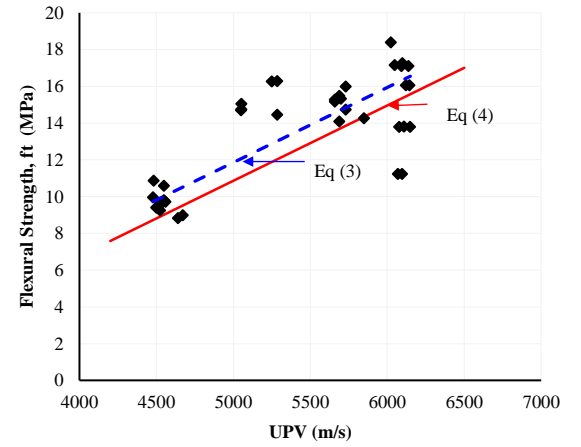


Fig. 11 Correlation between UPV and flexural strength

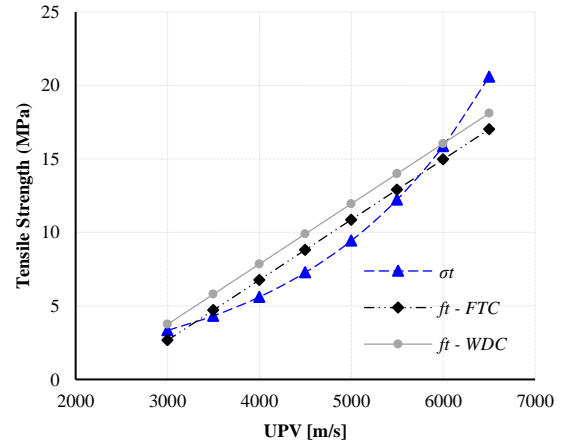


Fig. 12 Predicted direct and flexural tensile strength using UPV

4. Conclusions

The effect of accelerated weathering through WDC on thin granite cladding panels commonly used on high-rise buildings is reported in this paper. A total of 45 specimens, 15 each of Calca, Imperial Black and Grandee type Australian granites were used in the experimental program. The specimens were subjected to total of 100 cycles of wetting and drying in two separate stages. In stage – I, total 30 specimens, 10 from each granite type was divided in two identical groups namely tapwater and acidified, and were subjected to 50 WDC, where the wetting cycles were conducted in tap water. In stage – II, the tapwater and the acidified group specimens from the stage – I weathering, were separately subjected to the next 50 wetting cycles in tapwater and an acidified solution of $pH \approx 4.5$, respectively. All the drying cycles were conducted using a controlled drying chamber. UPV was measured along the width and thickness

of the unweathered and weathered specimens. All 30 weathered and 15 unweathered control specimens underwent destructive flexural testing to determine the flexural tensile strength.

The WDC test results showed slight changes in strength of the granite specimens according to UPV and destructive testing. While the Imperial Black and Calca specimens showed small decline in the flexural strength, no changes were noticed in case of the Grandee specimens. Such behaviour is accompanied by the losses in weight and measured UPV. Difference in UPV measured along the width and thickness of the specimen gives indication of the material anisotropy of the granite specimens.

The WDC test results were compared with those obtained from the FTC test [5]. It is concluded that Imperial Black and Grandee is the most and the least affected granite cladding panel type under weathering. The reduction in flexural

tensile strength of Imperial Black specimens under WDC is 2.39 times lower than that under FTC. A correlation between UPV and flexural strength of unweathered and weathered granite is established, which is slightly different to that obtained from the FTC test program. This can be particularly useful in on-site assessment of granite cladding panels during the service life of the primary steel structure.

Acknowledgements

The authors would like to acknowledge the assistance of Adrian Lau and Gerrit Lebbink in conducting the experimental work and Dr R. Blackwell for his comments and discussion.

References

- [1] Blackwell R., "No Stone Unturned: Towards the Design of Thin Structural Stone Veneers PhD Thesis, University of Queensland, 2005.
- [2] Royer-Carfigni G., "Some considerations on the warping of marble facades: the example of Alvar Aalto's Finland Hall in Helsinki", *Construction and Building Materials*, 13(8), 449-457, 1999.
- [3] Mauko A., Mirtiè B., Mladenović A. and Grell B., "Deterioration of the granodiorite façade case example Maximarket, Ljubljana Propadanje granodioritne fasade tudijski primer Maximarket, Ljubljana", *RMZ-Materials and Geoenvironment*, 53(1), 23-37, 2006.
- [4] Pires V., Rosa L.G. and Dionisio A., "Implications of exposure to high temperatures for stone cladding requirements of three Portuguese granites regarding the use of dowel-hole anchoring systems", *Construction and Building Materials*, 64, 440-450, 2014.
- [5] Noor-E-Khuda S., Albermani F. and Veidt M., "Flexural strength of weathered granites: influence of freeze and thaw cycles", *Construction and Building Materials*, 156, 891-901, 2017.
- [6] Colombo I.S., Main I. and Forde M., "Assessing damage of reinforced concrete beam using "b-value" analysis of acoustic emission signals", *Journal of Materials in Civil Engineering ASCE*, 15, 280-286, 2003.
- [7] Cerrillo C., Jiménez A., Rufo M., Paniagua J. and Pachón F., "New contributions to granite characterization by ultrasonic testing", *Ultrasonics*, 54, 156-167, 2014.
- [8] Vasconcelos G., Lourenço P., Alves C. and Pamplona J., "Ultrasonic evaluation of the physical and mechanical properties of granites", *Ultrasonics*, 48, 453-466, 2008.
- [9] Vasanelli E., Colangiuli D., Calia A., Sileo M. and Aiello M.A., "Ultrasonic pulse velocity for the evaluation of physical and mechanical properties of a highly porous building limestone", *Ultrasonics*, 60, 33-40, 2015.
- [10] Chen J., Xu Z., Yu Y. and Yao Y., "Experimental characterization of granite damage using nonlinear ultrasonic techniques", *NDT & E International*, 67, 10-16, 2014.
- [11] Baldock T.E., Karampour H., Sleep R., Vyltla A., Albermani F., Golshani A., Callaghan D.P., Roff G. and Mumby P.J., "Resilience of branching and massive corals to wave loading under sea level rise—A coupled computational fluid dynamics-structural analysis", *Marine Pollution Bulletin*, 86(1), 91-101, 2014.
- [12] Barbera G., Barone G., Mazzoleni P. and Scandurra A., "Laboratory measurement of ultrasound velocity during accelerated aging tests: Implication for the determination of limestone durability", *Construction and Building Materials*, 36, 977-983, 2012.
- [13] Cardani G., Cantini L., Munda S., Zanzi L. and Binda L., "Non-invasive measurements of moisture in full-scale stone and brick masonry models after simulated flooding: effectiveness of GPR", *Non-destructive Testing of Materials and Structures: Springer*, 1143-1149, 2013.
- [14] Franzoni E., Sassoni E., Scherer G.W. and Naidu S., "Artificial weathering of stone by heating", *Journal of Cultural Heritage*, 14, 85-93, 2013.
- [15] Franzoni, E. and Sassoni, E., "Correlation between microstructural characteristics and weight loss of natural stones exposed to simulated acid rain", *Science of the Total Environment*, 412, 278-285, 2011.
- [16] CEN (European Committee for Standardisation), EN 13919: Natural Stone Test Methods. Determination of Resistance to Ageing by SO₂ Action in the Presence of Humidity, CEN, Brussels, 2002.
- [17] Vazquez P., Carrizo L., Thomachot-Schneider C., Gibaux S. and Alonso F.J., "Influence of surface finish and composition on the deterioration of building stones exposed to acid atmospheres", *Construction and Building Materials*, 106, 392-403, 2016.
- [18] Tecer L., "Laboratory experiments on the investigation of the effects of sulphuric acid on the deterioration of carbonate stones and surface corrosion", *Water, Air & Soil Pollution*, 114(1), 1-12, 1999.
- [19] Alkattan M., Oelkers E.H., Dandurand J.L. and Schott J., "An experimental study of calcite and limestone dissolution rates as a function of pH from -1 to 3 and temperature from 25 to 80 °C", *Chemical Geology*, 151(1), 199-214, 1998.
- [20] Anatolaki C. and Tsitouridou R., "Relationship between acidity and ionic composition of wet precipitation: a two years study at an urban site, Thessaloniki, Greece", *Atmospheric Research*, 92(1), 100-113, 2009.
- [21] Australian Environment Council, Acid Rain in Australia: a National Assessment, AEC Report no.25, Australian Government Publishing Service, Canberra, Australia, 1989.
- [22] ASTM.C880/C880M-15, Standard Test Method for Flexural Strength of Dimension Stone, American Society for Testing and Materials, 2015.
- [23] Xie S., Qi L. and Zhou D., "Investigation of the effects of acid rain on the deterioration of cement concrete using accelerated tests established in laboratory", *Atmospheric Environment*, 38(27), 4457-4466, 2004.
- [24] ASTM.D2845-05, Standard Test Method for Laboratory Determination of Pulse Velocities and Ultrasonic Elastic Constants of Rock, American Society for Testing and Materials, 2005.
- [25] Alonso F.J., Vázquez P., Esbert R.M. and Ordaz J., "Ornamental granite durability: evaluation of damage caused by salt crystallization", *Materiales de Construcción*, 58(289-290), 191-201, 2008.
- [26] Winter G.M., "Determination of the Design Strength of Thin Structural Veneer Cladding Panels", PhD Thesis, University of Queensland, Brisbane, Australia, 2002.

FATIGUE REPAIRING CRAFTSMANSHIP OF DECK-TO-VERTICAL STIFFENER WELD IN THE STEEL BRIDGE DECK

Yi-xun Wang¹, Bo-hai Ji^{1,*}, Zhong-qiu Fu¹ and Yue Yao¹

¹ School of Civil and Transportation Engineering, Hohai University, Nanjing 210098, China

* (Corresponding author: E-mail: bhji@hhu.edu.cn)

ABSTRACT

Experiments and FE analysis were conducted on the fatigue repairing techniques of deck-to-vertical stiffener weld in the steel bridge deck. The steel bridge deck was modeled to analyze cracking reason of deck-to-vertical stiffener weld. The fatigue repairing experiment was carried out on three repairing techniques. The fatigue life and stress distribution of the deck-to-vertical stiffener weld were analyzed and repairing effects were compared. Repairing craftsmanship with different parameters was modeled to study change of stress distribution. Besides, influence of welding residual stress, stop-hole and CFRP reinforcement on fatigue repairing was discussed. The results showed that cracks of welding end on the deck were induced by out of plane deformation while those on the vertical stiffener were caused by combined out-of-plane and in-plane deformation, which was more prone to cracking. Residual tensile stress reached yield strength of steel after re-welding, thus hammering and polishing after re-welding could improve fatigue life of the weld. The re-welding techniques had more favorable repairing effects than stop-hole and CFRP reinforcement.

ARTICLE HISTORY

Received: 22 April 2018
Revised: 9 September 2018
Accepted: 28 October 2018

KEYWORDS

Steel bridge deck;
Vertical stiffener;
Fatigue crack;
Cracking reason;
Repairing techniques

Copyright © 2019 by The Hong Kong Institute of Steel Construction. All rights reserved.

1. Introduction

The orthotropic steel bridge deck is widely applied in long-span steel bridges in the globe for its light self-weight, high strength and convenient construction [1]. The orthotropic steel bridge deck is prone to fatigue damage under daily traffic loads which reduce its service life [2-3]. The deck-to-vertical stiffener weld is one of the fatigue details most likely to be cracking in the steel bridge. An investigation by the Japanese Steel Structure Committee of Civil Society was conducted on the steel bridge deck of Hanshin Expressway and Capital Expressway in 2007. The results indicated that a large number of cracks was detected in the deck-to-vertical stiffener weld [4]. Therefore, it is necessary to study on the fatigue repairing techniques on the deck-to-vertical stiffener weld for its life extension. At present, repairing techniques commonly applied on the steel bridge deck include re-welding, drilling stop-hole, CFRP reinforcement, etc. [5-7]. The crack propagation is slowed down by removing crack tips or increasing local bearing capacity.

A lot of studies have been conducted on fatigue repairing techniques of steel bridge deck by scholars worldwide. Aljabar, NJ [8] researched on CFRP reinforcement on the cracks in steel bridge deck under combination of tensile and shearing stress and a hybrid modal parameter was proposed to estimate fatigue life of the steel bridge deck with initial cracks. J Crain [9] established finite element models of stop-hole to investigate its enhancement for fatigue performance of steel bridge deck and Figured out a method to improve crack arresting effects. To study the bending performance of steel girder by CFRP reinforcement, Yail J. Kim[10] designed 6 steel girders with different parameters for experiment and found that the fatigue response of CFRP-steel interface was bilinear and determined by stress ranges and cycles. Hyun-Chan Park[11] conducted a re-welding experiment on the deck welds and the result indicated that re-welding could effectively improve fatigue performance of welding details. A lot of current research achievements have been applied to fatigue repairing in real bridges, which rarely involves in cracking of deck-to-vertical stiffener weld, though. A series of repairing parameters have been proposed for deck-U rib welds, weld scallop of diaphragm and other typical fatigue details, whereas these repairing parameters are supposed not to be applied directly to the deck-to-vertical stiffener weld since fatigue performance varies a lot in different fatigue details.

Therefore, experiments and FE analysis were carried out on the fatigue repairing techniques of deck-to-vertical stiffener weld in steel bridge deck. The cracking reason of deck-to-vertical stiffener weld was analyzed and improvement of fatigue performance by different repairing craftsmanship was verified by fatigue experiment. As various influence could not be included in the experiment, parameter analysis was carried out by FE analysis. Advice for different fatigue repairing techniques was proposed and reference was provided for fatigue repairing in steel bridge deck.

2. Stress characteristics of deck-to-vertical stiffener weld

2.1. The finite element model

The position and structure of deck-to-vertical stiffener weld in steel bridges are depicted in Fig. 1. The crossing of the vertical stiffener and deck by welds results in great stress concentration and the complex welding workmanship renders great residual stress on the heat affected zone (HAZ), making it one of the most common crack initiations under the cyclic vehicle loads. The crack propagation detected in the real bridge is usually divided into two types. Type 1: the crack initiates from the welding end on the deck and develops into semicircles around the weld toe, then propagates on both sides of the deck along the longitudinal direction. Type 2: the crack initiates from the welding end on the vertical stiffener and develops along the weld toe or propagates through the weld and then onto the deck. Part of steel deck from a certain real bridge was modeled by ABAQUS to study the cracking reason of deck-to-vertical stiffener weld. The stress characteristics of welding end under the vehicle loads were also analyzed.

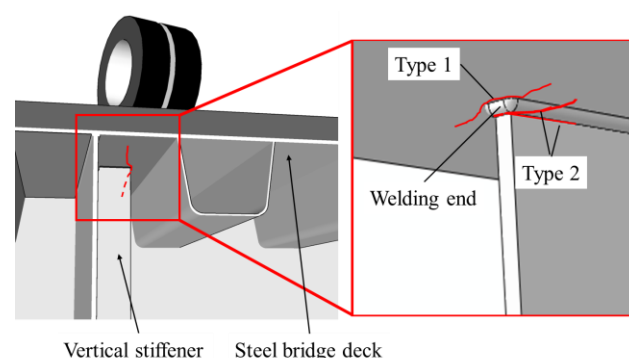


Fig. 1 The vertical stiffener in the steel bridge

The finite element model including 6 U ribs transverse to the bridge and 4 diaphragms longitudinal to the bridge was established according to a recent report in Japan [12]. Based on the dimensions of components in the real bridge, the thickness of deck and its pavement was set as 12mm and 80mm respectively. The section dimension of U rib was 320mm×240mm×6mm and vertical stiffener was 150mm×700mm. The web was 14mm in thickness and the radius of weld scallop connecting the vertical stiffener, web and deck was 35mm. The specific dimensions were illustrated in Fig. 2. It was assumed all components in the steel deck worked in linear elasticity during the periods of vehicle loads. The elasticity modulus of steel was 2.06×10^5 MPa. The elasticity modulus of pavement was 1000MPa considering distinct change of elasticity modulus with

the temperature, irrespective of the interface slippage between the deck and pavement [13]. All degrees of freedom at the diaphragm and three translational degrees of freedom around the model were restrained considering the constraints of the model in real bridge as a whole [14].

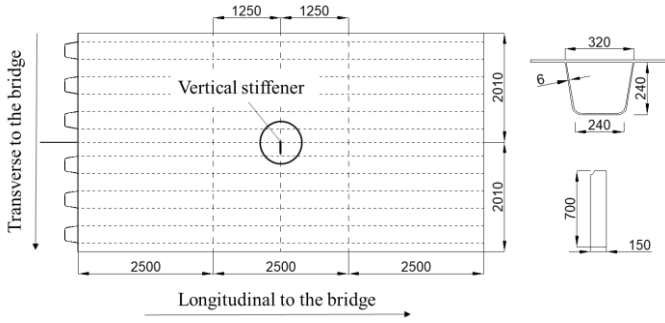


Fig. 2 The geometric dimension of the steel deck model

The huge difference in dimension of local details and model as a whole made mesh refinement difficult, thus the submodel method was commonly applied to build the model and improve computing efficiency. To establish the steel bridge deck with crossing longitudinal and transverse ribs which were sophisticated in geometric dimensions, deck-to-vertical stiffener weld was modeled by the submodel method. Both C3D8R element and C3D10 elements were applied for the base model and its submodel. The base model was meshed by hex elements with dimension of 20mm. The submodel was meshed by hex elements with dimension of 20mm and refined on its welding region by hex elements with dimension of 1mm. Five different mesh sizes were applied to verify the accuracy of FE analysis of the submodel. The hex element which owned a size of 1mm, 2mm, 3mm, 4mm and 5mm was calculated separately. It could be observed that the greatest stress difference was between the mesh size of 3mm and 1mm, which was only 3.0%. The stress curves showed a convergent solution for FE analysis with different mesh sizes. Therefore, the mesh size of 1mm was applied to the FE model for calculating accuracy and efficiency. The tet element was applied to transit mesh from the refinement region to coarse region. The refinement of the submodel was shown in Fig. 3.

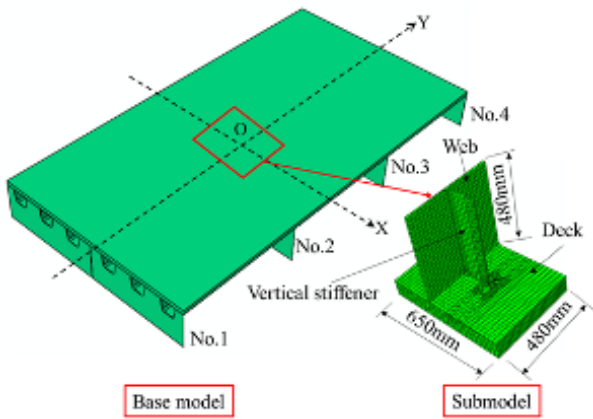


Fig. 3 The base model and submodel

A wheel load was picked up from the standard fatigue vehicle in the specification [15]. The wheel contact area was 600mm×200mm and the wheel force was 60kN. The DLOAD subroutine was compiled based on FORTRAN to apply wheel load on the steel deck. The origin of coordinates was set on the welding end of deck-to-vertical stiffener weld, which was shown in Fig. 4. The transverse subload consisted of 15 static load cases with a loading space of 50mm between case 5-9 and 100mm between the rest of cases. The wheel load ran from the diaphragm No.2 to No.3 and longitudinal subload consisted of 25 static load cases with a loading space of 100mm.

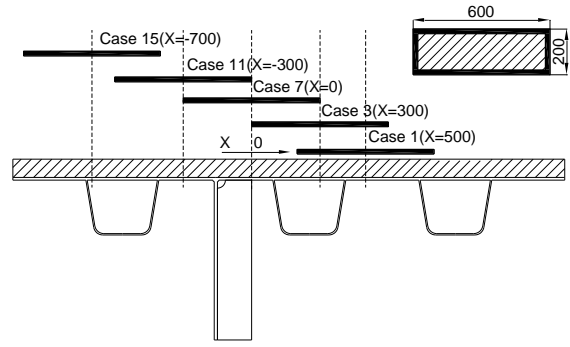


Fig. 4 The loading conditions

The premise to apply the submodel method was to ensure the boundary of the submodel was far enough from the stress concentration region, thus the stress on the boundary of the submodel should agree well with the identical position on the base model. By comparison of several trails with different submodel dimensions, the stress curves on the boundary of the submodel were proved to be consistent with those of the base model if the submodel's dimension was equal or greater than that in Fig. 3. Therefore, the following submodel analysis was based on this dimension.

2.2. Stress analysis under the wheel load

The cracks usually initiated at the welding end of the deck-to-vertical stiffener weld, thus the normal stress history of welding end on the deck and stiffener was obtained respectively and shown in Fig. 5.

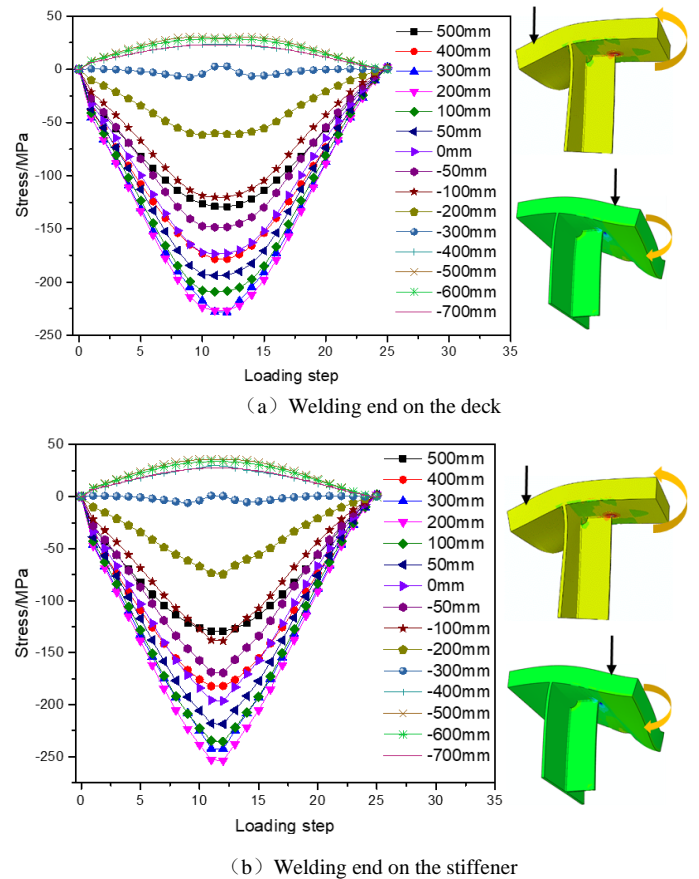


Fig. 5 Stress history under vehicle loading

As shown in Fig. 5, when the wheel load was applied on the left of the web, i.e., $X \leq -300$ mm, tensile-compressive stress cycles or complete tensile stress cycles were observed on the welding end. Assuming the web as a pivot, the wheel load on the left of the web rendered the downward compressive deformation of the deck on the left web, driving the upward warping of the deck on the right web. Therefore, it caused tensile stress on the welding end connecting the deck and vertical stiffener, which was in the analogy of the

“seesaw” action to some extent. When the wheel load was applied on the right of the web, i.e., $X \geq 300\text{mm}$, complete compressive stress cycles were observed on the welding end. It could be deemed that the small fraction of the deck above the web had a larger stiffness because of the web support. Taking it as the fixed end, the wheel load applied on the right of the web rendered the constant compressive deformation of the deck on the right web, causing the compressive stress on the welding end connecting the deck and vertical stiffener. Generally speaking, the tensile-compressive stress cycles or complete tensile stress cycles, which were generated by wheel load applied on the left of the web, gave rise to the fatigue cracking on the deck-to-vertical stiffener weld. As the wheel load applied on the right web caused complete compressive stress cycles, it had a negligible influence on the cracking of this detail.

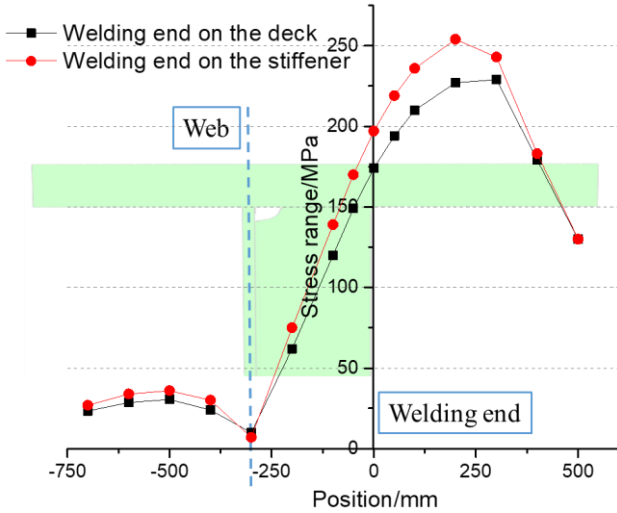
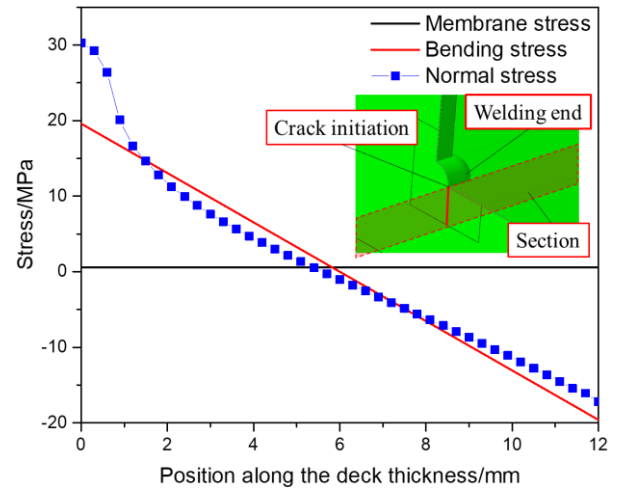


Fig. 6 Stress range

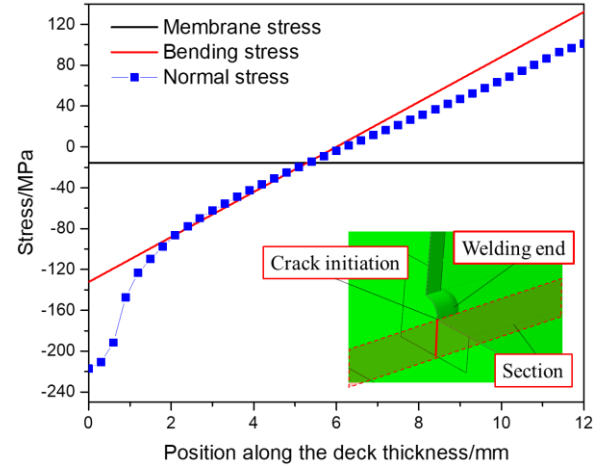
The rainflow method [15] was applied to count the stress history and obtain the stress ranges on the welding end of deck-to-vertical stiffener weld respectively. The minor stress ranges were neglected if several ranges were generated under the wheel load. The stress ranges under different transverse positions were illustrated in Fig. 6. Taking the welding end as the origin of coordinates, the tensile stress ranges on the left of web ($\leq -300\text{mm}$) and compressive stress ranges on the right of web ($> -300\text{mm}$) both increased first and then declined with the increment of distance from the welding end. Assume the web as a pivot. When wheel load was applied on the left of the web, the farther the wheel load was from the pivot, the longer the arm of force was, thus the greater the tensile stress range on the welding end would be. While a certain distance between the wheel load and web was reached, the effect of wheel load was weakened because of the stiffness by the neighboring U ribs on the left. Therefore, as the distance increased, the tensile stress ranges of the welding end declined. Assume the small fraction of deck above the web as the fixed end. When wheel load was applied on the right of the web, the farther the wheel load was from the fixed end, the longer the arm of force was, thus the greater the compressive stress on the welding end would be. While a certain distance between the wheel load and web was reached, the effect of wheel load was weakened because of the stiffness by the neighboring U ribs on the right. Therefore, as the distance increased, the compressive stress ranges of the welding end declined. Generally speaking, the stress range of welding end on the vertical stiffener was greater than that on the deck, thus welding end on the vertical stiffener was more prone to crack with identical material and welding craftsmanship.

2.3. Analysis of the cracking reason

The results of stress ranges showed that the transverse position of wheel load on the -500mm was the most unfavorable working conditions for the tensile range, and 200mm was the most unfavorable working conditions for the compressive range. For the welding end on the deck, the membrane stress, bending stress and normal stress of the cracking section when the wheel load was applied on the -500mm and 200mm in transverse and the 13th static cases (the most unfavorable working conditions longitudinal to the bridge) in longitudinal were depicted in Fig. 7. The bending stress and membrane stress were extracted by Stress Linearization to judge the deformation features of this detail. The definition of membrane stress is the average normal stress across the thickness of a plate or shell. The bending stress refers to stresses which are linearly distributed across the thickness.



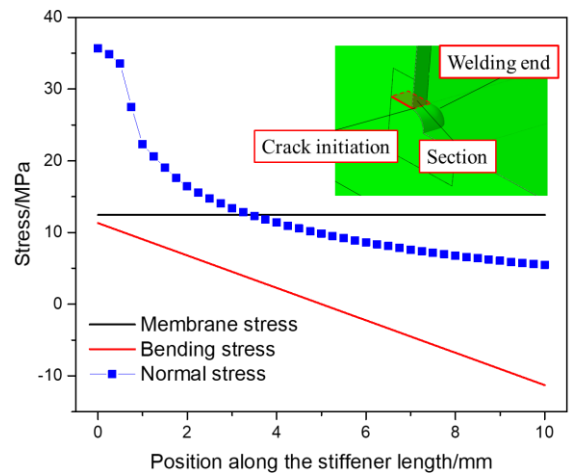
(a) -500mm



(b) 200mm

Fig. 7 Stress of welding end on the deck

As seen in Fig. 7, for wheel load on the -500mm in transverse, bending stress of the cracking section was 19.6MPa , while the membrane stress was only equal to 3% of the bending stress, namely 0.6MPa . It indicated that the fatigue cracking in this detail mainly resulted from the bending stress induced by out of plane deformation and membrane stress had a negligible influence on the cracking. Meanwhile, the nonlinear stress caused by geometric structure increased the normal stress by 33.3%. Similarly, for wheel load on the 200mm in transverse, the bending stress of the cracking section was -132.4MPa , while the membrane stress was only equal to 11.8% of the bending stress, namely -15.6MPa . Meanwhile, the nonlinear stress caused by geometric structure increased the normal stress by 32.3%. Therefore, the cracking Type 1 of the deck-to-vertical stiffener weld, i.e., the crack initiated from the welding end on the deck, was caused by great out of plane deformation under the wheel load.



(a) -500mm

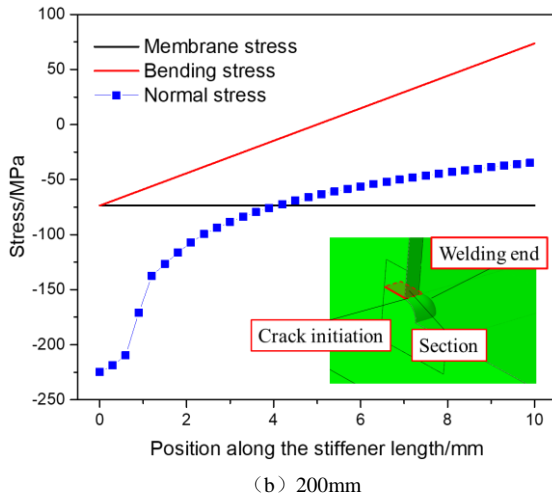


Fig. 8 Stress of welding end on the vertical stiffener

For the welding end on the vertical stiffener, the membrane stress, bending stress and normal stress of the cracking section when the wheel load was applied on the -500mm and 200mm in transverse and the 13th static cases in longitudinal were depicted in Fig. 8. For wheel load on the -500mm in transverse, the bending stress of the cracking section was 12.5MPa, while the membrane stress was almost identical to the bending stress, namely 11.3MPa. It indicated that the fatigue cracking in this detail resulted from combination of the out-of-plane and in-plane deformation. These two kinds of deformation accounted for nearly same degree in fatigue damage. Meanwhile, the nonlinear stress caused by geometric structure increased the normal stress by 34.3%. Similarly, for wheel load on the 200mm in transverse, the bending stress of the cracking section was -73.7MPa, while the membrane stress was almost identical to the bending stress, namely -73.4MPa. Meanwhile, the nonlinear stress caused by geometric structure increased the normal stress by 34.4%. Therefore, the cracking Type 2 of the deck-to-vertical stiffener weld, i.e., the crack initiated from the welding end on the vertical stiffener, was caused by the combined out-of-plane and in-plane deformation under the wheel load.

3. The fatigue repairing experiment of deck-to-vertical stiffener weld

3.1. Experiment program

The fatigue repairing experiment was carried out on the deck-to-vertical

stiffener weld. It's known that the fatigue cracking on the steel bridge deck mainly resulted from the local stress concentration on the details and local structures, thus local full-sized specimens were designed for fatigue experiment according to the fatigue detail in real bridges and relevant literatures [16]. The deck and vertical stiffener were welded by gas metal arc (GMA) welding. The welding leg of fillet weld with complete-joint-penetration (CJP) was 6mm. The geometric dimension of the specimen was shown in Fig. 9. A total of 6 specimens were designed including one repaired by re-welding, one by re-welding, hammering and polishing, one by drilling stop-holes, one by Carbon Fiber Reinforced Plastics (CFRP), one by re-welding and CFRP reinforcement, another by drilling stop-holes and CFRP reinforcement. Number them from SJ1 to SJ6 and the repairing workmanship was shown in Table 1. Some certain specimens during or after repairing process were illustrated in Fig. 10.

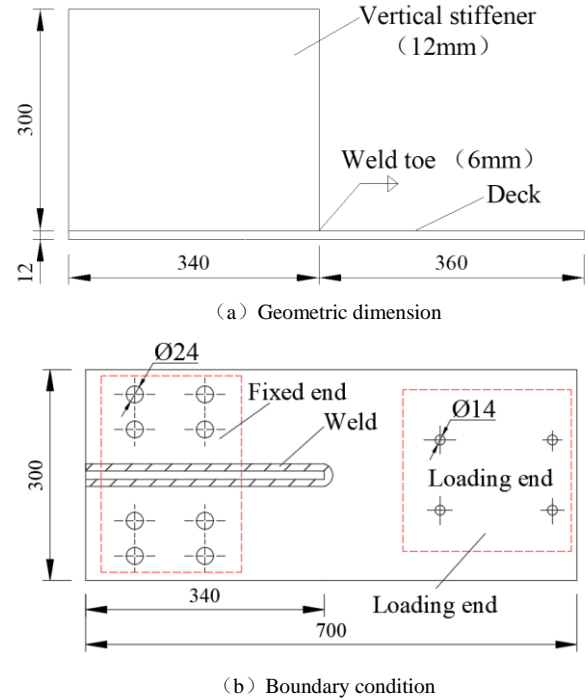


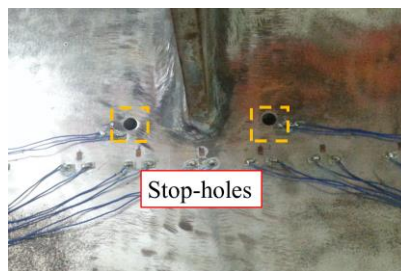
Fig. 9 The design of specimens (unit: mm)

Table 1
The repairing workmanship of the deck-to-vertical stiffener weld

Repairing method	Repairing workmanship
Re-welding (SJ1)	The welding length was 80mm. The hydrogen controlled electrode of Type E5015-X was applied. The diameter was 4mm and tensile strength was 490MPa.
Re-welding, hammering and polishing (SJ2)	The surface of specimen after re-welding was peened followed by hammering and polishing.
Stop-hole (SJ3)	The stop-hole diameter was 8mm. The hole center was set on the crack tip.
CFRP reinforcement (SJ4)	The CFRP of Type I-300 was applied. The thickness was 0.17mm, tensile strength was 3400MPa, elasticity modulus was 240GPa and the elongation was 1.7%. The CFRP completely covered surface of deck but avoided the position of strain gages. The epoxy adhesive was used to stick the CFRP to the deck.
Re-welding, hammering, polishing and CFRP reinforcement (SJ5)	The repairing workmanship of re-welding, hammering, polishing (SJ2) and CFRP reinforcement (SJ4) was referred.
Stop-hole and CFRP reinforcement (SJ6)	The repairing workmanship of stop-hole (SJ3) and CFRP reinforcement (SJ4) was referred.



(a) SJ1



(b) SJ3



(c) SJ6

Fig. 10 Repairing process of certain specimens

The bending load was applied on the specimen by eccentricity vibrating machine, which had widespread use in fatigue tests [17]. One side of the specimen was constrained on the reaction frame and the eccentricity vibrating machine was constrained on the other side. The harmonic vibration load was applied and the stress ratio R was equal to -1 . Adjust the load frequency to render the nominal stress range of welding end (D4 in Fig. 12) equal to 100MPa at the beginning of the fatigue test. The loading installation was shown in Fig. 11.

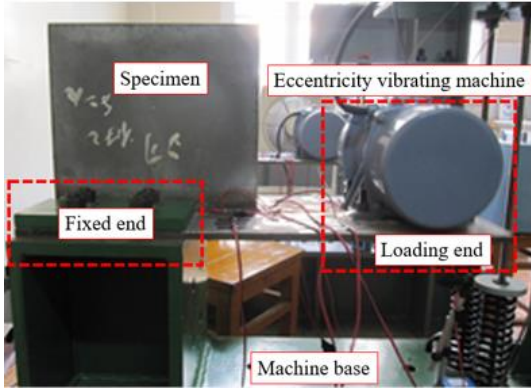


Fig. 11 The vibration loading machine

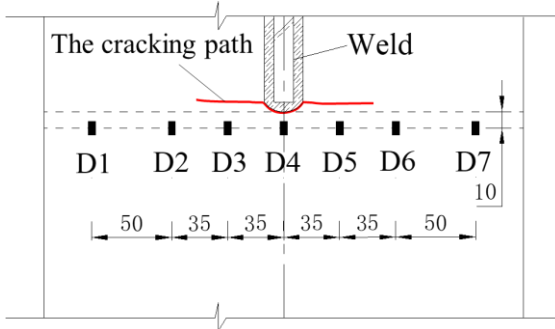


Fig. 12 Measuring points (unit: mm)

Table 2

Comparison of stress ranges

Number	Initial stress range (MPa)		Final stress range (MPa)		Stress range change (MPa)		Change rate (%)	
	SJ1	SJ2	SJ1	SJ2	SJ1	SJ2	SJ1	SJ2
D1	61.8	54.5	97.8	62.9	36.1	8.4	58.4	15.4
D2	64.7	64.7	93.0	81.0	28.3	16.3	43.7	25.2
D3	81.7	78.2	68.3	93.4	-13.4	15.2	-16.4	19.4
D4	100.2	102.8	59.2	48.2	-41.0	-54.6	-40.9	-53.1
D5	79.4	77.9	62.3	63.0	-17.1	-14.9	-21.6	-19.1
D6	67.6	66.2	94.3	78.3	26.8	12.1	39.6	18.3
D7	60.5	56.1	97.0	67.4	36.4	11.3	60.2	20.1

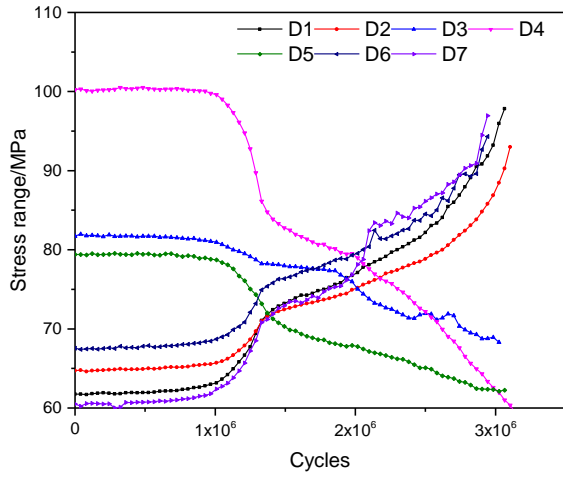
The Fig. 13 illustrated the curves of stress ranges in SJ1 and SJ2 changing with loading cycles. The cracks initiated from the welding end on the deck and then propagated transverse to the deck. The stress ranges of measuring points in the vicinity of the welding end declined and the rest increased. This was because the initiation of crack cut off the stress flow on the deck surface, resulting in the decrease of stress range where the crack tip reached and increase of other measuring points because of the stress redistribution. For specimen SJ1, the stress range of D3 and D5 declined quickly with the decrease of stress range of D4, showing that the crack propagated fast after initiation on the welding end and reached length of 35mm which corresponded to the position of D3 and D5. For specimen SJ2, after the decline of stress range of D4, the stress range of D5 increased first then decreased during certain period of fatigue cycles. This was because the crack tip didn't propagate to the position of D5 before the stress

The cracks in the specimens were prefabricated by the eccentricity vibrating machine, and the repairing process was not carried out until the crack propagated into approximate 30mm. The cracks of all these specimens were observed to initiate from the welding end on the deck, i.e., the cracking Type 1. This was because the bending load was applied on the specimens and welding end was mainly endured bending stress. The load was applied to the specimen after repairing and discharged when the crack length reached 50mm. The strain gages were pasted on the specimens and shown in Fig. 12. Considering the cracking characteristics in real bridges, 7 gages were set along the transverse of the deck, which were 10mm from the welding end to measure the nominal stress. The distance 10mm was determined by the stress gradients of the welding end to ensure the nominal stress was not affected by the geometric discontinuity [18]. In the vicinity of the welding end, the space between the gages was comparatively smaller, namely 35mm. For gages far from the welding end, the space was 50mm.

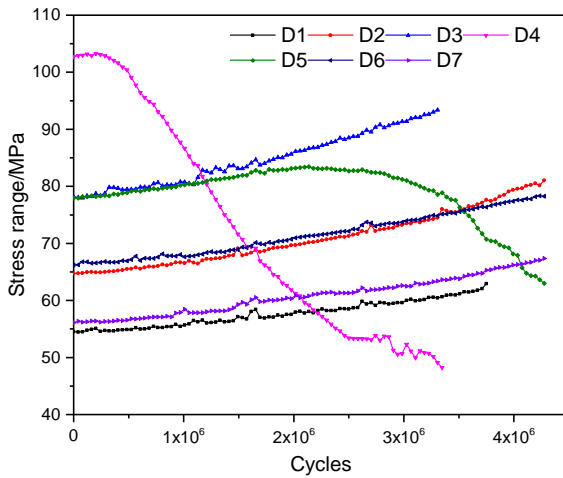
3.2. Change of stress ranges

In the application of re-welding techniques, the cracking region was digged by pneumatic digger then the cracking section was welded again, thus the re-welding workmanship was a kind of complete repairing. It was known that the fatigue life of specimens repaired by re-welding would be much longer than that by the stop-hole and CFRP reinforcement. It could also be observed from the fatigue experiments that the stress histogram of specimen by re-welding (SJ1, SJ2) was long enough. Taking the specimen SJ1 by re-welding and specimen SJ2 by re-welding, hammering and polishing as examples, the initial, final stress ranges, final stress changes and change of stress ranges of different gages were shown in Table 2. The initial stress ranges refer to stress ranges of the testing position at the beginning of the fatigue loading and the final stress ranges refer to stress ranges when the fatigue loading ends. For SJ1, the final stress range of measuring points (D3-D5) in the vicinity of the welding end declined. The final stress range of D4 corresponding to the initiation of cracking on the welding end dropped a lot, namely 40.9%. The final stress ranges of measuring points where the crack tip hadn't reached yet increased dramatically. For SJ2 after hammering and polishing, the final stress range of D4 decreased by 53.1%, while change rate of other measuring points which experienced increase in stress ranges was much smaller than that of SJ1. The change of stress ranges was smooth, showing that the stress distribution of weld after hammering and polishing was more favorable.

range of D5 reached the peak and the stress redistribution resulted in the increase of stress range. When the crack tip reached the position of D5, the stress range declined. The stress range of D3 increased all the time, indicating that the crack tip never propagated to D3 throughout the loading procedure. The crack developed asymmetrically on two sides of the vertical stiffener. In analysis of stress range in specimen SJ1 and specimen SJ2, the residual stress of weld on specimen SJ1 was great because SJ1 was not hammered and polished after re-welding. The crack propagated quickly and exceeded the length of re-welding region after initiation on the welding toe. But cracking rate of SJ2 was comparatively slower since welding residual stress was removed, so it was necessary to hammer and polish the weld after re-welding to reduce the residual stress.



(a) SJ1

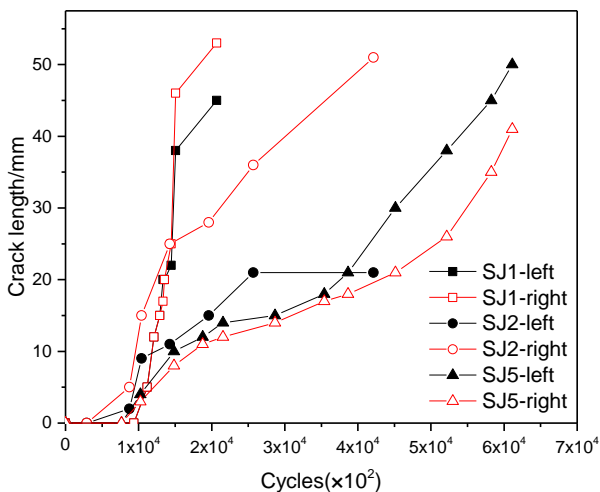


(a) SJ2

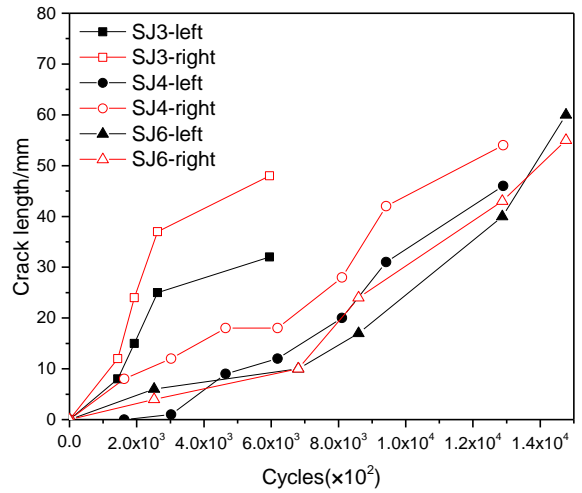
Fig. 13 Change of stress ranges

3.2. Fatigue life

The re-welding technique was a kind of complete fatigue repairing method, while the stop-hole and CFRP reinforcement were temporary. The different repairing purpose resulted in substantial discrepancies of fatigue life. Therefore, the comparison of fatigue life was carried out on the specimens with the re-welding technique (SJ1, SJ2 and SJ5) and without the re-welding technique (SJ3, SJ4 and SJ6). The relationship of crack length-to-fatigue cycles was depicted in Fig. 14, where in the legend “left” means crack tip on the left of the vertical stiffener and “right” means crack tip on the right.



(a) SJ1, SJ2, SJ5



(b) SJ3, SJ4, SJ6

Fig. 14 Fatigue life

In Fig. 14(a), the fatigue life of SJ2 was generally greater than that of SJ1. With crack length increasing, especially when the crack tip approached and exceeded the boundary of re-welding region, the curves of SJ1 and SJ2 separated from each other and great difference could be observed. It meant the welding residual stress weakened fatigue life seriously. Besides, hammering and polishing after re-welding could reduce the residual stress and slow down the cracking rate. The cracking rate of SJ5 was comparatively small and its fatigue life was usually greater than that of SJ1 and SJ2 under the same crack length. It was indicated that by reinforcement of CFRP, the material stuck to the deck by epoxy adhesive was subjected to fatigue load together with the structure, thus restraining the open of crack tip and improving stress distribution on the welding end. By the comparison of SJ5 by re-welding, hammering, polishing and CFRP reinforcement, SJ2 by re-welding, hammering and polishing, and SJ4 by CFRP reinforcement, the cracking rate of SJ5 was comparatively small, indicating that repairing effect by simultaneous two techniques was more favorable than that of a single technique.

In Fig. 14(b), the stop-hole of SJ3 removed the original crack tip and no crack propagation occurred before the new crack initiated. Then fatigue cracks initiated from the edge of hole, which was the new position of stress concentration, after a certain period of stress cycles. The propagation rate of SJ3 was greater than that of SJ4 and SJ6, indicating that the repairing effect of stop-hole was comparatively unfavorable. For SJ4 by CFRP reinforcement and SJ6 by stop-hole and CFRP reinforcement, the curves were close to each other, indicating that repairing effects were generally the same. According to the relationship of crack length-cycles, the fatigue life of SJ6 was longer under the same crack length, thus repairing effect by simultaneous two techniques was more favorable than that of a single techniques. Moreover, the fatigue life of SJ2 by re-welding and polishing was 7.1 times that of SJ3 by stop-hole and 3.3 times that of SJ4 by CFRP reinforcement, indicating that the repairing effects of complete method were obviously more favorable than that of temporary method.

4. Influences of fatigue repairing effects

4.1. Welding residual stress

The welding residual stress was one of the most significant factors affecting the repairing effects of re-welding. The experiment results in section 3 also showed that the fatigue life of SJ2 after eliminating the residual stress was much longer than that of SJ1. The heats during welding of steel deck changed sharply both in time and space and were a kind of typical nonlinear transient transfer, thus the welding stress field was usually simulated by thermal elastoplastic analysis and the incremental method was applied to solve the temperature field and stress field. Based on the welding plug-in AWI (ABAQUS Welding Interface) which was developed by 3DEXPERIENCE Accompany, the re-welding process was modeled and the residual stress distribution was analyzed.

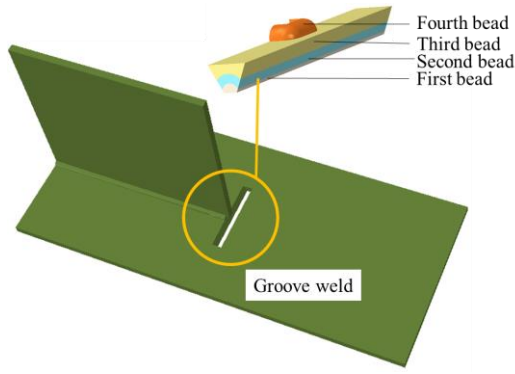


Fig. 15 The re-welding model

The deck-to-vertical stiffener weld on steel bridge deck was modeled by ABAQUS and then introduced to the plug-in AWI for welding simulation. The model by re-welding was shown in Fig. 15. According to the specimens in section 3, the length of deck was 700mm and width was 300mm. To simulate the re-welding workmanship in the experiment, the deck was beveled on both sides of vertical stiffener and length of the groove weld was 30mm on each side. The welding process was completed by four beads. In the heat affected zone (HAZ), the temperature gradient was great and stress changed dramatically, thus the mesh of the weld and re-welding region was refined. Six degrees of freedom (DOFs) of the bottom surface were restrained to simulate the platform in the workshop. The DC3D8 element was used for thermal analysis, and C3D8R for thermal stress analysis. Five different mesh sizes were applied to verify the accuracy of FE analysis of local and full-sized specimen. The hex element which owned a size of 1mm, 2mm, 3mm, 4mm and 5mm was calculated separately. It could be observed that the greatest stress difference was between the mesh size of 3mm and 4mm, which was 14.8%. The stress curves with mesh size of 2mm and 3mm were close to that with mesh sized of 1mm, which was

assumed to have the greatest accuracy. The stress curves showed a convergent solution for FE analysis with different mesh sizes. Therefore, the mesh size of 2mm was applied to the FE model for calculating accuracy and efficiency. The technique of element birth and death was applied to simulate the process of welding, which was realized by activation and inactivation of element sets in sequence. The welding speed was 10mm/s and interval of each time step was 0.2s. A total of 61 steps were set for heating and then the specimen was cooled in room temperature.

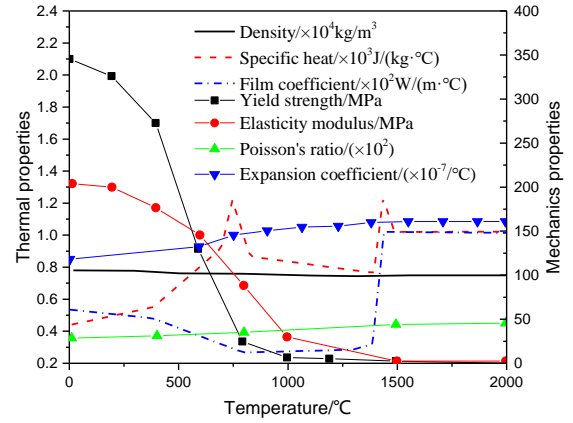


Fig. 16 The physical properties

The thermophysical and thermodynamical parameters of Q345 steel [19] were depicted in Fig. 16. Considering two forms of heat transfer, namely heat conduction and heat convection, the Stefan-Boltzmann constant was equal to $5.67 \times 10^{-11} \text{ mJ/s/mm}^2/\text{K}^4$, the absolute zero was -273.15°C , the room temperature was 21.1°C and the convective heat coefficients was $0.013 \text{ mJ/s/mm}^2/\text{K}^4$.

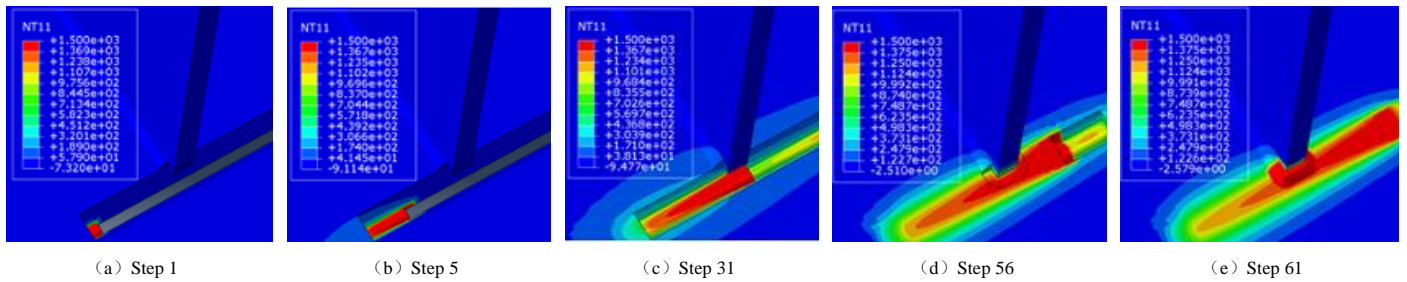


Fig. 17 The temperature field

The temperature contour during the welding process was shown in Fig. 17. It could be seen that the temperature field of the specimen changed constantly with the moving of heat source. The temperature of the specimen was unstable at first and heat up quickly, then temperature of quasi stable state would be formed on the specimen. The temperature of specimen changed over time while the temperature field moved with the heat source in a certain pattern. The temperature gradient was steep in front of the heat source and gentle behind it.

The Von Mises stress of specimen after welding and cooling was illustrated in Fig. 18. During the welding process, stress of melting weld was very small while stress of regions surrounding the weld pool was close to the yield strength of steel. Therefore, great residual stress was generated in the welds. The stress concentration caused by geometric construction was avoided and section stress 10mm to the weld toe was analyzed. The stress path was 100mm long on each side of the vertical stiffener and the nominal stress of bottom, middle and top surface was extracted and shown in Fig. 19. It could be seen that the residual stress on the top surface was greater than that of the middle and bottom surface. This was because specimen was re-welded from the bottom weld pass to the top one. The cooling time of various beads was different during the welding and the beads welded previously were solidified and had suitable strength, which would stop free expansion of beads welded latterly and induce the plastic deformation in the weld. When the weld as a whole cooled down, shrinkage of beads welded latterly was restrained by the solidified bead. The tensile stress was generated in the beads welded latterly and compressive stress was generated in the beads welded previously. This also embodied in the phenomenon that residual stress on the top surface increased dramatically in the weld while it declined sharply on the bottom surface. The welding end welded at last generated tensile stress

on the top surface during cooling and compressive stress on the bottom surface which cooled down previously.

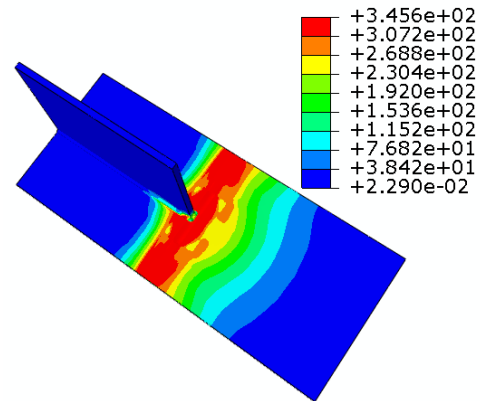


Fig. 18 Residual Von Mises stress after cooling (unit: MPa)

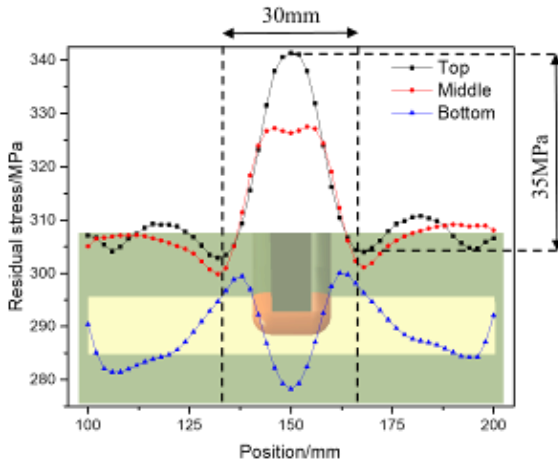


Fig. 19 Residual stress of the deck

It could be seen in Fig. 19 that the peak of residual stress on the deck surface approached the yield strength of steel. The stress changed dramatically in the range of approximate 30mm on the welding end and the amplitude was 35MPa. The crack of deck-to-vertical stiffener weld generally initiated from the weld toe and propagated to both sides of the deck. As the residual tensile stress had already reached the yield stress of steel on the weld, the fatigue limit would be achieved and weld would crack quickly under the fatigue load. This also verified the experiment results of SJ1 and SJ2. Therefore, it was necessary to hammer and polish the weld region after re-welding to get rid of the tensile stress and render the weld surface smooth.

4.2. Parameters of stop-hole

The position and diameter of the stop-hole were significant factors influencing the repairing effects. To study the influence of different stop-hole workmanship on the fatigue repairing of the deck-to-vertical stiffener weld, five stop-hole positions, namely -0.5D, 0, 0.5D, 1.0D and 1.0t, and three stop-hole diameter, namely 6mm, 8mm and 10mm were considered. D referred to diameter of the stop-hole and t referred to deck thickness. A total of 15 working conditions were modeled, and the dimension of the specimen and loading conditions were consistent with the experiment in Section 3. The specific information of working conditions was illustrated in Table 3.

Table 3
Working conditions of the stop hole

Stop-hole diameter D(mm)	Stop-hole position X(mm)				
	-0.5D	0	0.5D	1.0D	1.0t
6	-3	0	3	6	12
8	-4	0	4	8	12
10	-5	0	5	10	12

The specimen was modeled by ABAQUS and extended finite element method (XFEM) was applied to solve the stress singularity at crack tip. The fatigue crack section was considered to be semi-elliptical in deck thickness [16]. Therefore, the ratio of minor to major axis lengths (b/a) was 0.33 according to previous statistics, as shown in Fig. 20. The semi-major axis length and the semi-minor axis length were defined as approximate 32mm and 12mm considering the actual crack length in the current experiment. The interaction between the crack and the model is "hard contact". Element types C3D8R and C3D10 were adopted. The mesh size of the model was 20 mm (overall). The element size was refined to be 2 mm at the welding end by C3D8R. In the width of 20 mm out from the weld, C3D10 was adopted to model the transition region.

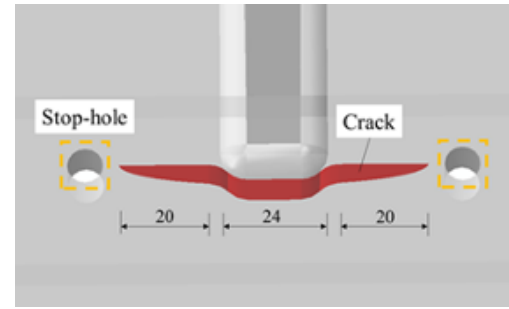


Fig. 20 Set of the crack (mm)

According to the fatigue analysis in the current experiment and previous studies, stress of 0.35 MPa was applied on four loading surfaces with length of 45mm and width of 40mm. It caused a stress of 50 MPa at the center of the model (with no crack) at some 10 mm from the welding end. Fixed restraint was applied within a distance of 225mm and 136mm from the deck edge, 6 DOFs were constrained. No constraints were set in other parts (Fig. 21).

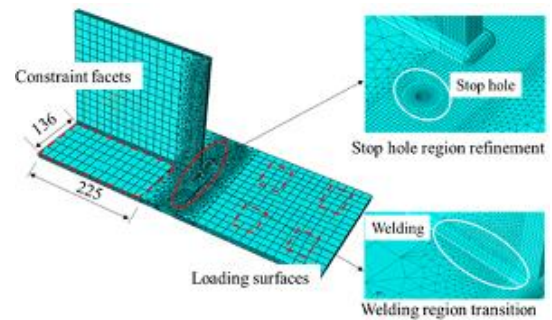


Fig. 21 Model of the stop-hole

When the diameter of stop-hole equaled to 6mm, stress changing from the stop-hole edge to the model edge with different stop-hole positions was shown in Fig. 22. Only one side of stress was drawn as the model was symmetrical by the vertical stiffener. It could be seen that the trend of stress changes with different stop-hole positions was the same with stress dropping down sharply near the stop-hole edge. Great stress gradients were generated and the maximum stress was observed on the stop-hole edge. Then decline of stress slowed down at certain distance (approximate 10mm) from the stop-hole edge and converged eventually. The stress peak decreased with increasing of stop-hole position. When the stop-hole position was greater than 0.5D, the decline of peak stress was gradually not so obvious.

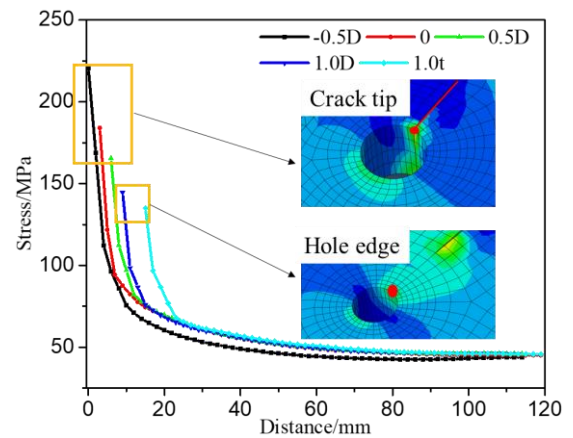


Fig. 22 The stress change with 6mm stop hole

The original crack was removed by the stop-hole while new stress concentration was generated on the stop-hole edge in the direction of initial cracking propagation. So the stress on the stop-hole edge was obtained and illustrated in Fig. 23. It could be seen that the greater the stop-hole diameter was, the stress of the stop-hole edge was smaller, which indicated a more favorable repairing effects. Therefore, greater stop-hole diameter was recommended in

fatigue repairing of real bridges. But as greater stop-hole diameter would weaken the bearing capacity of the section, it should be smaller than a certain limit. The peak stress at the new initiation decreased with increasing of stop-hole position except for particular cases in the position of 0 when hole diameter was 8mm and 10mm. The reason of smaller peak stress at the hole edge was that the distance between the crack tip and the hole edge was too long to have great influence on the hole edge. However, the crack was not removed and would continue to propagate to shorten the distance. Moreover, the crack extension path was uncertain and crack might even propagate away from the stop-hole. These results led to unfavorable crack-stopping effects. The change of peak stress with stop-hole position had an inflection point at $X = 0.5D$ (stop-hole diameter equaled to 8mm and 10mm). In this case, the stop-hole covered the crack tip and removed the plastic zone around the crack tip. Therefore, $X = 0.5D$ was suggested as being a reasonable stop-hole position.

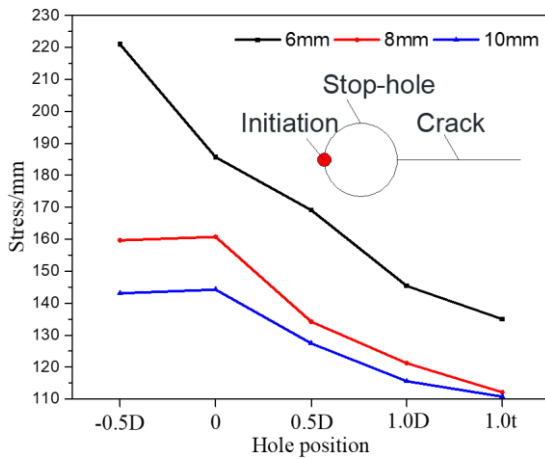


Fig. 23 Stress peak of the stop hole

4.3. Parameters of CFRP reinforcement

The covering area of CFRP on the crack influenced the restriction on crack propagation. Moreover, the favorable mechanical property of CFRP improved the repairing performance. Therefore, different transverse length (20mm, 25mm, 30mm, 60mm, 90mm, 100mm and 130mm) and elasticity modulus (240GPa and 210GPa) of CFRP were considered, and totally 12 working conditions were shown in Table 4. The longitudinal length of CFRP was set as constant 140mm.

Table 4
Working conditions of CFRP

Elasticity modulus (GPa)	Transverse length /mm					
	20	25	30	60	90	130
240						
210						

The model of deck-to-vertical stiffener weld reinforced by CFRP was shown in Fig. 24. The model size was consistent with the experiment in Section 3. The parameter of CFRP was in accordance with the specification [20]. The thickness of CFRP was 0.17mm and Poisson's ratio was 0.261. As it could be assumed that there was no relative slippage between the CFRP and deck [21], a kind of constrain named "TIE" was set between the two in the model. The crack shape, mesh size and loading conditions were referred to the stop-hole model in Section 4.2 and the CFRP, modeled by S4R of shell elements, had a mesh size of 2mm. The stress of the cracking section from crack tip to the model edge was obtained and shown in Fig. 25.

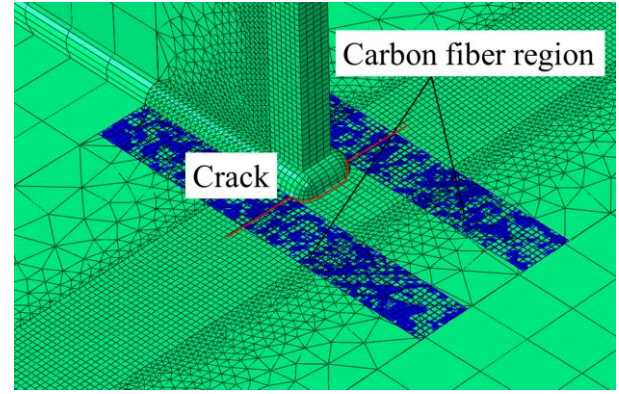


Fig. 24 Model of the CFRP

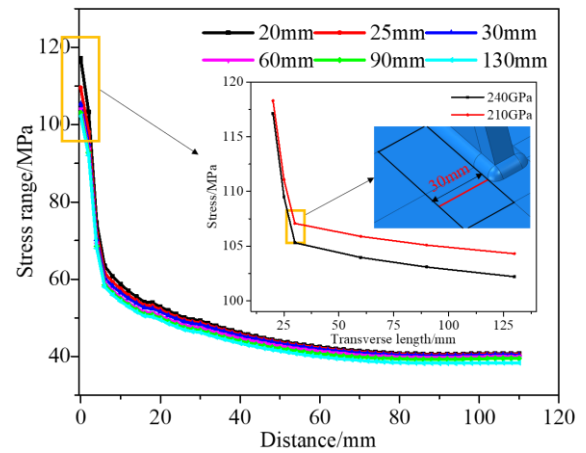


Fig. 25 The stress of cracking section with various parameters

Fig. 25 depicted stress of cracking section changing with the transverse length of CFRP when the elasticity modulus equaled to 240GPa, which was similar to the stop-hole model. Stress declined dramatically near the crack. Great stress gradients were generated and the maximum stress was observed on the crack tip. Then decline of stress slowed down at certain distance (approximate 10mm) from the stop-hole edge and converged eventually. By comparison of stress with different CFRP length, the longer the length was, the smaller the crack propagation would be when the CFRP length was less than 30mm. It indicated that greater covering area of CFRP contributed to more favorable repairing performance. When the CFRP length was greater than 30mm, i.e., the CFRP completely covered the crack surface, increase of covering area didn't have a favorable performance to decline stress of cracking section. Therefore, length of CFRP which was able to cover the crack surface was enough in theory. However, the crack propagated with increment of fatigue cycles and the crack length would exceed the covering area of CFRP, so it was necessary to apply greater length of CFRP than crack length according to real conditions.

It could also be observed that stress change of CFRP with two different elasticity modulus were almost the same, but CFRP with 240GPa of elasticity modulus led to smaller stress than that with 210GPa of elasticity modulus, so preliminary conclusion could be drawn that greater elasticity modulus could contribute to smaller stress. CFRP with greater elasticity modulus was recommended in real fatigue repairing.

5. Conclusions

Based on the experiments and FEM analysis, the following preliminary conclusions can be obtained.

(1) Cracks of welding end on the deck was induced by out of plane deformation and that on the vertical stiffener was induced by combined out-of-plane and in-plane deformation, which led to the same degree of fatigue damage on this detail. Stress ranges of welding on the vertical stiffener were greater than that on the deck, thus welding end on the vertical stiffener was more prone to cracking with identical material and welding craftsmanship.

(2) The cracking rate of re-welding model with polishing was much smaller than that without hammering and polishing, so it could be speculated that welding residual stress was reduced. The analysis of residual indicated that residual tensile stress reached yield strength of steel after re-welding, thus it's necessary to hammer and polish the re-welding area to improve the fatigue repairing performance.

(3) The new stress concentration appeared at the stop-hole edge after remove of crack. The greater the stop-hole diameter was, the smaller the stress of the stop-hole edge would be. But oversized diameter weakened the bearing capacity of section, so it should be smaller than a certain limit. The crack was not removed and might propagate away from the stop-hole if the stop-hole position was oversized, thus the stop-hole position which was half of the hole diameter from the crack tip was recommended.

(4) The greater the elasticity modulus of CFRP was, the more significantly it decreased stress at the crack tip. The greater the area covering the crack was,

the greater the effects that CFRP stopped crack propagation would be. When the CFRP completely covered the crack surface, increase of covering area didn't have a favorable performance to decline stress of cracking section. The length of CFRP was suggested to be greater than crack length based on real conditions.

(5) The re-welding technique removed the crack tip and welded the cracking region again, which had more favorable repairing effects than stop-hole and CFRP reinforcement. In the current experiment, fatigue life of specimen by re-welding, hammering and polishing was 7.1 times that of stop-hole specimen and 3.3 times that of CFRP specimen.

Acknowledgements

The authors appreciate the support of The National Natural Science Fund (No.51678215 and No.51678216) and the Fundamental Research Funds for the Central Universities (Grant 2018B50314).

References

- [1] Seo J., Phares B. and Wipf T.J., "Lateral live-load distribution characteristics of simply supported steel girder bridges loaded with implements of husbandry", *Journal of Bridge Engineering*, 19(2), 04013021, 2013.
- [2] Ji B., Liu R., Chen C., Maeno H. and Chen X., "Evaluation on root-deck fatigue of orthotropic steel bridge deck", *Journal of Constructional Steel Research*, 90(5), 174-183, 2013.
- [3] Kim I.T., "Fatigue strength improvement of longitudinal fillet welded out-of-plane gusset joints using air blast cleaning treatment", *International Journal of Fatigue*, 48(2), 289-299, 2013.
- [4] Steel Structure Committee of Civil Society, Report of Thick Plate Welding Joint Related Research, Japan, 2007. (in Japanese)
- [5] Alemdar F., Gangel R., Matamoros A., Bennett C., Barrett-Gonzalez R., Rolfe S. and Liu H., "Use of CFRP overlays to repair fatigue damage in steel plates under tension loading", *Journal of Composites for Construction*, 18(4), 04013052, 2013.
- [6] Alemdar F., Nagati D., Matamoros A., Bennett C. and Rolfe S., "Repairing distortion-induced fatigue cracks in steel bridge girders using angles-with-plate retrofit technique. I: Physical simulations", *Journal of Structural Engineering*, 140(5), 04014003, 2013.
- [7] Tabrizi S., Kazem H., Rizkalla S. and Kobayashi A., "New small-diameter CFRP material for flexural strengthening of steel bridge girders", *Construction and Building Materials*, 95, 748-756, 2015.
- [8] Aljabar N.J., Zhao X.L., Al-Mahaidi R., Ghafoori E., Motavalli M. and Powers N., "Effect of crack orientation on fatigue behavior of CFRP-strengthened steel plates", *Composite Structures*, 152, 295-305, 2016.
- [9] Crain J., Simmons G., Bennett C., Barrett-Gonzalez R., Matamoros A.B. and Rolfe S.T., "Development of a technique to improve fatigue lives of crack-stop holes in steel bridges", *Transportation Research Record Journal of the Transportation Research Board*, 2200, 69-77, 2010.
- [10] Kim Y.J. and Harries K.A., "Fatigue behavior of damaged steel beams repaired with CFRP strips", *Engineering Structures*, 33(5), 1491-1502, 2011.
- [11] Park H.C., Lee C.H. and Chang K.H., "Strengthening a damaged steel girder bridge by the replacement repair welding", *KSCE Journal of Civil Engineering*, 16(7), 1243-1249, 2012.
- [12] Ogasawara T., Iguchi S., Uchida D., Okumura M., Katano S., Saitou S., Hayashi N. and Matsushita H., "The fatigue maintenance method for the welding end of vertical stiffener on the steel bridge and steel lifting equipment", *Technique of the Bridge Symposium Report*, 2016. (In Japanese)
- [13] Fu Z., Ji B., Wang Y. and Xu J., "Fatigue performance of the U-rib and roof weld in steel bridge decks with corner braces", *Steel and Composite Structures*, 26(1), 103-113, 2018.
- [14] JTG D64-2015, "Specifications for Design of Highway Steel Bridge," Ministry of Transport of the People's Republic of China, 2015. (In Chinese)
- [15] Jiang X.L., Zeng G.L. and Tan J.H., "Structural reliability analysis of a steel truss bridge based on the monitoring data", *Applied Mechanics & Materials*, 105-107, 1342-1345, 2011.
- [16] Yang M., Ji B., Yuanzhou Z. and Fu Z., "Fatigue behavior and strength evaluation of vertical stiffener welded joint in orthotropic steel decks", *Engineering Failure Analysis*, 70, 222-236, 2016.
- [17] Baik B., Yamada K. and Ishikawa, T., "Fatigue crack propagation analysis for welded joint subjected to bending", *International Journal of Fatigue*, 33(5), 746-758, 2016.
- [18] Fu Z., Ji B., Kong X. and Chen X., "Grinding treatment effect on rib-to-roof weld fatigue performance of steel bridge decks", *Journal of Constructional Steel Research*, 129, 163-170, 2017.
- [19] Zhao Q. and Wu C., "Numerical analysis of welding residual stress of u-rib stiffened plate", *Engineering Mechanics*, 46(8), 262-268, 2012. (In Chinese)
- [20] Specifications for Strengthening Design of Highway Bridges, JTGT J22-2008, 2008. (In Chinese)
- [21] Risan H.K., Harba I.S.I., Abdulridha A.J., "Numerical analysis of RC wall with opening strengthened by CFRP subjected to eccentric loads", *Journal of the Croatian Association of Civil Engineers*, 69(7), 573-580, 2017.

RESISTANCE OF COLD-FORMED HIGH STRENGTH STEEL ANGLES

Anh Tuan Tran^{1,*}, Lars Bernspång¹, Milan Veljkovic², Carlos Rebelo³ and Luís Simões da Silva³

¹ Luleå University of Technology, Sweden

² Delft University of Technology, The Netherlands

³ ISISE, University of Coimbra, Portugal

* (Corresponding author: E-mail: trananhtuanguyt@gmail.com)

ABSTRACT

This paper describes a study of the behaviour of cold-formed high strength steel angles. Thirty-six specimens with different cold-formed angles (90°, 100°, 120°, 140°, 160°, and 170°) and different thicknesses (4 mm and 6 mm) were considered. The initial geometric imperfections of the specimens were determined using the 3D laser scanning method. The magnitudes of these geometric imperfections for torsional and torsional-flexural buckling and flexural buckling analyses were proposed. The commercial finite element analysis (FEA) programme ABAQUS with shell elements S4R was used for finite element analyses. Different material strengths in corner and flat parts along with different proof stresses (0.2%, 0.01%, and 0.006%) were considered in the numerical models. The experimental and FEA results showed good agreement. Influence of cold-formed angle on non-dimensional slenderness and reduction factor curves of the 4 mm thick columns with 90° and 120° cold-formed angles was analysed.

ARTICLE HISTORY

Received: 19 March 2018
Revised: 20 December 2018
Accepted: 28 December 2018

KEYWORDS

High strength steel;
Cold-formed angle;
Geometrical imperfections;
Proof stress;
Experimental investigation;
Finite element analysis;

Copyright © 2019 by The Hong Kong Institute of Steel Construction. All rights reserved.

1. Introduction

The use of high strength steel material for cold-formed members significantly improves their properties. It enables thinner, longer and stronger structures. Moreover, the quantity of steel material required for building cold-formed steel structures is considerably reduced, and producing a beneficial effect on the environment. There are several standards that can be used for designing cold-formed steel structures: Australian/New Zealand cold-formed steel structures standard (AS/NZS-4600) [1], North American Specification for the design of cold-formed steel structural members (AISI-S100-12) [2] and European standard EN 1993-1-3 [3].

Several studies about cold-formed angles have been published [4 – 11]. Cold-formed steel angles are considered as thin-walled members that are sensitive to effects of imperfections. The imperfections including initial geometric imperfections and loading eccentricity significantly reduce their buckling strength. However, it is hardly to eliminate the imperfections because of manufacturing tolerance, transportation and measurement. Popovic et al. (1999) experimentally studied 12 fixed-ended and 18 pin-ended cold-formed angles under axial compression load [4]. The thicknesses used were 2.5 mm, 4 mm and 5 mm. As well as material investigations using tensile coupon tests, residual strains were measured with a Cambridge Insitu Extensometer and initial geometric imperfections were determined using a theodolite. The authors of that paper reported that experimental results were between 15% and 40% higher than the Australian and American specifications, respectively and additional eccentricity of L/1000 should only be applied to slender sections. It notes that nominal eccentricity of L/1000 about the minor axis was used for 18 pin end tests. Young (2004) carried out 24 compression tests on fixed-ended cold-formed plain angle columns [5]. The angles were produced using the press brake method. The thicknesses of the columns were 1.2 mm, 1.5 mm and 1.9 mm. The materials used were high strength zinc-coated steel grades G500 and G450. The experimental results were compared with American and Australian/New Zealand standards, and design rules for such fixed-ended cold-formed plain angle columns under compression load were proposed. He noted that additional moment (axial load multiplied by an eccentricity of L/1000) is used in design of compression members according to the AISI Specification and AS/NZS Standard. Ellobody et al. (2005) numerically investigated the behaviour of cold-formed steel plain angle columns [6]. Shell elements S4R in ABAQUS software were used for these investigations, which took into account initial geometric imperfection, residual stresses and material nonlinearities. Experimental and FEA results for 21 columns showed good agreement. The numerical models were developed for a parametric study, the results of which generally fitted design strengths calculated using equations described by Young [5]. Yang et al. (2011) studied buckling behaviour of cold-formed angles in transmission tower applications [7]. One series of equal angle specimens and three series of equal lipped angle specimens were considered. The angle specimens with different slenderness ratios and six constrained types were studied under axial compression load. The slenderness

ratios were calculated based on minimum radius of gyration and length of specimens. The six constrained types at the end of the specimens were considered to reflect conditions of compression members in transmission towers. The six constrained types were determined based on slenderness ratio of the specimen and number of bolts used for the constraint. Shell elements SHELL181 in ANSYS software were used for a numerical investigation. FEA results were compared to experimental results, with the relationship between slenderness ratios and stability coefficients being modelled with a fitting curve and modification factors. Silvestre et al. (2013) summarised the development of the design of cold-formed steel angles [8]. The designs of fixed-ended and pin-ended equal-leg angle columns with short-to-intermediate lengths were considered. The experimental and FEA results from previous studies were taken into account in the study. The authors also described new design procedures based on the direct strength method (DSM). Shifferaw et al. (2014) presented a study of cold-formed steel lipped and plain angle columns with fixed ends [9]. In this study, the authors used ABAQUS with shell elements S9R5 to carry out a numerical investigation. Numerical models for fixed-ended and pin-ended angles with fixed and free warping were considered, with elastic critical buckling loads from the numerical investigations being compared to Young's experimental results. The authors presented new design procedures for strength prediction of the cold-formed angle columns. Resistance of cold-formed L columns under compression, bending and combination of compression and bending were investigated and reported in [10]. The L columns with different cold-formed angles and different thicknesses and with fixed and pinned boundary conditions were considered. Steel materials S650 and S500 were used in the study. As tensile coupon tests had not been carried out, the authors carried out FEA based on basic material properties. Influence of cold forming in hand calculation was considered according to EN 1993-1-3[3] based on nominal yield strength of the materials. Parametric study and comparison analyses were carried out. The authors recommend some changes in design procedure for cross sections with fixed boundary conditions. Landesmann et al. (2017) investigated the behaviour of short-to-intermediate slender pin-ended cold-formed steel equal-leg angle columns [11]. Nineteen columns with 1.55 mm nominal thickness, different leg widths (50 mm, 60 mm, 70 mm, 80 mm and 90 mm) and lengths ranging from 500 mm to 1200 mm were considered. The specimens were made of ZAR-345 mild steel. ANSYS software with shell elements SHELL181 was used for numerical investigation. Amplitude L/1000 was used for numerical investigations of non-critical minor-axis flexural components. The experimental and FEA results were compared to results from a DSM-based design approach. The authors also presented a modification factor for the DSM-based design approach.

Beside effects of initial imperfections and residual stress on cold-formed members were analysed in the publications [4-11]. Load-carrying capacity and material strength at corner also are significant differences in design of hot-rolled and cold-formed members. Yu (2000) indicated that load-carrying capacity of cold formed steel members are limited by buckling stress that are usually less than yield stress of the steel material [12]. Unlike hot-rolled

members, material strength in corners of cold-formed steel members significantly increase by manufacturing process. Ma et al. (2015) specified that 0.2% proof stresses in the corner part with 90° bends increased by up to 34% with effect of cold forming [13].

This paper describes experimental and numerical investigations of the resistance of cold-formed high strength steel angles for polygonal cross sections with different side number in application for wind turbine tubular towers. Thirty-six specimens with different cold-formed angles (90°, 100°, 120°, 140°, 160°, and 170°) and different thicknesses (4 mm and 6 mm) were studied. The initial geometric imperfections of the specimens were determined using the 3D laser scanning method. The magnitudes of initial geometric imperfections for torsional and torsional-flexural buckling and flexural buckling analyses were proposed. The commercial finite element analysis (FEA) programme ABAQUS [14] with shell elements S4R were used for finite element analyses. The influence of yield strength on the FEA was considered with different proof stresses (0.2%, 0.01%, and 0.006%). The experimental results were compared to FEA results. Furthermore, influence of cold-formed angle on non-dimensional slenderness ($\bar{\lambda}$) and reduction factor (χ) curves of the 4 mm thick columns with 90° and 120° cold-formed angles was analysed.

2. Experimental investigation

2.1. Test specimens

In order to investigate the influence of cold-formed angles on the angle resistance, an experimental programme was carried out. Thirty-six angle columns with different thicknesses (4 mm and 6 mm) were studied. The columns were divided into six categories with different cold-formed angles P1 (90°), P2 (100°), P3 (120°), P4 (140°), P5 (160°) and P6 (170°). The width of equal-leg angle (h) of the specimens was 60 mm. Compression tests were carried out on the thirty-six specimens. Figures 1 and 2 show the typical angle specimens with different cold-formed angles.

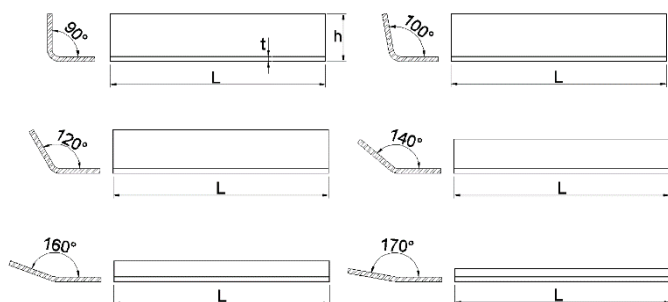


Fig. 1 Typical angle specimens with different cold-formed angles



Fig. 2 4 mm thick specimens with different cold-formed angles

The thicknesses and lengths of the specimens were measured with digital callipers. Each dimension was measured three times. The average values of the measured dimensions and the areas of the cross sections for the specimens are given in Tables 1 and 2. The specimens are labelled as follows: Angle {P1; P2; P3; P4; P5; P6} - Thickness {4 mm; 6 mm} - Test number in the test series {S1; S2; S3}.

Table 1

Average measured dimensions of the 4 mm thick specimens

Specimen	Angle	Thickness (mm)	Length (mm)	Area (mm ²)
P1-4-S1	90°	3.96	593	446
P1-4-S2	90°	4.02	594	453
P1-4-S3	90°	4.02	593	453
P2-4-S1	100°	3.97	590	454
P2-4-S2	100°	4.01	593	459
P2-4-S3	100°	3.94	593	451
P3-4-S1	120°	4.04	591	472
P3-4-S2	120°	4.03	590	471
P3-4-S3	120°	4.02	591	470
P4-4-S1	140°	3.98	593	471
P4-4-S2	140°	4.01	592	475
P4-4-S3	140°	4.02	589	476
P5-4-S1	160°	3.95	591	471
P5-4-S2	160°	4.02	593	479
P5-4-S3	160°	4.04	594	482
P6-4-S1	170°	4.04	592	483
P6-4-S2	170°	3.98	590	476
P6-4-S3	170°	3.96	591	474

Table 2

Average measured dimensions of the 6 mm thick specimens

Specimen	Angle	Thickness (mm)	Length (mm)	Area (mm ²)
P1-6-S1	90°	6.01	591	654
P1-6-S2	90°	6.03	593	656
P1-6-S3	90°	6.01	594	654
P2-6-S1	100°	5.96	589	665
P2-6-S2	100°	6.01	591	671
P2-6-S3	100°	6.01	592	671
P3-6-S1	120°	6.03	591	695
P3-6-S2	120°	5.92	590	682
P3-6-S3	120°	5.96	590	687
P4-6-S1	140°	6.00	591	704
P4-6-S2	140°	5.96	589	700
P4-6-S3	140°	5.92	593	695
P5-6-S1	160°	6.01	590	715
P5-6-S2	160°	5.95	592	708
P5-6-S3	160°	5.93	594	706
P6-6-S1	170°	6.05	590	723
P6-6-S2	170°	6.03	590	721
P6-6-S3	170°	5.94	591	710

2.2. Test set-up and instruments

A Dartec compression machine with a capacity of 600 kN was used for the compression tests. Fig. 3 shows a typical set-up for the compression tests. Two steel blocks were attached to the compression machine in order to create flat surfaces. The load was applied at the top of the specimen. Displacement control was used for the compression tests. Boundary conditions of the specimens were considered as a clamped support (all translations and rotations were restrained) at the bottom and at the top (all degrees of freedom were fixed except the displacement in the direction of the applied load).



Fig. 3 Set-up for the compression tests

Four LVDTs (linear variable displacement transducers) were used to measure the displacement. Three LVDTs were attached to the machine to measure displacement between the two steel blocks, with the other directly attached to the specimen, see Fig. 4.

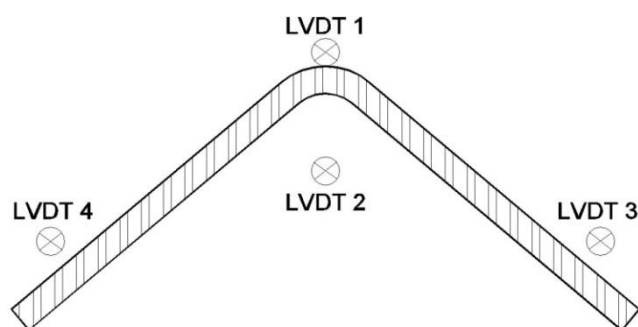


Fig. 4 Positions of LVDTs

2.3. Experimental results

Tables 3 and 4 present the ultimate loads and end shortenings of the 4 mm and 6 mm thick specimens, respectively. The cold-formed angle significantly affected both ultimate loads and end shortenings of the specimens. The average ultimate loads of the 4 mm and 6 mm thick specimens with 90° cold-formed angles were 194 kN and 445 kN, respectively. However, the average ultimate loads of the 4 mm and 6 mm thick specimens with 170° cold-formed angles were just 31 kN and 72 kN, respectively. The average ultimate loads of the 4 mm and 6 mm thick specimens decreased by approximately 84%. The end shortening values also decreased with increasing cold-formed angles from 90° to 170°. The average end-shortenings of the 4 mm and 6 mm thick specimens reduced by 87% and 85%, respectively. The average end shortenings of the 4 mm and 6 mm thick specimens with a cold-formed angle of 170° were 0.25 mm and 0.35 mm, respectively.

Table 3
Ultimate loads and end shortenings of the 4 mm thick specimens

Specimen	Angle	Length (mm)	Area (mm ²)	Ultimate load (kN)	End shortening (mm)
P1-4-S1	90°	593	446	195	2.06

P1-4-S2	90°	594	453	191	1.87
P1-4-S3	90°	593	453	195	2.03
P2-4-S1	100°	590	454	195	1.94
P2-4-S2	100°	593	459	199	1.93
P2-4-S3	100°	593	451	207	1.96
P3-4-S1	120°	591	472	203	1.85
P3-4-S2	120°	590	471	200	1.80
P3-4-S3	120°	591	470	198	1.72
P4-4-S1	140°	593	471	194	1.32
P4-4-S2	140°	592	475	194	1.42
P4-4-S3	140°	589	476	187	1.25
P5-4-S1	160°	591	471	81	0.58
P5-4-S2	160°	593	479	80	0.59
P5-4-S3	160°	594	482	79	0.58
P6-4-S1	170°	592	483	28	0.24
P6-4-S2	170°	590	476	33	0.26
P6-4-S3	170°	591	474	31	0.26

Table 4
Ultimate loads and end shortenings of the 6 mm thick specimens

Specimen	Angle	Length (mm)	Area (mm ²)	Ultimate load (kN)	End shortening (mm)
P1-6-S1	90°	591	654	443	2.35
P1-6-S2	90°	593	656	446	2.43
P1-6-S3	90°	594	654	445	2.37
P2-6-S1	100°	589	665	446	2.22
P2-6-S2	100°	591	671	466	2.41
P2-6-S3	100°	592	671	451	2.35
P3-6-S1	120°	591	695	450	2.02
P3-6-S2	120°	590	682	440	1.95
P3-6-S3	120°	590	687	442	2.02
P4-6-S1	140°	591	704	369	1.73
P4-6-S2	140°	589	700	389	1.85
P4-6-S3	140°	593	695	339	1.65
P5-6-S1	160°	590	715	147	0.78
P5-6-S2	160°	592	708	141	0.72
P5-6-S3	160°	594	706	147	0.77
P6-6-S1	170°	590	723	70	0.33
P6-6-S2	170°	590	721	73	0.33
P6-6-S3	170°	591	710	72	0.38

Fig. 5 shows the typical deformations of the specimens with cold-formed angles 90°, 120°, and 170° during the tests. Fig. 6 gives typical failure modes of the 4 mm specimens with different cold-formed angles 90°, 100°, 120°, 140°, 160°, and 170°. Cold-formed angles significantly affected buckling behaviour of the specimens. Flexural-torsional buckling occurred in the specimens with cold-formed angles of 90°, 100°, 120°, and 140°. Flexural buckling occurred in the specimens with cold-formed angles of 160° and 170°.

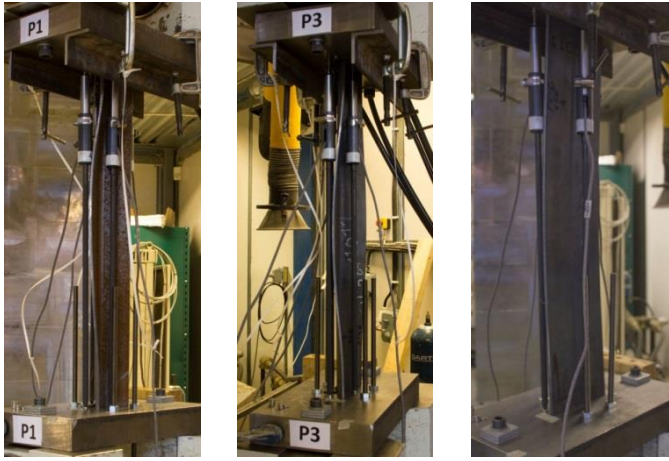


Fig. 5 Typical deformations of the specimens P1 (90°), P3 (120°) and P6 (170°)

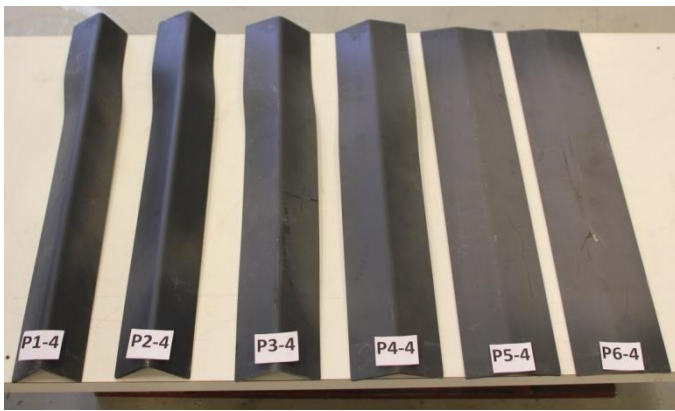


Fig. 6 Typical failure modes of the 4 mm thick specimens P1 (90°), P2 (100°), P3 (120°), P4 (140°) P5 (160°) and P6 (170°)

3. Numerical investigation

3.1. Numerical model

The commercial finite element analysis (FEA) programme ABAQUS [14] was used to simulate the columns with different cold-formed angles under axial compression load. It should be emphasised that the thicknesses of the 4 mm and 6 mm specimens are approximately 0.67% and 1% of their lengths, respectively. In ABAQUS, there are several types of shell elements available [15]. Shell elements S4R (shell elements with four nodes, quadrilateral, reduced numerical integration and a large-strain formulation) were used in this study. Fig. 7 shows a typical FE mesh used for the numerical models. The sizes of shell elements on each side of the columns were approximately 2 mm. The curves at the corner parts were seeded with 8 elements.



Fig. 7 Typical mesh of the numerical models

Fig. 8 shows the typical boundary conditions used for the numerical models. Numerical models with pinned and fixed supports were performed and compared with test results. FEA results from the numerical model with fixed support had good match with test results in terms of load-displacement curve, ultimate load and failure mode. Therefore, numerical models with fixed support were used in this study. A clamped support (all translations and rotations were restrained) was applied at the bottom and at the top, and all degrees of freedom were fixed except the displacement in the direction of the applied load.

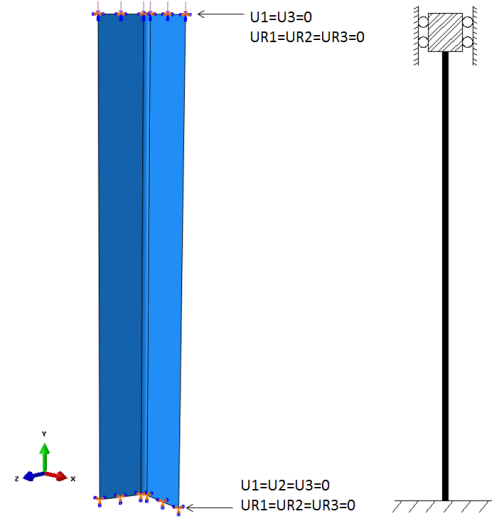


Fig. 8 Typical boundary conditions used for the numerical models

In EN 1993-1-3 [3], influence of cold forming is considered with assumption of increasing yield stress of whole cross sections (corner part and flat part as well) by an average yield stress. In this study, the cold-formed angle specimens were produced by press braking method. In this method, plastic deformation appears in corners of the specimens. It leads to increasing material strength in comparison with original material. An experimental programme using tensile coupon tests was carried out to investigate the mechanical properties of the high strength steel material S650 at the corner and flat parts. In this study, material strengths in corner part and flat part are considered separately.

Key parameters such as yield stress (σ_y), tensile stress (σ_u), and yield strain (ϵ_y) and tensile strain (ϵ_u) of the material at the corner and flat parts are shown in Tables 5, 6 and 7. The following nomenclature was adopted for the specimens: Angle of coupon specimen {C1(90°), C2(100°), C3(120°), C4(140°), C5(160°) and F(flat)} - Thickness {4 mm and 6 mm}-Test number in the test series {S1; S2; S3}. In some cases, the failure sections occurred outside the gauge lengths and, hence, those values (C5-4, C4-6, C1-4-S2, C4-4-S1 and C5-6-S1) were not recorded.

Table 5

Key material properties determined from tensile tests of flat coupon specimens

Specimen	Angle	σ_y (N/mm ²)	ϵ_y (%)	σ_u (N/mm ²)	ϵ_u (%)
F-4-S1	180°	762	0.60	802	10.6
F-4-S2	180°	763	0.60	807	8.6
F-4-S3	180°	762	0.60	806	8.5
F-6-S1	180°	801	0.40	845	5.7
F-6-S2	180°	793	0.40	843	6.0
F-6-S3	180°	791	0.40	843	5.9

Table 6

Key material properties determined from tensile tests of 4 mm thick coupon specimens

Specimen	Angle	σ_y (N/mm ²)	ϵ_y (%)	σ_u (N/mm ²)	ϵ_u (%)
C1-4-S1	90°	889	0.62	929	1.18
C1-4-S2	90°	-	-	-	-
C1-4-S3	90°	925	0.64	951	1.24
C2-4-S1	100°	932	0.64	948	1.02
C2-4-S2	100°	927	0.64	948	1.12
C2-4-S3	100°	914	0.64	944	1.16
C3-4-S1	120°	837	0.60	895	1.25
C3-4-S2	120°	865	0.61	917	1.17
C3-4-S3	120°	859	0.61	898	1.15
C4-4-S1	140°	-	-	-	-
C4-4-S2	140°	839	0.60	876	1.51
C4-4-S3	140°	831	0.60	859	1.07

Table 7

Key material properties determined from tensile tests of 6 mm thick coupon specimens

Specimen	Angle	σ_y (N/mm ²)	ϵ_y (%)	σ_u (N/mm ²)	ϵ_u (%)
C1-6-S1	90°	782	0.57	896	1.50
C1-6-S2	90°	830	0.60	923	1.46
C1-6-S3	90°	874	0.62	896	1.22
C2-6-S1	100°	843	0.60	898	1.37
C2-6-S2	100°	861	0.61	893	1.31
C2-6-S3	100°	853	0.61	890	1.37
C3-6-S1	120°	878	0.62	916	1.33
C3-6-S2	120°	883	0.62	917	1.32
C3-6-S3	120°	845	0.60	905	1.69
C5-6-S1	160°	-	-	-	-
C5-6-S2	160°	778	0.57	867	1.67
C5-6-S3	160°	826	0.59	881	1.34

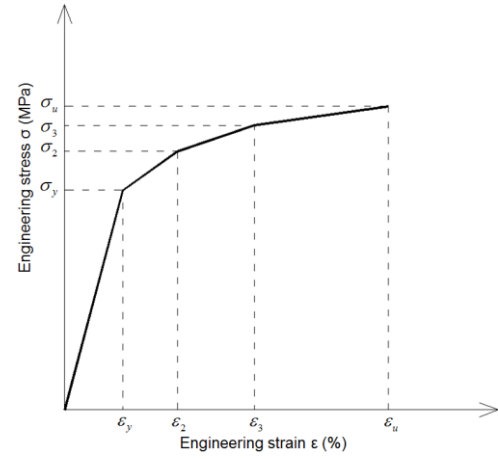
Multi-linear constitutive model was used to model the material properties, Fig. 9. In the commercial finite element analysis (FEA) programme ABAQUS, the engineering stress-strain relationships need to be converted into the form of true stress and true plastic strains using Eq. (1) and (2) [15]:

$$\sigma_{true} = \sigma_{eng}(1 + \epsilon_{eng}) \quad (1)$$

$$\epsilon_{true,p} = \ln(1 + \epsilon_{eng}) - \frac{\sigma_{true}}{E} \quad (2)$$

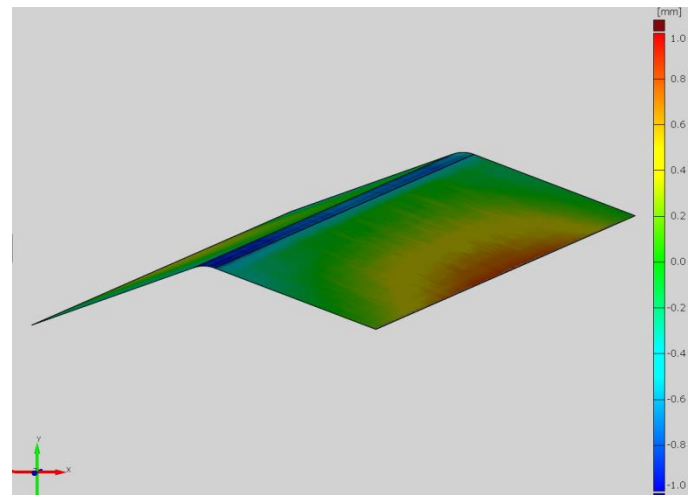
where: σ_{true} is true stress, σ_{eng} is engineering stress, $\epsilon_{true,p}$ is true plastic strain, and ϵ_{eng} is engineering strain.

Residual stress in cold-formed steel plain angle columns was studied by E. Ellobody and B. Young [6]. The authors specified that ultimate load and shortening of the columns with and without residual stress are almost identical. Therefore, residual stress was not considered in this study.

**Fig. 9** Material model

3.2. Initial geometric imperfections

Initial geometric imperfections significantly affect the resistance of the specimens. Therefore, the geometric imperfections of the specimens were determined before testing. There are several methods to determine initial geometric imperfections of specimens. B. W. Schafer et al. [16] used a milling machine, a direct current differential transformer (DCDT) and a computer to measure the initial geometric imperfections of eleven specimens. This method was also used to determine the geometric imperfections of S460NH and S690QH specimens by J. Wang et al. [17]. A theodolite with micrometer plates was used to measure the geometric imperfections at the tips of the legs and at the corners of thirty cold-formed angles [4]. B. Young used two theodolites to obtain the geometric imperfections at the mid-length and near both ends of nineteen cold-formed steel plain angle columns [5]. E. Ellobody and B. Young used a coordinate measuring machine to measure the geometric imperfections at the middle and quarter length of their specimens [6]. Tran et al. used a 3D laser scanning method to measure the geometric imperfections of thirty-two cold-formed circular and polygonal specimens with and without openings [18]. In this study, the 3D laser scanning method was also used to measure the initial geometric imperfections of the thirty-six cold-formed angles. Fig. 10 shows the initial geometric imperfections of the P4-4-S2 specimen.

**Fig. 10** Initial geometric imperfections of the P4-4-S2 specimen

In order to determine geometric imperfections of the specimens, approximately 4100 points on the surface of each specimen were considered. The biggest geometric imperfection amplitudes of the specimens at the sides (e_s) and at the middle (e_m) of angles are given in Tables 8 and 9. Direction of e_s and e_m are perpendicular to side surface and vertical direction of specimen respectively.

Table 8
Initial geometric imperfections of the 4 mm thick specimens

Specimen	Angle	Thickness (mm)	Length (mm)	Max imperfection amplitude	
				e_t (mm)	e_l (mm)
P1-4-S1	90°	3.96	593	0.76	0.64
P1-4-S2	90°	4.02	594	0.90	0.61
P1-4-S3	90°	4.02	593	0.60	0.50
P2-4-S1	100°	3.97	590	0.67	0.58
P2-4-S2	100°	4.01	593	0.93	0.70
P2-4-S3	100°	3.94	593	0.96	0.76
P3-4-S1	120°	4.04	591	0.60	0.53
P3-4-S2	120°	4.03	590	0.71	0.71
P3-4-S3	120°	4.02	591	0.70	0.63
P4-4-S1	140°	3.98	593	0.80	0.80
P4-4-S2	140°	4.01	592	0.72	0.72
P4-4-S3	140°	4.02	589	0.71	0.69
P5-4-S1	160°	3.95	591	0.80	0.79
P5-4-S2	160°	4.02	593	0.81	0.78
P5-4-S3	160°	4.04	594	0.90	0.88
P6-4-S1	170°	4.04	592	0.70	0.67
P6-4-S2	170°	3.98	590	0.59	0.51
P6-4-S3	170°	3.96	591	0.74	0.65
Mean				0.76	0.67
Standard deviation				0.11	0.11

Table 9
Initial geometric imperfections of the 6 mm thick specimens

Specimen	Angle	Thickness (mm)	Length (mm)	Max imperfection amplitude	
				e_t (mm)	e_l (mm)
P1-6-S1	90°	6.01	591	1.04	0.94
P1-6-S2	90°	6.03	593	1.11	0.80
P1-6-S3	90°	6.01	594	1.04	0.72
P2-6-S1	100°	5.96	589	1.17	0.83
P2-6-S2	100°	6.01	591	1.25	0.82
P2-6-S3	100°	6.01	592	0.62	0.87
P3-6-S1	120°	6.03	591	0.90	0.69
P3-6-S2	120°	5.92	590	1.01	0.65
P3-6-S3	120°	5.96	590	0.89	0.62
P4-6-S1	140°	6.00	591	0.75	0.73
P4-6-S2	140°	5.96	589	0.94	0.71
P4-6-S3	140°	5.92	593	0.70	0.82
P5-6-S1	160°	6.01	590	0.61	0.74
P5-6-S2	160°	5.95	592	0.78	0.84
P5-6-S3	160°	5.93	594	0.71	0.51
P6-6-S1	170°	6.05	590	0.72	0.65
P6-6-S2	170°	6.03	590	1.14	0.60
P6-6-S3	170°	5.94	591	1.04	0.91
Mean				0.91	0.75
Standard deviation				0.20	0.12

According to EN 1993-1-5 [19], in relation to local buckling of a panel or subpanel with a short span a or b , the magnitude of the equivalent geometric imperfections is the lower value of $a/200$ and $b/200$. In respect of flexural buckling, according to EN 1993-1-1 [20], the magnitudes of initial imperfections for elastic analysis and plastic analysis are $L/200$ and $L/150$ respectively (buckling curve c). The magnitudes of initial geometric

imperfections have been described in several papers. The average geometric imperfections of 30 cold-formed angles at the tips of the legs and at the corners were $L/1305$ and $L/2310$, respectively [4]. The authors also specified that the geometric imperfections at the tips were much higher than at the corners. F. Yang et al. used $L/750$ at the middle of cold-formed angles for the initial overall geometric imperfection [7]. E. Mesacasa Jr et al. used geometric imperfection amplitude $L/1000$ at middle height of thin-walled equal-leg angle columns in FEA for flexural-torsional buckling and flexural buckling analyses [27]. According to EN 1090-2:2008+A1:2011, the permitted deviation Δ of cold-formed profiled sheets should be $\Delta \leq \pm b/50$ (b is the nominal width) [25]. It should be emphasised that the width of the equal-leg angle (h) of the specimens was 60 mm. Therefore, the maximum imperfection amplitudes of our specimens were within the recommendation according to EN 1090-2:2008+A1:2011.

In attempt to determine geometric imperfections for cold-formed angle specimens, collected data on geometric imperfections of thirty-six specimens were performed. Fig. 11 shows the ratios between the maximum geometric imperfection magnitude at the sides of the angles and the thicknesses of the specimens, as a percentage. Fig. 12 shows the ratios between the lengths and the maximum geometric imperfection magnitude at the middle of the specimens. Average values of the ratios are determined and also presented in Figs 11 and 12. The magnitude of initial geometric imperfections for local and torsional/torsional-flexural buckling and flexural buckling analyses of cold-formed angle specimens are proposed as $17\% t$ and $L/855$ respectively, where L and t are the length and thickness of the specimen, respectively. It emphasized that the specimens in this study were provided by Ruukki Company in Finland.

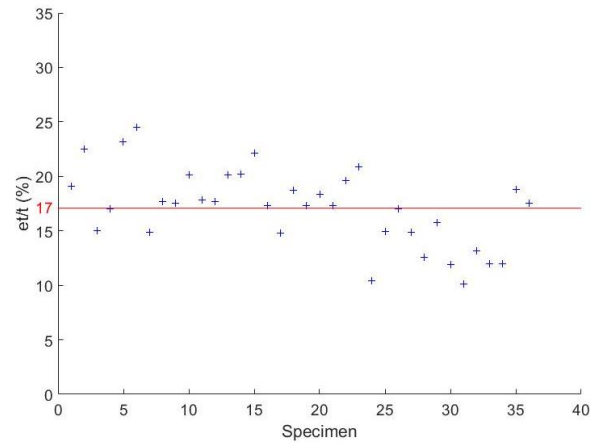


Fig. 11 Ratio of percentage between maximum initial geometric imperfection at sides and thickness of each specimen

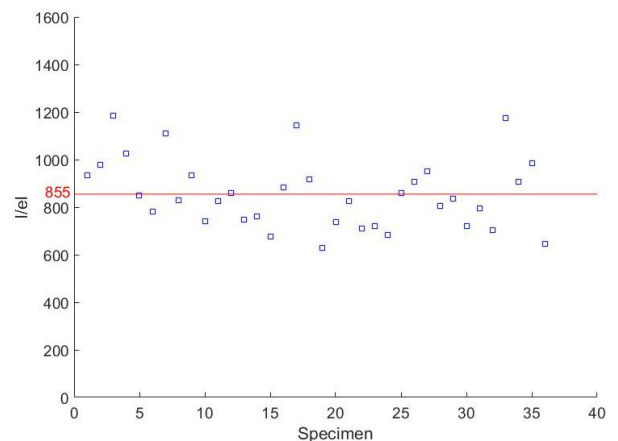


Fig. 12 Ratio between maximum initial geometric imperfection at the middle and length of each specimen

3.3. Influence of yield strength on the FEA

Proof stress significantly affects the resistance of finite element analysis (FEA) models [21]. According to EN 1993-1-6, if the behaviour between stress and strain is nonlinear, the yield strength should be taken as 0.2% proof stress [22]. However, N.S. Ottosen and M. Ristinmaa specified that offset strains used in most scientific experimental investigations are much smaller than 0.2% [23].

D. Rees recommended that offset strains are in the range from 0.001% to 0.01% [24]. In this study, 0.2%, 0.01% and 0.006% proof stresses were used to investigate the influence of proof stress on the resistance of the FEA models. The specimens studied had different thicknesses (4 mm and 6 mm) and different cold-formed angles (90°, 100°, 120°, and 140°). Resistance values from the FEA were compared to corresponding results from the experiments, see Table 10. Mean values and standard deviation values are also shown in this

table. Mean values of resistance ratios between experimental and FEA results with 0.2%, 0.01%, and 0.006% proof stresses were 0.91, 0.99, and 1.06, respectively. The difference in average between the experimental and FEA results with 0.01% proof stress was just 1%. Therefore, 0.01% proof stress was used in this study.

Table 10
Initial geometric imperfections of the 6 mm thick specimens

Specimen	Angle	Ultimate load (kN)						
		Experiment	FEA					
		Ptest	P0.2	P0.01	P0.006	Ptest/P0.2	Ptest/P0.01	Ptest/P0.006
P1-4-S1	90°	195	211	196	191	0.93	1.00	1.02
P1-6-S3	90°	445	489	423	375	0.91	1.05	1.19
P2-4-S2	100°	199	214	200	194	0.93	0.99	1.02
P2-6-S1	100°	446	498	448	411	0.89	0.99	1.08
P3-4-S2	120°	200	217	201	194	0.92	1.00	1.03
P3-6-S1	120°	450	522	467	426	0.86	0.96	1.06
P4-4-S2	140°	194	213	203	196	0.91	0.96	0.99
Mean						0.91	0.99	1.06
Standard deviation						0.02	0.03	0.06

3.4. Finite element model validation

Resistance comparisons of the specimens with different thicknesses and different cold-formed angles between the experimental and FEA results are presented in Table 10. It should be noted that materials of corner part and flat part in the numerical models were modelled separately based on tensile coupon tests. Therefore, FEA results of some cold-formed angles are not presented in Table 11 because of lacking data from the tensile coupon tests. The mean and standard deviation values were 1.01 and 0.04, respectively. The difference in average between the experimental and FEA results was just 1%. The good agreement between ultimate loads derived from the FEA and experimental

results validate the simulations. It should be noticed that different materials were used for the different parts (flat and corner parts) and the initial geometric imperfections of the specimens were determined using the 3D laser scanning method described in section 3.2. Experimental and numerical load-displacement curves for the 4 mm thick specimen with 90° cold-formed angle and 120° cold-formed angle are presented in Figs 13 and 14 respectively. They show good agreement in terms of shapes and ultimate loads. Figs 15 and 16 show the deformation and failure mode of the 4 mm thick specimen with 100° cold-formed angle, respectively. The experimental results matched those from the FEA well.

Table 11
Comparisons between experimental and FEA results

Specimen	Angle	Thickness (mm)	Length (mm)	Ultimate load (kN)		
				FEA (PFEA)	Experiment (Ptest)	PFEA/Ptest
P1-4-S1	90°	3.96	593	196	195	1.00
P1-4-S2	90°	4.02	594	197	191	1.03
P1-4-S3	90°	4.02	593	197	195	1.01
P2-4-S1	100°	3.97	590	200	195	1.03
P2-4-S2	100°	4.01	593	200	199	1.01
P2-4-S3	100°	3.94	593	200	207	0.97
P3-4-S1	120°	4.04	591	200	203	0.99
P3-4-S2	120°	4.03	590	201	200	1.01
P3-4-S3	120°	4.02	591	201	198	1.01
P4-4-S1	140°	3.98	593	202	194	1.04
P4-4-S2	140°	4.01	592	203	194	1.04
P4-4-S3	140°	4.02	589	203	187	1.08
P1-6-S1	90°	6.01	591	423	443	0.95
P1-6-S2	90°	6.03	593	421	446	0.94
P1-6-S3	90°	6.01	594	423	445	0.95
P2-6-S1	100°	5.96	589	448	446	1.01
P2-6-S2	100°	6.01	591	445	466	0.96
P2-6-S3	100°	6.01	592	462	451	1.02
P3-6-S1	120°	6.03	591	467	450	1.04
P3-6-S2	120°	5.92	590	463	440	1.05

P3-6-S3	120°	5.96	590	467	442	1.06
Mean						1.01
Standard deviation						0.04

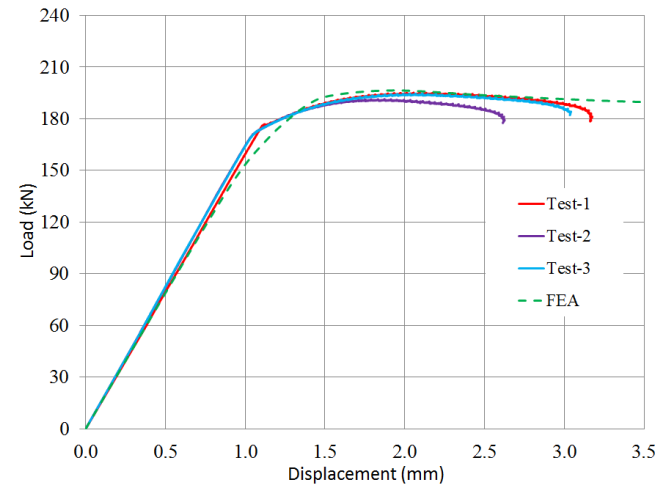


Fig. 13 Load-displacement curves obtained from the FEA and test results for 4 mm thick specimens with 90° cold-formed angle

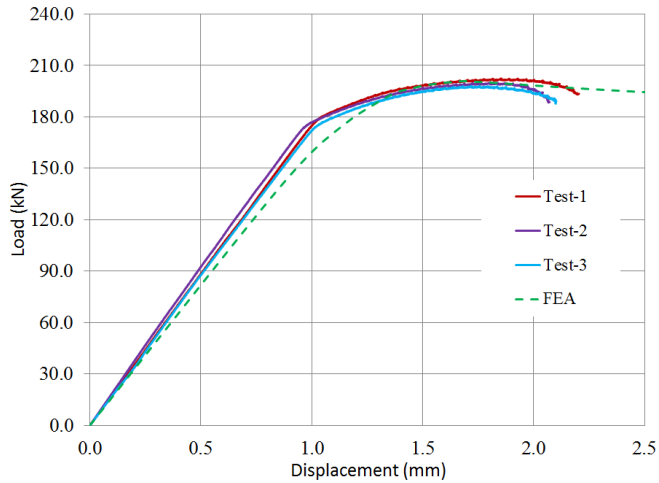


Fig. 14 Load-displacement curves obtained from the FEA and test results for 4 mm thick specimens with 120° cold-formed angle

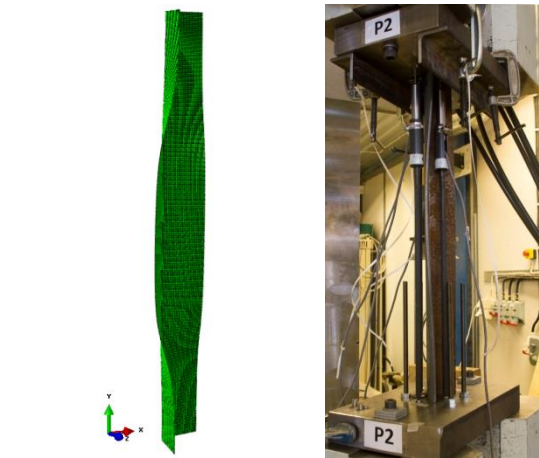


Fig. 15 Deformation of the 4 mm thick specimen with 100° cold-formed angle (FEA and experimental results)

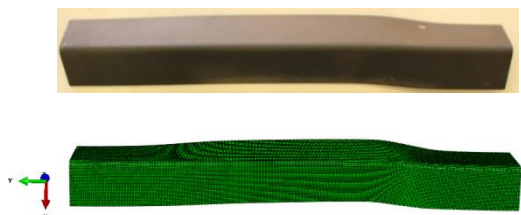


Fig. 16 Failure mode of the 4 mm thick specimen with 100° cold-formed angle (experimental and FEA results)

4. Parametric study

Behaviour of angle columns with various lengths were numerically investigated and presented in [26-27]. Dinis et al [26] and Mesacasa Jr. et al [27] used the commercial finite element analysis (FEA) programmes ABAQUS and ANSYS with shell elements for their studies respectively. Dinis et al [26] used cross section L70x70x1.2 mm3 and Mesacasa Jr. et al [27] used cross section L70x70x2.0 mm3 for the columns. It is worth to mention that class of the cross-sections is 4.

The authors specified that behaviours of short-to-intermediate and intermediate-to-long columns are flexural-torsional buckling and pure flexural buckling, respectively and 'transition length' between the two buckling behaviours. In the transition length, behaviour of the columns is coupling between two global buckling (flexural-torsional buckling and pure flexural buckling). Ultimate strengths of the columns significantly grow as the length reaches the transition value [27]. It notes that transition value is the coincident flexural-torsional and flexural critical buckling load.

In this work, the commercial finite element analysis (FEA) programmes ABAQUS [14] used to determine critical loads of the column with various lengths. Fig. 17 shows relationship between critical loads and column lengths of the cross section L60x60x4 mm3. The curve presented by Mesacasa Jr. et al in [27] is also showed in this figure. It notes that F and P in the curve from Mesacasa Jr. et al are fixed and pinned boundary conditions respectively. The curves of the L70x70x2 mm3 columns and L60x60x4 mm3 columns with 90° cold-formed angle show good match in term of shape and trend.

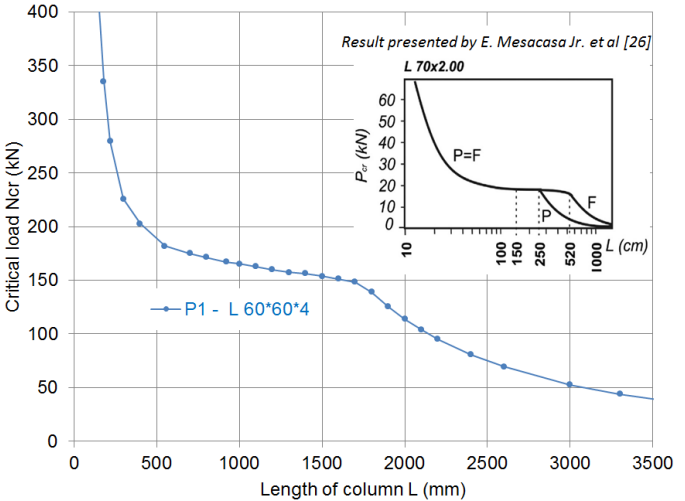


Fig. 17 Critical load and column length curve of the 4 mm thick column with 90° cold-formed angle

After FE models validated in section 3.4, a series of FE models were developed to investigate relationships between non-dimensional slenderness ($\bar{\lambda}$) and reduction factor (χ) curves of the columns with 90° and 120° cold-formed angles. Cross-section dimensions of the columns were fixed with 4 mm thickness and 60 mm width of equal-leg angle. Slenderness of the columns was determined by changing length of the columns. Material in corner part and flat part of the columns were modelled separately based on tensile coupon tests. Initial geometric imperfections of the columns were used as 17% of thickness and 1/855 of length of the columns for torsional-flexural buckling behaviour and flexural buckling behaviour respectively. Boundary

conditions of the columns were a clamped support (all translations and rotations were restrained) at the bottom and at the top (all degrees of freedom fixed except the displacement in the direction of the applied load).

The reduction factor was calculated as follows:

$$\chi = \frac{N_{ult}}{N_y} \quad (3)$$

where N_{ult} is the ultimate load determined by experiment or from FEA, and N_y is determined using the following equation:

$$N_y = A_{corner} f_{y,corner} + A_{eff} f_{y,flat} \quad (4)$$

where A_{corner} , A_{eff} are the areas of the corner part and the effective area of the flat part, respectively, $f_{y,corner}$ and $f_{y,flat}$ are the yield strengths of the corner part and the flat part, respectively. It should be noted that the class of the specimens is 4. According to EN 1993-1-5 [19], a gross cross-sectional area for a class 4 cross section is reduced to an effective area of a compression zone. The effective area is determined by Eq. (5).

$$A_{eff} = \rho A_g \quad (5)$$

where ρ is the reduction factor for plate buckling, and A_g is the gross cross-sectional area. The reduction factor for the plate buckling is determined as follows:

$$\rho = 1 \quad \text{for } \bar{\lambda}_\rho \leq 0.748 \quad (6)$$

$$\rho = \frac{\bar{\lambda}_\rho - 0.188}{\bar{\lambda}_\rho^2} \leq 1.0 \quad \text{for } \bar{\lambda}_\rho > 0.748 \quad (7)$$

$$\text{where: } \bar{\lambda}_\rho = \frac{h/t}{28.4 \varepsilon \sqrt{k_\sigma}} \quad (8)$$

and h is the width of the equal-leg angle, t is the thickness, k_σ is the buckling factor, and

$$\varepsilon = \sqrt{\frac{235}{f_{y,flat}}} \quad (9)$$

The non-dimensional slenderness $\bar{\lambda}$ is obtained from the following equation:

$$\bar{\lambda} = \sqrt{\frac{A_{corner} f_{y,corner} + A_{eff} f_{y,flat}}{N_{cr}}} \quad (10)$$

where N_{cr} is the elastic critical force for flexural buckling and torsional-flexural buckling.

Fig. 18 presented relationship between the non-dimensional slenderness and reduction factor curves of the 4 mm thick columns with 90° and 120° cold-formed angles. The figure also shows results tested by Popovic et al [4] and test results of the P1 and P3 columns with approximately 600 mm length. Popovic et al [4] tested columns with L50x50x2.5 mm3 cross-section under compression. The material properties in corner and flat part and compression test results of the L50x50x2.5 mm3 columns presented in Tables 12 and 13 respectively. The test results agree well to the FEA results.

Table 12

Tensile coupon test results from Popovic et al [4]

Section	Material	$f_{y,static}$ (MPa)	$f_{y,static}$ (MPa)	E (MPa)	e_u (%)
L50x50x2.5	Corner	568	618	200516	10
L50x50x2.5	Flat	396	475	208318	23

Table 13

Compression test results* from Popovic et al [4]

Section*	Sample length L (mm)*	Ultimate load (kN)*	N_{rest}	Reduction factor $\frac{N_{rest}}{N_y}$
L50x50x2.5	550	54.0		0.85

L50x50x2.5	970	41.5	0.65
L50x50x2.5	1379	37.0	0.58
L50x50x2.5	1747	31.3	0.49
L50x50x2.5	2199	26.4	0.41
L50x50x2.5	2598	22.3	0.35

Characteristic comparison between the 120° and 90° cross-sections is presented in Table 14. The torsion constant, warping constant and second moment of area for major axis of the 120° cross-section are 4%, 12% and 57% higher than 90° cross-section respectively. It is worth to note that, in this work, slenderness of the columns was determined by changing length of the columns. The column length decrease (non-dimensional slenderness decrease) causes increasing effect of cross section characteristic (for the major axis) on the flexural-torsional buckling. It leads the reduction factor of 120° cross-section column is higher than 90° cross-section column as the non-dimensional slenderness decreases.

Table 14

Characteristic comparison between 90° and 120° cross-sections

Characteristic of cross section	Cross section P3 (120°)	Cross section P1 (90°)	$\frac{P_3}{P_1}$
Torsion constant (I_t mm ⁴)	2426	2328	1.04
Warping constant (I_w mm ⁶)	691070	618780	1.12
Second moment of area for major axis (I_y mm ⁴)	407680	260350	1.57

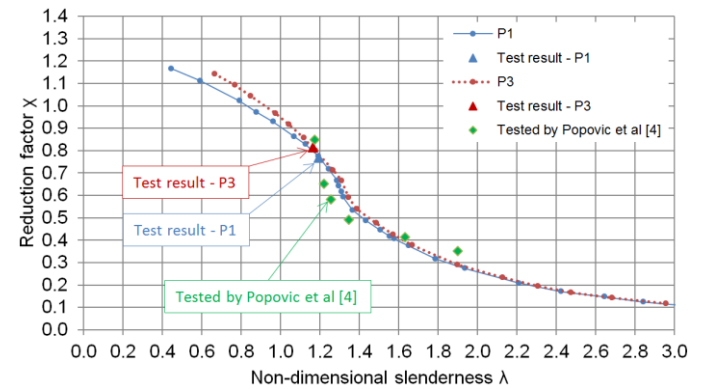


Fig. 18 Non-dimensional slenderness and reduction factor curves of the 4 mm thick columns with 90° and 120° cold-formed angles

5. Conclusions

The resistance of the thirty-six specimens with different thicknesses (4 mm and 6 mm) and different cold-formed angles (90°, 100°, 120°, 140°, 160°, and 170°) was investigated experimentally. Numerical models were developed and calibrated against the experimental results. Based on experimental and FEA results, the following conclusions are suggested:

- The resistance of the specimens significantly decreases by 84% with increasing cold-formed angles from 90° to 170°.
- The initial geometric imperfections of the thirty-six specimens are investigated using the 3D laser scanning method. Magnitudes of the initial geometric imperfection for torsional and torsional-flexural buckling and flexural buckling analyses are proposed 17% b and L/855 respectively.
- The influence of 0.2%, 0.01%, and 0.006% proof stresses on the resistances in FEA are considered. The differences between experimental and FEA results corresponding to 0.2%, 0.01% and 0.006% proof stresses are 9%, 1%, and 6% respectively.
- Relationships between non-dimensional slenderness ($\bar{\lambda}$) and reduction factor (χ) of the 4 mm thick columns with 90° and 120° cold-formed angles were analysed and presented.

Acknowledgements

The authors wish to thank the Research Fund for Coal and Steel for financially supporting the research in this paper through the Research Project HISTWIN 2 (RFSR-CT-2010-00031).

References

- [1] AS/NZS-4600, Cold-formed Steel Structures, Australian/New Zealand standard, 2005.
- [2] AISI-S100-12, North American Specification for the Design of Cold Formed Steel Structural Members, AISI, 2012.
- [3] EN 1993-1-3, Design of Steel Structures, Part 1-3: General Rules – Supplementary Rules for Cold-formed Members and Sheet piling, Brussels, Belgium: European Committee for Standardization, 2006.
- [4] Popovic D., Hancock G.J. and Rasmussen K.J.R., “Axial compression tests of cold-formed steel angles”, *Journal of Structural Engineering*, 125, 515–523, 1999.
- [5] Young B., “Tests and design of fixed-ended cold-formed steel plain angle columns”, *Journal of Structural Engineering*, 130, 1931–1940, 2004.
- [6] Ellobody E. and Young B., “Behavior of cold-formed steel plain angle columns”, *Journal of Structural Engineering*, 131, 457–466, 2005.
- [7] Yang F., Han J., Yang J. and Li Z., “Study on the buckling behaviour of cold-formed steel angles in transmission towers”, *International Journal of Steel Structures*, 11, 495–508, 2011.
- [8] Silvestre N., Dinis P.B. and Camotim D., “Developments on the design of cold-formed steel angles”, *Journal of Structural Engineering*, 139, 680–694, 2013.
- [9] Shifferaw Y. and Schafer B.W., “Cold-formed steel lipped and plain angle columns with fixed ends”, *Thin-walled Structures*, 80, 142–152, 2014.
- [10] Doležal J. and Podgaysky M., “Resistance of cold-formed L-columns made of high strength steel”, Master thesis, 2014.
- [11] Landesmann A., Camotim D., Dinis P.B. and Cruz R., “Short-to-intermediate slender pin-ended cold-formed steel equal-leg angle columns: Experimental investigation, numerical simulations and DSM design”, *Engineering Structures*, 132, 471–493, 2017.
- [12] Yu W.W., “Cold-formed Steel Design”, John Wiley and Sons, 2000.
- [13] Ma J.L., Chan T.M. and Young B., “Material properties and residual stresses of cold-formed high strength steel hollow sections”, *Journal of Constructional Steel Research*, 109, 152–165, 2015.
- [14] Abaqus 6.12-1, Simulia Dassault Systmes, 2012.
- [15] Abaqus/Standard User’s Manual, Version 6.12.
- [16] Schafer B.W. and Peköz T., “Computational modeling of cold-formed steel: characterizing geometric imperfections and residual stresses”, *Journal of Constructional Steel Research*, 47, 193–210, 1998.
- [17] Wang J., Afshan S. and Schillo N., Theofanous, M., Feldmann, M., Gardner, L., “Material properties and compressive local buckling response of high strength steel square and rectangular hollow sections”, *Engineering Structures*, 130, 297–315, 2017.
- [18] Tran A.T., Veljkovic M., Rebelo C. and Simões da Silva L., “Resistance of cold-formed high strength steel circular and polygonal sections - Part 1: Experimental investigations”, *Journal of Constructional Steel Research*, 120, 245–257, 2016.
- [19] EN 1993-1-5, Design of Steel Structures, Part 1-5: Plated Structural Elements, Brussels, Belgium: European Committee for Standardization, 2006.
- [20] EN 1993-1-1, Design of Steel Structures, Part 1-1: General Rules and Rules for Buildings, Brussels, Belgium: European Committee for Standardization, 2005.
- [21] Tran A.T., Veljkovic M., Rebelo C. and Simões da Silva, L., “Resistance of cold-formed high strength steel circular and polygonal sections - Part 2: Numerical investigations”, *Journal of Constructional Steel Research*, 125, 227–238, 2016.
- [22] EN 1993-1-6, Design of Steel Structures, Part 1-6: Strength and Stability of Shell Structures, Brussels, Belgium: European Committee for Standardization, 2007.
- [23] Ottosen N.S. and Ristinmaa M., “The Mechanics of Constitutive Modeling”, Elsevier, 2005.
- [24] Rees R., “Basic Engineering Plasticity: An Introduction With Engineering and Manufacturing Applications”, Elsevier, 2006.
- [25] EN 1090-2:2008+A1:2011, Execution of Steel Structures and Aluminium Structures, Part 2: Technical Requirements for Steel Structures, Brussels, Belgium: European Committee for Standardization, 2011.
- [26] Dinis P.B., Camotim D. and Silvestre N., “On the mechanics of thin-walled angle column instability”, *Thin-walled Structures*, 52, 80–89, 2012.
- [27] Mesacasa E. Jr., Dinis P.B., Camotim D. and Malite M., “Mode interaction in thin-walled equal-leg angle columns”, *Thin-walled Structures*, 81, 138–149, 2014.

STUDY ON LOAD-DEFLECTION RELATIONSHIP OF RECYCLED SELF-COMPACTING CONCRETE FILLED STEEL TUBULAR COLUMNS SUBJECTED TO ECCENTRIC COMPRESSION

Feng Yu ¹, Long Chen ¹, Yuan Fang ^{1,*}, Jun-jie Jiang ¹, Shi-long Wang ¹ and Zheng-yi Kong ¹

¹ Department of Civil Engineering and Architecture, Anhui University of Technology, Maanshan, China

* (Corresponding author: E-mail: fyuan86@126.com)

ABSTRACT

Behaviors of recycled self-compacting concrete filled steel tubular (RSCCFST) columns under eccentric compression were experimentally investigated in this paper. The influences of the recycled coarse aggregate (RCA) replacement ratios, length-diameter ratios, eccentricities, and concrete strength were examined. According to the tests, the RSCCFST columns demonstrated a satisfying performance under the eccentric loads. The failure modes of short and long RSCCFST columns are drum-like bending and flexural buckling, respectively. Large replacement ratio of RCA and length-diameter ratio would reduce the member stiffness and increase the yielding and ultimate deflections; while the variation of concrete strength has little effect on the deflections. Therefore, to improve the member bearing capacity, the most effective way is to reduce the RCA replacement ratio, length-diameter ratio and increase the concrete strength. Furthermore, based on the fiber strip method, a numerical analysis approach for conveniently evaluating the load-deflection relationship of the RSCCFST columns was developed. The load-deflection curves of the specimens were calculated with the numerical method and compared with the test data. The verifications illustrated the proposed method has good accuracy and can be adopted in engineering practices.

ARTICLE HISTORY

Received: 22 November 2018
Revised: 18 January 2019
Accepted: 25 January 2019

KEYWORDS

Concrete filled steel tube;
Recycled self-compacting concrete;
Replacement ratio of RCA;
Length-diameter ratio;
Eccentricity

Copyright © 2019 by The Hong Kong Institute of Steel Construction. All rights reserved.

1. Introduction

Due to rapid urbanization and city renewal, increasing use of natural aggregates and deposit of construction waste result in severe environmental problems. To resolve this issue, the recycled coarse aggregate (RCA) using the crushed waste concrete has been proposed [1].

According to previous research [2-6], RCA would influence the splitting tensile strength, flexural strength and durability of recycled aggregate concrete. Gupta [7] conducted an experiment to investigate the mechanical properties of recycled aggregate concrete showing the tensile and flexural strength of recycled aggregate concrete can be improved by increasing the water-cement ratio, and the capacity of the RCA concrete with the high water-cement ratio is greater than the conventional concrete. Kou et al. [8] and Tam et al. [9] found that the mechanical properties of the concrete with the recycled aggregate immersed in sulfide, chloride and polyvinyl alcohol were better than ordinary concrete. Xiao et al. [10] investigated the dynamic performance of the recycled concrete frame, which indicated that the structure with a higher replacement ratio of RCA, ratio between the mass of recycled coarse aggregate and total coarse aggregate, had a good seismic resistance.

The self-compacting concrete (SCC) could improve both concrete performance and construction safety due to its good homogeneity, fluidity and compactness [11,12]. Silva et. al. [13], Kenai et. al. [14] and Zoran et. al. [15] indicated that the properties of recycled self-compacting concrete (RSCC) was excellent with an appropriate RCA replacement ratio, which demonstrated RSCC has a potential to be a useful material in civil engineering.

Furthermore, the concrete-filled steel tube (CFST) has been widely used due to its extraordinary bearing capacity, ductility and low construction costs [16-18]. It has a superior performance under compression [19-22], dynamic load [23] and fire [24]. From this point of view, the recycled concrete filled steel tubular (RCFST) column was proposed. Mohanraj et al. [25] experimentally investigated the axial compressive behavior of RCFST columns that indicated the ultimate bearing capacity of RCFST columns was higher than conventional reinforced concrete and reinforced recycled concrete columns with 10% less cost of concrete. Yang and Han [26] examined the performance of RCFST columns under eccentric compression. Results showed that the failure modes of RCFST columns were similar to the ordinary CFST columns, i.e., the overall buckling failure. Tang et al. [27] analyzed the behavior of RCFST columns under cyclic loading, where the RCFST columns exhibited excellent deformation capacity and ductility compared with ordinary CFST columns.

However, the compactness of the core concrete, relating to the bearing capacity, in the composite structure is difficult to guarantee. Muciaccia et al. [28] illustrated that the good compactness and homogeneity could be obtained under the self-gravity of SCC in CFST. Mahgub et al. [29] conducted an experiment on axially loaded SCC filled elliptical steel tubular columns

demonstrating that the composite columns with large length-diameter ratio has overall buckling failure mode and low bearing capacity.

Although a lot of investigations on RCFST and self-compacting concrete filled steel tube (SCCFST) have been carried out, little research focuses on the mechanical properties of RSCCFST columns. In this study, twenty-one RSCCFST columns were tested to investigate the member performance under eccentric compression. The influences of the RCA replacement ratio, length-diameter ratio, eccentricity and concrete strength on the load-deflection relationship were discussed. A convenient numerical analysis approach for evaluating the column capacity is presented.

2. Experimental Program

2.1. Preparation of Specimens

To comparatively investigate the RSCCFST column performance, twenty-one specimens with various properties, replacement ratios of RCA, length-diameter ratios, eccentricities and concrete strength grades, were tested. The parameters of the specimens are given in Table 1. Both ends of the tubes were polished, flatted and welded with 300 mm×300 mm×10 mm steel plates. During the specimen fabrication, after the bottom end plate was connected to the steel tube, the RSCC was poured without vibration. A plastic film was used to temporarily seal the upper end of the specimen to reduce the water evaporation. When the core RSCC was set, the plastic film was removed, and the upper steel plate was welded to the top of the specimen.

2.2. Material properties

Q235 steel was used to make the straight seamless outer tube. The material properties of the steel measured from the coupon test are provided in Table 2. The RSCC consisted of coarse aggregates (RCA and ordinary graded gravel), continuously graded fine aggregates (sand and fly-ash), P. O 42.5 cement, tap water, and Polycarboxylate acid superplasticizer. RCA was obtained by crushing the waste C20-C60 concrete blocks. The sieve analysis of RCA was performed according to the Chinese standard JGJ 52-2006 [30]. The particle sizes of RCA and ordinary graded gravel were 5 mm-31.5 mm. The components of RSCC and the mechanical properties determined from the specified method in Chinese Regulation JGJ/T283-2012 [31] are shown in Table 3.

2.3. Test setup and procedure

The experiments were conducted on the hydraulic compression testing machine. The detailed test setup and strain measuring points were shown in Fig. 1.

Two linear variable displacement transducers (LVDTs) were employed to monitor the column's axial deformation. Another three LVDTs were horizontally arranged at 0.25L, 0.5L, and 0.75L height to determine the lateral column deflections. For the short column, eight strain gauges were evenly arranged at the column mid-height to measure the axial and circumferential strains, see Fig. 1(a). For the long column, twenty-four strain gauges were glued evenly at 0.25L, 0.5L, and 0.75L, see Fig. 1(c).

The experiments were initiated with the load-controlled loading scheme with the rate of 50 kN/min. After the axial load reached approximately 85% of the estimated ultimate bearing capacity, the displacement-controlled loading scheme with the rate of 0.5 mm/min was adopted.

Table 1
Parameters of specimens

Specimen ID	D/mm	t/mm	L/mm	γ /%	e/mm	e/r	L/D	Concrete number
RSCSE-1	140	3.63	500	0	20	0.30	3.57	S1/C30
RSCSE-2	140	3.63	500	0	40	0.60	3.57	S1/C30
RSCSE-3	140	3.63	500	0	60	0.90	3.57	S1/C30
RSCSE-4	140	3.63	500	50	20	0.30	3.57	S2/C30
RSCSE-5	140	3.63	500	50	40	0.60	3.57	S2/C30
RSCSE-6	140	3.63	500	50	60	0.90	3.57	S2/C30
RSCSE-7	140	3.63	500	100	20	0.30	3.57	S3/C30
RSCSE-8	140	3.63	500	100	40	0.60	3.57	S3/C30
RSCSE-9	140	3.63	500	100	60	0.90	3.57	S3/C30
RSCSE-10	140	3.63	500	100	20	0.30	3.57	S4/C50
RSCSE-11	140	3.63	500	100	40	0.60	3.57	S4/C50
RSCSE-12	140	3.63	500	100	60	0.90	3.57	S4/C50
RSCSE-13	140	3.63	500	100	20	0.30	3.57	S5/C60
RSCSE-14	140	3.63	500	100	40	0.60	3.57	S5/C60
RSCSE-15	140	3.63	500	100	60	0.90	3.57	S5/C60
RSCSE-16	140	3.63	1000	100	20	0.30	7.14	S4/C50
RSCSE-17	140	3.63	1000	100	40	0.60	7.14	S4/C50
RSCSE-18	140	3.63	1000	100	60	0.90	7.14	S4/C50
RSCSE-19	140	3.63	1500	100	20	0.30	10.71	S4/C50
RSCSE-20	140	3.63	1500	100	40	0.60	10.71	S4/C50
RSCSE-21	140	3.63	1500	100	60	0.90	10.71	S4/C50

Note: RSCSE indicates eccentrically loaded columns, D , L , t , and γ are the measured steel tube outside diameter, length, thickness, and the replacement ratio of RCA, respectively, r and e are the radius of concrete and the eccentricity, respectively.

Table 2
The main material properties of the steel tube

Tube thickness (mm)	Yield strength (MPa)	Tensile strength (MPa)	Young's modulus (10^5 MPa)	Poisson's ratio
3.63	233.23	295.68	2.00	0.297

3. Experimental results and analysis

3.1. Failure modes

The failure process of the eccentrically loaded RSCCFST columns contained three stages as elasticity, elastoplasticity and plasticity. The elastic stage, specimens kept intact. With the deformation increasing, rust on the surface of the outer tubes peeled off gradually. When the load approached the ultimate bearing capacity, the slight crushing noise of the internal RSCC can be heard, and the lateral deformation became apparent. The failure modes of the specimens are shown in Fig. 2, where the eccentrically loaded RSCCFST short columns and long columns presented drum-like bending failure and overall flexural buckling failure modes, respectively.

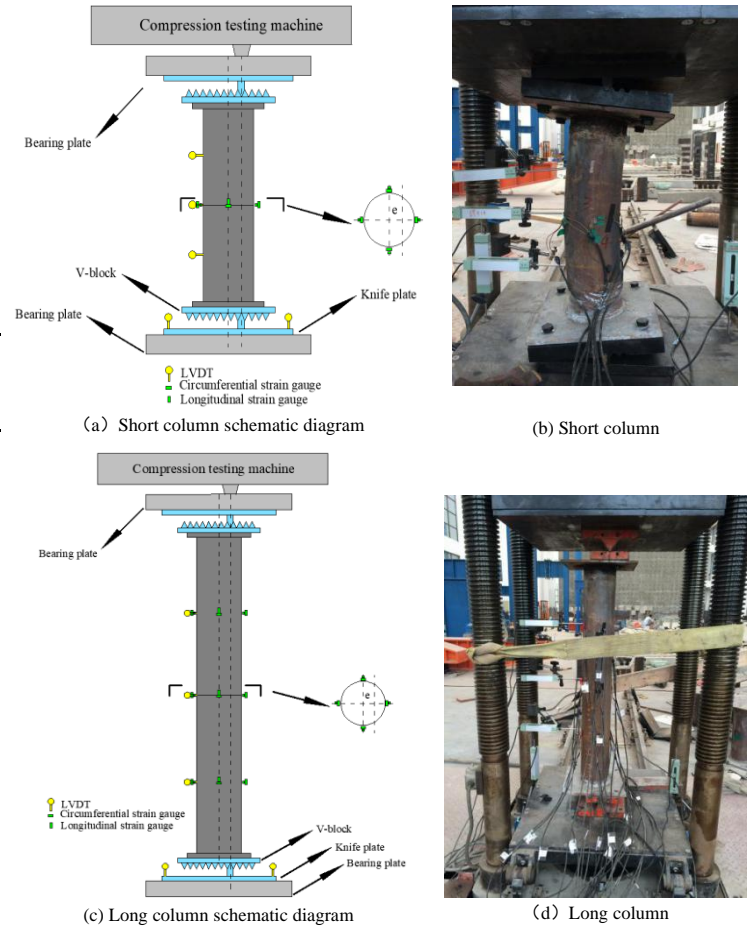


Fig. 1 Test set up and strain measuring points arrangement

3.2. Load-deflection relationship analysis

Load-deflection ($N - \Delta$) curves of the specimens are plotted in Fig. 3, where N stands for the axial load, Δ is the lateral deflection at mid-height (0.5L) of the columns.

The load-deflection curves can be roughly divided into three parts. The first part is the linear phase, where the load and deflection were approximately proportional. In the second part, the nonlinear phase, the relation between the load and deflection became nonlinear. With the load further increased, the specimens almost lost the capacity. The load-deflection curves entered the third part, the horizontal phase.

The yield and ultimate deflections and the displacement ductility coefficient of the RSCCFST specimens are summarized in Table 4.

3.2.1. Effect of replacement ratio of RCA

The comparison shown in Fig. 3(a) demonstrates the influences of the replacement ratio of RCA. It can be seen the use of RAC would reduce the bearing capacity of RSCCFST columns. This is mainly because the bonding effects between aggregates were weakened by the residual mortar attached on the surface of RCA. This defect decreased the elastic modulus of RSCC and the lateral deflection at the yield strength. However, the displacement ductility coefficient could be increased with a large amount of RCA.

3.2.2. Effect of length-diameter ratio

The load-deflection curves of the specimens with different length-diameter ratios are shown in Fig. 3(b). The conception of the length-diameter ratio of CFST is similar to the slender ratio. Member with the high length-diameter ratio has a low initial stiffness, large P- δ effects and a weak constraint on the inner concrete. Therefore, as shown in the Figure., raising the length-diameter ratio would increase the deflections and decrease the ductility of the RSCCFST columns.

Table 3

Component of RSCC and measured strength

Number	Material usage /kg							Cube compressive strength (MPa)	Axial compressive strength (MPa)	Poisson's ratio	Young's modulus (10 ⁴ MPa)
	Water	Sand	Cement	Fly ash	Water reducer	NCA	RCA				
S1	210	736	305	144	3.143	798	0	36.2	29.1	0.217	2.63
S2	210	736	305	144	3.143	399	399	34.6	27.8	0.174	2.57
S3	210	736	305	144	3.143	0	798	33.0	26.3	0.152	2.31
S4	176	936	395	151	1.638	0	798	53.4	42.8	0.168	2.73
S5	164	736	477	113	1.770	0	798	61.8	49.5	0.165	3.02

3.2.3. Effect of eccentricity

The eccentricity inducing the secondary moment would reduce the member yielding and ultimate load capacity. Moreover, the bending moment changes the stress state of the part inner concrete from triaxial axial compress to tension leading to a great drop of its strength. As shown in Fig 3(c), similar to CFST columns, the eccentricity has a negative effect on the capacity and stiffness of RSCCFST columns.

3.2.4. Effect of concrete strength grade

The compressive strength of the RSCCFST column is mainly provided by the inner concrete. According to Fig. 3(d), the use of the concrete with high strength improves the bearing capacity of the columns. However, the influences on the lateral deflection and the ductility are not obvious.

**Fig. 2** Failure mode of the RSCCFST columns

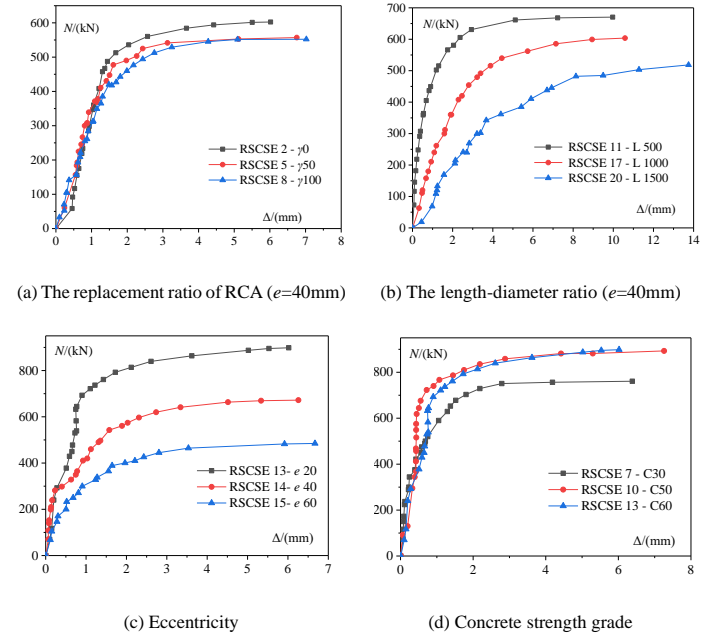
4. Numerical analysis of load-deflection relationship

4.1. Modelling of steel tube

The stress-strain relationship of steel is usually generalized as the curve shown in Fig.4, which can be described as [32, 33]

$$\sigma_s = \begin{cases} E_s \varepsilon_s & \varepsilon_s \leq \varepsilon_p \\ -A\varepsilon_s^2 + B\varepsilon_s + C & \varepsilon_p < \varepsilon_s \leq \varepsilon_{y1} \\ f_y & \varepsilon_{y1} < \varepsilon_s \leq \varepsilon_{y2} \\ f_y [1 + 0.6(\varepsilon_s - \varepsilon_{y2}) / (\varepsilon_u - \varepsilon_{y2})] & \varepsilon_{y2} < \varepsilon_s \leq \varepsilon_u \\ 1.6f_y & \varepsilon_s > \varepsilon_u \end{cases} \quad (1)$$

where, σ_s , ε_s are the stress and strain of steel, respectively, E_s is the Young's modulus of steel, f_y , f_u are the yield strength and ultimate strength of steel, f_p is the proportional limit of steel, $\varepsilon_p = 0.8f_y/E_s$ is the strain corresponding to the proportional limit of steel, $\varepsilon_{y1} = 1.5\varepsilon_p$ and $\varepsilon_{y2} = 10\varepsilon_p$ stand for the strain at the starting yield point and the ending yield point, respectively, $\varepsilon_u = 100\varepsilon_p$ is the strain corresponding to the ultimate strength, and $A = 0.2f_y(\varepsilon_{y1} - \varepsilon_p)^2$, $B = 2A\varepsilon_{y1}$, $C = 0.8f_y + A\varepsilon_p^2 - B\varepsilon_p$.

**Fig. 3** The effect of four parameters on load-deflection relationship

4.2. Modelling of RSCC

Based on the research of Xiao [34] and Han et al. [35], the stress-strain relationship of RSCC including the effects of the RCA is proposed in this study. The stress-strain curve of RSCC under compression is plotted in Fig.5, which can be represented with Eq (2) as

$$\frac{\sigma_c}{\sigma_{cp}} = \begin{cases} g\left(\frac{\varepsilon_c}{\varepsilon_{cp}}\right) + (3-2g)\left(\frac{\varepsilon_c}{\varepsilon_{cp}}\right)^2 + (g-2)\left(\frac{\varepsilon_c}{\varepsilon_{cp}}\right)^3 & \varepsilon_c < \varepsilon_{cp} \\ \frac{\left(\frac{\varepsilon_c}{\varepsilon_{cp}}\right)}{h\left(\frac{\varepsilon_c}{\varepsilon_{cp}} - 1\right)^2 + \left(\frac{\varepsilon_c}{\varepsilon_{cp}}\right)} & \varepsilon_c \geq \varepsilon_{cp} \end{cases} \quad (2)$$

where, σ_c , ε_c are the compressive stress and strain of RSCC, respectively, σ_{cp} , ε_{cp} are the maximum compressive stress and strain of RSCC respectively, g and h are the parameters obtained from the regression analysis of test data as

$$g = 2.125 - 1.171\gamma - 0.0035f \quad (3)$$

$$h = 3.51 \times 10^{-4} \cdot (2.36 \times 10^{-5})^{[0.25 + (\xi - 0.5)^2]} \cdot (f_c - 3.2\gamma)^2 \quad (4)$$

where, f_c is the axial compressive strength of RSCC, γ is the replacement ratio of RCA, $\xi = (A_s f_y) / (A_c f_{ck})$ is the confinement effect coefficient that considering the influence of the replacement ratio of RCA.

Table 4
The yield, ultimate deflection and the displacement ductility coefficient

Specimen ID	γ	Concrete number	e/mm	L/D	N/kN	Δ_y/mm	Δ_u/mm	μ_Δ
RSCSE-1	0	S1/C30	20	3.57	819	1.51	5.02	3.32
RSCSE-2	0	S1/C30	40	3.57	603	2.17	6.02	2.77
RSCSE-3	0	S1/C30	60	3.57	512	2.66	6.18	2.32
RSCSE-4	50	S2/C30	20	3.57	776	1.08	5.54	5.13
RSCSE-5	50	S2/C30	40	3.57	557	1.40	6.76	4.83
RSCSE-6	50	S2/C30	60	3.57	457	1.51	6.92	4.58
RSCSE-7	100	S3/C30	20	3.57	761	0.90	6.39	7.10
RSCSE-8	100	S3/C30	40	3.57	552	1.07	7.02	6.56
RSCSE-9	100	S3/C30	60	3.57	441	1.34	7.04	5.25
RSCSE-10	100	S4/C50	20	3.57	893	1.01	7.26	7.2
RSCSE-11	100	S4/C50	40	3.57	670	1.15	9.97	8.67
RSCSE-12	100	S4/C50	60	3.57	504	1.38	10.93	7.92
RSCSE-13	100	S5/C60	20	3.57	898	0.75	6.02	8.02
RSCSE-14	100	S5/C60	40	3.57	672	1.00	6.26	6.22
RSCSE-15	100	S5/C60	60	3.57	585	1.28	6.67	5.21
RSCSE-16	100	S4/C50	20	7.14	783	1.23	9.77	7.94
RSCSE-17	100	S4/C50	40	7.14	604	1.5	10.59	7.06
RSCSE-18	100	S4/C50	60	7.14	431	2.20	11.01	5.0
RSCSE-19	100	S4/C50	20	10.71	748	4.03	12.51	3.10
RSCSE-20	100	S4/C50	40	10.71	518	4.60	13.75	2.98
RSCSE-21	100	S4/C50	60	10.71	408	4.95	14.16	2.86

Note: Δ_y is the deflection at yielding strength, Δ_u is the deflection at ultimate strength, μ_Δ is the displacement ductility coefficient.

$A_s = 2\pi(r+t/2)t$ is the cross section area of steel tube in compression zone, $A_c = \pi r^2 \sin^2 \theta$ is the cross section area of internal RSCC in compression zone, $\beta_r = 1 + 0.055\gamma - 0.171\gamma^2$ is the replacement ratio of RCA influence coefficient obtained by regression analysis, f_{ck} is the axial compressive characteristic strength of RSCC.

The stress-strain relationship model for internal RSCC in tension zone is [32]

$$\frac{\sigma_1}{\sigma_{1p}} = \begin{cases} 1.2\left(\frac{\varepsilon_1}{\varepsilon_{1p}}\right) - 0.2\left(\frac{\varepsilon_1}{\varepsilon_{1p}}\right)^6 & \varepsilon_1 < \varepsilon_{1p} \\ \frac{\left(\frac{\varepsilon_1}{\varepsilon_{1p}}\right)}{0.31\sigma_{1p}^2\left(\frac{\varepsilon_1}{\varepsilon_{1p}} - 1\right)^{1.7} + \frac{\varepsilon_1}{\varepsilon_{1p}}} & \varepsilon_1 \geq \varepsilon_{1p} \end{cases} \quad (5)$$

where, σ_1 , ε_1 are the tensile stress and strain of RSCC, respectively. σ_{1p} , ε_{1p} are the maximum tensile stress and strain of RSCC, respectively.

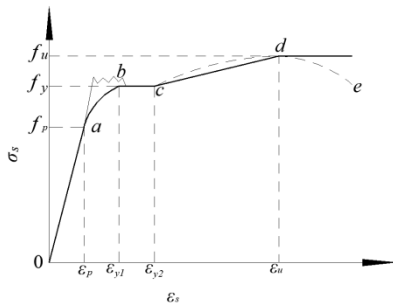


Fig. 4 Stress-strain curve of steel tube

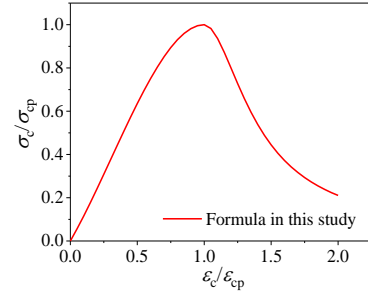


Fig. 5 Stress-strain relationship of RSCC

4.3. Numerical analysis

4.3.1. Assumptions

In the numerical analysis of the load-deflection relationship for the RSCCFST columns under eccentric compression, the following calculation assumptions were proposed: (1) The stress-strain relations of steel and RSCC given in Eqs.(1), (2) and (5) are adopted; (2) The RSCCFST column under eccentric loads was simply supported, and the deflection is a half sinusoidal curve; (3) The core RSCC and the outer steel tube work together, and the deformation was coordinated; (4) The shear deformation is ignored; (5) Plane sections remain plane.

4.3.2. Section fiber model

According to the assumption (2), the member deflection curve is plotted in Fig. 6. The section at the middle height is the most critical and will be chosen as the monitoring section. The lateral deflection of the column and the curvature ϕ of the section can be calculated as

$$y = \Delta \sin \frac{\pi}{L} x \quad (6)$$

$$\phi = \frac{\pi^2}{L^2} \Delta \quad (7)$$

To evaluate the column deflection, the section internal forces should be accurately obtained, where the finite strip method is adopted. As shown in Fig.7, the cross-section of the specimen is meshed into several strips. Each strip includes a steel tube and a core RSCC unit. By calculating the stress of each fiber, the moment of the section would be determined.

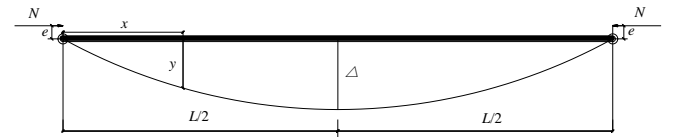


Fig. 6 The deflection curve of the specimen

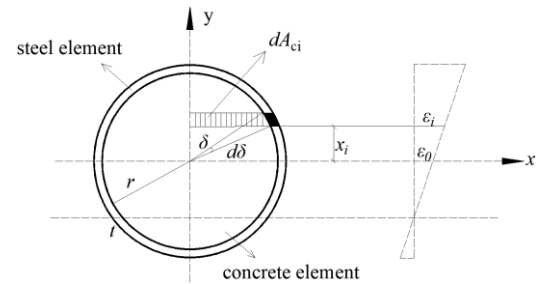


Fig. 7 Element division of sections and strain distribution

4.3.3. Equilibrium equation

According to the assumption (5), the strain ε_i at the center of each strip are

$$\varepsilon_i = \varepsilon_0 + x_i \phi \quad (8)$$

where, ε_0 is the strain at the centroid of cross-section, and x_i is the distance from the center of the strip to the cross-section centroid. The strip stress of the outer steel tube σ_{si} and the core RSCC σ_{ci} can be calculated according to the assumption (1). Based on the section stress, the axial force N_{in} and bending moment M_{in} of cross-section can be determined as

$$N_{in} = \sum_i (\sigma_{ci} dA_{ci} + \sigma_{si} dA_{si}) = N_i \quad (9)$$

$$M_{in} = \sum_i (\sigma_{ci} x_i dA_{ci} + \sigma_{si} x_i dA_{si}) = N_i (e + \Delta) \quad (10)$$

4.3.4. Calculation process

The numerical analysis approach is proposed to obtain the load-deflection curve of eccentrically loaded RSCCFST columns. The specific processes are: (1) to input the parameters and divide the section into strips; (2) to initialize the deflection, curvature and the strain at the centroid as $\Delta_0 = 0$, $\phi = 0$ and $\varepsilon_0 = 0.01$, respectively; (3) to determine the strip strains ε_i according to Eq. (8); (4) to determine stress σ_{ci} and σ_{si} at the centroid of different strips based on the material stress-strain relationship; (5) to calculate the axial force N_{in} and bending moment M_{in} using Eqs. (9) and (10). If the equilibrium condition $|M_{in}/N_{in} - e - \Delta| \leq 0.01$ was satisfied, output the load N_i and deflection Δ_i ; otherwise, adjust the strain ε_0 and repeat the steps (3-6); (7) to output the load-deflection ($N - \Delta$) curves of the RSCCFST columns. The flow chart of the numerical analysis approach was shown in Fig.8.

The $N - \Delta$ curves of the RSCCFST columns under eccentric loads obtained from the experiments and the proposed numerical analysis method are plotted and compared in Fig.9. Results indicated that the calculated value based on the fiber model method agreed well with the experimental results.

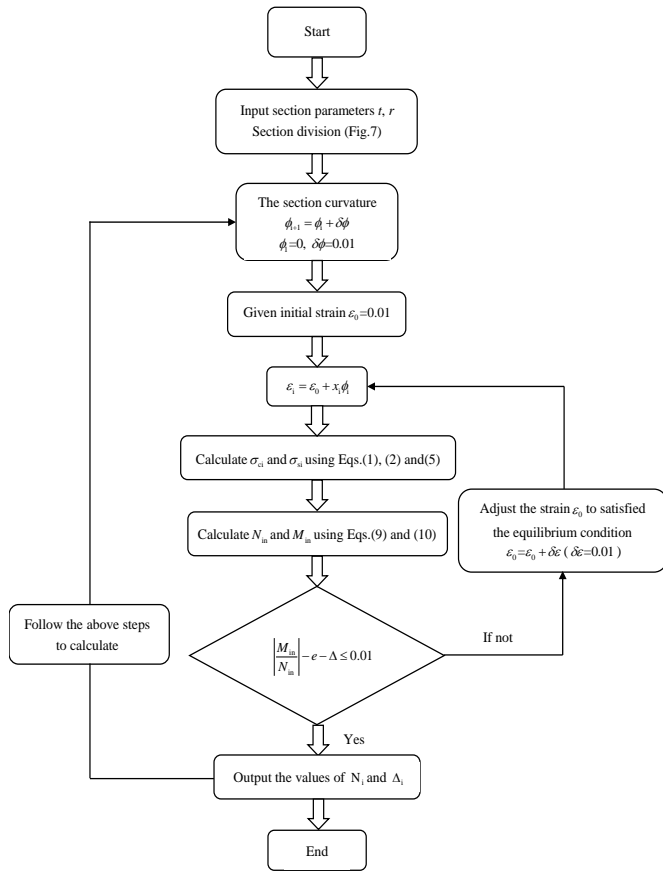
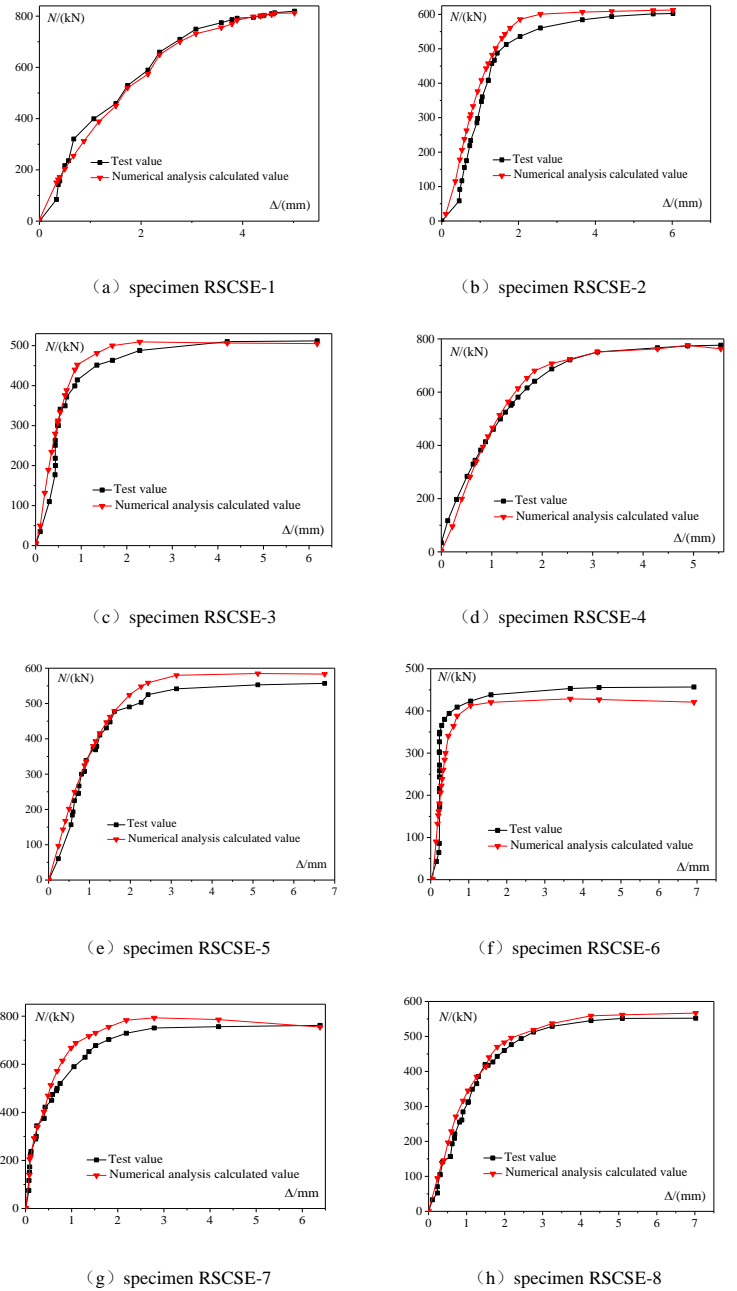
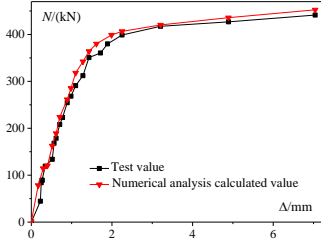


Fig. 8 The $N - \Delta$ program flow chart

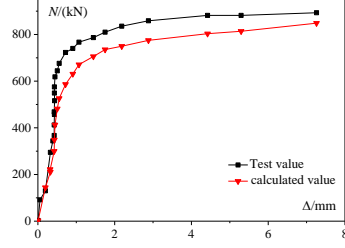
4.4. Parametric studies

Parametric study using the proposed numerical analysis method is conducted in this section to investigate the influences of different parameters on the member behavior, including the steel yield strength f_y , the steel ratio $\alpha = A_s/A_c$, the steel tube diameter-to-thickness ratio D/t , the concrete strength grade f_c , the length-diameter ratio L/D , the eccentricity e , and the replacement ratio of RCA γ . Specimens RSCSE-5, RSCSE-7 and RSCSE-8 are employed as the comparative reference. The load-deflection curves of the members with different parameters are shown in Fig.10. Compared to the experimental studies, the influences of the concrete strength, the length-diameter ratio, the eccentricity, and the replacement ratio of RCA predicted by the parametric analysis is the same, which further demonstrates the accuracy of the numerical analysis approach. Fig.10 (a) illustrates the effects of the steel yield stress, where the member with higher f_y has a higher bearing capacity because of the stronger confining force provide by the outer steel tube. With the same reason, the increase of the steel ratio or decrease the diameter-to-thickness ratio could enhance the behavior of the members as shown in Fig.10 (b) and Fig.10 (c).

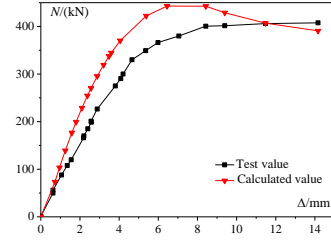




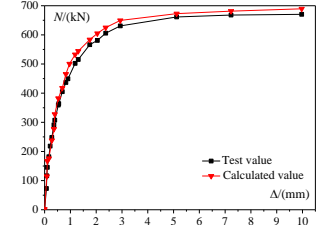
(i) specimen RSCSE-9



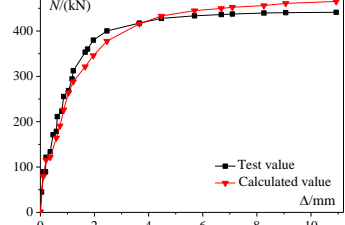
(j) specimen RSCSE-10



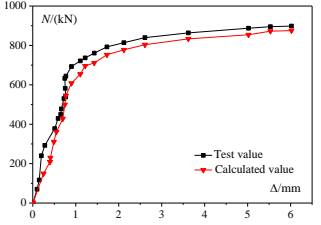
(u) specimen RSCSE-21



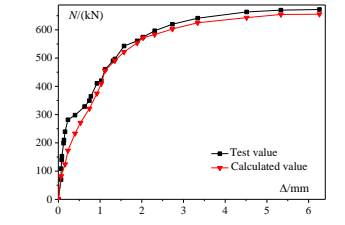
(k) specimen RSCSE-11



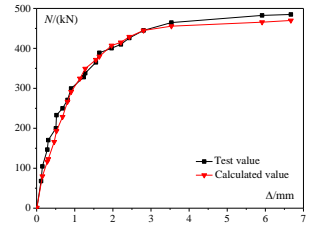
(l) specimen RSCSE-12



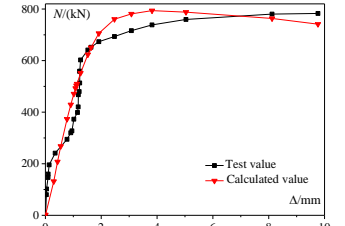
(m) specimen RSCSE-13



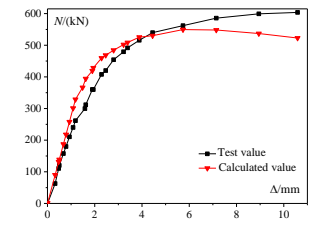
(n) specimen RSCSE-14



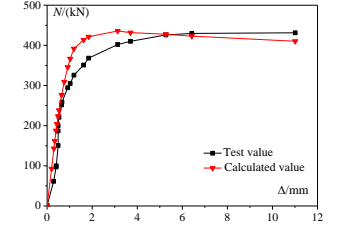
(o) specimen RSCSE-15



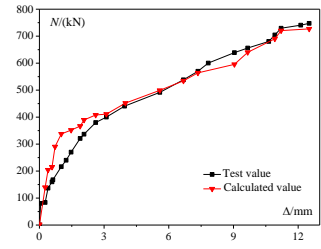
(p) specimen RSCSE-16



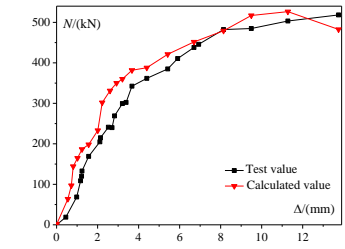
(q) specimen RSCSE-17



(r) specimen RSCSE-18



(s) specimen RSCSE-19



(t) specimen RSCSE-20

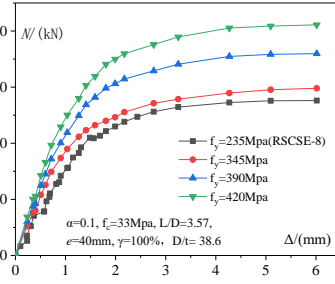
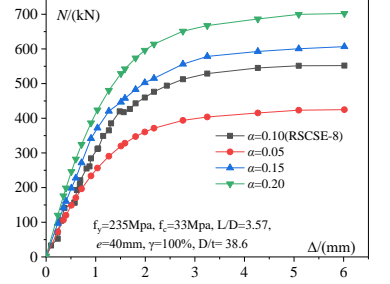
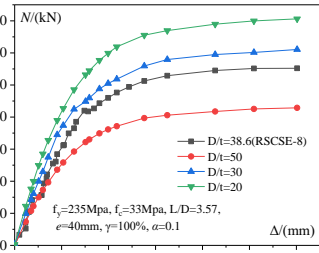
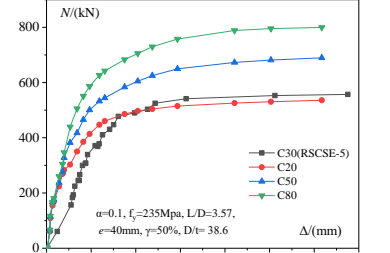
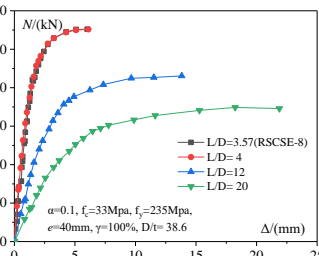
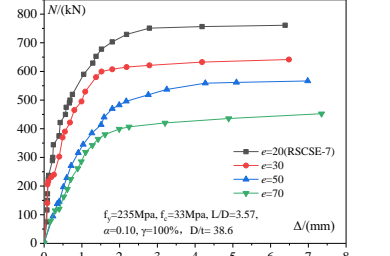
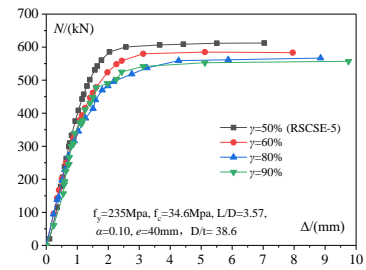
Fig. 9 The comparison of $N-\Delta$ curve obtained by numerical analysis and test data(a) Effect of f_y based on specimen RSCSE-8(b) Effect of α based on specimen RSCSE-8(c) Effect of D/t based on specimen RSCSE-8(d) Effect of f_c based on specimen RSCSE-5(e) Effect of L/D based on specimen RSCSE-8(f) Effect of e based on specimen RSCSE-7(g) Effect of γ based on specimen RSCSE-5

Fig. 10 Load-deflection curve of parametric studies

5. Conclusion

The behavior of eccentrically loaded RSCCFST columns was investigated in this study. The influences of the replacement ratio of RCA, length-diameter ratio, eccentricity, and concrete strength on bearing capacity and deflection were analyzed. The main conclusions can be drawn as

(1) The failure modes of short and long RSCCFST columns under eccentric compression are the drum-like bending failure and overall flexural buckling failure, respectively.

(2) The ultimate bearing capacity of the composite member can be enhanced by reducing the replacement ratio of RCA, length-diameter ratio, eccentricity or increasing the concrete strength.

(3) The rise of the length-diameter ratio or the eccentricity would increase the lateral deflections at the mid-span. Nevertheless, the use of RCA has different effects on the yield and ultimate deflections with the former and latter decreases and increases, respectively.

(4) The member with the low length-diameter ratio, small eccentricity or high RCA replacement ratio has good ductility.

(5) A numerical analysis method for calculating the load-deflection relationship of simply supported eccentrically compressed RSCCFST columns is developed based on the finite strip method. The results obtained from the proposed method are close to the test data.

Acknowledgements

This work was supported by the National Natural Science Foundation of China (No. 51578001, 51878002, 51608003, and 51008001), Natural Science Foundation granted by Department of Education, Anhui Province (No. KJ2015ZD10 and KJ2018A0046), Key Research and Development Plan of Anhui Province (No. 1704a0802131), and the Outstanding Young Talent Support Program of Anhui Province (No. gxyqZD2016072).

References

- [1] Omary S., Ghorbel E. and Wardeh G., "Relationships between recycled concrete aggregates characteristics and recycled aggregates concretes properties", *Construction and Building Materials*, 108, 163-174, 2016.
- [2] Xiao J.Z., *Recycled Concrete*, China Architecture & Building Press, Beijing, 2008.
- [3] Gabr A.R. and Cameron D.A., "Properties of recycled concrete aggregate for unbound pavement construction", *Journal of Materials in Civil Engineering*, 24(6), 754-764, 2013.
- [4] Thomas J., Thaikavil N.N. and Wilson P.M., et al, "Strength and durability of concrete containing recycled concrete aggregates. *Journal of building engineering*", 19, 349-365, 2018.
- [5] Verian K.P., Ashraf W. and Cao Y., "Properties of recycled concrete aggregate and their influence in new concrete production", *Resources Conservation and Recycling*, 133, 30-49, 2018.
- [6] Sagoe-Crentsil K.K., Brown T. and Taylor A.H., "Performance of concrete made with commercially produced coarse recycled concrete aggregate", *Cement and Concrete Research*, 31(5), 707-712, 2001.
- [7] Gupta S.M., "Strength characteristics of concrete made with demolition waste as coarse aggregate", *Proceedings of the International Conference on Recent Development in Structural Engineering*, 364-373, 2001.
- [8] Kou S.C. and Poon C.S., "Properties of concrete prepared with PVA-impregnated recycled concrete aggregates", *Cement and Concrete Composites*, 32(8), 649-654, 2010.
- [9] Tam V., Tam C.M. and Le K.N., "Removal of cement mortar remains from recycled aggregate using pre-soaking approaches", *Resources Conservation and Recycling*, 50(1), 82-101, 2007.
- [10] Xiao J., Sun Y. and Falkner H., "Seismic performance of frame structures with recycled aggregate concrete", *Engineering Structures*, 28(1), 1-8, 2006.
- [11] Manzi S., Mazzotti C. and Bignozzi M.C. et al, "Self-compacting concrete with recycled concrete aggregate: Study of the long-term properties", *Construction and Building Materials*, 157, 582-590, 2017.
- [12] González-Taboada I., González-Fonteboa B., Martínez-Abella F. and Seara-Paz S., "Evaluation of self-compacting recycled concrete robustness by statistical approach", *Construction & Building Materials*, 176, 720-736, 2018.
- [13] Silva Y.F., Robayo R.A., Matthey P.E. and Delvasto S., "Properties of self-compacting concrete on fresh and hardened with residue of masonry and recycled concrete", *Construction and Building Materials*, 124, 639-644, 2016.
- [14] Kenai S., Menadi B., Debbih A. and Kadri E.H., "Effect of recycled concrete aggregates and natural pozzolana on rheology of self-compacting concrete", *Key Engineering Materials*, 600, 256-263, 2014.
- [15] Zoran Jure Grdic., Gordana A., Toplicic-Curcic., Iva M., Despotovic., Nenad S. and Ristic., "Properties of self-compacting concrete prepared with coarse recycled concrete aggregate", *Construction and Building Materials*, 24(7), 1129-1133, 2010.
- [16] Georgios Giakoumelis. and Dennis Lam., "Axial capacity of circular concrete-filled tube columns", *Journal of Constructional Steel Research*, 60(7), 1049-1068, 2004.
- [17] Choi K.K. and Xiao Y., "Analytical studies of concrete-filled circular steel tubes under axial compression", *Journal of Structural Engineering-asce*, 136(5), 565-573, 2010.
- [18] Yang Y.F. and Han L.H., "Behaviour of concrete filled steel tubular (CFST) stub columns under eccentric partial compression", *Thin-Walled Structures*, 49(2), 379-395, 2011.
- [19] Dundu M., "Compressive strength of circular concrete filled steel tube columns", *Thin-Walled Structures*, 56, 62-70, 2012.
- [20] Chitawadagi M.V., Narasimhan M.C. and Kulkarni S.M., "Axial strength of circular concrete-filled steel tube columns-doe approach", *Journal of Constructional Steel Research*, 66(10), 1248-1260, 2010.
- [21] Li G., Chen B. and Yang Z. et al, "Experimental and numerical behaviour of eccentrically loaded high strength concrete filled high strength square steel tube stub columns", *Thin-walled Structures*, 127: 483-499, 2018.
- [22] Yang Y.F. and Han L.H., "Concrete filled steel tube (CFST) columns subjected to concentrically partial compression", *Thin-Walled Structures*, 50(1), 147-156, 2012.
- [23] Susantha K.A.S., Aoki T. and Hattori M., "Seismic performance improvement of circular steel columns using precompressed concrete-filled steel tube", *Journal of Constructional Steel Research*, 64(1): 30-36, 2008.
- [24] Tao Z., Han L.H., Uy B. and Chen X., "Post-fire bond between the steel tube and concrete in concrete-filled steel tubular columns", *Journal of Constructional Steel Research*, 67(3), 484-496, 2011.
- [25] Mohanraj E.K., Kandasamy S. and Malathy R., "Behaviour of steel tubular stub and slender columns filled with concrete using recycled aggregates", *Journal of the South African Institution of Civil Engineering*, 53(2), 31-38, 2011.
- [26] Yang Y.F. and Han L.H., "Experimental behaviour of recycled aggregate concrete filled steel tubular columns", *Journal of Constructional Steel Research*, 62(12), 1310-1324, 2006.
- [27] Tang Y.C., Li L.J., Feng W.X., Liu F. and Zhu M., "Study of seismic behavior of recycled aggregate concrete-filled steel tubular columns", *Journal of Constructional Steel Research*, 148, 1-15, 2018.
- [28] Muciaccia G., Giussani F., Rosati G. and Mola F., "Response of self-compacting concrete filled tubes under eccentric compression", *Journal of Constructional Steel Research*, 67(5), 904-916, 2011.
- [29] Mahgub M., Ashour A., Lam D. and Dai X., "Tests of self-compacting concrete filled elliptical steel tube columns", *Thin-Walled Structures*, 110(C), 27-34, 2017.
- [30] JGJ52-2006., *Standard for technical requirements and test method of sand and crush stone (or gravel) for ordinary concrete*, China Architecture & Building Press, Beijing, China, 2006.
- [31] JGJ/T283-2012., *Technical specification for application of self-compacting concrete*, China Architecture & Building Press, Beijing, China, 2012.
- [32] GB50936-2014., *Technical code for concrete filled steel tubular structures*, China Architecture & Building Press, Beijing, China, 2014.
- [33] Zhong S. T., *The concrete-filled steel tubular structures (third edition)*, Tsinghua University Press, Beijing, 2003.
- [34] Xiao J.Z., "Experimental investigation on complete stress-strain curve of recycled concrete under uniaxial loading", *Journal of Tongji University*, 35(11), 1445-1449, 2007.
- [35] Han L. H., *Concrete filled steel tubular structure-theory and practice*, Science Press, Beijing, 2007.

A REVIEW OF CLASS 4 SLENDER SECTION PROPERTIES CALCULATION FOR THIN-WALLED STEEL SECTIONS ACCORDING TO EC3

Chi-King Lee ^{1,*} and Sing-Ping Chiew ²

¹ School of Engineering and Information Technology, University of New South Wales Canberra, Australia

² Singapore Institute of Technology, Dover Campus, Singapore

* (Corresponding author: E-mail: c.lee@adfa.edu.au)

ABSTRACT

A review is given to the procedure suggested by the Eurocode 3 for the section properties calculations of thin-walled Class 4 slender steel sections consists of plate elements. Focus will be given to the effective width approach described in the Eurocode 3. The essential steps for the effective width calculation for single plate element subjected to different direct stress distribution are first given. It is then followed by a study that compares the two different procedures, namely the full iteration procedure and the simplified procedure adopted by Eurocode 3 for Class 4 slender section properties calculation. Calculation examples are then given to demonstrate the calculation steps for both the full and the simplified approaches. Results of the calculation examples indicate that while the simplified procedure eliminates the tedious iteration steps and is much more convenient for manual calculation, the full iteration method in general will lead to less conservative effective area and section modulus and thus could result in more economical design in practice.

ARTICLE HISTORY

Received: 02 October 2018
Revised: 26 February 2019
Accepted: 03 June 2019

KEYWORDS

Class 4 Slender Sections;
Thin-walled steel sections;
Effective width method;
Effective area and modulus

Copyright © 2019 by The Hong Kong Institute of Steel Construction. All rights reserved.

1. Introduction

In the design of steel structures, classification of steel section is fundamentally important as it determines many basic properties of the section as well as how the section resistances are calculated in many design guidelines [1-3]. In the Eurocode 3 (EC3) [1], the following four classes of section are defined.

Class 1 Plastic: Sections belong to this class can develop plastic hinge with large rotation capacity. No reduction of plastic moment capacity is needed in plastic analysis and design [1]. The sectional compressive and bending resistances of a Class 1 section are defined by the gross area A_{gross} and the plastic modulus W_{pl} , respectively.

Class 2 Compact: Sections belong to this class can develop plastic hinge but with limited rotation capacity. While EC3 [1] does not allow this section class to be used in plastic analysis for design, the sectional compressive and bending resistances of a Class 2 section are again defined by the gross area A_{gross} and the plastic modulus W_{pl} , respectively.

Class 3 Semi-compact: Sections belong to this class can only develop resistance up to the elastic limit so that only the extreme fiber stresses can reach the material yield strength. The sectional compressive and bending resistances of a Class 3 section are defined by the gross area A_{gross} and the elastic modulus W_{el} , respectively.

Class 4 Slender: A Class 4 section will develop local buckling *before* the extreme fiber stresses attaining yield and therefore parts of the compressive zone of the section will be ineffective. As a result, the sectional compressive and bending resistances of a Class 3 section are defined by the effective area A_{eff} and the effective modulus W_{eff} , respectively.

The procedure to classify a given section is mainly governed by Table 5.2 of EC3 Part 1-1 [1]. It should be noted that the limiting width to thickness ratios (the term c/t in Table 5.2 of [1]) for different classes are depended on the stress distributions of the section (hence the loadings applied to the section) as well as the strength of steel used via the parameter $\varepsilon=(235/f_y)^{0.5}$. This implies that once the section is classified as a non-Class 4 section, since for a given value of f_y , A_{gross} , W_{el} and W_{pl} are intrinsic geometrical properties of the cross-section, the section resistances will be independent of the applied loads. However, for a Class 4 section since the effective width of the compression part shall depend on its stress distribution [2, 3], this implies that both A_{eff} and W_{eff} (thus the section resistances) are depended on the applied loads. It should be mentioned that due to such loading dependent nature of Class 4 sections, the section properties calculation steps for Class 4 sections are more complicated than those for Class 1 to 3 sections. The main objective of this study is to summarize the principles adopted by the EC3 for Class 4 section properties calculation. In particular, both the *full iteration procedure* and the *simplified procedure* recommended by the EC3 Part 1-1[1] and Part 1-5[2] for Class 4 section properties calculations are reviewed and discussed. In addition, a few practical calculation examples will

also be provided to demonstrate the essential calculations steps and the differences between the simplified and the full iteration procedures. It will be shown that while the simplified procedure is much more suitable for manual calculation and does not require the ratio between the axial force and the bending moments applied for calculation, the full iteration procedure will produce less conservative values of A_{eff} and W_{eff} and therefore should be encouraged to use in practice.

2. The EC3's "Effective width" method for section properties calculation

2.1. An overview

It is well known that a side supported thin steel plate with aspect ratio $\alpha=a/b \geq 1$ (Fig. 1) subject to direct loading along in-plane direction tends to buckle at a stress level σ_{cr} less than the yield stress f_y [4, 5]. However, after σ_{cr} is reached, resistance of the plate is not completely exhausted and it shall have sufficient post-buckling strength due to stress redistribution. The ultimate resistance of the plate will be reached after yielding occurred at the two supported sides and this will result in final a non-uniform stress distribution $\sigma_{act} < f_y$ (Fig. 2). This phenomenon is commonly known as "plate like buckling" [4, 5] and is most obvious for geometrical perfect elastic plate but less remarkable for a realistic imperfect inelastic plate. It is also well known that as the value of α reduces, the post-buckling resistance of the plate will diminish gradually and the 2D plate like buckling behaviour of the plate will change back to the 1D buckling behaviour like a column. Obviously, the non-uniform distribution of σ_{act} is not ideal for design of thin plate subjected to direct stress. Hence, in EC3 Part 1-5 [2], two different design methods, namely the effective width method (Fig. 2b) and the effective stress (Fig. 2c) method are suggested. In short, both methods aim to employ uniform stress block for design. While the effective width method reduces the gross width to an appropriate effective width $b_{eff} = \rho b < b$ that subjected to the constant yield strength f_y for design (Fig. 2b), the effective stress method maintains a uniform stress $\sigma_{equ} = \chi f_y < f_y$ along the whole width. The reduction factors ρ and χ are calculated based on the principle of equivalent in-plane force such that

$$\text{For the effective width method: } \int_0^b \sigma_{act} dx = b_{eff} f_y = \rho b f_y \quad (1)$$

$$\text{For the effective stress method: } \int_0^b \sigma_{act} dx = b \cdot \sigma_{equ} = b \chi f_y = \chi b f_y \quad (2)$$

It is obvious that for a cross section consist of a single plate, the two methods are equivalent to each another such that (Fig. 2b and Fig. 2c) $\chi b f_y = \rho b f_y$ and $\chi = \rho$. However, for cross sections that consist of more than one plate element (e.g. an I section), the two methods are not equivalent to each another [2, 4] and the effective stress method are generally more conservative.

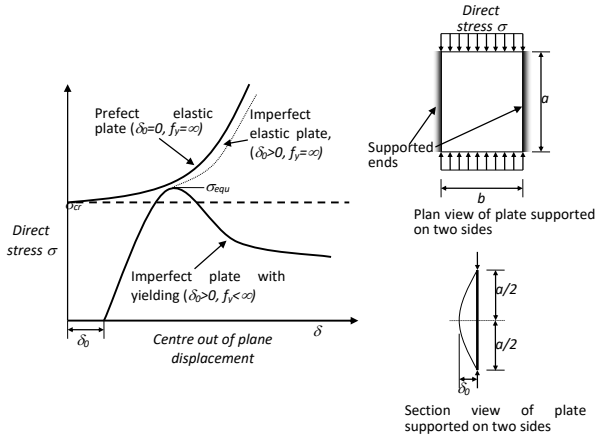


Fig. 1 Failure of plate with $\alpha=a/b > 1$ subject to in-plane direct loading

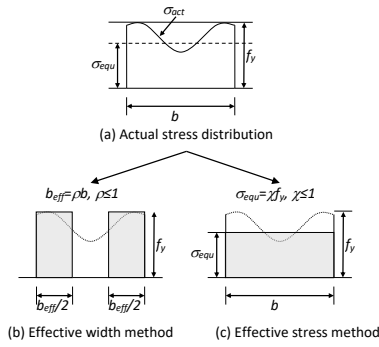


Fig. 2 Actual stress distribution at failure, effective width and stress methods

Table 1

Calculation of k_σ

Internal compression part (Fig. 3)	
Range of ψ	k_σ
$-3 \leq \psi < -1$ (Fig. 3c)	$5.98(1-\psi)^2$
$-1 \leq \psi < 0$ (Fig. 3c)	$7.81-6.29\psi+9.78\psi^2$
$0 \leq \psi \leq 1$ (Figs. 3a and 3b)	$8.2/(1.05+\psi)$
Outstand compression part with high stress at supported ends (Figs. 4a and 4b)	
Range of ψ	k_σ
$-1 \leq \psi < 0$ (Fig. 4b)	$1.7-5\psi+17.1\psi^2$
$1 \leq \psi \leq 0$ (Fig. 4a)	$0.578/(\psi+0.34)$
Outstand compression part with lower stress at supported ends (Figs. 4c and 4d)	
Range of ψ	k_σ
$1 \leq \psi < -3$ (Figs. 4c and 4d)	$0.57-0.21\psi+0.07\psi^2$

It should be noted that EC Part 1-5 can be considered as largely “biased” towards the effective width method as Sections 4 to 7 (16 pages in length) of EC3 Part 1-5 were written based on this method while only Section 10 (2 pages in length) was devoted to describe the design approach if the effective stress method is employed. Hence, in the design of thin-walled structural components like plate girder and box section using EC3, the calculation of effective width of a Class 4 section is one of the most important steps during the section properties calculation [6-8].

2.2. Effective width calculation

In EC3 Part 1-5, for a given plate element (either supported on a single or on both sides) the effective width reduction factor ρ is solely based on two parameters: (i) \bar{b}/t , the appropriate width (\bar{b}) to the plate thickness (t) ratio of the element and (ii) the stress ratio at the two ends $\psi = \sigma_2/\sigma_1$ where $\sigma_2 < \sigma_1$. In general, \bar{b} is the appropriate clear width between the supports of the plate element. \bar{b} is always slightly less than b , the overall width of the plate element, and should be calculated according to the section classification table (Table 5.2) of EC3 [1] and Section 4.4 of [2]. Figs. 3 and 4 respectively show the possible stress distributions for an internal compression element (i.e. the plate is

supported at both ends) and an outstanding compression element (i.e. only one end of the plate is supported). Note that in Fig. 3 and Fig. 4, it is assumed that the stress distribution is linear and compressive stress is taken as positive. Furthermore, for $\psi < 0$, the whole plate element is divided into two parts that are under tension and compression respectively with widths equal to b_t and b_c , so that $\bar{b} = b_t + b_c$ and $b_c = \bar{b}/(1-\psi)$ (Fig. 3c, Fig. 4b and Fig. 4d). In general, the effective parts of the plate element consist of those parts that are either under tensile stress (i.e. the stress is negative) or those compressive parts that locate near the supported ends where local buckling is prevented to occur. Once the values of \bar{b}/t and $\psi = \sigma_2/\sigma_1$ are known, the effective width of the plate element could be computed by using the following steps.

- (1) Use the equations listed in Table 1 to calculate the buckling factor k_σ according to the stress ratio ψ for different stress distributions shown in Fig. 3 and Fig. 4.
- (2) Compute the plate slenderness ratio $\bar{\lambda}_p$ such that

$$\bar{\lambda}_p = \frac{\bar{b}/t}{28.4\epsilon\sqrt{k_\sigma}}, \quad \epsilon = \sqrt{\frac{235}{f_y}} \quad (3)$$

- (3) Calculate the reduction factor ρ for the compressive part of the element such that (EC3 Part 1-5, Equations. 4.2 and 4.3)
For an internal plate element (Fig. 3):

$$\rho = \frac{\bar{\lambda}_p - 0.055(3+\psi)}{\bar{\lambda}_p^2} \leq 1.0 \quad \text{and} \quad \bar{\lambda}_p > 0.5 + \sqrt{0.085 - 0.055\psi} \quad (4a)$$

For an outstanding plate element (Fig. 4):

$$\rho = \frac{\bar{\lambda}_p - 0.188}{\bar{\lambda}_p^2} \leq 1.0 \quad \text{and} \quad \bar{\lambda}_p > 0.784 \quad (4a)$$

- (4) Calculate b_{eff} , the effective width for the compressive part of the plate element, (Fig. 3 and Fig. 4)

$$\text{For } \psi \geq 0: \quad b_{eff} = \rho \bar{b} \quad (5a)$$

$$\text{For } \psi < 0: \quad b_{eff} = \frac{\rho \bar{b}}{(1-\psi)} = \rho b_c \quad (5b)$$

Note that for the case of an internal compression element with $\psi \geq 0$ (i.e. the whole plate element is under compression), the effective width of the element b_{eff} is further divided into two parts (Figs. 3(a) and 3(b)) with width b_{e1} and b_{e2} such that $b_{e1} + b_{e2} = b_{eff}$. The relative sizes of b_{e1} and b_{e2} are defined in Fig. 3.

- (5) Finally, the total effective width of the whole plate elements is computed as b_{eff} (Fig. 3a, Fig. 4a and Fig. 4c) for $\psi \geq 0$ when the whole plate element is under compression or $b_{eff} + b_t$ for $\psi < 0$ when part of the plate element is under tension (Fig. 3c, Fig. 4b, and Fig. 4d).

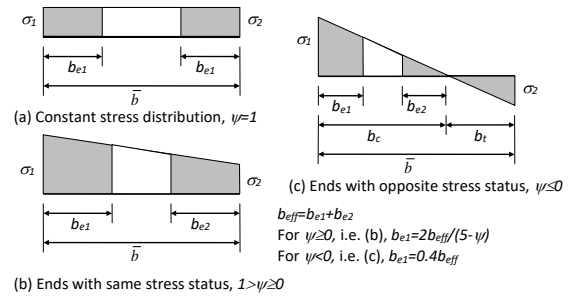


Fig. 3 Stress distribution and effective width for internal compression elements (i.e. both end supported), effective part of the plate is shaded

Note: Compressive stress is positive with $\sigma_2 < \sigma_1$

Fig. 5 shows the plots of the ratio $(b_{eff} + b_t)/\bar{b}$ against the stress ratio ψ for a plate element with $f_y = 355 \text{ MPa}$ and $\epsilon = 0.8136$ for different values of \bar{b}/t . From Fig. 5, it is obvious that for any value of \bar{b}/t , the ratio $(b_{eff} + b_t)/\bar{b}$ always attends a minimum when $\psi = 1$ when the plate element is subjected to uniform compression. It should be also noted from these figures that for $\psi = -1$ or when $b_c = b_t$ for the plate elements, there always exist a limiting value of \bar{b}/t below which the plate element is fully effective (i.e. becomes a Class 3 section). For a plate with $f_y = 355 \text{ MPa}$, these limiting values are corresponding to $\bar{b}/t = 100$ for an internal element (Fig. 5a) and an outstanding element with compressive stress at supported end (Fig. 5b) and $\bar{b}/t = 15.8$ for an outstanding element with tensile stress at supported end (Fig. 5c).

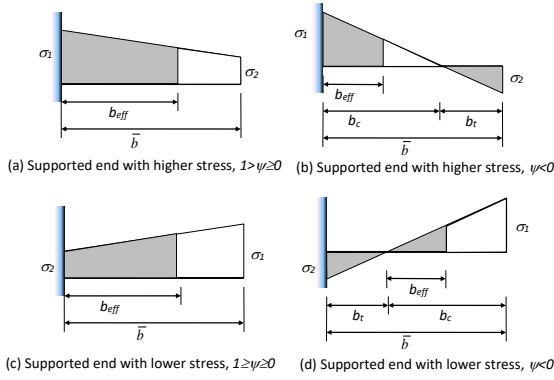
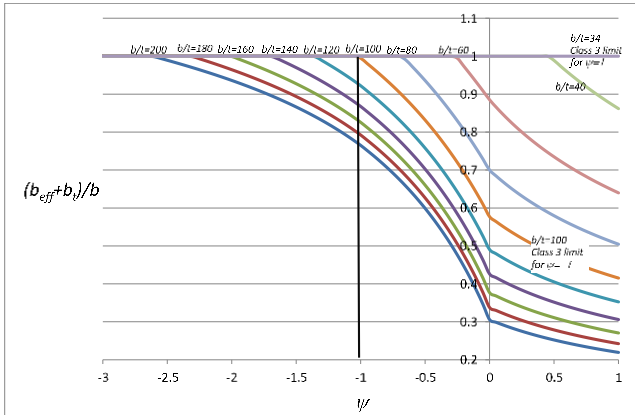
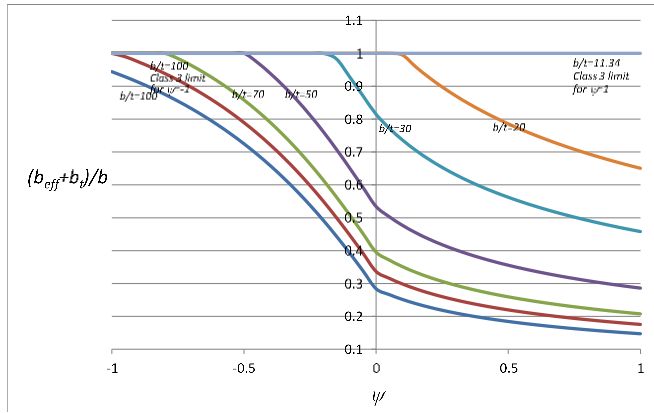


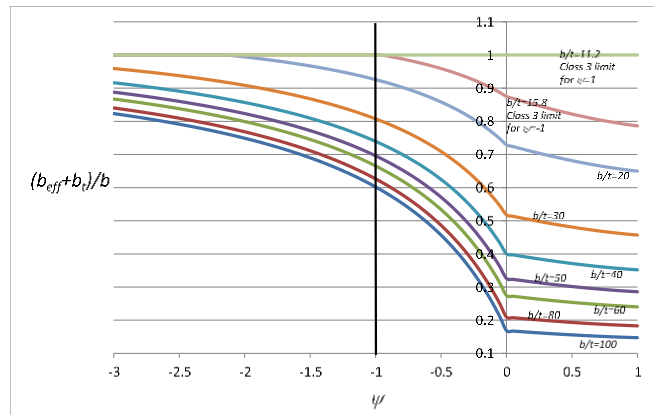
Fig. 4 Stress distribution and effective width for outstand compression elements (i.e. only end supported), effective part of the plate is shaded



(a) Internal compression plate element (Fig. 3)



(b) Outstand plate element, support end with higher stress (Figs. 4a and 4b)



(c) Outstand plate element, support end with lower stress (Figs. 4c and 4d)

Fig. 5 Curves of $(b_{eff} + b_y)/\bar{b}$ against ψ for different values of \bar{b}/t for a plate element with $f_y = 355 \text{ MPa}$

2.3. Alternative value of ρ for stress level below the yield strength

From Clauses 4.4(3) and E.1 of EC3 Part 1-5, if the maximum design compressive stress caused by *all* simultaneous actions is *below* the yield strength, the reduction factor ρ for the compressive part of the element could be increased by first adjusting the factor $\bar{\lambda}_p$ defined in Equation 3 as

$$\bar{\lambda}_{p,red} = \bar{\lambda}_p \sqrt{\frac{\sigma_{com,Ed}}{f_y/\gamma_{M0}}} \quad (6)$$

In Equation 6, $\sigma_{com,red} < f_y$ is the maximum design compressive stress in the element caused by all simultaneous actions, calculated by using the effective area of the section. After $\bar{\lambda}_{p,red}$ is computed, the value of ρ is then given by (c.f. Equation 4a)

$$\rho = \frac{1 - 0.55(3 + \psi)/\bar{\lambda}_{p,red}}{\bar{\lambda}_{p,red}} + 0.18 \frac{(\bar{\lambda}_p - \bar{\lambda}_{p,red})}{(\bar{\lambda}_p - 0.6)} \text{ but } \rho \leq 1 \quad (7)$$

Equations 6 and 7 will increase the value of ρ but they require engineers to use the actual values of N_{Ed} and M_{Ed} for design. Furthermore, EC3 Part 1-1, Clause 5.2.2 (9) also allows one to increase the Class 3 width to thickness ratio limit if $\sigma_{com,red}$ is used such that

$$\varepsilon = \sqrt{\frac{f_y}{\sigma_{com,red}}} \sqrt{\frac{235}{f_y}} = \sqrt{\frac{235}{\sigma_{com,red}}} \quad (8)$$

However, Equation 8 is not allowed to apply for buckling resistance calculation. Hence, in practice, while it could help to increase the section resistance (EC3 Part 1-1, 6.2.9.3), it will not be able to increase the buckling strength of the member.

3. Principle of section properties calculation by EC3

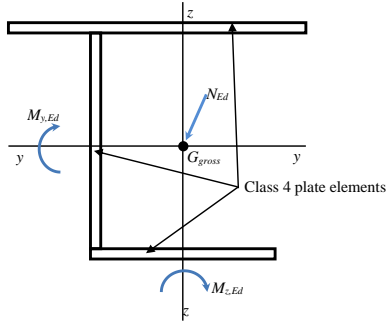
As shown in Fig. 6a, a thin-walled steel section consists of a number of plate elements is subjected to the simultaneous actions of an axial loading (N_{Ed}) acting at the centroid of the gross section, G_{gross} and the biaxial bending moments $M_{y,Ed}$ and $M_{z,Ed}$ respectively above the major axis y-y and the minor axis z-z of the gross section. For convenient, G_{gross} is taken as the origin the y-z coordinate system. It is assumed that at least one of the plate elements with \bar{b}/t ratio exceeds the Class 3 limit so that some areas of the sections are ineffective and have to be removed during the cross-sectional properties calculation. According to EC3 [2, 4], in order to calculate the effective area of the whole section, it is first assumed that all the plate elements of the section could be separated into individual elements at their intersection points (Fig. 6b). After this, by assuming that the intersection points could provide sufficient end supports to the plate elements, effective areas of all plate elements will be obtained by considering the direct stress distribution within the elements. Finally, the section properties of the whole thin-walled section are obtained by recombining all plate elements together (Fig. 6c). As all ineffective areas are removed, the effective area of the section A_{eff} is less than the section gross area A_{gross} . In addition, in general, there will be a shift in the position of the centroid G_{eff} of the remaining effective area. Such shift in position can be generally expressed as $(\Delta y, \Delta z)$ with respect to the y-z coordinate system. From elementary beam bending theory, the direct stress $\sigma(y, z)$ at a given point (y, z) of the section can be expressed as (again compressive stress is taken as positive)

$$\sigma(y, z) = \frac{N_{Ed}}{A_{eff}} + \frac{(M_{y,Ed} + N_{Ed}\Delta z)}{I_{y,eff}(\Delta y, \Delta z)} y + \frac{(M_{z,Ed} + N_{Ed}\Delta y)}{I_{z,eff}(\Delta y, \Delta z)} z \quad (9)$$

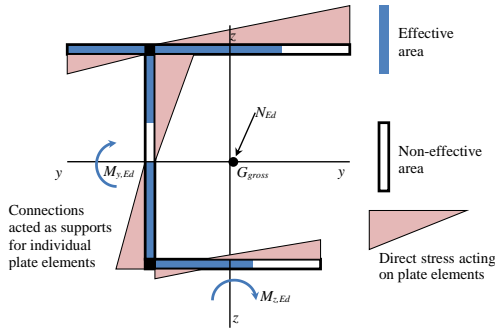
In Equation 9, $I_{y,eff}$ and $I_{z,eff}$ are the effective second moment of area of the section about the y-y and z-z axes, respectively. $N_{Ed}\Delta z$ and $N_{Ed}\Delta y$ are additional moments generated due to the change of the location of the centroid of the effective area. Since all the plate elements of the section are straight elements, the direct stress within all plate elements will vary linearly. The method and equations described in Section 2 could be employed for the calculation of the effective areas of individual plate elements.

From Equation 6, it can be seen that if the section *symmetrical* above *both* the y-y axis and the z-z axis and is subjected to axial force only, one will have $\Delta z = \Delta y = 0$ since any reduction in effective area will be symmetrical with respect to both the y-y and z-z axes. As a result, there shall be no shift of the location of G_{gross} and the section properties of the effective areas could be calculated directly without any iteration. However, whenever the section is unsymmetrical *or* when bending moment is applied, due to the presence of the terms $N_{Ed}\Delta z$ and $N_{Ed}\Delta y$ and the fact that $I_{y,eff}$ and $I_{z,eff}$ are both functions of $(\Delta y, \Delta z)$, the stress ratio ψ at the two ends of the plate will be depended on the location of G_{eff} . Eventually, as the stress ratio ψ itself also affects the effective area and eventually the

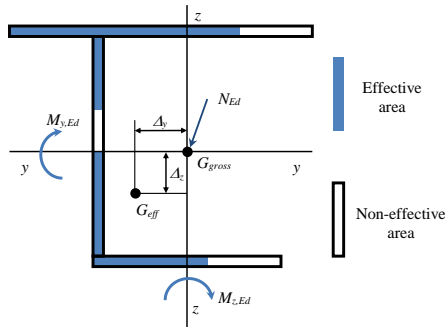
location of G_{eff} , the exact position of G_{eff} will not be expressed explicitly in simple analytical form and it could only be calculated iteratively [2, 4].



(a) A thin-walled section consists of class 4 plate elements under axial force N_{Ed} and biaxial bending moments $M_{y,Ed}$ and $M_{z,Ed}$



(b) Separation of the thin-walled section into individual plate elements



(c) Final effective section after combining individual plates

Fig. 6 Calculation of section properties of a Class 4 thin-walled section

3.1. The full iteration and the simplified procedures

As explained in the previous section and stated in Section 4.3 of EC3 Part 1-5 [2], an iterative procedure is generally required to compute the section properties of a Class 4 slender section. In this paper, such approach is referred as the full iteration procedure and the calculation steps are summarized in Box 1.

Box 1

Full iteration calculation procedure for class 4 section properties calculation

- (1) By assuming the whole section is effective, calculate the gross section properties (G_{gross} , A_{gross} and I_{gross}).
- (2) Set $G_{eff} = G_{gross}$, $A_{eff} = A_{gross}$, $I_{eff} = I_{gross}$ and $\Delta y = \Delta z = 0$
- (3) Base on the current section properties, calculate the direct stress at end points of all the plate elements using Equation 9 and then compute the stress ratio ψ for all plate elements.
- (4) Base on the stress ratio ψ , determine the effective area of all plate elements by using Table 1, Equations. 3 to 5 and Fig. 3 and Fig. 4.
- (5) Compute the new centroid of the effective area G_{eff}' and the corresponding effective area A_{eff}' and effective second moment of area I_{eff}' .
- (6) Determine the shift of the centroid $G_{eff} - G_{eff}' = (\Delta y, \Delta z)$ and the relative change of effective area and effective second moment of area such that

$$S_G(\%) = \frac{\sqrt{\Delta y^2 + \Delta z^2}}{\min(b, h)} \times 100\% \quad (10a)$$

$$C_A(\%) = \frac{|A_{eff}' - A_{eff}|}{A_{eff}} \times 100\% \text{ and } C_I(\%) = \frac{|I_{eff}' - I_{eff}|}{I_{eff}} \times 100\% \quad (10b)$$

where b and h in Equation 10a is the overall width and depth of the section.

- (7) Update the section properties so that $G_{eff} \leftarrow G_{eff}'$, $A_{eff} \leftarrow A_{eff}'$ and $I_{eff} \leftarrow I_{eff}'$.
- (8) Check for convergence of the section properties: The section properties are assumed to be converged if the following criteria are satisfied

$$S_G \leq S_{tol} \quad C_A \leq C_{Atol} \quad C_I \leq C_{Itol} \quad (11)$$

where S_{tol} , C_{Atol} and C_{Itol} are tolerances for the convergences of G_{eff} , A_{eff} and I_{eff} , respectively.

- (9) If the section properties are converged, output the value of G_{eff} , A_{eff} and I_{eff} and stop. Otherwise, go to step (3)

Note that in in Section 4.3 of EC3 Part 1-5 [2], no recommendation is made on the convergence criteria of the full iteration procedure. Furthermore, Beg et al. [4] suggested that the iteration procedure should be stopped when the location of G_{eff} converged which is equivalent to adopting the first criterion of $S_G \leq S_{tol}$ in Equation 11. Since the axial and bending resistances of the section are largely depended on the values of A_{eff} and I_{eff} , their values are also critical when conducting the section resistance check. Hence, it is suggested that a maximum value of 1% should be employed for the tolerance factors S_{tol} , C_{Atol} and C_{Itol} during practical calculations.

From Box 1, it can be seen that if full iteration procedure is used, repeat evaluations of Equations 3, 5 and 9 as well as calculations of the position of G_{eff} and the values of A_{eff} and I_{eff} are needed. Furthermore, it is shown in Appendix A that for an unsymmetrical section subject to axial force and biaxial bending, in order to elevate the new position of G_{eff} , the ratios between the axial force and bending moments applied (i.e. $M_{y,Ed}/N_{Ed}$ and $M_{z,Ed}/N_{Ed}$) are required. For complex sections consist of many plate elements such calculations are tedious and are not convenient for manual calculation. Hence, in EC3 Part 1-5, two simplified procedures as summarized Box 2 are suggested to allow designer to calculate the effective area and section modulus manually.

Box 2

Simplified procedure for class 4 section properties calculation

Simplification 1

For I and box sections under bending moment only, only one iteration step of the full iteration procedure is required. That is, the first new position of centroid G_{eff}' and A_{eff}' and I_{eff}' the section properties in Step (5) of Box 1 could be used for resistance check.

Simplification 2

When both axial force and bending moments are presents, A_{eff} could be calculated by considering the stress ratio ψ due to axial force only, while I_{eff} could be calculated by considering the stress ratio due to bending moment only. However, in both cases, the addition moment generated by the axial load due to the shift of centroid should be considered during resistance check.

It should be mentioned that in Simplification 2, while the calculation of A_{eff} does not require any iteration, in general iterations are still required for the calculation of I_{eff} . However, in case that the section under consideration is an I or a box section, Simplification 1 could be applied and only one iteration steps are needed to compute the value of I_{eff} . Furthermore, another important consequence of using the Simplification 2 is that as the ratio $(b_{eff} + b_1)/b$ always attends a minimum when $\psi = 1$, the simplification will always lead to a smaller (and thus conservative) value of A_{eff} when comparing with the full iteration procedure. However, it will be shown in the next section that, both Simplifications 1 and 2 will give a larger (and thus a non-conservative) value of I_{eff} .

4. Section properties calculation examples

In this section, five examples involving symmetrical I and square box sections are given to demonstrate how the simplified or the full iteration procedure could be employed to compute the section properties (A_{eff} and I_{eff}) of a Class 4 section. Loading cases involving pure axial force (N_{Ed} only), pure bending (M_{Ed} only) and both axial force and uniaxial bending moment above the major axis (N_{Ed} and M_{Ed}) are considered. In case that the full iteration procedure is employed, convergence of the solution is assumed if an accuracy of $C_{Atol} = C_{Itol} = 0.1\%$ (Equations. 10 and 11) is reached or at most up to four

iterations are completed.

4.1. Example 1: An I section under pure bending [4]

In the first example, an I section with a Class 4 web and Class 1 flange (Fig. 7) under pure bending is employed as an example to demonstrate the calculation steps for effect section properties. The gross section properties of the section are given by:

$$h_w=1920\text{mm}, t_w=10\text{mm}, A_{\text{gross}}=51200\text{mm}^2, \\ I_{\text{gross}}=3663530.67\text{cm}^4 \text{ and } W_{\text{el}}=37382.96\text{cm}^3$$

In this example, the actual value of M_{Ed} applied is immaterial as the stress ratio can be obtained by determining the location of the neutral axis. The detailed calculation steps for the first two iterations are shown in Box 3 and Fig. 8.

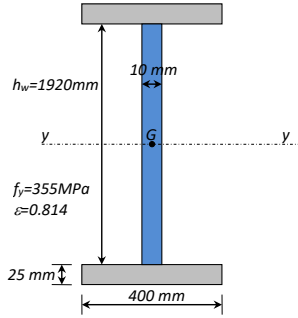


Fig. 7 Example 1: An I section under pure bending

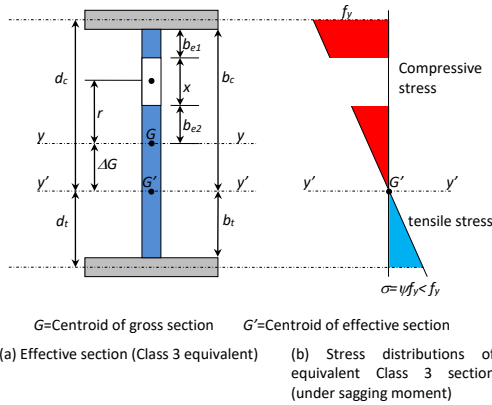


Fig. 8 Calculation of effective cross section

Box 3

Details calculation steps for iterations 1 and 2 for Example 1

First iteration

Calculation of effective area, A_{eff}

$$\psi = -1 \text{ (pure bending, fully effective section)}, k_{\sigma} = 23.9$$

$$\bar{\lambda}_p = \frac{h_w/t_w}{28.4\sqrt{k_{\sigma}}} = \frac{1920/10}{28.4 \times 0.814\sqrt{23.9}} = 1.699 > 1.08$$

$$\rho = \frac{\bar{\lambda}_p - 0.055(3 + \psi)}{\bar{\lambda}_p^2} = \frac{1.699 - 0.055(3 - 1)}{1.699^2} = 0.550$$

$$b_c = 1920/2 = 960\text{mm}, b_{\text{eff}} = 0.55 \times 960 = 528\text{mm}, \\ b_{e1} = 0.4 \times 528 = 211.2\text{mm}, b_{e2} = 0.6 \times 528 = 316.8\text{mm}, \\ x = 960 - 211.2 - 316.8 = 432\text{mm} \text{ (Fig. 8)}$$

$$\text{Reduction of area: } \Delta A = 10 \times 432 = 4320\text{mm}^2$$

$$A_{\text{eff}} = 51200 - 4320 = 46880\text{mm}^2$$

$$C_A = 8.44\% > 0.1\% \text{ (Equation 10b).}$$

Calculation of W_{eff}

$$r = h_w/2 - b_{e1} - x/2 = 1920/2 - 211.2 - 432/2 = 532.8\text{mm}$$

$$r\Delta A + A_{\text{eff}}\Delta G = 0 \text{ or } \Delta G = -532.8 \times 4320 / 46880 = -49.10\text{mm}$$

$$I_{\text{eff}} = I_{\text{gross}} + A(\Delta G)^2 - \left(\frac{x^3 t_w}{12} + \Delta A(r + \Delta G)^2 \right)$$

$$= \left(3663530.67 \times 10000 + 51200 \times 49.10^2 - \left(\frac{432^3 \times 10}{12} + \right. \right. \\ \left. \left. 4320(532.8 + 49.10)^2 \right) \right) / 10000 = 3522877.067\text{cm}^4$$

$$C_I = 3.84\% > 0.1\% \text{ (Equation 10b). } d_c = 1000 - 20 + 49.10 = 1029.1\text{mm}, d_t = 1000 - 20 - 49.10 = 930.9\text{mm}$$

$$W_{\text{eff}} = 3522877.067 / 102.91 = 34232.60\text{cm}^3$$

Since both C_A and $C_I > 0.1\%$, further iteration is carried out.

Second iteration

Calculation of effective area, A_{eff}

$$\psi = (-960 - 49.1) / (960 + 49.1) = -0.903, k_{\sigma} = 7.81 - 6.29\psi + 9.78\psi^2 = 21.46$$

$$\bar{\lambda}_p = \frac{1920/10}{28.4 \times 0.814\sqrt{21.46}} = 1.793 > 1.08, \rho = \frac{1.793 - 0.055(3 - 0.903)}{1.793^2} = 0.522$$

$$b_c = h_w/2 + \Delta G = 1920/2 + 49.10 = 1009.1\text{mm}, b_{\text{eff}} = 0.522 \times 1009.1 = 526.8\text{mm}$$

$$b_{e1} = 0.4 \times 526.8 = 210.7\text{mm}, b_{e2} = 0.6 \times 526.8 = 316.1\text{mm}$$

$$x = b_c - b_{e1} - b_{e2} = 1009.1 - 210.7 - 316.1 = 482.3\text{mm}$$

$$\text{Effective area reduction: } \Delta A = 10 \times 482.3 = 4823\text{mm}^2 \text{ and } A_{\text{eff}} = 51200 - 4823 = 46377\text{mm}^2$$

Hence, $C_A = 1.07\% > 0.1\%$ (Equation 10b).

Calculation of W_{eff}

$$r = h_w/2 - b_{e1} - x/2 = 1920/2 - 210.7 - 482.3/2 = 508.15\text{mm}$$

$$r\Delta A + A_{\text{eff}}\Delta G = 0 \text{ or } \Delta G = -508.15 \times 4823 / 46377 = -52.84\text{mm}$$

This means that shift of G' to $G'' = (-49.10 - (-52.84)) = 3.74\text{mm}$ (downward)

$$I_{\text{eff}} = \left(3663530.67 \times 10000 + 51200 \times 52.84^2 - \left(\frac{482.3^3 \times 10}{12} + \right. \right.$$

$$\left. 4823(508.15 + 52.84)^2 \right) / 10000 = 3516692.4\text{cm}^4$$

$$C_I = 0.176\% > 0.1\%, d_c = 1000 - 20 + 52.84 = 1032.84\text{mm}$$

$$d_t = 1000 - 20 - 52.84 = 927.16\text{mm}$$

$$W_{\text{eff}} = 3516692.41 / 103.281 = 34049.76\text{cm}^3$$

Eventually, after the third iteration, $A_{\text{eff}} = 46338.5\text{mm}^2$, $W_{\text{eff}} = 34036.04\text{cm}^3$ so that $C_A = 0.08\%$ and $C_I = 0.01\%$. The calculation results are summarized in Table 2. It can be seen that both A_{eff} and W_{eff} essentially converged after the first iteration and this justifies the simplify approach suggested in EC2 (Box 2).

Table 2

Summary of Example 1

Iteration	A_{eff} (mm ²)	I_{eff} (cm ⁴)	W_{eff} (cm ³)	ΔG (mm)	ψ
0 (Gross)	51200	3663530.67	37382.96	---	-1.0
1	46880	3522877.07	34232.60	49.10	-0.903
2	46377	3516692.40	34049.76	52.84	-0.8960
3 (Full)	46385	3516296.83	34036.04	53.11	-0.8952
Simplified	46880	3522877.07	34232.60	49.10	-0.903
Full/Simplified	0.99	0.99	0.99	---	---

4.2. Example 2: A class 4 square box section under pure compression

In this example, a class 4 square box section under pure compression is considered (Fig. 9). The gross section properties of the section are given by

$$b_{\text{fl}} = 1000\text{mm}, t_f = t_w = 10\text{mm}, h_w = 980\text{mm}, A_{\text{gross}} = 39600\text{mm}^2$$

$$I_{\text{gross}} = 646932\text{cm}^4, W_{\text{el, gross}} = 13069.33\text{cm}^3.$$

Under pure compression, both the flanges and webs are Class 4 with their central parts become non-effective (Fig. 10). However, as the section is doubly symmetric, the non-effective parts at the centre of each side do not change the location of the centroid and will not generate any additional moment. Hence, no iteration is needed to calculate A_{eff} as shown in Box 4. Obviously, in this example, the actual value of N_{Ed} applied is immaterial.

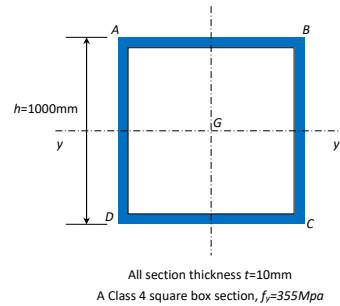


Fig. 9 Example 2: A class 4 square section under pure compression

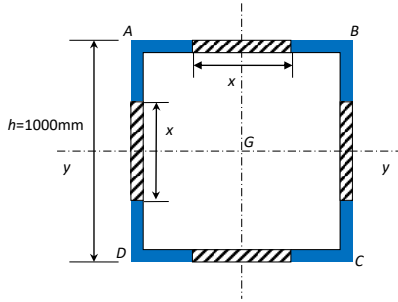


Fig. 10 Effective cross section of Example 2

Box 4Calculation of A_{eff} for Example 2Calculation of A_{eff} under pure axial compressionFor the two flanges and the two webs $\psi=1$ (pure axial compression), $k_\sigma=4$

$$\bar{\lambda}_p = \frac{b_n/t_n}{28.4\epsilon\sqrt{k_\sigma}} = \frac{980/10}{28.4 \times 0.814\sqrt{4}} = 2.12$$

$$\rho = \frac{\bar{\lambda}_p - 0.055(3 + \psi)}{\bar{\lambda}_p^2} = \frac{2.12 - 0.055(3 + 1)}{2.12^2} = 0.423$$

$$b_{eff} = 0.423 \times 980 = 414.5 \text{ mm},$$

$$b_{e1} = 0.5 \times 414.5 = 207.25 \text{ mm},$$

$$b_{e2} = 0.5 \times 414.5 = 207.25 \text{ mm},$$

$$x = 980 - 414.5 = 565.5 \text{ mm}$$

$$\text{Hence, } A_{eff} = 39600 - 4 \times (10 \times 565.5) = 16980 \text{ mm}^2$$

$$A_{eff}/A_{gross} = 16980/39600 = 42.9\%.$$

4.3. Example 3: A class 4 square box section under pure bending

In this example, the square box section employed in Example 2 is considered again but now it is subject to pure bending so that the top flange AB is under compression while the bottom flange CD is under tension and is fully effective (Fig. 11). There is a shift of the centroid from G to G' . For the webs, their classifications shall depend on the stress ratio at the top and bottom extreme fibres. The distance between G and G' shall depend on whether the webs remain Class 3 or 4 after the new stress ratio of the webs is taken into account. For a box section under pure bending, Simplification 1 allows the designer to use one iteration to calculate W_{eff} . Box 5 summarizes the calculation steps.

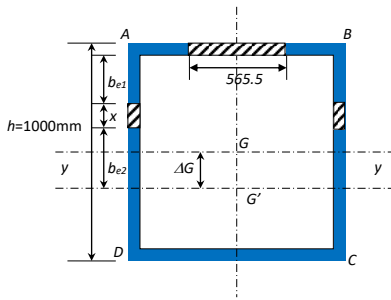


Fig. 11 Examples 3 and 4 with flange CD under tension

Box 5Calculation of W_{eff} for Example 3Calculation of A_{eff} by assuming only the top flange CD is class 4

For the flange AB, same as Example 2:

$$b_{eff} = 414.5 \text{ mm}, b_{e1} = 207.25 \text{ mm}, b_{e2} = 207.25 \text{ mm}, x_1 = 565.5 \text{ mm},$$

$$A_{eff} = A_{gross} - 565.5 \times 10 = 33945 \text{ mm}^2$$

$$\text{Hence, } r = 500 - 5 = 495 \text{ mm}, \Delta G = -495 \times 565.5 / 33945 = -82.46 \text{ mm}.$$

Recheck for Class 3 limit for the two webs

$$\psi = -(980/2 - 82.46) / (980/2 + 82.46) = -0.712$$

$$\text{Hence, } 42\epsilon / (0.67 + 0.33\psi) = 78.59 < h_w/t_w = 98$$

The two webs shall become Class 4.

First iteration

$$\psi = -0.712, k_\sigma = 7.81 - 6.29\psi = 9.78, \psi^2 = 17.25.$$

$$\text{For the two flanges: } \bar{\lambda}_p = 1.021, \rho = 0.859$$

$$b_{eff} = 0.859 \times (980/2 + 82.46) = 491.74 \text{ mm}$$

$$b_{e1} = 0.4 \times 491.74 = 196.70 \text{ mm}, b_{e2} = 0.6 \times 491.54 = 295.04 \text{ mm},$$

$$x = 980/2 + 82.46 - 491.74 = 80.72 \text{ mm}.$$

$$A_{eff} = A_{gross} - 565.5 \times 10 - 2 \times 10 \times 80.72 = 32330.6 \text{ mm}^2$$

$$A_{eff}/A_{gross} = 32330.6/39600 = 81.64\%$$

(Note: This A_{eff} should only be used if the section is under pure bending only)Calculation of W_{eff} New position of G' after considering the webs are Class 4

$$\Delta G' = -(495 \times 5650 + 80.72 \times 10 \times 2 \times (980/2 - 196.70 - 80.72/2)) / 32330.6 = -99.21 \text{ mm}$$

$$I_{eff} = (646932 \times 10000 + 39600 \times 99.21^2 - \left(\frac{10^3 \times 565.5}{12} + 5655 \times (5 + 980/2 + 99.21)^2 \right) - 2 \times \left(\frac{80.72^3 \times 10}{12} + 80.72 \times 10 \times (99.21 + 980/2 - 196.70 - 80.72/2)^2 \right)) / 10000 = 466126.44 \text{ cm}^4$$

$$d_c = 1000/2 - 5 + 99.21 = 594.21 \text{ mm}, W_{eff} = 7844.47 \text{ cm}^3$$

$$W_{eff}/W_{gross} = 7844.47/13069.33 = 60\%$$

4.4. Example 4: A class 4 square box section under axial compression and bending

In this example, the same square box section used in Examples 2 and 3 is reconsidered again but now it is subjected to both axial compression and bending above the y - y axis. In this case, if the Simplification 2 is used, one could determine A_{eff} based on the compression force only (Example 2) and W_{eff} based on moment only (Example 3) so that $A_{eff} = 16980 \text{ mm}^2$ and $W_{eff} = 7844.47 \text{ cm}^3$.

However, in full iteration method, the stress ratio (and hence the classification) of the web shall depend on the magnitude of the compressive force and the bending moment. Under some loading conditions, it is possible that the web will remain as Class 3/4 but the bottom flange will be Class 4 as the compressive force may be large enough to make the bottom flange under compression. In this case, in order to compute the section properties, it is necessary to know the values of N_{Ed} and M_{Ed} (or their ratio, as shown in Appendix A). In this example, it is assumed that $N_{Ed} = 3500 \text{ kN}$ and $M_{Ed} = 800 \text{ kNm}$ so that the flange CD will be under compression. Similar to the previous example, calculation is started by assuming that the section is fully effective first so that $A_{gross} = 39600 \text{ mm}^2$, $I_{gross} = 646932 \text{ cm}^4$ and $W_{el,gross} = 13069.33 \text{ cm}^3$. Box 6 shows the first two iteration steps and eventually three iterations are carried out to achieve convergence. Table 3 summarizes the results obtained from the full and simplified procedures. Regarding the adequacy of the Section, for the simplified method, from Equation 9, the maximum resultant stress is given by

$$\sigma_{max} = 3500 \times 1000 / (16980) + 800 \times 1000 \times 1000 / (7844.47 \times 1000) = 308.14 \text{ MPa} < 355 \text{ MPa}$$

while based on full iteration

$$\sigma_{max} = 3500 \times 1000 / (19054.4) + 800 \times 1000 \times 1000 / (6821.53 \times 1000) = 300.7 \text{ MPa} < 355 \text{ MPa}$$

Hence, while the simplified method overestimated W_{eff} , it underestimated A_{eff} a lot but it is still conservative in term of section resistance calculation.

Table 3

Summary of Example 4

Iteration	$A_{eff} (\text{mm}^2)$	$I_{eff} (\text{cm}^4)$	$W_{eff} (\text{cm}^3)$	$\Delta G (\text{cm})$	ψ
0 (Gross)	39600	646932	13069.33	---	-1.0
1	19313.2	352077.57	6824.93	20.87	0.186
2	19058.4	351119.10	6820.50	19.80	0.251
3 (Full)	19054.4	351118.02	6821.53	19.72	0.255
Simplified	16980*	466126.44^	7844.47^	99.21^	-0.712^
Full/Simplified	1.12	0.75	0.87	---	---

*By considering N_{Ed} only, ^By considering M_{Ed} only**Box 6**

Detailed calculation steps of first two iterations for Example 4

1st iteration

Initial stress (assuming section is fully effective)

Stress at top of webs:

$$3500 \times 1000 / 39600 + 800 \times 1000 \times 1000 \times 490 / 646932 \times 10000 = 148.98 \text{ MPa}$$

Stress at bottom of webs:

$$3500 \times 1000 / 39600 - 800 \times 1000 \times 1000 \times 490 / 646932 \times 10000 = 27.79 \text{ MPa}$$

Since both flanges are under compression, they are Class 4 elements.

Effective width of top and bottom flanges (From Example 2)

$$b_{eff} = 0.423 \times 980 = 414.5 \text{ mm}, b_{e1} = 0.5 \times 414.5 = 207.25 \text{ mm},$$

$$b_{e2} = 0.5 \times 414.5 = 207.25 \text{ mm}$$

Effective width and areas of webs and section effective area

$$\psi = 27.79/148.98 = 0.186$$

Hence, $42\varepsilon/(0.67+0.33\psi) = 46.74 < h_w/t_w = 98$ and the webs are Class 4.

Stress ratio: $\psi = 0.186$, $k_\sigma = 8.2/(1.05 + \psi) = 6.63$, $\bar{\lambda}_p = 1.646$, $\rho = 0.542$

$$b_{eff} = 0.542 \times 980 = 531.16 \text{ mm}, b_{e1} = 2b_{eff}/(5 - \psi) = 220.67 \text{ mm},$$

$$b_{e2} = b_{eff} - b_{e1} = 310.49 \text{ mm}$$

$$x = 980 - 531.16 = 448.84 \text{ mm}.$$

$$\text{Hence, } A_{eff} = A_{gross} - 565.5 \times 10 \times 2 - 10 \times 448.84 = 19313.2 \text{ mm}^2$$

 I_{eff} and W_{eff} calculations

$$\text{Shift of centroid } \Delta G = -(448.84 \times 10 \times 2 \times (980/2 - 220.67 - 448.84/2)) / 19313.2 = -20.87 \text{ mm}$$

$$I_{eff} = 352077.57 \text{ cm}^4, W_{eff} = 352077.57 \times 10 / (490 + 20.87 + 5) = 6824.93 \text{ cm}^3$$

Updated stress at webs

Compressive stress due to axial force: $3500 \times 1000 / 19313.2 = 181.22 \text{ MPa}$

Bending stress at top of webs:

$$800 \times 1000 \times 1000 \times (490 + 20.87) / (352077.57 \times 10000) = 116.08 \text{ MPa}$$

Bending stress at bottom of webs:

$$800 \times 1000 \times 1000 \times (490 - 20.87) / (352077.57 \times 10000) = 106.6 \text{ MPa}$$

Total stress at top of webs: $181.22 + 116.08 = 297.3 \text{ MPa}$ (compression)

Total stress at bottom of webs: $181.22 - 106.6 = 74.62 \text{ MPa}$ (compression)

2nd iteration

New stress ratio: $\psi = 74.62/297.3 = 0.251$

Effective width for webs and new A_{eff}

$$k_\sigma = 8.2/(1.05 + \psi) = 6.303, \bar{\lambda}_p = 1.689, \rho = 0.529$$

$$b_{eff} = 0.529 \times 980 = 518.42 \text{ mm}, b_{e1} = 2b_{eff}/(5 - \psi) = 218.33 \text{ mm},$$

$$b_{e2} = b_{eff} - b_{e1} = 300.09 \text{ mm}$$

$$x = 980 - 518.42 = 461.58 \text{ mm}.$$

$$A_{eff} = A_{gross} - 565.5 \times 10 \times 2 - 10 \times 461.58 = 19058.4 \text{ mm}^2$$

 I_{eff} and W_{eff} calculations

Shift of centroid $\Delta G = -19.80 \text{ mm}$. I.e. $\Delta G' - \Delta G'' = 20.87 - 19.80 \text{ mm} = 1.07 \text{ mm}$ (upward)

$$I_{eff} = 351119.10 \text{ cm}^4, W_{eff} = 351119.10 \times 10 / (490 + 19.80 + 5) = 6820.5 \text{ cm}^3$$

Updated stress at webs

Compressive stress due to axial force: $3500 \times 1000 / 19058.4 = 183.65 \text{ MPa}$

Bending stress at top of webs:

$$800 \times 1000 \times 1000 \times (490 + 19.80) / (351119.10 \times 10000) = 116.15 \text{ MPa}$$

Bending stress at bottom of webs:

$$800 \times 1000 \times 1000 \times (490 - 19.80) / (351119.10 \times 10000) = 107.13 \text{ MPa}$$

Total stress at top of webs: $183.65 + 116.15 = 299.8 \text{ MPa}$ (compression)

Total stress at bottom of webs: $183.65 - 107.13 = 76.52 \text{ MPa}$ (compression)

The new stress ratio for next iteration is $\psi = 76.52/299.8 = 0.255$

4.5. Example 5: A class 4 square box section under axial compression and bending with bottom flanges under tension

In the last example, the same square box section used in Example 4 is subjected to a lower axial compression of $N_{Ed} = 1000 \text{ kN}$ but a larger $M_{Ed} = 2000 \text{ kNm}$ so that flange CD is eventually under *tension* and four iterations are conducted. Detailed calculations for the first two iterations are shown in Box 7 and all iterations results are summarized in Table 4. Regarding the adequacy of the section, based, for the simplified method, the maximum resultant stress of the section is given by

$$\sigma_{max} = 1000 \times 1000 / (16980) + 2000 \times 1000 \times 1000 / (7844.47 \times 1000) = 313.5 \text{ MPa} < 355 \text{ MPa}$$

while for the full iteration,

$$\sigma_{max} = 1000 \times 1000 / (30762.2) + 2000 \times 1000 \times 1000 / (7374.97 \times 1000) = 303.5 \text{ MPa} < 355 \text{ MPa}$$

Again, the simplified method overestimated W_{eff} but underestimated A_{eff} so that the resistance estimation is still conservative.

Box 7

Detailed calculation steps of first two iterations for Example 5

1st iteration

Initial stress (assuming section is fully effective)

Stress at top of webs:

$$1000 \times 1000 / 39600 + 2000 \times 1000 \times 1000 \times 490 / 646932 \times 10000 = 176.74 \text{ MPa}$$

Stress at bottom of webs:

$$1000 \times 1000 / 39600 - 2000 \times 1000 \times 1000 \times 490 / 646932 \times 10000 = -126.23 \text{ MPa}$$

Effective width of top flange

The top flange is clearly Class 4 and remains Class 4 in all subsequent iterations so that

$$b_{eff} = 0.423 \times 980 = 414.5 \text{ mm}, b_{e1} = 0.5 \times 414.5 = 207.25 \text{ mm},$$

$$b_{e2} = 0.5 \times 414.5 = 207.25 \text{ mm}$$

Effective width of webs and section effective area

$$\psi = 126.23/176.74 = -0.714$$

Hence, $42\varepsilon/(0.67+0.33\psi) = 78.71 < h_w/t_w = 98$ and therefore the webs are again Class 4.

Stress ratio: $\psi = -0.714$, $k_\sigma = 7.81 - 6.29\psi = 9.78$, $\psi^2 = 17.29$, $\bar{\lambda}_p = 1.019$,

$$\rho = 0.860$$

$$b_{eff} = 0.860 \times (980/2) = 421.4 \text{ mm}, b_{e1} = 0.4 \times 421.4 = 168.56 \text{ mm},$$

$$b_{e2} = 0.6 \times 421.4 = 252.84 \text{ mm},$$

$$x = 980/2 - 421.4 = 68.6 \text{ mm}.$$

$$\text{Hence, } A_{eff} = A_{gross} - 565.5 \times 10 \times 2 - 10 \times 68.6 = 32573 \text{ mm}^2$$

 I_{eff} and W_{eff} calculations

Shift of centroid: $\Delta G = -98.03 \text{ mm}$

$$I_{eff} = 465696.55 \text{ cm}^4, W_{eff} = 465696.55 \times 10 / (495 + 98.03) = 7852.83 \text{ cm}^3$$

Updated stress at webs

Compressive stress due to axial force: $1000 \times 1000 / 32573 = 30.7 \text{ MPa}$

Bending stress at top of webs:

$$2000 \times 1000 \times 1000 \times (490 + 98.03) / 465696.55 \times 10000 = 252.54 \text{ MPa}$$

Bending stress at bottom of webs:

$$-2000 \times 1000 \times 1000 \times (490 - 98.03) / 465696.55 \times 10000 = -168.34 \text{ MPa}$$

Total stress at top of webs: $252.54 + 30.7 = 283.04 \text{ MPa}$ (compression)

Total stress at bottom of webs: $-168.34 + 30.7 = -137.64 \text{ MPa}$ (tension)

2nd iteration

New stress ratio $\psi = -137.64/283.04 = -0.486$

Effective width for webs and new A_{eff}

$$k_\sigma = 7.81 - 6.29\psi = 13.177, \bar{\lambda}_p = 1.168, \rho = 0.755$$

$$b_{eff} = 0.755 \times (980/2 + 98.03) = 443.96 \text{ mm}, b_{e1} = 0.4 \times 443.96 = 177.58 \text{ mm},$$

$$b_{e2} = 0.6 \times 443.96 = 266.38 \text{ mm}$$

$$x = 980/2 + 98.03 - 443.96 = 144.07 \text{ mm},$$

$$A_{eff} = A_{gross} - 565.5 \times 10 \times 2 - 10 \times 144.96 = 31063.6 \text{ mm}^2$$

 I_{eff} and W_{eff} calculation

Shift of centroid $\Delta G' = -112.41 \text{ mm}$.

I.e. $\Delta G' - \Delta G'' = -98.03 - (-112.41) = 14.38 \text{ mm}$ (downward)

$$I_{eff} = 451965.18 \text{ cm}^4, W_{eff} = 451965.18 \times 10 / (490 + 112.41 + 5) = 7440.86 \text{ cm}^3$$

Updated stress at webs

Compressive stress due to axial force: $1000 \times 1000 / 31063.6 = 32.19 \text{ MPa}$

Bending stress at top of webs:

$$2000 \times 1000 \times 1000 \times (490 + 112.41) / (451965.18 \times 10000) = 266.57 \text{ MPa}$$

Bending stress at bottom of webs:

$$-2000 \times 1000 \times 1000 \times (490 - 112.41) / (451965.18 \times 10000) = -167.09 \text{ MPa}$$

Total stress at top of webs: $266.57 + 32.19 = 298.76 \text{ MPa}$ (compression)

Total stress at bottom of webs: $-167.09 + 32.19 = -134.9 \text{ MPa}$ (tension)

The new stress ratio for next iteration is $\psi = -134.9/298.76 = -0.442$

Table 4

Summary of Example 5

Iteration	$A_{eff} (\text{mm}^2)$	$I_{eff} (\text{cm}^4)$	$W_{eff} (\text{cm}^3)$	$\Delta G (\text{cm})$	ψ
0 (Gross)	39600	646932	13069.33	---	-1.0
1	32573	465696.55	7852.83	98.03	-0.714
2	31063.6	451965.18	7440.86	112.41	-0.486
3	30764.2	449659.07	7370.37	115.09	-0.442
4 (Full)	30762.2	449872.97	7374.97	115.00	-0.445
Simplified	16980*	466126.44^	7844.47^	99.21^	-0.712^
Full/Simplified	1.81	0.97	0.94	---	---

*By considering N_{Ed} only, ^By considering M_{Ed} only

Since the values of N_{Ed} and M_{Ed} are known and their simultaneous actions do not cause the section to yield, one could employ alternative Equations. 6 and 7 to get a larger ρ so that a less conservative section resistance could be obtained. The corresponding results obtained are summarized in Table 5. From Table 5, it can be seen that by using the alternative equations, the values of A_{eff} and W_{eff} are respectively increased by 5.8% and 7.6% when comparing with the original method.

Table 5Summary of Example 5 by using alternative value of ρ

Iteration	$A_{eff} (mm^2)$	$I_{eff} (cm^4)$	$W_{eff} (cm^3)$	$\Delta G (cm)$	ψ
0 (Gross)	39600	646932	13069.33	---	-1.0
1	33945	485284.56	8403.78	82.46	-0.714
2	33074.8	474994.33	8100.31	91.39	-0.522
3	32712.4	470995.57	7982.43	95.04	-0.5
4 (Alternative)	32564.4	469407.75	7935.62	96.52	-0.492
Full	30762.2	449872.97	7374.97	115.00	-0.445
Simplified	16980*	466126.44^	7844.47^	99.21^	-0.712^
Alternative/Full	1.059	1.043	1.076	---	---
Alternative/ Simplified	1.92	1.01	1.01	---	---

5. Conclusions

In this review, the basic principle adopted by EC3 for the calculation of Class 4 slender thin-walled steel section properties is summarized. A detailed discussion is given for the EC3's effective width method for section properties calculation. A summary of the effective width calculation steps for Class 4 plate element are given. Summary charts for the variations of effective width for internal and external plate elements under different direct stress ratio are also presented. For the calculation of section properties of Class 4 slender sections, both the full iteration procedure and the simplified procedure suggested by EC3 are discussed and summarized. In order to demonstrate the actual calculation procedure for slender section subjected to different loading conditions, five practical calculation examples are given and both the full iteration and the simplified procedures are employed to obtain the section properties for comparison. The calculation results show that while the simplified procedure could reduce the number of iterations needed and does not require the ratios between the axial force and the bending moments applied, it is encouraged to use the full iteration procedure as in general it will lead to slightly higher sectional resistance.

Appendix A: Elevation of stress ratio ψ

From Sections 2.3 and 3.1, in order to compute the effective width (or area) of any arbitrary plate element 1-2 (Fig. A1), one must first obtain the direct stress ratio ψ of the plate element. From Equation 9, the direct stress at the two ends 1 and 2 of the elements can be expressed as

$$\sigma_1(y, z) = \frac{N_{Ed}}{A_{eff}} + \frac{(M_{y,Ed} + N_{Ed}\Delta z)}{I_{y,eff}(\Delta y, \Delta z)}y_1 + \frac{(M_{z,Ed} + N_{Ed}\Delta y)}{I_{z,eff}(\Delta y, \Delta z)}z_1 \quad (A1)$$

$$\sigma_2(y, z) = \frac{N_{Ed}}{A_{eff}} + \frac{(M_{y,Ed} + N_{Ed}\Delta z)}{I_{y,eff}(\Delta y, \Delta z)}y_2 + \frac{(M_{z,Ed} + N_{Ed}\Delta y)}{I_{z,eff}(\Delta y, \Delta z)}z_2 \quad (A2)$$

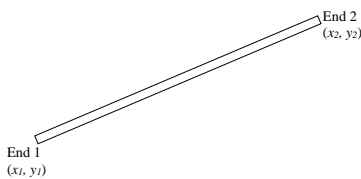
where (y_1, z_1) and (y_2, z_2) are the coordinates of ends 1 and 2, respectively. Assume that $\sigma_2 < \sigma_1$, the stress ratio ψ can be expressed as

$$\psi = \frac{\sigma_2}{\sigma_1} = \frac{\frac{N_{Ed}}{A_{eff}} + \frac{(M_{y,Ed} + N_{Ed}\Delta z)}{I_{y,eff}(\Delta y, \Delta z)}y_2 + \frac{(M_{z,Ed} + N_{Ed}\Delta y)}{I_{z,eff}(\Delta y, \Delta z)}z_2}{\frac{N_{Ed}}{A_{eff}} + \frac{(M_{y,Ed} + N_{Ed}\Delta z)}{I_{y,eff}(\Delta y, \Delta z)}y_1 + \frac{(M_{z,Ed} + N_{Ed}\Delta y)}{I_{z,eff}(\Delta y, \Delta z)}z_1} \quad (A3)$$

or

$$\psi = \frac{\sigma_2}{\sigma_1} = \frac{\frac{1}{\frac{N_{Ed}}{A_{eff}} + \frac{(M_{y,Ed} + N_{Ed}\Delta z)}{I_{y,eff}(\Delta y, \Delta z)}y_2 + \frac{(M_{z,Ed} + N_{Ed}\Delta y)}{I_{z,eff}(\Delta y, \Delta z)}z_2}}{\frac{1}{\frac{N_{Ed}}{A_{eff}} + \frac{(M_{y,Ed} + N_{Ed}\Delta z)}{I_{y,eff}(\Delta y, \Delta z)}y_1 + \frac{(M_{z,Ed} + N_{Ed}\Delta y)}{I_{z,eff}(\Delta y, \Delta z)}z_1}} \quad (A4)$$

Hence, only the values of the ratios $\frac{M_{y,Ed}}{N_{Ed}}$ and $\frac{M_{z,Ed}}{N_{Ed}}$ are needed for the calculation of ψ and then the evaluation of the effective section properties.

**Fig. A1** Stress ratio calculation for a straight plate element 1-2

References

- [1] British Standard Institution, Eurocode 3: Design of Steel Structures: Part 1-1 General rules and rules for buildings, BS EN 1993-1-1, BSI London, 2005.
- [2] British Standard Institution, Eurocode 3: Design of Steel Structures: Part 1-5 Plated Structural elements, BS EN 1993-1-5, BSI London, 2006.
- [3] Gardner L. and Nethercot D.A., "Designer's guide to Eurocode 3: Design of steel buildings EN 1993-1-1, -1-3 and -1-8", Second edition, ICE publishing, 2011.
- [4] Beg D., Kuhlmann, U., Davaine L. and Braun, B., "Design of plated Structures Eurocode 3: Design of steel structures: Part 1-5- Design of plated structures", ECCS and Ernst & Sohn, 2010.
- [5] Timoshenko S.P and Gere J.M., Theory of Elastic Stability, McGraw Hill Book Company, International Edition, 1963.
- [6] Lee C.K. and Chiew S.P., "An efficient modified flanges only method for plate girder bending resistance calculation", Journal of Constructional Steel Research, 89, 98-106, 2013.
- [7] Gardner L. and Chan T.M., "Cross-section classification of elliptical hollow sections", Steel and Composite Structures, 7(3), 185-200, 2007.
- [8] Prachar M., Hricak J., Jandera M., Wald F., Zhao B., "Experiments of Class 4 Open section beams at elevated temperature", Thin-Walled Structures, 98, 2-18, 2016.

FINITE ELEMENT ANALYSIS FOR THE PROGRESSIVE FAILURE OF FRP-REINFORCED STEEL COMPONENT UNDER LOW-VELOCITY IMPACT

Qi-Jian Wu^{1, 2}, Xu-Dong Zhi^{1, 2, *} and Meng-Hui Guo^{1, 2}

¹ Key Lab of Structures Dynamic Behavior and Control of the Ministry of Education, Harbin Institute of Technology, Harbin, China

² Key Lab of Smart Prevention and Mitigation of Civil Engineering Disasters of the Ministry of Industry and Information Technology, Harbin Institute of Technology, Harbin, China

* (Corresponding author: E-mail: zhixudong@hit.edu.cn)

ABSTRACT

This study proposed a finite element simulation method to analyze the progressive failure of fiber-reinforced polymer (FRP) reinforced steel component under low-velocity impact. In this method, the Johnson-Cook model and fracture criterion were used to consider the strain rate effect of steel; additionally, a VUMAT subroutine was proposed to discuss the 6 initial failure modes (fiber tension/compression failure, matrix tension/compression failure and in-layer tension/compression delamination failure) and damage evolution of FRP. In order to verify the simulation results, a series of axial low-velocity impact tests on GFRP-reinforced circular steel tube were performed, the comparative study confirmed that the simulations were in good agreement with the test results. Besides, the advantages of proposed VUMAT subroutine were made obviously by comparing to the Puck criterion, the Hashin criterion, and the Chang-Chang criterion.

ARTICLE HISTORY

Received: 18 September 2018
Revised: 27 February 2019
Accepted: 6 March 2019

KEYWORDS

FRP-reinforced steel component;
Low-velocity impact;
Simulation;
Progress failure;
Damage mechanics

Copyright © 2019 by The Hong Kong Institute of Steel Construction. All rights reserved.

1. Introduction

Nowadays, steel components are used widely in important structures due to their advantages of easy construction and high bearing capacity. During the service period of these structures, low-velocity impacts are possible loads and can bring a great loss to the society, such as the collisions by cars or airplanes. Thus, improving the impact resistance of steel component is a necessary way to reduce the collapsed risk of these structures.

Fiber reinforced polymer (FRP) served as energy dissipation member have already been widely applied to the aerospace and automotive manufacturing [1, 2]. Reinforcing the steel component by FRP can harness the advantages of each material and increase both the bearing capacity and energy dissipation capacity [3, 4]. Besides, the wrapped FRP can also protect the inner steel component from corrosion. Hence, there is a good application prospect of this kind of components in architectural structure.

Because of the advantages of powerful function and saving resources, the finite element analysis has already been extensively applied to the engineering field. The key consideration to simulate FRP-reinforced steel component (FSC) is selecting appropriate constitutive models, including stress-strain relationships, failure criteria, and damage evolution laws. The J-C constitutive model [5, 6] are widely used in metal impact simulation [7-9], since they can consider the metal plastic deformation, the strain rate strengthening effect, and the temperature softening effect. The Hashin criterion [10], the Puck criterion [11], and the Chang-Chang criterion [12] are the most commonly used failure criteria for FRP, nowadays. Many researchers [13-18] had studied the low-velocity impact problems of FRP component based on these three criteria. However, these studies always ignored the in-layer delamination of FRP which is an important failure mode when the thickness of unidirectional FRP lamina is large.

In the present study, a VUMAT subroutine to discuss the 6 initial failure modes (fiber tension/compression failure, matrix tension/compression failure and in-layer tension /compression delamination failure) and damage evolution of FRP was proposed. Besides, based on the VUMAT subroutine and J-C constitutive model, a method to simulate FSC under low-velocity impact was introduced.

2. Constitutive models for FSC

2.1. Stress-strain relationships for steel and FRP

The mechanical behavior of material is expressed by its stress-strain relationship. Normally, the 3D stress-strain relationship for material is shown in Eq. 1. Where σ_i is the stress component; C_{ij} is the stiffness coefficient; ε_j is the strain component ($i, j=1, 2, \dots, 6$).

Steel is an isotropic material so that each point in it has the same elastic properties in any direction. The relationship between the stiffness coefficients of steel is expressed in Eq. 2.

$$\begin{pmatrix} \sigma_1 \\ \sigma_2 \\ \vdots \\ \sigma_6 \end{pmatrix} = \begin{bmatrix} C_{11} & C_{12} & \cdots & C_{16} \\ C_{21} & C_{22} & \cdots & C_{26} \\ \vdots & \vdots & \ddots & \vdots \\ C_{61} & C_{62} & \cdots & C_{66} \end{bmatrix} \begin{pmatrix} \varepsilon_1 \\ \varepsilon_2 \\ \vdots \\ \varepsilon_6 \end{pmatrix} \quad (1)$$

$$\begin{cases} C_{11} = C_{22} = C_{33} \\ C_{12} = C_{13} = C_{23} \\ C_{44} = C_{55} = C_{66} = 1/2(C_{11} - C_{12}) \end{cases} \quad (2)$$

Engineering parameters can be obtained directly through the material tests. Therefore, these parameters including elasticity modulus (E), Poisson's ratio (ν), and shear modulus (G) are typically used to express the stiffness coefficients of steel, as shown in Eq. 3. In this equation, $S = 1 - 2\nu^3 - 3\nu^2$.

$$\begin{pmatrix} \sigma_1 \\ \sigma_2 \\ \sigma_3 \\ \sigma_4 \\ \sigma_5 \\ \sigma_6 \end{pmatrix} = \begin{bmatrix} E(1-\nu^2)/S & E(\nu^2+\nu)/S & E(\nu^2+\nu)/S & 0 & 0 & 0 \\ E(\nu^2+\nu)/S & E(1-\nu^2)/S & E(\nu^2+\nu)/S & 0 & 0 & 0 \\ E(\nu^2+\nu)/S & E(\nu^2+\nu)/S & E(1-\nu^2)/S & 0 & 0 & 0 \\ 0 & 0 & 0 & G & 0 & 0 \\ 0 & 0 & 0 & 0 & G & 0 \\ 0 & 0 & 0 & 0 & 0 & G \end{bmatrix} \begin{pmatrix} \varepsilon_1 \\ \varepsilon_2 \\ \varepsilon_3 \\ \varepsilon_4 \\ \varepsilon_5 \\ \varepsilon_6 \end{pmatrix} \quad (3)$$

$$\begin{pmatrix} \sigma_1 \\ \sigma_2 \\ \sigma_3 \\ \sigma_4 \\ \sigma_5 \\ \sigma_6 \end{pmatrix} = \begin{bmatrix} \frac{E_1(1-\nu_{23}\nu_{32})}{S} & \frac{E_2(\nu_{21}+\nu_{23}\nu_{31})}{S} & \frac{E_3(\nu_{31}+\nu_{21}\nu_{32})}{S} & 0 & 0 & 0 \\ \frac{E_2(\nu_{21}+\nu_{23}\nu_{31})}{S} & \frac{E_2(1-\nu_{13}\nu_{31})}{S} & \frac{E_3(\nu_{32}+\nu_{12}\nu_{31})}{S} & 0 & 0 & 0 \\ \frac{E_3(\nu_{31}+\nu_{21}\nu_{32})}{S} & \frac{E_3(\nu_{32}+\nu_{12}\nu_{31})}{S} & \frac{E_3(1-\nu_{12}\nu_{21})}{S} & 0 & 0 & 0 \\ 0 & 0 & 0 & G_{23} & 0 & 0 \\ 0 & 0 & 0 & 0 & G_{31} & 0 \\ 0 & 0 & 0 & 0 & 0 & G_{12} \end{bmatrix} \begin{pmatrix} \varepsilon_1 \\ \varepsilon_2 \\ \varepsilon_3 \\ \varepsilon_4 \\ \varepsilon_5 \\ \varepsilon_6 \end{pmatrix} \quad (4)$$

FRP is an orthotropic material with two orthorhombic elastic symmetry planes, so that its material stiffness matrix has nine independent coefficients ($C_{11}, C_{22}, C_{33}, C_{44}, C_{55}, C_{66}, C_{12}=C_{21}, C_{13}=C_{31}, C_{23}=C_{32}$). Similarly, the stiffness coefficients of FRP are usually represented by the engineering parameters,

including elasticity modulus (E_i), Poisson's ratio (ν_{ij}), and shear modulus (G_{ij}), where $i, j=1, 2, 3$, but $i \neq j$, as shown in Eq. 4. In this equation, $S = 1 - \nu_{12}\nu_{21} - \nu_{23}\nu_{32} - \nu_{13}\nu_{31} - 2\nu_{12}\nu_{23}\nu_{31}$.

2.2. The constitutive model and fracture criterion for steel

Steel is a strain rate sensitive material so that the strain rate effect can't be ignored during an impact process. The J-C model [5] can consider the metal plastic deformation, the strain rate strengthening effect, and the temperature softening effect; therefore it was chosen to simulate steel, as shown in Eq. 5. In this equation, A, B, n, C , and m are the material correlation constants; ε_{eq} is the equivalent plastic strain; $\dot{\varepsilon}^*$ is the dimensionless equivalent plastic strain, where $\dot{\varepsilon}_0$ is the reference strain rate; T^* is the dimensionless temperature.

$$\sigma = (A + B\varepsilon_{eq}^n)(1 + C \ln \dot{\varepsilon}^*)(1 - T^{*m}) \quad (5)$$

Metal materials fracture because of the formation and expansion of internal microcracks. The development of these microcracks is significantly correlated with the stress state (stress triaxiality), temperature and strain rate. The J-C fracture criterion [6] considered these factors (Eq. 6), which contributes to its widespread use. In Eq. 6, ε_f is the failure strain; d_1-d_5 are the material correlation constants; σ^* is the stress triaxiality and can be calculated by $\sigma^* = \sigma_m / \sigma_{eq}$, where σ_{eq} is the equivalent stress, σ_m is the hydrostatic pressure.

$$\varepsilon_f = [d_1 + d_2 \exp(d_3 \sigma^*)] (1 + d_4 \ln \dot{\varepsilon}^*) (1 + d_5 T^*) \quad (6)$$

Besides, the J-C fracture criterion decouples the damage and the strength. The damage evolution law is represented as Eq. 7, where, $\Delta \varepsilon_{eq}$ is the equivalent plastic strain increment; D is the damage coefficient (the initial value of D is 0, and when metal fractured the value of D is 1). Moreover, the damaged stress component matrix σ^d can be represented by Eq. 8.

$$D = \sum \frac{\Delta \varepsilon_{eq}}{\varepsilon_f} \quad (7)$$

$$\sigma^d = \begin{pmatrix} \sigma_1^d \\ \sigma_2^d \\ \sigma_3^d \\ \sigma_4^d \\ \sigma_5^d \\ \sigma_6^d \end{pmatrix} = \begin{bmatrix} 1-D & 0 & 0 & 0 & 0 & 0 \\ 0 & 1-D & 0 & 0 & 0 & 0 \\ 0 & 0 & 1-D & 0 & 0 & 0 \\ 0 & 0 & 0 & 1-D & 0 & 0 \\ 0 & 0 & 0 & 0 & 1-D & 0 \\ 0 & 0 & 0 & 0 & 0 & 1-D \end{bmatrix} \cdot \begin{pmatrix} \sigma_1 \\ \sigma_2 \\ \sigma_3 \\ \sigma_4 \\ \sigma_5 \\ \sigma_6 \end{pmatrix} \quad (8)$$

2.3. Failure criteria and damage evolution laws for unidirectional laminate

Currently, FRP failures are generally considered to be fiber failures, matrix failures, and interlayer delamination failures [13-18]. However, during actual deformation and destruction the in-layer delamination is also a possible failure mode. Thus, there are seven possible failure modes for FRP laminates, including fiber tension/compression failure, matrix tension/compression failure, in-layer stretch/compression delamination failure, and interlayer failure, as shown in Fig. 1. As the basic element of laminated shell, the unidirectional FRP layer should consider the first 6 kinds of failures. A short description of these failure modes and damage evolution laws is included below.

2.3.1. Fiber tension and compression

Previous studies [15, 19] have shown that the strain was more continuous than the stress during the evolution of damage. Therefore, the Hashin criterion for fiber tension and compression are expressed in the form of strain, as shown in Eq. 9. In this equation, ε_1^i and ε_1^c are the fiber initial failure strains and can be calculated by $\varepsilon_1^i = X_t / \varepsilon_1$ and $\varepsilon_1^c = X_c / \varepsilon_1$, where X_t and X_c are respectively the fiber tensile and the compressive strength.

$$F_1^t = \left(\frac{\varepsilon_1^t}{\varepsilon_1^i} \right)^2 \geq 1, \quad F_1^c = \left(\frac{\varepsilon_1^c}{\varepsilon_1^c} \right)^2 \geq 1 \quad (9)$$

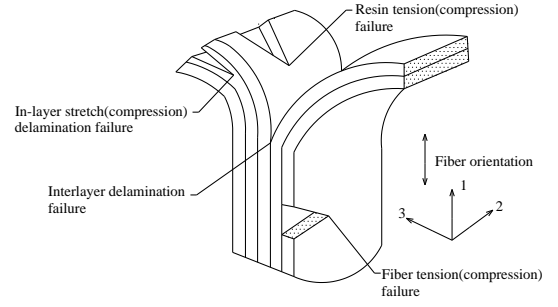


Fig. 1 The possible failure modes of a FRP shell

The damage coefficients for fiber tension and compression are shown in Eq. 10. When denote the final failure strain (ε_1^t and ε_1^c), the element characteristic length l is introduced to eliminate the mesh sensitivity problem [15-16], the expression is given by Eq. 11, where Γ_1^t and Γ_1^c are the fiber fracture energy.

$$D_1^t = \frac{\varepsilon_1^t}{\varepsilon_1^t - \varepsilon_1^i} \left(1 - \frac{\varepsilon_1^i}{\varepsilon_1} \right), \quad D_1^c = \frac{\varepsilon_1^c}{\varepsilon_1^c - \varepsilon_1^i} \left(1 - \frac{\varepsilon_1^i}{\varepsilon_1} \right) \quad (10)$$

$$\varepsilon_1^t = \frac{2\Gamma_1^t}{X_t l}, \quad \varepsilon_1^c = \frac{2\Gamma_1^c}{X_c l} \quad (11)$$

2.3.2. Matrix tension and compression

Similar to the fiber tension, the failure criterion and damage coefficient for matrix tension are shown in Eq. 12 and Eq. 13, respectively. In these two equations, ε_2^i and ε_2^t are the matrix initial and final failure strains, respectively; Y_t is the matrix tensile strength; Γ_2^t is the matrix tensile fracture energy.

$$F_2^t = \left(\frac{\varepsilon_2^t}{\varepsilon_2^i} \right)^2 \geq 1 \quad (12)$$

$$D_2^t = \frac{\varepsilon_2^t}{\varepsilon_2^t - \varepsilon_2^i} \left(1 - \frac{\varepsilon_2^i}{\varepsilon_2} \right), \quad \varepsilon_2^i = Y_t / \varepsilon_2, \quad \varepsilon_2^t = \frac{2\Gamma_2^t}{Y_t l} \quad (13)$$

Puck et al. [12] introduced a failure criterion that could consider the fracture plane due to matrix compression. Many literatures [14-17] have proved that the Puck criterion have more advantages than the Hashin criterion and the Chang-Chang criterion in discussing the matrix compression. Thus, this criterion was chosen to simulate the matrix compression; moreover, the Puck criterion was also expressed in the form of strain, as shown in Eq. 14. In this equation, θ is the angle between the fracture plane and the direction of thickness (Puck recommended the value of this angle could be 53°); $\varepsilon_n(\theta)$, $\gamma_{nt}(\theta)$ and $\gamma_{nl}(\theta)$ are the strain components on the fracture plane, as shown in Fig. 2; ϕ is the material friction angle; E_{23}^A is the transverse shear strain on the fracture plane; S_{12} is the in-plane shear strength; G_{12} is the in-plane shear modulus.

$$\begin{cases} F_2^c = \left(\frac{\gamma_{nt}(\theta)}{E_{23}^A + \mu_{nt} \varepsilon_n(\theta)} \right)^2 + \left(\frac{\gamma_{nl}(\theta)}{S_{12} / G_{12} + \mu_{nl} \varepsilon_n(\theta)} \right)^2 \\ \varepsilon_n(\theta) = \varepsilon_2 \cos^2 \theta + \varepsilon_3 \sin^2 \theta + 2\varepsilon_5 \sin \theta \cos \theta \\ \gamma_{nt}(\theta) = (\varepsilon_3 - \varepsilon_2) \sin \theta \cos \theta + \varepsilon_5 (\cos^2 \theta - \sin^2 \theta) \\ \gamma_{nl}(\theta) = \varepsilon_6 \sin \theta + \varepsilon_4 \cos \theta \\ \mu_{nt} = \tan(2\theta - 90^\circ), \quad \mu_{nl} = \frac{\mu_{nt} S_{12}}{E_{23}^A G_{12}} \\ E_{23}^A = \frac{Y_c}{2E_2^c} \left(\frac{1 - \sin \phi}{\cos \phi} \right), \quad \phi = 2\theta - 90^\circ \end{cases} \quad (14)$$

The damage coefficient of matrix compression can be calculated by Eq. 15, where γ_r^t and γ_r^c are the initial and final combined strains, respectively; $\tau_{nt}^i(\theta)$ and $\tau_{nt}^t(\theta)$ are the shear stresses on the fracture plane at a time of $F_2^c=1$; Γ_2^c is the matrix compressive fracture energy.

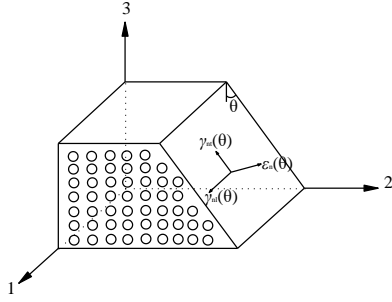


Fig. 2 The fracture plane of matrix under compression

$$\begin{cases} D_2^c = \frac{\gamma_r^f}{\gamma_r^f - \gamma_r^i} \left(1 - \frac{\gamma_r^i}{\gamma_r} \right) \\ \gamma_{nt}(\theta) = (\varepsilon_3 - \varepsilon_2) \sin \theta \cos \theta + \varepsilon_5 (\cos^2 \theta - \sin^2 \theta) \\ \gamma_{nl}(\theta) = \varepsilon_6 \sin \theta + \varepsilon_4 \cos \theta \\ \gamma_r = \sqrt{\gamma_{nt}^2(\theta) + \gamma_{nl}^2(\theta)} \\ \gamma_r^f = \frac{2\Gamma_2^c}{S_{rl}^i}, \quad S_{rl}^i = \sqrt{(\tau_{nt}^i(\theta))^2 + (\tau_{nl}^i(\theta))^2} \end{cases} \quad (15)$$

2.3.3. In-layer delamination

In order to consider the in-layer delamination, the present study defined the failure criterion and the damage coefficients for the in-layer delamination as shown in Eq. 16 and Eq. 17. In these equations, Z_t and Z_c are the tension and compression strength in the thickness direction of unidirectional laminate, respectively; ε_3^i and ε_3^f are the initial and final failure strains, respectively; ε_3^{ic} and ε_3^{fc} are the initial and final failure strains, respectively; Γ_1^t and Γ_1^c are the fracture energy in the thickness direction of unidirectional laminate.

$$F_3^t = \left(\frac{\varepsilon_3}{\varepsilon_3^i} \right)^2 \geq 1, \quad F_3^c = \left(\frac{\varepsilon_3}{\varepsilon_3^c} \right)^2 \geq 1 \quad (16)$$

$$\begin{cases} D_3^t = \frac{\varepsilon_3^f}{\varepsilon_3^f - \varepsilon_3^i} \left(1 - \frac{\varepsilon_3^i}{\varepsilon_3} \right), \quad \varepsilon_3^f = \frac{2\Gamma_1^t}{Z_t l} \\ D_3^c = \frac{\varepsilon_3^{fc}}{\varepsilon_3^{fc} - \varepsilon_3^{ic}} \left(1 - \frac{\varepsilon_3^{ic}}{\varepsilon_3} \right), \quad \varepsilon_3^{fc} = \frac{2\Gamma_1^c}{Z_c l} \end{cases} \quad (17)$$

Because the strength of matrix is much lower than fiber, the matrix in a FRP unidirectional layer is broken easier. As a result, the in-layer delamination is always caused by matrix fracture in the thickness direction; and the strength and fracture energy in this direction can be regarded approximately equal to the strength and fracture energy of matrix.

2.3.4. The stress-strain relationships after initial failure

Once the initial failure occurred, the FRP unidirectional lamina would begin to damage. The damaged stress component σ^d can be written by Eq. 18, where D_i ($i=1, 2, \dots, 6$) is the component of damage matrix \mathbf{D} and can be defined by the damage coefficients (Eq. 19). In Eq. 19, S_{mt} and S_{mc} are the parameters to control the shear stiffness loss caused by matrix tension and compression. According to the literature [13], the loss control factors are postulated as $S_{mt}=0.9$ and $S_{mc}=0.5$.

2.4. Interlaminar damage model

In actual engineering, the FRP components are always consisted of many different unidirectional layers, which mean the interlayer failure should be considered. Especially for the FRP-reinforced steel component, the interlaminar damage is caused by interface cracking (where the interface is the matrix that connects two adjacent layers, and the steel component can be seen as one layer). This failure is always simulated using a bilinear traction-separation relationship (Fig. 3) in commercial FEM software, such as the cohesive behavior in ABAQUS/Explicit [20].

$$\sigma^d = \mathbf{D} \cdot \sigma \Rightarrow \begin{pmatrix} \sigma_1^d \\ \sigma_2^d \\ \sigma_3^d \\ \sigma_4^d \\ \sigma_5^d \\ \sigma_6^d \end{pmatrix} = \begin{bmatrix} 1-D_1 & 0 & 0 & 0 & 0 & 0 \\ 0 & 1-D_2 & 0 & 0 & 0 & 0 \\ 0 & 0 & 1-D_3 & 0 & 0 & 0 \\ 0 & 0 & 0 & 1-D_4 & 0 & 0 \\ 0 & 0 & 0 & 0 & 1-D_5 & 0 \\ 0 & 0 & 0 & 0 & 0 & 1-D_6 \end{bmatrix} \begin{pmatrix} \sigma_1 \\ \sigma_2 \\ \sigma_3 \\ \sigma_4 \\ \sigma_5 \\ \sigma_6 \end{pmatrix} \quad (18)$$

$$\begin{cases} D_1 = \max(D_1^t, D_1^c) \\ D_2 = \max(D_2^t, D_2^c) \\ D_3 = \max(D_3^t, D_3^c) \\ D_4 = 1 - (1-D_1^t)(1-D_1^c)(1-S_{mt}D_2^t)(1-S_{mc}D_2^c) \\ D_5 = 1 - (1-S_{mt}D_2^t)(1-S_{mc}D_2^c)(1-S_{mt}D_3^t)(1-S_{mc}D_3^c) \\ D_6 = 1 - (1-D_1^t)(1-D_1^c)(1-S_{mt}D_3^t)(1-S_{mc}D_3^c) \end{cases} \quad (19)$$

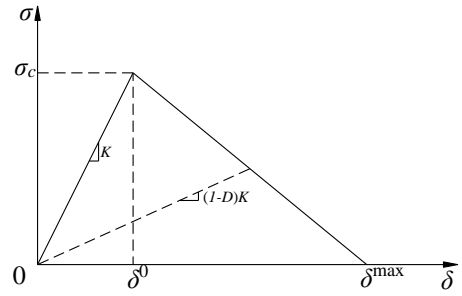


Fig. 3 The bilinear traction-separation relationship

There are three kinds of stresses on the interface (normal stress S_n , shear stress S_t , and S_l), which are defined within Eq. 20. In this equation, G_i ($i=n, t, l$) is the critical strain energy release rate, which is the area covered by the σ - δ curve.

$$\begin{cases} \int_0^{\delta_n^{\max}} S_n d\delta_n = G_n \\ \int_0^{\delta_t^{\max}} S_t d\delta_t = G_t \\ \int_0^{\delta_l^{\max}} S_l d\delta_l = G_l \end{cases} \quad (20)$$

The stress-strain relationship on the interface is represented by Eq. 21. Where K_i ($i=nn, tt, ll$) denotes the slope of Fig. 3 and D^i is the damage coefficient for interlaminar damage.

$$\begin{pmatrix} S_n \\ S_t \\ S_l \end{pmatrix} = \begin{bmatrix} (1-D^t)K_{nn} & 0 & 0 \\ 0 & (1-D^t)K_{tt} & 0 \\ 0 & 0 & (1-D^t)K_{ll} \end{bmatrix} \begin{pmatrix} \varepsilon_n \\ \varepsilon_t \\ \varepsilon_l \end{pmatrix} \quad (21)$$

The interlaminar damage process is as follows. When the interface is in elastic state ($\delta \leq \delta^0$), the value of damage coefficient D^i is 0; once it begins to damage ($\delta^0 < \delta < \delta^{\max}$), the damage evolution law is expressed in Eq. 22; finally, the interface totally fractured ($\delta \geq \delta^{\max}$), the D^i reaches a value of 1.

$$D^i = \frac{\delta_m^f (\delta_m^{\max} - \delta_m^0)}{\delta_m^{\max} (\delta_m^f - \delta_m^0)}, \quad \delta_m = \sqrt{\delta_n^2 + \delta_t^2 + \delta_l^2} \quad (22)$$

In Eq. 22, δ_m^f is the mixed-mode displacement, which is defined by the Benzeggagh-Kenane fracture criterion [21] (as shown in Eq. 23, where ξ and η are the Benzeggagh-Kenane law parameters).

$$\delta_m^f = \begin{cases} \frac{2}{K\delta_m^0} [G_{IC} + (G_{IC} - G_{IC})\xi^\eta] & \delta_n > 0 \\ \sqrt{(\delta_r^f)^2 + (\delta_l^f)^2} & \delta_n \leq 0 \end{cases} \quad (23)$$

3. Simulation method

3.1. Axial low-velocity impact tests

A series of impact tests were developed to verify the simulations. The specimen was manufactured through a filament winding process (Fig. 4), and had a GFRP enhancement layer (S2-1200 glass fiber reinforced E-51 epoxy resin) and a circular Q235 steel tube base layer (Fig. 5). A total of 6 conditions were discussed in the tests, as shown in Table 1; moreover, 58-1.5-30-3 was replicated thrice to verify the stability of tests.

The tests were conducted on a drop hammer test system, as shown in Fig. 6. During the test process, the specimen was anchored in a 60 mm deep steel groove using high strength gypsum; besides, the impact force was obtained by a piezoelectric force transducer; and a magnet-grid linear displacement system was used to measure the displacement of hammer. Additionally, a high-speed camera (Fig. 7) was used to record the axial impact process.



Fig. 4 The filament winding process

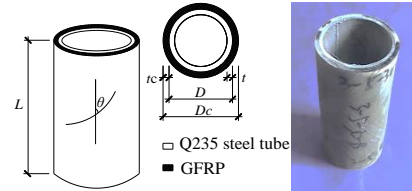


Fig. 5 A detail of the specimens tested

Table 1

Descriptions of the specimens tested

Label	D/mm	t/mm	$[\theta]_n$	D_c /mm	t_c /mm	L/mm	V/m/s
58-1.5-30-3	58.0	1.5	$[30/-30]_3$	62.0	2.0	100.0	3.0
58-1.5-90-3	58.0	1.5	$[90]_9$	62.0	2.0	100.0	3.0
58-1.5-30-4.5	58.0	1.5	$[30/-30]_3$	62.0	2.0	100.0	4.5
58-1.5-45-4.5	58.0	1.5	$[45/-45]_3$	62.0	2.0	100.0	4.5
58-1.5-90-4.5	58.0	1.5	$[90]_9$	62.0	2.0	100.0	4.5

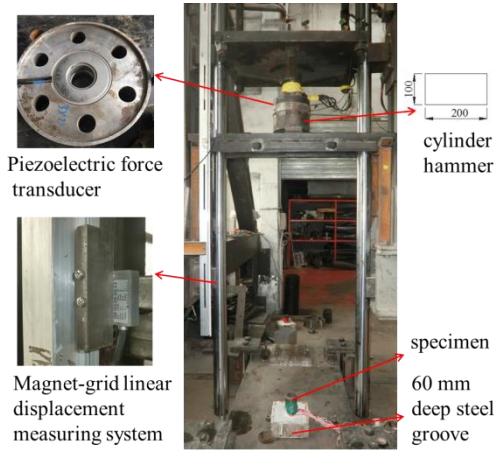


Fig. 6 The drop hammer test system



Fig. 7 High-speed camera

(b)), energy dissipation (the cover area of load-displacement curve, as shown in Fig. 8 (c)), and damage modes (as shown in Fig. 8 (d)). In conclusion, the results of the parallel samples were easily reproducible, and hence the test results obtained from the drop hammer test system were credible.

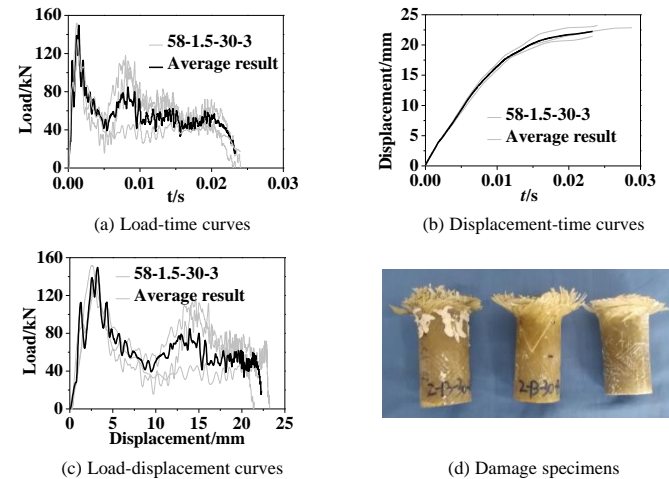


Fig. 8 Repeated test results of 58-1.5-30-3

3.2. Finite element model

ABAQUS 6.11/Explicit was chosen to develop the simulation works. Each layer was modeled separately (for both FRP layers and steel layers), such that the damage development in each individual layer could be simulated. In the thickness direction of each layer there was one element, including the C3D8R (8-node linear brick, reduced integration, hourglass control [20]) for FRP plies and C3D8I (8-node linear brick, incompatible modes [20]) for steel ply. The drop hammer was modeled by C3D10M (10-node modified quadratic tetrahedron [20]). The bottom of the specimen was completely clamped to the support, while its top was left free. The impact load was applied to the specimen through the drop hammer's mass and initial velocity. The finite

The three repeated test results of 58-1.5-30-3 were shown in Fig. 8. The results were compared from 4 aspects: impact load (load-time curve, as shown in Fig. 8 (a)), axial displacement (displacement-time curve, as shown in Fig. 8

element model is shown in Fig. 9.

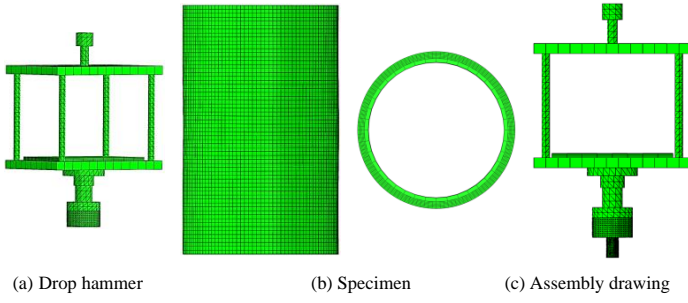


Fig. 9 The finite element model

3.3. Material parameters

The steel layer was simulated by the J-C constitutive model provided by ABAQUS. Its quasi-static material properties were obtained using uniaxial tensile tests, where the results for these tests are shown in Table 2. And the

Table 3
Parameters of the Johnson-Cook model and fracture criterion [7]

A/MPa	B/MPa	n	m	T_m/K	T_r/K	D1	D2	D3	D4	D5	$\dot{\epsilon}_0 /s^{-1}$
272.28	899.7	0.94	0.1515	1795	293	-43.408	44.608	0.016	0.0145	-0.046	0.000833

Table 4
Material properties of GFRP unidirectional laminate materials [22]

Parameters	Value
Modulus/GPa	$E_1=41.29$; $E_2=E_3=4.21$; $G_{12}=G_{13}=3.16$; $G_{23}=3.0$
Poisson's ratio	$\nu_{12}=\nu_{13}=0.31$; $\nu_{23}=0.42$
Strength/MPa	$X_t=884.5$; $X_c=837.17$; $Y_t=Z_t=37.38$; $Y_c=Z_c=145$; $S_{12}=S_{13}=44.765$; $S_{23}=50.88$
Fracture energy/(N/mm)	$\Gamma_1^t = 28.25$; $\Gamma_1^c = 80.1$; $\Gamma_2^t = \Gamma_3^t = 0.36$; $\Gamma_2^c = \Gamma_3^c = 7.24$

Table 5
Cohesive behavior parameters [22]

Parameters	Value
Elastic properties/GPa	$K_{nn}=4210$; $K_{tt}=3160$; $K_{ll}=3160$
Strength/MPa	$T_n=37.38$; $T_t=44.765$; $T_l=44.765$
Fracture toughness/(N/mm)	$G_n=0.36$; $G_t=1.33$; $G_l=1.33$
Mode interaction-BK	$\eta=2.6$

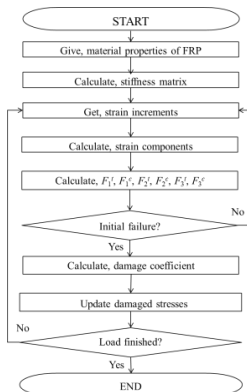


Fig. 10 Computational algorithm of the VUMAT subroutine

The drop hammer was assumed to keep elastic during the impact process. Its material properties were defined as $E=217\text{GPa}$, $\nu=0.3$. The contact between

parameters for J-C model were determined according to the previous study [7], as shown in Table 3.

Table 2
Mechanical properties of the steel tubes [22]

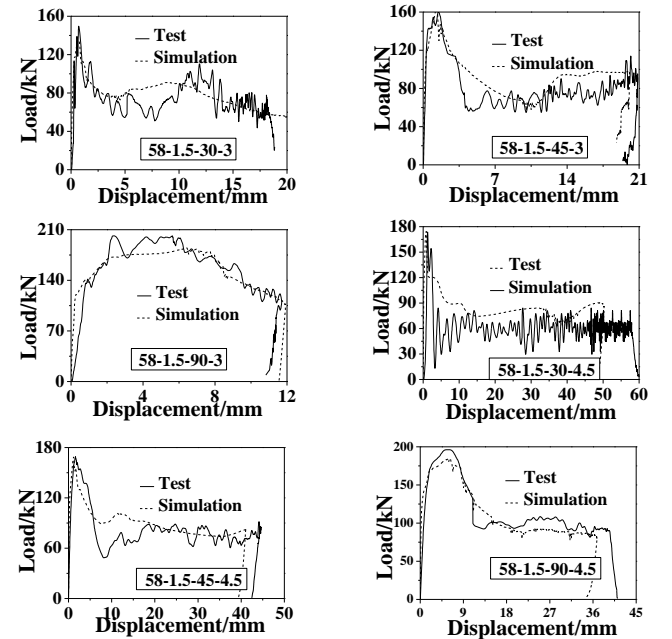
t/mm	σ_y/MPa	σ_u/MPa	$\epsilon_y/\mu\epsilon$	$\epsilon_u/\mu\epsilon$	E/GPa
1.5/2.0	272.28	410.64	1991	240000	208

As for FRP a VUMAT subroutine based on the mechanics of composite material was developed. The subroutine can consider the 6 initial failure modes and damage evolutions of FRP unidirectional laminate, its computational algorithm is shown in Fig. 10. Because GFRP is anisotropic, its properties were obtained by tensile tests (longitudinal and transverse), compression tests (longitudinal and transverse), interlayer shear-strength tests, in-plane shear tests, and debonding test. The properties of S2-1200 glass fiber/E-51 epoxy unidirectional laminate are shown in Table 4 [22]. Moreover, the interfaces between steel layer and GFRP layer, or between GFRP layers, were simulated by the cohesive behavior provided by ABAQUS, where these cohesive parameters are shown in Table 5 [22].

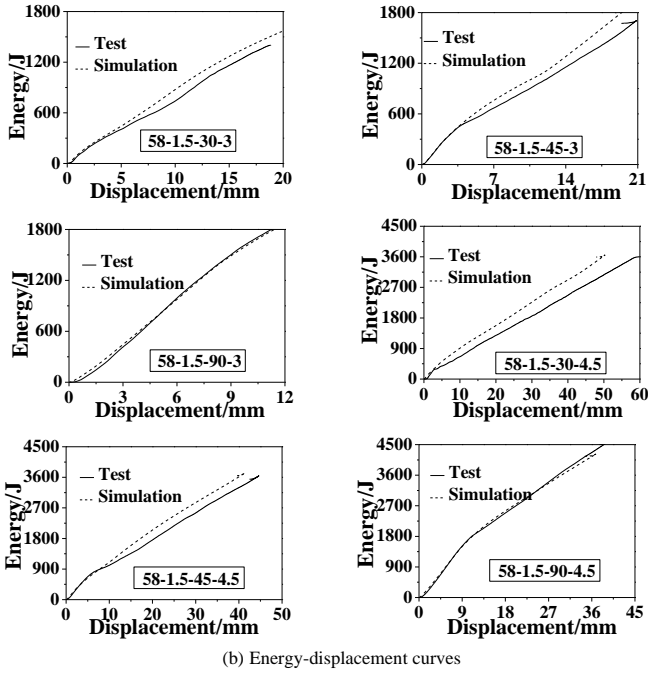
the drop hammer and FSC was simulated using the penalty method; according to Perillo's study [23], an average friction coefficient of $\mu=0.3$ was appropriate.

3.4. Verification of the simulation method

The measured results including load-displacement curves and energy-displacement curves were compared with simulations, as shown in Fig. 11. Compared to the simulations the load-displacement curves obtained from the tests exhibited larger vibrations, this was because the drop hammer would vibrate during axial impact process. Besides, the specimens in the impact tests inevitably had some initial imperfections; however, these imperfections were ignored in the finite element simulation to simplify the analysis, so that the simulations were a little larger than the test results. Even so, the simulations still have a good agreement with the test results.

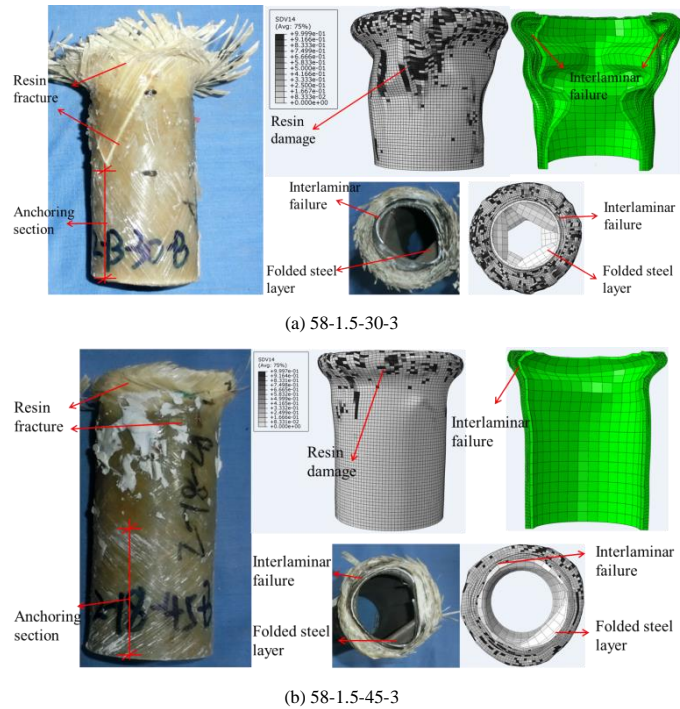


(a) Load-displacement curves

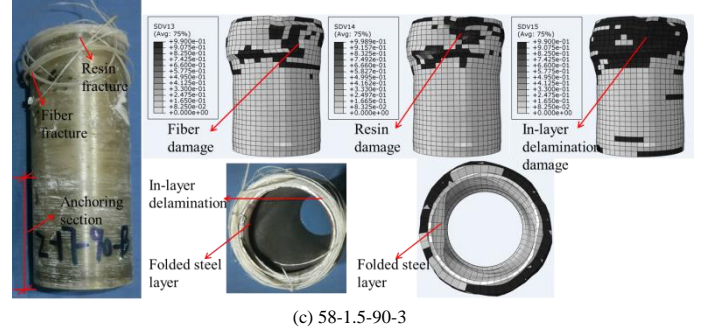


(b) Energy-displacement curves
Fig. 11 Compared between experimental and simulated results

Take the specimens with impact velocity 3 m/s for example. Fig. 12 shows a comparison of damage modes between the tests and the simulations. Moreover, Fig. 13 detailedly compares the impact process of 58-1.5-45-4.5. The axial low-velocity impact process can be divided into two stages: elastic stage and energy dissipation stage. During the elastic stage GFRP and steel were in an elastic state, where the sample kept vertical and its midspan expanded along the radial direction (0–0.001 seconds for the test, and 0–0.000825 seconds for the simulation). After this, the specimen entered an energy dissipation stage until the end of the first impact process (0.001–0.0295 s for the test, and 0.000825–0.0292 s for the simulation). During this stage, the steel tube dissipated energy through plastic deformation, and the FRP dissipated energy through both fiber and resin failure and delamination damage. According to the comparison, the simulated damage modes and impact process matched the tests well.

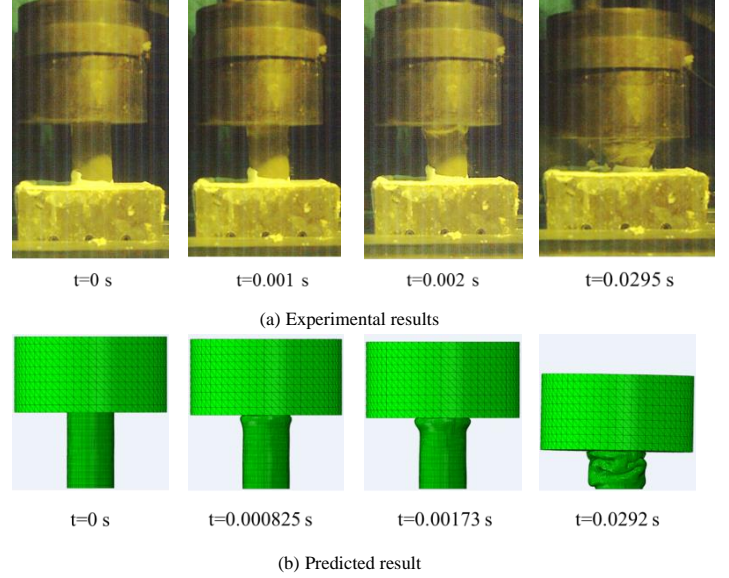


(b) 58-1.5-45-3



(c) 58-1.5-90-3

Fig. 12 Comparing damage between predicted and tested samples



(b) Predicted result
Fig. 13 Compared damage process of 58-1.5-45-4.5 between predicted and experimental

4. Comparison between common failure criteria and VUMAT

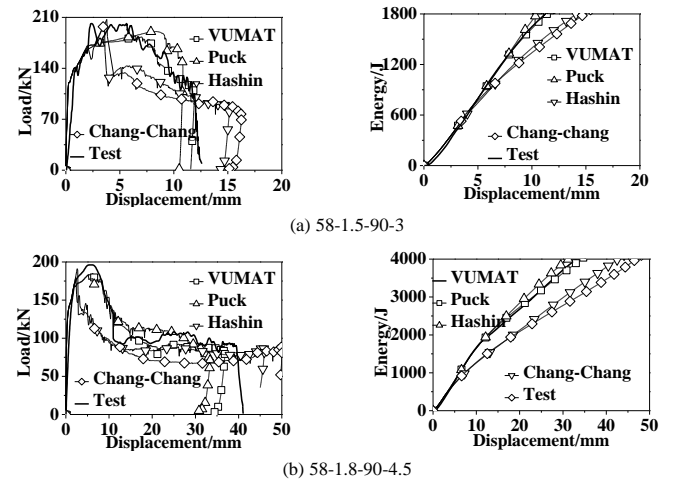


Fig. 14 Results of 58-1.5-90-3 and 58-1.8-90-4.5 using different failure criteria

To show the advantages of the proposed VUMAT subroutine, 58-1.5-90-3 and 58-1.5-90-4.5 were simulated using the Puck criterion, the Hashin criterion, the Chang-Chang criterion, and the VUMAT subroutine (where the steel tube used the J-C model). Results of this comparison are shown in Fig. 14. Because of considering the influence of fracture plane, the results from the Puck criterion and the VUMAT subroutine were better than them from the Hashin criterion and the Chang-Chang criterion. To be specific, the curves from the Hashin criterion and the Chang-Chang criterion had a sharper decrease in the load-descending phase, and their shapes are thinner than the experimental results (Fig. 14 (a) and (c)); additionally, the energy-dissipation simulated by these two criteria was distinctly lower than the experimental results (Fig. 14 (b) and (d)).

There was relatively good agreement among the results for the Puck criterion, the VUMAT subroutine, and the experimental results when the impact energy was 1800.9 J or 4052.025 J (Fig. 14); however, since the Puck criterion did not consider the in-layer delamination, its results were a little higher than the results for either the VUMAT subroutine or the experimental results. This tendency was more distinct when the impact energy increased, as shown in Fig. 15 (where data in Fig. 15 were obtained via simulation).

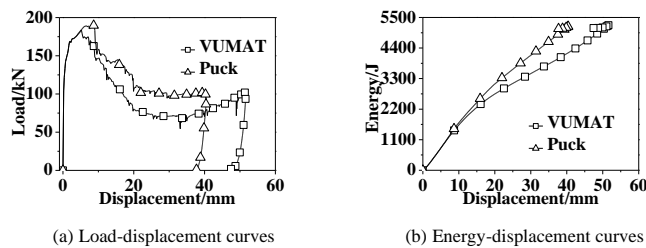


Fig. 15 Results from samples 58-1.5-90-5.5 using the Puck criterion and the VUMAT

This paper proposed a method to simulate the low-velocity impact process of FRP-reinforced steel component. This method used the J-C model to simulate the steel component, and developed a VUMAT subroutine to analyze the initial failures and damage evolution of FRP. Different from the common FRP failure criteria, the proposed subroutine considered not only the fiber tension/compression failure and the matrix tension/compression failure, but the in-layer stretch/compression delamination failure. Moreover, when initial failure occurred, the progressive damage evolution law based on strain was applied in the subroutine.

Axial low-velocity impact tests were developed on GFRP-reinforced circular steel tubes to verify the simulations. This comparative study confirmed that the simulations agreed well with experimental tests not only for load-displacement curves, but also for damage modes. Additionally, a comparison among the Puck criterion, the Hashin criterion, the Chang-Chang criterion and the VUMAT subroutine indicated that the proposed simulation method can simulate the FSC better.

Acknowledgements

The financial support of Chinese National Natural Science Foundation (Grant No. 51478144 and No. 51778183) is gratefully acknowledged.

5. Conclusions

References

- [1] Siromani D., Henderson G., Mikita D., et al. "An experimental study on the effect of failure trigger mechanisms on the energy absorption capability of CFRP tubes under axial compression", *Composites: Part A*, 64, 25-35, 2014.
- [2] Song H.W., Wan Z.M., Xie Z.M. and Du X.W., "Axial impact behavior and energy absorption efficiency of composite wrapped metal tubes", *International Journal of Impact Engineering*, 24, 385-401, 2000.
- [3] Bambach, M.R., "Axial capacity and crushing of thin-walled metal, fibre-epoxy and composite metal-fibre tubes", *Thin-walled structures*, 48, 440-452, 2010.
- [4] Harries Kent A., Peck Andrew J. and Abraham Elizabeth J., "Enhancing stability of structural steel sections using FRP", *Thin-walled structures*, 47, 1092-1101, 2009.
- [5] Johnson G.R. and Cook W.H., "A Constitutive Model and Data for Metals Subjected to Large Strains, High Strain Rates and High Temperatures", *Proceedings of the seventh international symposium on ballistics*, 541-7, 1983.
- [6] Johnson G.R. and Cook W.H., "Fracture characteristics of three metals subjected to various strains, strain rates, temperatures and pressures", *Eng. Fract. Mech.*, 21, 31-48, 1985.
- [7] Lin L., Fan F. and Zhi X.D., "Dynamic constitutive relation and fracture model of Q235A steel", *Appl. Mech. Mater.*, 274, 463-6, 2013.
- [8] Senthil K., Iqbal M.A., Chandel P.S., et al., "Study of the Constitutive Behavior of 7075-T651 Aluminum Alloy", *Int. J. Impact Eng.*, 108, 171-90, 2017.
- [9] Wang X. and Shi J., "Validation of Johnson-Cook plasticity and damage model using impact experiment", *Int. J. Impact Eng.*, 60, 67-75, 2013.
- [10] Hashin Z., "Failure criterion for unidirectional fiber composite", *J. Appl. Mech.*, 47, 329-34, 1980.
- [11] Chang F.K. and Chang K.Y., "A progressive damage model for laminated composites containing stress concentrations", *J. Compos. Mater.*, 21(2), 834-55, 1987.
- [12] Puck A. and Schürmann H., "Failure analysis of FRP laminates by means of physically based phenomenological models", *Compos. Sci. Technol.*, 42, 1633-62, 2002.
- [13] Lee C.S., Kim J.H., Kim S.K., et al., "Initial and progressive failure analyses for composite laminates using Puck failure criterion and damage-coupled finite element method. *Composite Structures*", 121, 406-419, 2015.
- [14] Singh H., Mahajan P. and Namala K.K., "A Progressive Failure Study of E-glass Epoxy Composite in Case of Low Velocity Impact", *Advances in Structural Engineering*, 273-300, 2015.
- [15] Liu P.F., Liao B.B., Jia L.Y., et al. "Finite element analysis of dynamic progressive failure of carbon fiber composite laminates under low velocity impact", *Composite Structures*, 149, 408-422, 2016.
- [16] Liao B.B. and Liu P.F., "Finite element analysis of dynamic progressive failure of plastic composite laminates under low velocity impact", *Composite Structures*, 159, 567-578, 2017.
- [17] Shi Y., Swait T. and Soutis C., "Modelling damage evolution in composite laminates subjected to low velocity impact", *Composite Structures*, 94, 2902-2913, 2012.
- [18] Singh H., Namala K.K. and Mahajan P.A. "Damage evolution study of E-glass/epoxy composite under low velocity impact", *Composites: Part B*, 76, 235-248, 2015.
- [19] Huang C.H. and Lee Y.J., "Experiments and simulation of the static contact crush of composite laminated plates", *Composite Structures*, 61, 265-70, 2003.
- [20] ABAQUS I. ABAQUS 6.11 User's manual, 2011.
- [21] Camanho P.P. and Davila C.G., "Mixed-mode decohesion finite elements for the simulation of delamination in composite materials", *Tech Rep NASA/TM-2002-211737*, 2002.
- [22] Zhi X.D., Wu Q.J. and Wang C., "Experimental and numerical study of GFRP-reinforced steel tube under axial impact loads", *International Journal of Impact Engineering*, 122, 23-37, 2018.
- [23] Perillo, G., Vedicik, N.P. and Echtermeyer, A.T., "Damage development in stitch bonded GFRP composite plates under low velocity impact: Experimental and numerical results", *Composite materials*, 49(5), 601-615 2015.

DESIGN OPTIMIZATION OF TUBULAR LATTICE GIRDERS

Tugrul Talaslioglu

Department of Civil Engineering, Osmaniye Korkut Ata University, 80000, Osmaniye, Turkey

* (Corresponding author: E-mail: ttalaslioglu@osmaniye.edu.tr, talaslioglu@cu.edu.tr)

ABSTRACT

The lattice girder, members of which are constructed by use of ready profiles with tubular cross-sections, has a simple but an effective structural framing form. In this regard, this study proposes to optimize the design of tubular lattice girders in a way of minimizing its entire weight and joint displacement and maximizing its load-carrying capacity considering the design codes of API RP2A-LRFD. As an optimization tool, a multi-objective optimization methodology named pareto archived genetic algorithm (PAGA) was utilized. The search capability of PAGA was improved by involving a designer module for automatically creation of a lattice girder form. The improved PAGA has a big responsibility of increasing the convergence degree of optimal designs against the stability problem. Furthermore, the content of this study is enriched by evaluating the computing efficiency of PAGA with respect to several multi-objective optimization algorithms. Consequently, the improved PAGA achieves to explore the optimal lattice girder designs with the higher convergence, diversity and capacity degrees. Therefore, the proposed optimum lattice girder design tool is recommended for the designers due to its capability of obtaining a wide range of promising designs.

ARTICLE HISTORY

Received: 21 November 2017
Revised: 9 January 2019
Accepted: 31 March 2019

KEYWORDS

Multi-objective optimization;
Tubular lattice girder;
Pareto dominance;
Genetic algorithm;

Copyright © 2019 by The Hong Kong Institute of Steel Construction. All rights reserved.

1. Introduction

A lattice girder is constructed through connecting a number of diagonal, longitudinal and horizontal structural members. The lattice girder have a big advantages over the other structural framing forms (configurations) due to: *i*) its ability of spanning the long distances without requiring either any intermediate support or an extra height as in the dome structure *ii*) its flexibility of having an option of using a steel manufacturing factory, *iii*) its capacity of easily disassembling and reassembling, *iv*) its capability of altering their current appearance with the different framing configurations. These significant features lead to a decrease in the manufacturing, building, shipping, and maintaining costs of lattice girder. Therefore, the lattice girders are preferably utilized in a number of structural systems (roofs, bridge, cranes etc.) (Nageim & Macginley [1], Talaslioglu [2]).

Particularly, the development in the steel-related technology accelerates to elevate the variety in the available steel profiles. In fact, this development also leads to a big differentiation in the current framing configuration of lattice girder. Thus, the possibility of making a further decrease in the constructional cost of lattice girder correspondingly increases. Moreover, in order to gain an extra economic profit in the construction of the tubular lattice girder, it is suggested that an optimization tool to be involved into the design stage is the best way. As an optimization tool, the evolutionary algorithms (EAs) have already been utilized for the weight minimization of various structures (Hasancebi and *et al.* [3]; Saka [4], Seyedpoor and *et al.* [5]).

A generational optimal design approach for steel structures has still been utilized by a number of designers. According to the generational optimal design approach for the tubular lattice girder, a designer firstly determines the shape of lattice girder for a certain spanning length and topology. Then, the size of lattice girder members is optimized using only a single objective function, for example the constructional cost of tubular structure. Thus, the entire weight of tubular structure is minimized to obtain a further economic design. The design constraints are assigned to check the strengths of the lattice girder members according to an allowable member stress and/or joint displacement value (Cagnina and *et al.* [6]; Chen & Huang [7]; Lu and *et al.* [8]; Torii and *et al.* [9]). However, it has to be taken into account of being governed the strength of members by a number of coupled strength-related criteria (Beer and *et al.* [10]). Therefore, the best way is to include the provisions of a national or international design specification into the design stage in order to increase the design reliability of lattice girder (Talaslioglu [11]).

Furthermore, the proposed optimal design approach must take the responsibility of not only decreasing the entire weight of lattice girder for an economic constructional cost, but also achieving to provide an increased load-carrying capacity along with a higher serviceability for the design of lattice girders (Talaslioglu [11]).

Thus, the generational optimal design approach with a single-objective function becomes unfortunately to be insufficient in case of optimizing the design of lattice girder considering its load-carrying capacity, serviceability and weight at the same time. In order to deal with this design problem, the most

appropriate remedy is to integrate a multi-objective optimization procedure with the proposed design approach. Thus, the designer has also an opportunity to make a trade-off analysis among the multiple objective function values. Fortunately, EAs are also proved to be the perfect optimization tools with multiple objectives (Talaslioglu [11], Salajegheh and *et al.* [12]).

A general multi-objective optimization problem is formulated as:

$$\min \text{ and / or } \max F(X) = \{f_1(X), f_2(X), \dots, f_K(X)\} \quad (1)$$

K objective functions are defined depending on a *design (decision) variable set* X , each which is a member of *design variable space* DS . When a multi-objective optimization algorithm (MOA) is executed, a set of random solutions is generated. Several solutions are *dominated* with respect to the other remaining ones ($f_i(X) \leq f_i(X^*)$ and $f_j(X) \neq f_j(X^*)$, $\forall i \in \{1, \dots, K\}$) (Srinivas & Deb [13]). The dominated optimal solutions are defined as *pareto solution*. The state of *pareto dominance* is formulated in DS as:

$$P^* = \left\{ f_i(X) \leq f_i(X^*), \forall i \in \{1, \dots, K\} \text{ and } \forall X \in DS : \begin{cases} g_n(X^*) \leq 0, & n = (1, \dots, N) \\ h_m(X^*) = 0, & m = (1, \dots, M) \end{cases} \right\} \quad (2)$$

The combination of pareto solutions makes a form named *Pareto front*:

$$PF^* = \{F(X), X \in P^*\} \quad (3)$$

The pareto front is updated throughout the search of MOA. If a new dominant pareto solution is never obtained for the *current pareto front*, then the current pareto front is defined as *true pareto front*. In fact, the current and true pareto front has a big importance for not only the trade-off analysis but also a performance comparison of MOAs.

Although evaluating the computing performance of any optimization algorithm with a single objective is carried out by only assessing the quality of optimal solution, it is difficult for the multi-objective optimization algorithm due to the number of objective functions. In order to evaluate the computing efficiencies of employed MOAs, the several performance metrics named *capacity*, *density*, *convergence-diversity*, *coverage* are utilized. These performance metrics utilized in this study are also called as “unary metrics”, the working mechanisms of which are governed by the predetermined approximation sets (Zitzler and *et al.* [14]). The predetermined approximate sets are generated using the current and true pareto fronts.

The measuring metric named “capacity” informs us about the number of current pareto solutions. Particularly, this quantity metric has a big importance for the optimal engineering design problems since the designer mostly desires to make a trade-off analysis considering pareto solutions. Therefore, the larger

size of pareto solutions becomes a big advantage for the designer. The density metric “average distance” is utilized to measure the density degree of current pareto solutions in a way of computing the average value of deviation between Euclidian distance and average Euclidian distance values among current pareto solutions. The lowest average distance value indicates about a higher density degree. The other two diversity metrics “epsilon” and “spread” also measure the diversity in a way of computing the maximum distance and covering degrees of current pareto solutions with respect to true pareto fronts, respectively (Zitzler and *et al.* [14], Wu and Azarm [15], Deb and *et al.* [16], Veldhuizen and Lamont [17]). In fact, the quantity metric “epsilon” is also utilized to indicate about the pure convergence degree since its minimum value shows about being covered the entire region of true pareto front by the current pareto front. This quantity metric is computed using both Euclidian and average Euclidian distances among the current pareto solutions along with true pareto fronts. In order to measure the volume of current pareto solutions with respect to the true pareto fronts, the quantity metric “R2” is utilized (Hansen and Jaszkiewicz, [18]). In fact, R2 indicator has a responsibility for determining both convergence and diversity degree of current pareto solutions in a way of utilizing two extreme data points named “nadir” (maximum point) and “ideal” (minimum point) along with a utility function named “weights” for obtaining the equally scattered solutions on a certain range. It is noted that R2 indicator, which is computed depending on the use of utility function and data of current pareto fronts, is a member of R family. Thus, the value of R2 indicator is obtained as an average value of differences between the maximum values of current data and utility functions. Whereas Matlab scripts of quality indicators R2 and epsilon are available in Reference (Wagner & Kretschmar [19-20]), the average distance and spread indicators are embedded in the Matlab scripts named “distanceAndSpread.m” (see the further details in Matlab [21]).

This study proposes to optimize the design of tubular lattice girder considering its load-carrying capacity, serviceability and entire weight. The design optimization of lattice girder is carried out using a multi-objective optimization tool, named “pareto archived genetic algorithm (PAGA)”. PAGA developed by Author has been also utilized to optimize the design of dome structures considering the nonlinear structural behavior (Talaslioglu [22]). In this study, the exploration capacity of PAGA for the optimization of lattice girder design is enhanced through a designer module for automatically creation of a lattice girder configuration. While the shape and topology of lattice girder is automatically arranged, its size is accordingly chosen among the available steel profiles. The computing efficiency of PAGA is assessed through not only the tubular lattice girder designs, but also three MOAs named NSGAI, EVMOGA and SMSEMOA considering the performance metrics named capacity, density, convergence-diversity and coverage.

In this regard, the outline of this study begins by introducing the working mechanism of proposed evolutionary-based multi-objective optimization methodology “PAGA” and its integration with design of tubular lattice girder in section 2 and 3, respectively. Then, the results outcome from the application of employed MOAs for a tubular lattice girder with various spans and loading situations along with several benchmark examples are discussed in section 4. The summarization of results is given in the conclusion section.

2. The Working Mechanism of Proposed Evolutionary-Based Multi-Objective Optimization Methodology: Pareto Archived Genetic Algorithm (PAGA)

It is mentioned that EAs are also perfect optimization tools for the multi-objective optimization problems. EAs belongs to the evolutionary-based field in the area of artificial intelligent (Yang [23]). In fact, the fundamentals of EAS are completely constituted on the Darwinian’s evolutionary theory. The evolutionary theory contains the basic biological issues: breeding suitable *individuals* of population, propagating the valuable *genetic material*, which are coded in *chromosomes*, into next *generations*, eliminating the unsuitable one and finally surviving the *individuals* with a higher *fitness*. The concept of *fitness* informs us about the adaptation degree of individuals to both nature and life under an environmental pressure. In this regard, EAs mimics the working mechanism of biological evolution by means of *genetic operators*. The quality of fitness is easily computed by using a *fitness function* and utilized in the management of genetic-based processes. Thus, the evolutionary based computation begins by initiating a *population*. Then, the genetic operators are employed to process the genetic material embedded in the initial population considering the *fitness values* which is computed by fitness function. The genetic material inherited from the initial population is also utilized to generate the new populations. The generation of populations is generally terminated when a pre-defined *maximum generation number* is completed. The evolutionary-based loop is resulted by a number of pareto solutions. In this regard, the closeness, diversity and spread degrees of its current pareto front

with respect to a true pareto front are the most important criteria in order to evaluate the computing efficiency of MOAs. In fact, these quality measuring metrics are also utilized to develop or improve the new multi-objective evolutionary algorithms (MEAs) (Reed and *et al.* [24]; Metaxiotis & Liagkouras [25]; Richardson and *et al.* [26]). Some promising approaches are developed as: *i*) aggregation of fitness values (Aggregation Method (Srinivas & Deb [13]; Hwang & Masud [27]), Weighted Metrics (Miettinen [28]), Goal Programming (Charnes & Cooper [29]) etc...), *ii*) dominance of fitness values (NSGAI (Deb and *et al.* [30]), SPEA2 (Zitzler and *et al.* [31]) etc. (see further details about the other similar approaches in (Talaslioglu [32]), *iii*) quantitative-based assessment of fitness values (IBEA (Zitzler and *et al.* [33]), ESP (Huband and *et al.* [34]) etc.). Especially, non-dominated sorting genetic algorithm II (NSGAI) (Deb and *et al.* [30]) achieve to gain more attention from the scientific research audience (Talaslioglu [11, 35]). The hybridized variants of MOAs have been also developed. Particularly, two recently developed MOAs are e-dominance based MOA (EVMOGA) (Martínez and *et al.* [36]) and hyper-volume dominance-based MOA (SMSEMOA) (Beume and *et al.* [37-38]).

One of MEAs, Genetic Algorithm (GA) achieves to take more attention from different engineering fields due to its simple but effective search mechanism (Yang [23]). However, one of the difficulties in the evolutionary-based multi-objective optimization procedure is generally concerned with determining an optimal solution with higher quality in a way of simultaneously using the multi-objective functions. Although it is known that the valuable genetic material is embedded to the pareto solutions, how to propagate this genetic material to next generations is not known. At this point, the fundamentals of PAGA are constituted on the transmission of pareto solutions to the next populations through pareto-inseminated populations (see the pseudo code of PAGA in Fig. 1). PAGA is managed by four different sub-populations Spop1, Spop2, Spop3 and Spop4, which are obtained thereby dividing the entire population sub-populations by a division number *div_num*. In this regard, an evolutionary search proposed by PAGA begins to randomly generate these four sub-populations. Then, fitness values (f_1 , f_2 , etc.) and pareto solutions (*pareto_OF_ALL*) are correspondingly computed and determined, respectively. The limit values of objective functions stored in the pareto solutions *max_pareto_OF1_ALL*, *max_pareto_OF2_ALL* and etc. are determined and utilized to compute the size of sub-populations *PS1*, *PS2*, *PS3*, and *PS4* along with *div_num*. Then, the sub-populations sizes are determined. The crossover and mutation operations, the parameter values of which are adjusted depending on sub-generations numbers (*subGN1*, *subGN2*), are utilized to operate the genetic material in the sub-populations *Spop1*, *Spop2*, *Spop3* and *Spop4*. After the fitness values of sub-populations *Spop1*, *Spop2*, *Spop3* and *Spop4* are computed, the pareto solutions are determined. In the last stage, the bounds of individuals located in the each of sub-populations are checked according to the *maxDV* and *minDV*. This main loop is terminated once the maximum generation number is completed. The further details about working principle of PAGA are presented in Reference Talaslioglu [22].

3. The Integration of PAGA with Design of Tubular Lattice Girder

The design optimization of tubular lattice girder is carried out by both minimizing its entire weight, f_1 (m , number of lattice girder members; w , unit weight per member length) and its joint displacements, f_2 (n , number of nodes; i , number of freedom) and maximizing its member forces, f_3 (see Eqn. (1-3)) considering design constraints obtained by use of member-related provisions.

The proposed design constraints are converted into the two ratios for the member-related design constraints and joint displacements. While one of these ratios named *UnityMem* is obtained by dividing the current strength of dome member to the allowable nominal strength, the other ratio named *UnityDisp* is computed by dividing the maximum value of current joint displacement to the predefined value. In order to penalize the unfeasible designs, a penalizing function is accordingly utilized to compute a penalizing value. The penalizing value is added to the fitness value. It is noted that the same penalizing process with an alteration of design constraints is also proposed for the optimization of benchmark design examples.

$$f_1 = \min\left(\sum_{k=1}^m (wL)_k + Pen_1\right) \quad (4)$$

$$f_2 = \min(d_{ij} + Pen_2) \quad (i=1,...,12 \text{ and } j=1,...,n) \quad (5)$$

$$f_3 = \max(f_{ij} + Pen_3) \quad (i=1,...,12 \text{ and } j=1,...,n) \quad (6)$$

Where,

$$\begin{aligned}
Pen_1 &= \left(\sum_{k=1}^m (wD)_k \right) \left(\frac{CGN}{MGN} \right)^{P_{Mem} + P_{Disp}} \\
Pen_2 &= \min(d_{ij}) \left(\frac{CGN}{MGN} \right)^{P_{Mem} + P_{Disp}} \\
Pen_3 &= \max(f_{ij}) \left(\frac{CGN}{MGN} \right)^{P_{Mem} + P_{Disp}}
\end{aligned}
\quad
\begin{cases}
P_{Mem} = \sum_{k=1}^m p_k, \{p_k = 1 \text{ if } Member_Strength_Contrains \geq 1 \\
P_{Disp} = \sum_{j=1}^{12} \sum_{i=1}^{12} p_{ij}, \{p_{ij} = 1 \text{ if } Unity_{Disp}^{ij} \geq 1 \\
Pen_1 = 0 \text{ and } Pen_3 = 0 \text{ if } Member_Strength_Contrains < 1 \\
Pen_2 = 0 \text{ if } Unity_{Disp}^{ij} < 1
\end{cases} \quad (7)$$

$$Member_Strength_Contrains = \begin{cases} Unity_{Axial}^k, Unity_{Bending}^k, Unity_{CombinedBending}^k, Unity_{Shear}^k \\ Unity_{Torsion}^k, Unity_{AxialCompr \& BendingBuck}^k, Unity_{Axial \& BendingYield}^k \end{cases} \quad (8)$$

In Eq. 5, penalizing process is managed by two parameters: *current generation number* CGN and *maximum generation number* MGN. The formulations of design constraints in Eq. 5 are given in References (Talaslioglu [11]).

In order to improve the search capability of PAGA, a designer module is included to automatically create a lattice girder configuration (see a pseudo code for an automatically generation of lattice girder in Fig. 2). Thus, it is possible to generate various framing configurations using the design variables (size, topology and shape). The cross-sectional properties which represents the design variables (size) $D1, D2, D3$ and $D4$ are chosen from 37 available tubular cross-sections (see Fig. 3). The limit values of these design variables Par_{UDV} and Par_{LDV} are taken as 37 and 1. The other design variable (topology) is managed

by the division number Par_{DN} in order to form the tubular lattice girder with small nesting parts. The limit values of this design variables Par_{DN} are indicated by Par_{DNU} and Par_{DNL} . Furthermore, the other topology-related design variable Par_{CTop} is also utilized to represent each nesting part of tubular lattice girder named "Cell". The brace members manage the topology of cell. Therefore, the topologic configuration of each cell is represented by four different numbers: 1 for no bracing, 2 for left-sided bracing (\backslash), 3 for right-sided bracing ($/$) and 4 for double bracing (X). The last design variable (shape) is managed by the first and middle heights of tubular lattice girder H1 and H2 due to the symmetrically adjusted by the designer module and indicated by Par_{H1} and Par_{H2} . The limit values of shape-related design variables are indicated by the parameters Par_{H1U} , Par_{H1L} , Par_{H2U} and Par_{H2L} . Thus, these design parameters are stored in a matrix named "Chrom" ("Chromosome"), which contains the design variables Par_{DN} , Par_{CTop} , Par_{H1} , Par_{H2} , $D1$, $D2$, $D3$, $D4$. However, the main difficulty is related to the determination of topologic configurations for each cell of tubular lattice girder since Par_{CTop} , which varies depending on Par_{DN} is a row matrix. In order to handle with this problem, a unique value for the size of Par_{CTop} is assigned as the half of upper limit value of division number as $Par_{DNU}/2$ due to generating the tubular lattice girder using its symmetrical semi-part. Although Par_{CTop} is generated in a unique size, the required data is easily picked from Par_{CTop} . The tubular lattice girder outcome from the designer module has also a responsibility in the preparation of input data for the ready computer program ANSYS. Thus, it is possible to compute both the structural responses for an external static load and check the strengths of tubular lattice girder members and accordingly objective functions.

```

Step1 Code f1, f2, f3 and assign the values of maxDV and minDV,
Step2 Assign GN=50, PS=50, subGN1=15, subGN2=30 and div_num=2, pareto_OF_ALL=[]
Step3 Generate Spop1, Spop2, Spop3 and Spop4 considering their sizes as PS1=PS2=PS3=PS4=PS/4
Step4 Compute f1, f2, f3
for i=1:GN
Step5 if size(pareto_OF_ALL)==0, re-generate Spop1, Spop2, Spop3 and Spop4 considering PS1=PS2=PS3=PS4=PS/4, end
Step6 Compute f1, f2, f3 and determine pareto_OF_ALL
Step7 if size(pareto_OF_ALL)~=0, go to Step5, end
Step8 Determine the bounds of pareto solutions max_pareto_OF1_ALL, max_pareto_OF2_ALL, and etc. using div_num,
Step9 Re-arrange PS1, PS2, PS3 and PS4 (PS= PS1 + PS2 + PS3 + PS4) considering Spop1 and etc. along with
max_pareto_OF1_ALL and etc. and correspondingly re-compute div_num.
Step10 Assign Genetic Parameter values as
if i < subGN1
var_crossover_prob=0.20, var_crossover_dist =15.00, var_mutation_prob =0.80, var_mutation_dist =2.00
elseif i > subGN1 && i < subGN2
var_crossover_prob=0.80, var_crossover_dist =2.00, var_mutation_prob =0.40, var_mutation_dist =10.00
else
var_crossover_prob=0.80, var_crossover_dist =2.00, var_mutation_prob =0.01, var_mutation_dist =20.00
end
Step11 Evaluate Spop1 and etc. considering the crossover and mutation genetic operators and their corresponding genetic
parameter values
Step12 Correct Spop1 and etc. considering maxDV and minDV
end

```

Fig. 1 Pseudo Code for Computing Steps of PAGA

```

Form the cell topology of tubular lattice girder:
%only one of the symmetric parts
%(DivisionNumber must be even number)
Horizontal_Length=10 (or 20)
DivisionNumber=Chrom(1,1);
for i4=1:(DivisionNumber/2)
CellTopology(i4)=Chrom(1+i4);
end
Assign the heights of tubular lattice girder:
Vertical_Length1=Chrom(1, DivisionNumber/2 +2);
Vertical_Length2=Chrom(1, DivisionNumber/2 +3);
Assign the elements properties of tubular lattice girder for later
use:
prop_no(1)=1; % for Chrom(1,DivisionNumber/2+4)
prop_no(2)=2; % for Chrom(1,DivisionNumber/2+5)
prop_no(3)=3; % for Chrom(1,DivisionNumber/2+6)
prop_no(4)=4; % for Chrom(1,DivisionNumber/2+7)
Determine the nodal coordinates of tubular lattice girder:
NodeCoor=[];
CellNodeNo=[];
IncHorizLeng=Horizontal_Length/DivisionNumber;
IncVerLeng=(Vertical_Length2 -
Vertical_Length1)/(DivisionNumber/2);
%top level generation
IncHor=0;
IncVer=0;
for i1=1:DivisionNumber+1
if i1==1
NodeCoor(i1,1)=0;
NodeCoor(i1,2)=Vertical_Length1;
IncHor=IncHor+IncHorizLeng;
IncVer=IncVer+IncVerLeng;
elseif i1==(DivisionNumber+1)
NodeCoor(i1,1)=Horizontal_Length;
NodeCoor(i1,2)=Vertical_Length1;
elseif (i1 > 1) && (i1 < (DivisionNumber/2)+1)
NodeCoor(i1,1)=IncHor;
NodeCoor(i1,2)=Vertical_Length1+IncVer;
IncHor=IncHor+IncHorizLeng;
IncVer=IncVer+IncVerLeng;
elseif i1 == ((DivisionNumber/2)+1)
NodeCoor(i1,1)=IncHor;
NodeCoor(i1,2)=Vertical_Length2;
IncHor=IncHor+IncHorizLeng;
IncVer=IncVer+IncVerLeng;
else
NodeCoor(i1,1)=IncHor;
NodeCoor(i1,2)=Vertical_Length2+IncVer;
IncHor=IncHor+IncHorizLeng;
IncVer=IncVer+IncVerLeng;
end
end
Determine the node number for each cell
CellNodeNo(1,1)=1;
CellNodeNo(1,2)=2;
CellNodeNo(1,3)=DivisionNumber + 2;
CellNodeNo(1,4)=DivisionNumber + 3;
for i3=2:DivisionNumber
CellNodeNo(i3,1)=CellNodeNo(i3-1,2);
CellNodeNo(i3,2)=CellNodeNo(i3-1,2) + 1;
CellNodeNo(i3,3)=CellNodeNo(i3-1,4);
CellNodeNo(i3,4)=CellNodeNo(i3-1,4) + 1;
end
Generate Elements Considering CellNodeNo, CellTopology,
NodeCoor and prop_no
for i4=1:DivisionNumber
if i4==1
Generate first cell (symmetrically)
first_one(i4,CellTopology, NodeCoor, ...
CellNodeNo,ElemInc,DivInc,prop_no);
elseif i4==2
Generate second cell (symmetrically)
middle_two_first(i4,CellTopology, NodeCoor, ...
CellNodeNo, ,prop_no);
elseif i4 <= DivisionNumber
Generate other cells (symmetrically)
middle_two_later(i4,CellTopology,NodeCoor, ...
CellNodeNo,DivInc,prop_no);
end
end

```

Fig. 2 Pseudo Code for Automatically Generation of Lattice Girder

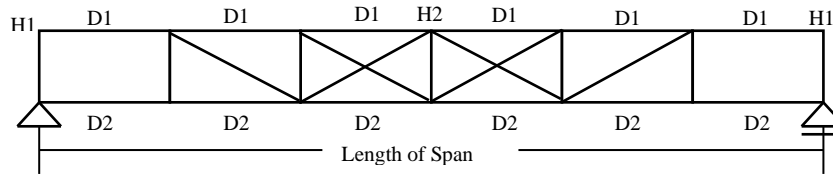


Fig. 3 A Lattice Girder Form Generated by Proposed Designer Module

4. Discussion of Findings

The proposed design approach integrated with the optimization tool, PAGA is utilized for the optimal design of tubular lattice girder. In this regard, this section is divided into two sub-sections in order to summarize the results obtained by the application of PAGA into the proposed design examples. In the first part of this section, the efficiency of PAGA is evaluated with respect to three MOAs, NSGAI, EVMOGA and SMSEMOA. For this purpose, three benchmark design examples named I-beam, welded beam and spring designs and a benchmark mathematical function named ZDT3 are utilized for the evaluation of employed MOAs coded in MATLAB. In the second sub-section, the design of tubular lattice girders as the real-world design examples are also optimized by the employed MOAs due to being fallen the benchmark examples into a category of small scaled ones. Thus, it is possible to both re-examine the computing performance of PAGA and determine the governing design factors

in the design of lattice girder. The successful algorithms are ranked in two levels and summarized in the separate Tables.

In order to provide an equal competition among the employed MOAs, the most appropriate operator parameter value sets, which manages the search mechanism of employed MOAs, have to be determined. For this purpose, a number of trials with different combinations of operator parameter values are separately performed for each of the employed MOAs. Then, the relatively better values of operator parameters are determined. Also, the values of two important parameters, evolutionary number and population size are taken as 50 and 50, respectively (see Tables 1 and 2).

Moreover, the relationship among them is assessed considering a statistical hypotheses test named “Kruskall Wallis” in a way of measuring the significance degree at a certain level ($P < 0.05$). Therefore, the execution number is taken as 100 runs.

Table 1. Parameter Names and Values of Governing Operators Utilized by Employed MOAs

Employed MOAs and Their Genetic Operator Parameter Names		Genetic Operator Parameter Values
NSGAI		
options. Generations		50
options.PopulationSize		50
options.MutationFcn= { @mutationuniform. }		0.2
options.CrossoverFcn= { @crossoverheuristic. }		0.4
options.SelectionFcn={ @selectiontournament. }		2
EVMOGA		
dd_ini	(crossover-related)	0.25
dd_fin	(crossover-related)	1
Pm	(mutation-related)	0.1
Sigma_Pm_ini	(mutation-related)	10
Sigma_Pm_fin	(mutation-related)	0.1
Nind_GA	(GA population size)	50
Nind_P	(P population size)	50
Nind_max_A	(A population size)	50
n_itations	(generation number)	50
SMSEMOA		
defopts.nPop	(size of the population)	50
defopts.maxEval	(maximum number of evaluations)	
defopts.useOCD	(use OCD to detect convergence)	True
defopts.OCD_VarLimit	(variance limit of OCD)	1e-9
defopts.OCD_nPreGen	(number of prec. generations used in OCD)	1
defopts.var_crossover_prob	(variable crossover probability)	0.9
defopts.var_crossover_dist	(distribution index for crossover)	15
defopts.var_mutation_prob	(variable mutation probability)	1/(Number of Design Variables)
defopts.var_mutation_dist	(distribution index for mutation)	20
defopts.var_swap_prob	(variable swap probability)	0.5
defopts.DE_F	(difference weight for DE)	0.2+rand(1)
defopts.DE_CR	(crossover probability for differential evo)	0.9
defopts.DE_CombinedCR	(crossover of blocks)	True
defopts.useDE	(perform differential evo instead of SBX&PM)	True
defopts.refPoint	(refPoint for HV)	0
PAGA		
PS (population size)		50
GN (generation number)		50
CombGen1 (gen. num. for first gen. operator comb. application)		20
CombGen2 (gen. num. for second gen. operator comb. application)		30

Table 2. Design Details of The Tubular Lattice Girder For The Design Optimization Purpose

Cases	Lattice Girder 1	Lattice Girder 2	Lattice Girder 3	Lattice Girder 4
Material Properties and Geometrical Configuration Details				
Load Values	Loading 1: 70 kipf	Loading 1: 140 kipf	Loading 1: 150 kipf	Loading 1: 300 kipf
	Loading 2: 20 kipf	Loading 2: 40 kipf	Loading 2: 50 kipf	Loading 2: 150 kipf
	Loading 3: 30 kipf	Loading 3: 60 kipf	Loading 3: 75 kipf	Loading 3: 75 kipf
Spanning Length	393.70 in. (10 m)	393.70 in. (10 m)	787.40 in. (20 m)	787.40 in. (20 m)
Joint Displ. Limit	3.94 in (100 mm)			
Max. Yielding	36 ksi (248.211 N/mm ²)			
Elast. Mod. Value	29732 ksi (205 kN/ mm ²)			
Design Parameters (Size)				
Par _{ND}	4	4	4	4
Par _{UDV}	37	37	37	37
Par _{LDV}	1	1	1	1
Design Parameters (Topology)				
Par _{UDN}	14	20	40	50
Par _{LDN}	6	6	10	10
Design Parameters (Shape)				
Par _{UH2}	35.433 in (0.9 m)	47.244 in (1.2 m)	59.055 in (1.5 m)	78.740 in (2.0 m)
Par _{LH2}	23.622 in (0.6 m)	23.622 in (0.6 m)	31.496 in (0.8 m)	31.496 in (0.8 m)
Par _{UH1}	23.622 in (0.6 m)	23.622 in (0.6 m)	31.496 in (0.8 m)	31.496 in (0.8 m)
Par _{LH1}	3.937 in (0.1 m)	3.937 in (0.1 m)	7.874 in (0.2 m)	7.874 in (0.2 m)

4.1. Preliminary Results Obtained from Optimization of Benchmark Function and Design Examples with Design Variables of Continuous and Mixed Types

The benchmark function named ZDT3 (Zitzler and *et al.* [33]) is firstly optimized (see the Matlab scripts in Reference Wagner and Kretschmar [19-20]). This benchmark function ZDT3, which has 30 continuous-type decision variables within a certain interval [0,1] is a mathematical function with a non-contiguous form. Its true pareto front with the optimal solutions is depicted in Fig. 4. Then, three benchmark designs named I beam, welded beam and spring are optimized (see their mathematical expressions in References Yang and *et al.* [39], Deb and Srinivasan [40], He and Wu [41]). While the designs of I and welded beams are represented by use of continues type-decision variables, both discrete and continues type-decision variable is utilized to represent the design of spring (see Fig. 5). Their true pareto fronts along with the optimal solutions are depicted in Figures (6-8). A statistical summarization of quality indicators obtained in the end of 100 runs are tabulated for each of benchmark test examples in Tables (3-6). The computing performances of employed MOAs are summarized in Table 7. Considering Figures (6-8) and Tables (3-7), the preliminary results are listed as:

- There does not exist any relation among the employed MOAs taking into account of the lower probability ratio (Prob>Chi-sq) as 2.42e-77 (see also the note as “3 groups have mean ranks significantly different from PAGA” in Fig. 9).
- The computing performance of PAGA is ranked in a second level according to the measuring metrics obtained for the mathematical function. The capacity,

density, convergence-diversity and covering features of PAGA show relatively lower performance than the other employed MOAs (see the rank of MOAs according to the measuring metrics in Table 7 and the true pareto front in Fig. 4)

- PAGA achieves to obtain more accurate approximation with a relatively better distribution for all design examples (see the rank of MOAs according to R2 in Table 7).
- The pure convergence degree of PAGA is ranked in the first place for the design example 1 and 2 but the second place for design example 3 (see the rank of MOAs according to Epsilon in Table 7). It is seen that the true pareto front of design example 3 is obtained as a non-contiguous form in Fig. 8.
- The density degree of pareto solutions obtained by PAGA is relatively higher for design example 1 and 2 but lower for design example 3 (see the rank of MOAs according to Average Distance in Table 7).
- Although PAGA shows a superior performance in obtaining the highest number of pareto solutions, the covering degree of these pareto solutions becomes relatively lower with respect to the other ones obtained by the other employed MOAs (see the rank of MOAs according to the Number of Pareto solutions and Spread in Table 7).

It is easily seen that the decrease in the pure convergence of pareto solutions is arisen from the fast-approximating feature of PAGA due to using the valuable genetic material exploited by the proposed evolutionary search for the exploration of promising candidate solutions. This feature of PAGA leads to an increase in the capacity performance while a decrease in the covering performance.

[illegible][illegible]

Table 5. Statistical Values of Quality Measuring Indicators (Benchmark Design Example 2: Welded Beam Design)

Employed MOAs	Epsilon Indicator				R2 Indicator				Average Distance				Spread				Number of Pareto Sol.		
	Max. Val.	Min. Val.	Aver. Val.	Stat. Sig.	Max. Val.	Min. Val.	Aver. Val.	Stat. Sig.	Max. Val.	Min. Val.	Aver. Val.	Stat. Sig.	Max. Val.	Min. Val.	Aver. Val.	Stat. Sig.	Max. Val.	Min. Val.	Aver. Val.
PAGA	0.242	0.000	0.028		0.000	0.000	0.000		0.087	0.005	0.014		1.754	0.283	0.552		233	104	163
NSGAI	985.499	0.423	70.295		0.043	0.000	0.003		0.202	0.000	0.041		1.302	0.000	0.651		21	1	17
SMSEMOA	0.346	0.001	0.050	1.93E-65	0.001	0.000	0.000	6.32E-62	0.128	0.019	0.036	6.63E-22	1.164	0.262	0.534	1.24E-21	51	50	50
EVMOGA	17.447	1.053	6.026		0.032	0.000	0.006		0.416	0.000	0.139		0.797	0.000	0.237		17	3	6

Table 6. Statistical Values of Quality Measuring Indicators (Benchmark Design Example 3: Spring Design)

Employed MOAs	Epsilon Indicator				R2 Indicator				Average Distance				Spread				Number of Pareto Sol.			
	Max. Val.	Min. Val.	Aver. Val.	Stat. Sig.	Max. Val.	Min. Val.	Aver. Val.	Stat. Sig.	Max. Val.	Min. Val.	Aver. Val.	Stat. Sig.	Max. Val.	Min. Val.	Aver. Val.	Stat. Sig.	Max. Val.	Min. Val.	Aver. Val.	
PAGA	3.19E+05	6.93E+03	1.63E+04		0.000	0.000	0.000		0.037	0.000	0.036		1.000	0.895	0.898		243	98	144	
NSGAI	3.41E+06	1.31E+04	1.10E+06		0.002	0.000	0.001		0.232	0.000	0.017		1.000	0.000	0.858		16	1	4	
SMSEMOA	5.40E+04	1.11E+01	1.11E+03	2.33E-72	0.080	0.000	0.002	1.08E-54	0.120	0.004	0.033	5.98E-26	1.000	0.232	0.992	1.44E-59	51	48	50	
EVMOGA	6.43E+10	8.05E+03	2.17E+09		0.510	0.000	0.235		0.600	0.000	0.049		0.998	0.000	0.094		15	1	3	

Table 7. A summary for Ranking The Employed MOAs Considering Benchmark Tests

Qual. Ind.	Rank	Mathematical Function	Design Ex. 1	Design Ex. 2	Design Ex. 3
Epsilon	Rank 1	SMSEMOA	PAGA	PAGA	SMSEMOA
	Rank 2	PAGA	NSGAI	SMSEMOA	PAGA
R2	Rank 1	SMSEMOA	PAGA	PAGA	PAGA
	Rank 2	PAGA	NSGAI	NSGAI	NSGAI
Average Distance	Rank 1	NSGAI	PAGA	PAGA	NSGAI
	Rank 2	PAGA	NSGAI	SMSEMOA	SMSEMOA
Spread	Rank 1	EVMOGA	EVMOGA	EVMOGA	EVMOGA
	Rank 2	SMSEMOA	NSGAI	SMSEMOA	NSGAI
Number of Pareto Sol.	Rank 1	NSGAI	PAGA	PAGA	PAGA
	Rank 2	PAGA	SMSEMOA	SMSEMOA	SMSEMOA

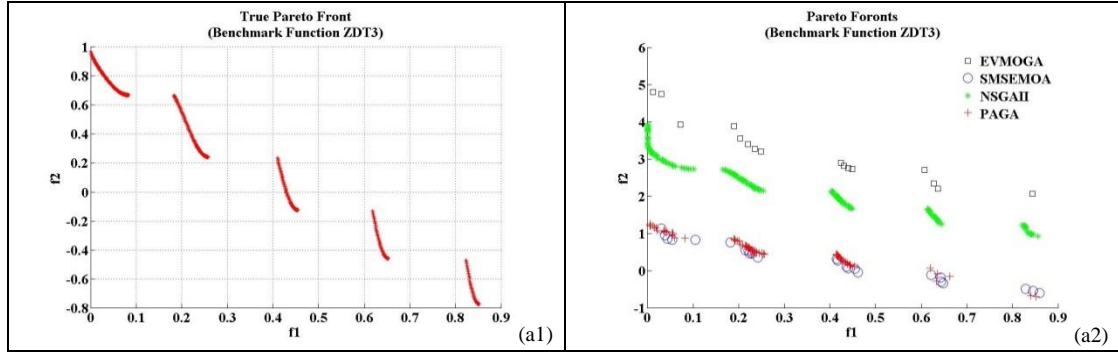


Fig. 4 True Pareto Front (a1) and Current Pareto Fronts Obtained by Use of Employed MOAs (a2) (Benchmark Function ZDT3)

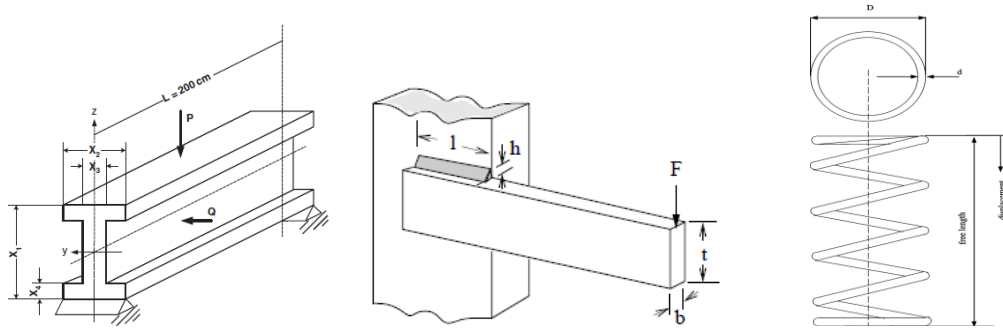


Fig. 5 Benchmark Design Examples I-Beam (Yang *et al.* [39]), Welded Beam (Deb & Srinivasan [40]) and Spring Design (He and *et al.* [41])

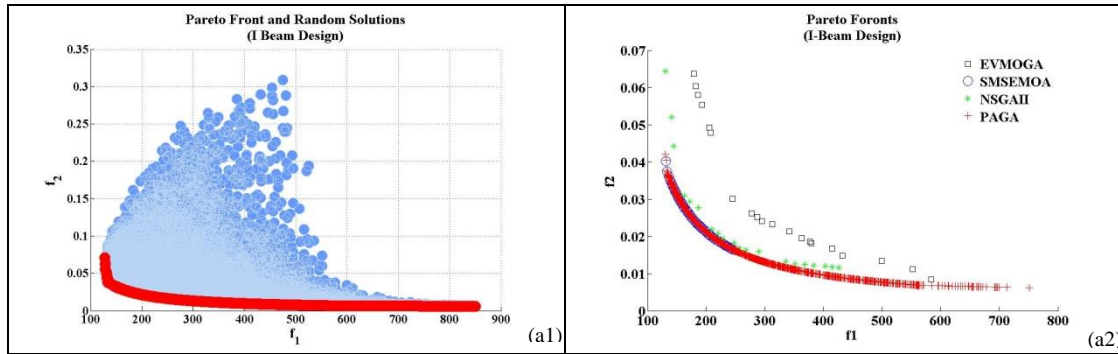


Fig. 6 True Pareto Front along with Random Solutions (a1) and Current Pareto Fronts Obtained by Use of Employed MOAs (a2) (Benchmark I-beam Design)

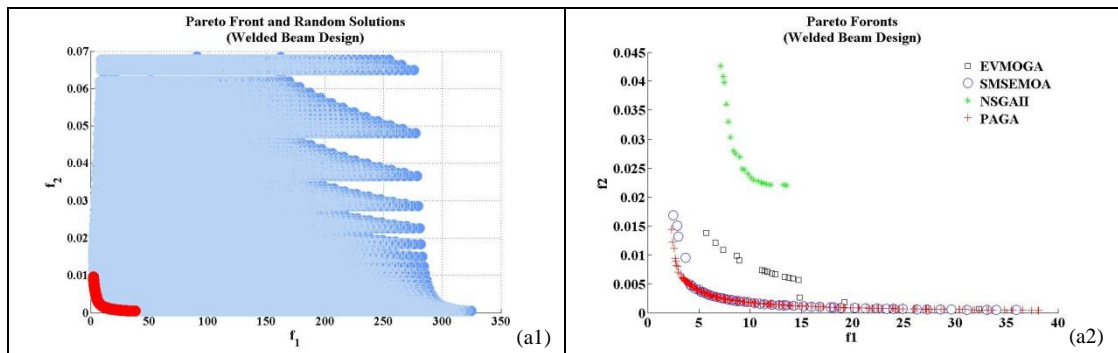


Fig. 7 True Pareto Front along with Random Solutions (a1) and Current Pareto Fronts Obtained by Use of Employed MOAs (a2) (Benchmark Welded Beam Design)

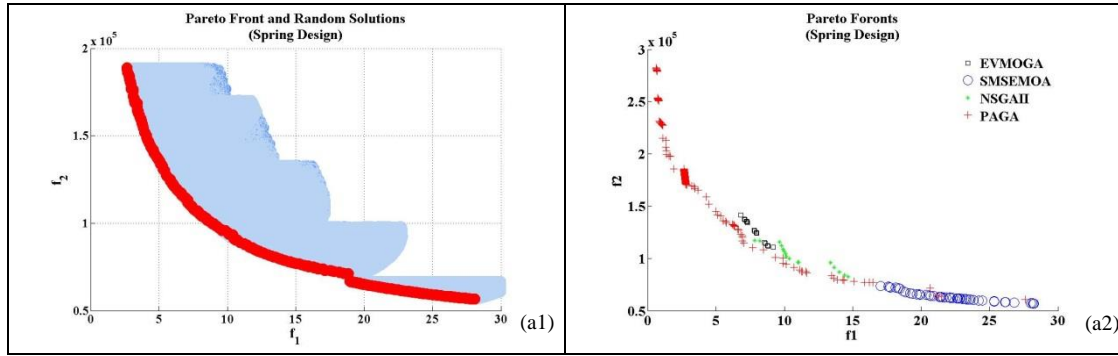


Fig. 8 True Pareto Front along with Random Solutions (a1) and Current Pareto Fronts Obtained by Use of Employed MOAs (a2)

(Benchmark Spring Design)

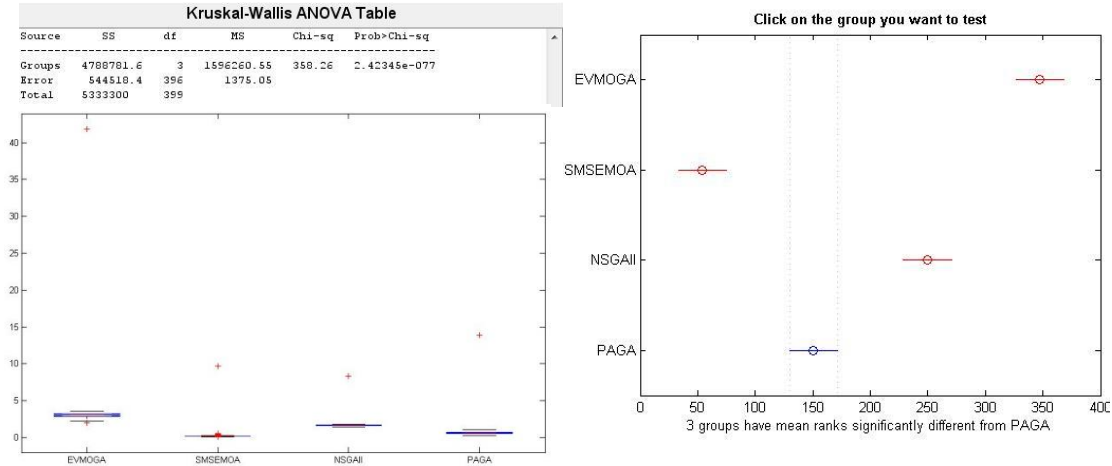


Fig. 9 Sketches Regarding to Statistical Analysing Results Outcome from MATLAB

4.2. Evaluation of Optimal Results Obtained from Design Optimization of Tubular Lattice Girders

This sub-section has two objectivities: *i*) evaluating the computing performance of PAGA considering the optimal design solutions of tubular lattice girders as a real-world design example, *ii*) determining the design factors which have the big responsibilities in the structural behavior of tubular lattice girders. Thus, it is also possible to examine the load-carrying capacity, serviceability and constructional cost of tubular lattice girders depending on its framing configurations and loading conditions. For this purpose, the designs of four tubular lattice girders with different spanning length and loading conditions are optimized (see Table 2). The extended formulations of design constraints in Eq. 5 are given in References (Talaslioglu [11 and 42]). The statistical data regarded to the proposed quality indicator values obtained by the employed MOAs are tabulated in Table (8-11). The true pareto fronts along with random solutions are displayed in Fig. 10. A summary of data tabulated in Table (8-11) is presented in Table 12. Thus, the preliminary results are summarized in the following part as:

- PAGA shows a success in obtaining more accurate approximation with a relatively better distribution for the designs of four tubular lattice girders (see the rank of MOAs according to R2 in Table 12 and see the true pareto fronts in Fig. 10).
- PAGA achieves to obtain the highest pure convergence degree in the designs of four tubular lattice girders (see the rank of MOAs according to Epsilon in Table 12).
- The density degree of pareto solutions obtained by PAGA is relatively lower for the designs of four tubular lattice girders except for the design of tubular lattice girder 3 (see the rank of MOAs according to Average Distance in Table 12).
- While PAGA shows a superior performance in obtaining the highest number of pareto solutions, the covering degree of these pareto solutions becomes relatively lower with respect to the other ones (see the rank of MOAs according to the Number of Pareto solutions and Spread in Table 12).
- The extreme optimal designs are tabulated in Table 13 including their framing configurations. Considering the entire weight values (1345.229 lb, 17565.640 lb) and maximum member forces (169.242 lb, 3829.295 lb) and joint

displacements (1.267 in, 2.227 in) corresponding to tubular lattice girder 1 and 4, it is obvious that an increase in the weight of tubular lattice girder correspondingly leads to an elevation in both its load-carrying capacity and joint displacement value (see Table 13). Although this claim seems to be an expected result, its invalidation is easily investigated by taking into account of the increased entire weight values from 3301.855 lb to 4360.518 lb and the decreased member force values from 1881.772 lb to 514.984 lb obtained for tubular lattice girders 1 and 2. In fact, there is also a similar dilemma between entire weight and joint displacement. In other words, it is expected that an increase in the entire weight of tubular lattice girder causes to an increase in the joint displacement value. But, its invalidation is approved considering the increased entire weight value from 1345.229 lb to 2181.964 lb and the decreased joint displacement value from 1.267 in to 0.895 (see the tubular lattice girders 1 and 2 in Table 13). The reason behind this dilemma is arisen from mainly the stability-related structural behavior. In other words, the inclusion of a slender member into current framing configuration of tubular lattice girder causes to inevitably a decrease in the joint displacements of tubular lattice girder although the entire weight of tubular lattice girder is increased.

- The other important result is concerned with the use of diagonal members in the construction of tubular lattice girders. Considering the sketches regarded to the framing configurations of tubular lattice girder in Table 13, a double bracing of diagonal members leads to an elevation in the load-carrying capacity even if under the severe loading conditions and expanded spanning lengths. Particularly, if the double bracing is increased along with an elevation of the first and last heights of tubular lattice girder, its load-carrying capacity is exponentially increased. This claim is easily confirmed considering the sketches corresponding to the increased member forces as 885.094 lb, 1229.182 lb, 1850.709 lb and 3829.295 lb for the tubular lattice girder 1,3 and 4 (see Table 13). Nevertheless, it is noted that there is a possibility of including a slender member into the current framing configuration of tubular lattice girder. At this point, the designer module gains a big importance in order to prevent the inclusion of slender members through its ability of continually differentiating the framing configurations of lattice girder. Therefore, the designer module increases the flexibility of PAGA. Thus, PAGA utilizes these promising optimal designs in order to generate new framing configurations of tubular lattice girder.

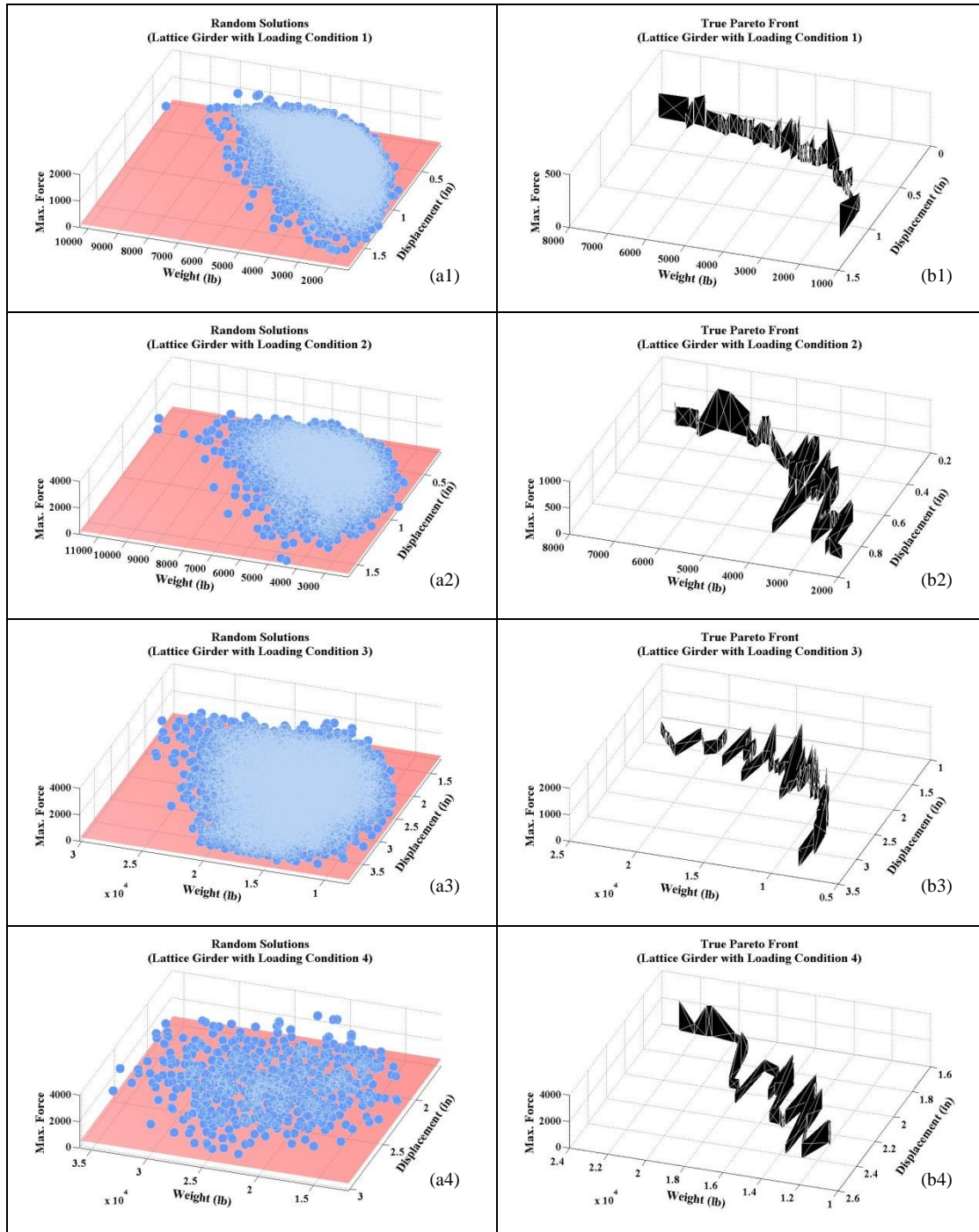


Fig. 10 True Pareto Front and Random Solutions (Tubular Lattice Girder 1 (a1,b1), Tubular Lattice Girder 2 (a2,b2), Tubular Lattice Girder 3 (a3,b3) and Tubular Lattice Girder 4 (a4,b4))

[illegible][illegible]

Table 10. Statistical Values of Quality Measuring Indicators (Lattice Girder 3)

Employed MOAs	Epsilon Indicator				R2 Indicator			Average Distance			Spread		Number of Pareto Sol.		
	Max. Val.	Min. Val.	Aver. Val.	Stat. Sig.	Max. Val.	Min. Val.	Aver. Val.	Stat. Sig.	Max. Val.	Min. Val.	Aver. Val.	Stat. Sig.	Max. Val.	Min. Val.	Aver. Val.
PAGA	3535.471	136.815	1702.061		0.019	0.002	0.011		0.257	0.040	0.144		0.998	0.703	0.856
NSGAII	3534.038	240.117	2266.605	4.08E-03	0.019	0.001	0.012	0.003554	0.257	0.043	0.175	0.001337	0.999	0.702	0.858
SMSEMOA	3546.729	451.603	2209.754		0.019	0.001	0.013		0.258	0.048	0.179		0.997	0.702	0.857
EVMOGA	3548.864	237.106	2212.249		0.019	0.002	0.011		0.259	0.040	0.162		0.996	0.708	0.859
													9	5	8













Table 11. Statistical Values of Quality Measuring Indicators (Lattice Girder 4)

Employed MOAs	Epsilon Indicator				R2 Indicator			Average Distance			Spread		Number of Pareto Sol.		
	Max. Val.	Min. Val.	Aver. Val.	Stat. Sig.	Max. Val.	Min. Val.	Aver. Val.	Stat. Sig.	Max. Val.	Min. Val.	Aver. Val.	Stat. Sig.	Max. Val.	Min. Val.	Aver. Val.
PAGA	16367.764	758.003	7518.177		0.114	0.004	0.064		0.333	0.016	0.192		0.996	0.703	0.854
NSGAII	16473.704	1230.183	10395.459	4.48E-06	0.117	0.013	0.081	0.00331346	0.330	0.023	0.216	0.00018697	1.000	0.702	0.847
SMSEMOA	16413.865	982.807	10636.180		0.117	0.004	0.069		0.332	0.027	0.190		0.999	0.701	0.849
EVMOGA	16404.696	2685.283	10888.279		0.117	0.013	0.079		0.329	0.038	0.210		0.998	0.705	0.875
													8	4	6

Table 12. A summary for Ranking The Employed MOAs Considering Tubular Lattice Girder Designs

Qual. Ind.	Rank	Lattice Girder 1	Lattice Girder 2	Lattice Girder 3	Lattice Girder 4
Epsilon	Rank 1	PAGA	PAGA	PAGA	PAGA
	Rank 2	SMSEMOA	SMSEMOA	SMSEMOA	NSGAII
R2	Rank 1	PAGA	PAGA	PAGA	PAGA
	Rank 2	SMSEMOA	SMSEMOA	NSGAII	SMSEMOA
Average Distance	Rank 1	SMSEMOA	SMSEMOA	PAGA	SMSEMOA
	Rank 2	PAGA	PAGA	NSGAII	PAGA
Spread	Rank 1	PAGA	SMSEMOA	PAGA	NSGAII
	Rank 2	SMSEMOA	NSGAII	SMSEMOA	SMSEMOA
Number of Par. Sol.	Rank 1	PAGA	PAGA	PAGA	PAGA
	Rank 2	NSGAII	SMSEMOA	NSGAII	SMSEMOA

Table 13. Design Variables (Size, Shape and Topology) Along with Objective Functions Obtained by Use of Proposed Tubular Lattice Girders

	Lattice Girder 1			Lattice Girder 2			Lattice Girder 3			Lattice Girder 4		
	Des1	Des2	Des3	Des1	Des2	Des3	Des1	Des2	Des3	Des1	Des2	Des3
	(MW)	(MJD)	(MEF)	(MW)	(MJD)	(MEF)	(MW)	(MJD)	(MEF)	(MW)	(MJD)	(MEF)
Par _{DN}	6	6	8	6	14	6	10	16	10	16	36	18
Par _{H2}	19.752	6.673	5.331	22.780	4.324	3.992	14.323	12.234	27.457	21.055	20.118	25.845
Par _{H1}	29.565	24.233	26.889	43.298	26.004	36.030	54.123	32.324	44.808	74.913	58.106	77.284
D1	PIPEST3-1/2 (3.44 in ²)	PIPOST8 (7.85 in ²)	PIPEEST2 (2.51 in ²)	PIPEST5 (5.72 in ²)	PIPEEST6 (14.7 in ²)	PIPEEST2 (2.51 in ²)	PIPOST10 (11.1 in ²)	PIPEEST2 (2.51 in ²)	PIPEEST2 (2.51 in ²)	PIPOST10 (15.0 in ²)	PIPEEST8 (20.0 in ²)	PIPEEST6 (14.7 in ²)
	PIPOST5 (4.03 in ²)	PIPEEST2 (2.51 in ²)	PIPOST3 (2.08 in ²)	PIPOST5 (4.03 in ²)	PIPEEST5 (10.7 in ²)	PIPEEST4 (4.14 in ²)	PIPOST10 (11.1 in ²)	PIPEEST2 (2.51 in ²)	PIPEEST6 (14.7 in ²)	PIPEEST2 (2.51 in ²)	PIPEEST2 (2.51 in ²)	PIPOST2 (2.51 in ²)
	PIPEEST2-1/2 (3.81 in ²)	PIPOST5 (4.03 in ²)	PIPOST4 (2.97 in ²)	PIPEEST2-1/2 (3.81 in ²)	PIPOST10 (11.1 in ²)	PIPEEST2 (2.51 in ²)	PIPEEST6 (14.7 in ²)	PIPEEST2 (2.51 in ²)	PIPEEST8 (20.0 in ²)	PIPOST8 (11.9 in ²)	PIPEEST2 (2.51 in ²)	PIPOST12 (13.6 in ²)
	PIPOST3 (2.08 in ²)	PIPEEST6 (7.88 in ²)	PIPOST5 (4.03 in ²)	PIPEST3-1/2 (3.44 in ²)	PIPEEST5 (10.7 in ²)	PIPEEST2 (2.51 in ²)	PIPOST4 (2.97 in ²)	PIPEEST2 (2.51 in ²)	PIPOST10 (15.0 in ²)	PIPEST3-1/2 (3.44 in ²)	PIPEEST6 (14.7 in ²)	PIPOST10 (15.0 in ²)
Entire Weight (lb)	1345.229	2651.333	3301.855	2181.964	4360.518	5608.938	8009.778	15905.602	14148.830	11895.340	24631.810	17565.640
Joint Disp. (in)	1.267	1.791	1.202	0.895	1.640	0.932	3.075	3.937	2.613	2.289	3.023	2.227
Member Force (lb)	169.242	885.094	1881.772	245.068	514.984	3118.521	1229.182	1531.490	3628.809	1850.709	1861.192	3829.295
												

5. Conclusions

This study proposes the design optimization of tubular lattice girders. For this purpose, the tubular lattice girders with different loading conditions and spanning lengths are utilized. As an optimization tool, a multi-objective optimization methodology named pareto archived genetic algorithm (PAGA) is employed to execute the optimization-related computing procedures. The

exploring capacity of PAGA is improved utilizing a designer module for the automatically generation of tubular lattice girder. Furthermore, the computing performance of PAGA is also evaluated considering several MOAs named NSGAI, EVMOGA and SMSEMOA. The preliminary results are summarized as:

- PAGA achieves to obtain relatively better convergence-diversity, pure convergence, density and capacity degrees of current pareto fronts for the small-scaled benchmark applications.
- PAGA has a capability of simultaneously handling the design variables with continuous, discrete and integer.
- PAGA is employed to optimize the tubular lattice girder design problem as large-scaled real-world design problem. It is shown that its success is increased obtaining better convergence-diversity, pure convergence, capacity and covering degrees of current pareto fronts. These results imply that PAGA is a successful optimization tool with an ability of both exploring an increased pareto optimal solutions and accurately approximating to a pareto front with a relatively better distribution.
- It is shown that the inclusion of designer module into the proposed optimal design approach increases the flexibility of PAGA, thereby preventing the stability problem.
- A diagonal lattice girder with increased double braced members increases the load-carrying capacity. However, it has to be noted that a possibility of including a slender member into the current framing configuration of tubular lattice girder causes to a stability loss. In this regard, the proposed designer module has a big importance for the design of tubular lattice girder due to its ability of exploring the stable frame configurations. Thus, it is possible to use these frame configurations in order to generate a tubular lattice girder with higher stability.
- It is emphasized that the multi-objective optimization procedure instead of the single-objective has to be utilized in order to obtain a tubular lattice girder with a higher load-carrying, serviceability capacities and a lower constructional cost at the same time.

In further research, the new design constraints regarded to the welding strengths will be employed along with the current ones. Also, PAGA will be improved thereby enriching its exploiting feature. For this purpose, a self-adaptive mechanism is developed in conjunction with new implementations in its current recombination procedure.

Acknowledgement

Author thanks the reviewers for improving the content of this manuscript. Furthermore, Author also thanks Dr. Tobias Wagner for both his support for highlighting the details about the use of quality indicators named epsilon and R, and his effort for coding SMSEMOA and R2-EMOA in Matlab.

References

- [1] Nageim H.K. and Macginley T.J., Steel structures, practical design studies, 3rd Edition, EF Spon Press, 2005.
- [2] Talaslioglu T., "Optimization of geometrically nonlinear lattice girders. Part I: Considering member strengths", Journal of Civil Engineering and Management, 21(4), 423-443, 2015
- [3] Hasancebi O., Çarbaş S., Doğan E., Erdal F. and Saka M.P., "Performance evaluation of meta-heuristic search techniques in the optimum design of real size pin jointed structures", Computers and Structures, 87(5-6), 284-302, 2009.
- [4] Saka M.P. "Optimum design of steel frames using stochastic search techniques based on natural phenomena: a review", In Proceedings of Civil engineering computations: tools and techniques, Saxe-Coburgh Publications, U.K., 2007.
- [5] Seyedpoor S.M., Gholizadeh S. and Talebian S.R., "An efficient structural optimization algorithm using a hybrid version of particle swarm optimization with simultaneous perturbation stochastic approximation", Civil Engineering and Environmental Systems, 27(4), 295-313, 2010.
- [6] Cagnina L.C., Esquivel S.C. and Coello C.A.C., "Solving constrained optimization problems with a hybrid particle swarm optimization algorithm", Engineering Optimization, 43(8), 843-866, 2011.
- [7] Chen T.Y. and Huang J.H., "An efficient and practical approach to obtain a better optimum solution for structural optimization", Engineering Optimization, 45(8), 1005-1026, 2013.
- [8] Lu Y.C., Jan J.C., Hung S.L. and Hung G.H., "Enhancing particle swarm optimization algorithm using two new strategies for optimizing design of truss structures", Engineering Optimization, 45(10), 1251-1271, 2013.
- [9] Torii A.J., Lopez R.H. and Biondini F., "An approach to reliability-based shape and topology optimization of truss structures", Engineering Optimization, 44(1), 37-53, 2012.
- [10] Beer F, Johnston ER, DeWolf J and Mazurek D "Mechanics of material", 6th Edition, McGraw-Hill 2011.
- [11] Talaslioglu T., "Multiobjective size and topology optimization of dome structures", Structural Engineering and Mechanics, 43(6), 795-822, 2012a.
- [12] Salajegheh E., Mashayekhi M., Khatibinia M. and Kaykha M., "Optimum Shape Design of Space Structures by Genetic Algorithm", International Journal of Space Structures, 24, 45-57, 2009.
- [13] Srinivas N. and Deb K., "Multi-objective optimization using non-dominated sorting in genetic algorithms", Evolutionary Computation, 2(3), 221-248, 1995.
- [14] Zitzler E., Thiele L., Laumanns M., Fonseca C. and Grunert da Fonseca V., "Performance Assessment of Multiobjective Optimizers: An Analysis and Review", IEEE Transactions on Evolutionary Computation, 7(2), 117-132, 2003.
- [15] Wu J. and Azarm S., "Metrics for quality assessment of a multiobjective design optimization solution set", J. Mech. Design, 123, 1, 18-25, 2001.
- [16] Deb K., Pratap A., Agarwal S. and Meyarivan T., "A fast and elitist multiobjective genetic algorithm: NSGA-II", IEEE Trans. Evol. Comput., 6(2), 182-197, 2002.
- [17] Veldhuizen D.A. and Lamont G.B., "Multiobjective evolutionary algorithm test suites," in Proc. ACM Symp. Appl. Comput., 351-357, 1999.
- [18] Hansen M.P. and Jaszkiewicz A., "Evaluating the quality of approximations of the non-dominated set," Technical University of Denmark, Tech. Rep. IMM-REP-1998-7, 1998.
- [19] <http://inriadortmund.gforge.inria.fr/r2emoa/>
- [20] Wagner T. and Kretschmar F.S., "Metric Selection Evolutionary Multi-objective Algorithm (SMSEMOA)" [online]. Available from: <http://ls11-www.cs.uni-dortmund.de/rudolph/hypervolume/start>
- [21] Matlab, [online], Available from: <http://www.mathworks.com/help/gads/gamultiobj.html>
- [22] Talaslioglu T., "Optimal dome design considering the member-related design constraints", accepted for the publication in the journal Frontiers of Structural and Civil Engineering, Springer, 2018.
- [23] Yang X.S., "Engineering Optimization: An Introduction with Meta-heuristic Applications", John Wiley and Sons, 2010.
- [24] Reed P.M., Hadka D., Herman J.D., Kasprzyk J.R. and Kollat J.B., "Evolutionary multi-objective optimization in water resources: The past, present, and future", Advances in Water Resources, 51, 438-456, 2013.
- [25] Metaxiotis K. and Liagkouras K., "Multiobjective Evolutionary Algorithms for Portfolio Management: A comprehensive literature review", Expert Systems with Applications, 39, 11685-11698, 2012.
- [26] Richardson J.N., Nordenson G., Laberrenne R., Coelho R.F. and Adriaenssens S., "Flexible optimum design of a bracing system for façade design using multi-objective genetic algorithms", Automation in Construction, 32, 80-87, 2013.
- [27] Hwang C.L. and Masud "ASM Multiple objective decision making-methods and applications: A state-of-the-art survey", Lectures Notes in Economics and Mathematical Systems, 164, 1979.
- [28] Miettinen K., "Nonlinear Multiobjective Optimization", Academic Kluwer Press, 1999.
- [29] Charnes A. and Cooper W.W., "Goal programming and multiple objective optimization", European Journal of Operational Research, 1(1), 39-45, 1977.
- [30] Deb K., Agrawal S., Pratap A. and Meyarivan T., "A fast and elitist multi-objective genetic algorithm: NSGA-II", IEEE Transactions on Evolutionary Computation, 6(2), 156-198, 2002.
- [31] Zitzler E., Laumanns M. and Thiele L., "SPEA2: Improving the strength pareto evolutionary algorithm for multiobjective optimization", In Evolutionary Methods for Design, Optimisation and Control with Application to Industrial Problems, International Center for Numerical Methods in Engineering (CIMNE), 2002.
- [32] Talaslioglu T., "Multi-objective Design Optimization of Grillage Systems according to LRFD-AISC", Advances in Civil Engineering, doi:10.1155/2011/932871, 2011.
- [33] Zitzler E., Deb K. and Thiele L., "Comparison of Multi-objective Evolutionary Algorithms: Empirical Results", Evolutionary Computation, 8(2), 173-195, 2000.
- [34] Huband S., Hingston P., While L. and Barone L., "An evolution Strategy with Probabilistic Mutation for Multi-objective Optimization", In Congress on Evolutionary Computation (CEC 2003), IEEE Press, 2003.
- [35] Talaslioglu T., "Multi-objective Design Optimization of Geometrically Nonlinear Truss Structures", Kuwait Journal of Science and Engineering (Issue 1B), 39(2), 47-77, 2012b.
- [36] Martínez M., Herrero J.M., Sanchis J., Blasco X. and García N.S., "Applied Pareto Multi-objective Optimization by Stochastic Solvers", Engineering Applications of Artificial Intelligence, 22, 455-465, 2009.
- [37] Beume N., Naujoks B. and Emerich M., "SMS-EMOA: Multiobjective selection based on dominated hyper-volume", European Journal of Operational Research, 181, 1653-1669, 2007.
- [38] Beume N., Naujoks B. and Rudolph G., "SMS-EMOA-Effective evolutionäre Mehrzieloptimierung (SMS-EMOA-Effective Evolutionary Multiobjective Optimization). Automatisierungstechnik, 56(7), 357-364, 2008.
- [39] Yang B.S., Yeun Y.S. and Ruy W.S., "Managing approximation models in multi-objective optimization", Structural and Multidisciplinary Optimization, 24, 141-156, 2002.
- [40] Deb K. and Srinivasan A., "Innovation: Innovative Design Principles Through Optimization", Kanpur Genetic Algorithms, [online]. Available from: <http://www.iitk.ac.in/kangal/pub.htm> KanGAL Report Number 2005007, 2005.
- [41] He S., Prempan E. and Wu Q.H., "An Improved Particle Swarm Optimizer for Mechanical Design Optimization Problems", Engineering Optimization, 36(5), 585-605, 2004.
- [42] Talaslioglu T., "Weight Minimization of Tubular Dome Structures by a Particle Swarm Methodology", Kuwait Journal of Science and Engineering (Issue 1B), 1, 145-180, 2013.

EXPERIMENTAL STUDY OF THE BEARING CAPACITY OF LONG-SPAN PROFILED STEEL SHEET–CONCRETE COMPOSITE SLABS

Xiao-Xiang He^{1,2}, Guo-Chang Li^{2,*} and Zhi-Jian Yang²

¹ School of Civil Engineering, Dalian University of Technology, Dalian, China

² School of Civil Engineering, Shenyang Jianzhu University, Shenyang, China

* (Corresponding author: E-mail: liguochang0604@sina.com)

ABSTRACT

This paper presents an experimental study on the structural performance of 26 composite slab specimens having trapezoidal and dovetail profiles. The influence of the span, details of the end anchorage, and cross-sectional depth on the mechanical performance and failure modes of the specimens was discussed. The effects of the thickness of the profiled steel sheets and additional reinforcement of the bottom on the longitudinal shear bearing capacity of long-span dovetail-profiled composite slabs were also investigated. Research on long-span composite slabs accounting for different details of the end anchorage and steel profiles is limited in the literature. The test results indicated that the end anchorage can significantly improve the mechanical performance and ultimate bearing capacity of composite slabs, whereas additional reinforcement and thick profiled steel sheets can slightly increase their bearing capacity. The test results also showed that, in long-span flooring systems, dovetail-profiled composite slabs have a higher load bearing capacity than trapezoidal-profiled composite slabs.

ARTICLE HISTORY

Received: 6 March 2019
Revised: 3 April 2019
Accepted: 7 April 2019

KEYWORDS

Long-span composite slabs;
Experimental study;
Load bearing capacity;
Failure mode;
Longitudinal shear

Copyright © 2019 by The Hong Kong Institute of Steel Construction. All rights reserved.

1. Introduction

Profiled steel sheet–concrete composite slabs are widely used in steel structures and steel–concrete composite structures owing to their advantages of rapid construction, enhanced safety, and high cost efficiency. During the design and construction of composite slab floors, a profiled steel sheet serves both as a template during construction and as load-bearing reinforcement during the service life of the slabs [1–3]. Although the performance of a composite slab is affected by the inherent material properties, geometrical characteristics, boundary conditions, and mode of external loading, it is mainly governed by the interactions at the profiled steel sheet–concrete interface. Profiled steel sheet–concrete composite slabs subjected to external loading, primarily experienced longitudinal shear or flexural failure [4–8]. For composite slabs with end anchorage such as a welded stud, the slip at the profiled steel sheet–concrete interface can be reduced, whereas the bond between the steel sheet and concrete can be enhanced. Consequently, their strength and rigidity can be improved [9–12].

Generally, the span of simply supported composite slabs is less than 4.5 m and that of continuous composite slabs is less than 5.1 m [13]. Composite slabs with short spans can enable rapid construction, and thus, have high operating efficiencies despite their inherent disadvantages. As a long-span structure is constructed by composite slab of short span, numerous filler beams and connectors welding with a high workload are required. Long-span composite slabs require several temporary supports but few filler beams. As the additional costs of the temporary supports are smaller than the use of filler beams, long-span composite slabs are significantly more cost efficient than short-span ones [14].

Extensive studies on the behavior of composite slabs have been reported in the literature. Porter and Greimann [1], Jolly and Lawson [15] investigated the effect of end-anchorage stud on the behavior of composite slabs by test. They found that the composite slabs without end anchorage experienced longitudinal shear failure at the steel sheet–concrete interface, whereas those with end anchorage underwent failure through local buckling or tearing of the steel sheet near the studs. Furthermore, the end anchorage contributed to a significant improvement in the shear bond strength, bearing capacity, and ductility of the composite slabs. Chen [16] conducted an experimental study on the behavior of simply supported and continuous composite slabs and found that the longitudinal shear strength was governed by the bond slip at the profiled steel sheet–concrete interface and not by the anchoring strength of the studs. Moreover, the longitudinal shear strength obtained from the linear regression of the test results of the simply supported composite slabs with end anchorage could be used to compute the bearing capacity of continuous composite slabs. Valivonis [7] distinguished three stages in the failure of the steel sheet–concrete interface of composite slabs: elastic deformation, plastic deformation, and cracking and failure. He found that the shear strength at the steel sheet–concrete interface was significantly affected by the cross-sectional

shape of the profiled steel sheet, transverse pre-compressing force, and restraining capacity of the interface. Chen et al. [5] studied the shear-bond failure mechanism and behavior of composite slabs and suggested that the distribution of the longitudinal shear stress along the length of the composite slabs was nonuniform. Moreover, the shear strength of the composite slabs was mainly governed by the same property of the shear span. Based on an investigation of the effect of end-anchorage studs on the longitudinal shear strength of composite slabs, Chen et al. [9] suggested that the contribution of the studs to the longitudinal shear bearing capacity of the composite slab was not simply an addition of the shear strengths of the individual studs.

Studies have also been conducted on composite slabs having different cross-sectional geometries. In a study on composite slabs decked with profiled steel sheets having three different cross-sectional geometries and subjected to static and dynamic loads, Bode and Minas [17] found that all the different composite slabs having an end anchorage exhibited a high load bearing capacity and ductility. Gholamhoseini et al. [18] conducted an experimental study on eight full-scale simply supported composite slab specimens using four types of profiled deckings subjected to a four-point bending to identify the influence of the type of decking on the shear–slip relationship. The experimental results revealed that all the four types of specimens underwent longitudinal shear failures, whose strength decreased with the increase in the shear span.

Regarding composite slabs with additional longitudinal reinforcements, Johnson and Shepherd [19] found that the additional reinforcement placed above the troughs of the steel sheet, significantly affected the shear strength. The failure of composite slabs is typically governed by deflection, and it may not be possible to completely utilize the advantage of the additional reinforcements.

Bending tests of full-scale composite slabs typically follow the standard experimental methods provided in Eurocode 4 [3] or BS 5950-4 [20]. Ríos et al. [21] compared the four and six-point loading methods using numerical analysis and found that the former was suitable for concentrated loads, whereas the latter was appropriate for uniform loads. Abdullah and Easterling [22] simulated a test of full-scale composite slab specimens using a new elemental test for cost efficiency and demonstrated that the elemental test results agreed well with the test results of the full-scale specimens.

The performance of long-span composite slabs has also been studied. Widjaja and Easterling [14] found that their performance was generally governed by deflection. In an experimental study on long-span composite slabs decked with profiled steel sheets with depths of not less than 200 mm, Brekelmans et al. [23] found that the fundamental theory provided in Eurocode 4: Part 1.1 was also applicable to long-span composite slabs.

The above-mentioned literature review reveals that previous research generally focused on composite slabs with short spans from 1.2 m to 4.5 m, and research on long-span composite slabs is limited. This paper presents an experimental study on the performance and failure behavior of composite

slabs with different spans. A total of 26 profiled steel-sheet-concrete composite slab specimens having two different cross-sectional geometries were tested. Parameters such as the cross-sectional geometry of the profiled steel sheet, depth of the composite slab, anchoring stud configuration, and additional reinforcement were investigated with the aim of providing test data and theoretical input for the design and application of long-span composite slabs.

2. Set-up of Experimental Test

2.1. Design of test specimens

A total of 26 simply supported composite slab specimens were designed, among which 11 were decked with trapezoidal-shaped profiled steel sheet and 15 were decked with dovetail-shaped profiled steel sheet.

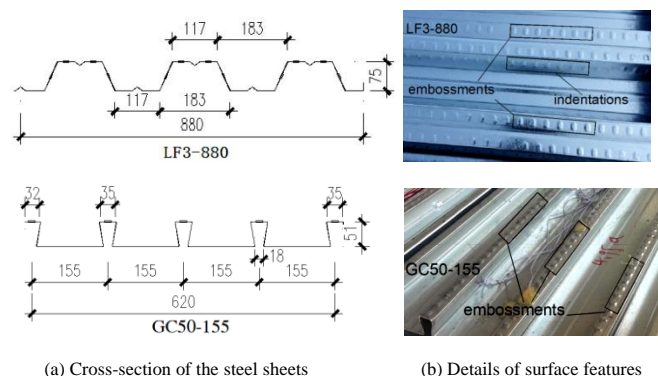


Fig. 1 Details of test specimens

Table 1
Details of test specimens with the LF3-880 type steel sheet

No.	Specimens	Span L (mm)	Slab depth d (mm)	Sheeting thickness t (mm)	Span/depth (mm)	End anchorage	Additional reinforcement
1	OBI-1	2000	180	1.0	11.1	D19	No
2	OBI-2	2000	180	1.0	11.1	D19	No
3	OBI-3	2000	180	1.0	11.1	No	No
4	OBII-1	3400	150	1.0	22.7	D19	No
5	OBII-2	3400	150	1.0	22.7	D19	No
6	OBIII-1	4800	160	1.0	30	No	No
7	OBIII-2	4800	160	1.0	30	D19	No
8	OBIII-3	4800	200	1.0	24	D19	No
9	OBIV-1	6000	200	1.0	30	D19	4 ϕ 10
10	OBIV-2	6000	200	1.0	30	No	4 ϕ 10
11	OBIV-3	6000	250	1.0	24	D19	4 ϕ 10

The following parameters were investigated:

- (1) Cross-sectional geometry of the profiled steel sheets: trapezoidal profile LF3-880 and dovetail profile GC50-155,
- (2) Span and depth of the composite slab,

- (3) Configuration of the end-anchorage studs,
- (4) Additional reinforcement (one for each trough of the profiled steel sheet for specimens with a span of 6.0 m).

Table 2
Details of test specimens with the GC50-155 type steel sheet

No.	Specimens	Span L (mm)	Slab depth d (mm)	Sheeting thickness t (mm)	Span/depth (mm)	End anchorage	Additional reinforcement
1	NBI-1	2000	180	1.0	11.1	No	No
2	NBI-2	2000	180	1.0	11.1	D19	No
3	NBI-3	2000	180	1.0	11.1	D19	No
4	NBII-1	3400	150	1.0	22.7	D19	No
5	NBII-2	3400	150	1.0	22.7	D19	No
6	NBIII-1	4800	200	1.0	24	D19	No
7	NBIII-2	4800	160	1.2	30	D19	No
8	NBIII-3	4800	160	1.0	30	D19	No
9	NBIII-4	4800	160	1.0	30	No	No
10	NBIV-1	6000	250	1.0	24	D19	No
11	NBIV-2	6000	200	1.2	30	D19	No
12	NBIV-3	6000	200	1.0	30	D19	No
13	NBIV-4	6000	200	1.0	30	No	No
14	NBIV-5	6000	200	1.2	30	D19	8 ϕ 10
15	NBIV-6	6000	200	1.0	30	D19	8 ϕ 10

Table 3
Geometry and strength properties of steel sheets

Types	Thickness t (mm)	Area A_p (cm ² /m)	I_x (cm ⁴ /m)	f_y (N/mm ²)	f_u (N/mm ²)
LF3W-880	1.0	14.7	156.68	335	566
GC50-155	1.0	19.3	75.60	330	461
GC50-155	1.2	22.0	85.60	414	512

Tables 1 and 2 list the parameters of the specimens. The depth design of the specimens accounted for the deflection and longitudinal shear strength required by the composite slabs. The specimens were designed with depth-to-span ratios of not less than 1/30 [24]. The trapezoidal-profiled steel sheets had embossments on the upper flange surface and indentations on the web surface, and the dovetail-profiled steel sheet had embossments on the upper flange surface. Fig. 1(a) and Fig. 1(b) show the cross-sectional geometries and surfaces of both the profiled steel sheets. Table 3 lists the material properties of both the profiled steel sheets. The additional reinforcement has a tensile strength of 540 N/mm² and yield strength of 360 N/mm². The end anchorage stud has a diameter of 19 mm and length of 100 mm. It is penetration-welded at the trough of the profiled steel sheets and welded to the steel sheet of the support. Four and eight studs were welded at the anchoring ends of the trapezoidal and dovetail-profiled steel sheets, respectively. The width of the trapezoidal-profiled composite slab specimens is 880 mm. The dovetail-profiled specimens used two profiled steel sheets joined transversely and with a width of 1240 mm, as shown in Fig. 1(c). To avoid cracking induced by concrete-contraction, $\phi 6@200$ reinforcement steel meshes were arranged at the compressive zone of the specimens. The cubic compressive strength of concrete is 33.1 N/mm².

2.2. Experimental scheme and layout of measurement points

Different loading devices were used according to the different spans of the specimens. A four-point loading device was used for specimens with a span smaller than 2.0m, with two equal point loads applied by a load-distribution beam, as illustrated in Fig. 2(a). A six-point loading device was used for the specimens with spans of 3.4m, 4.8m, and 6.0 m, with four equal point loads applied by two levels of load-distribution beams, as displayed in Fig. 2(b).

The vertical load was applied with a staged increase, which was about 10% of predicted bending moment capacity of the specimen. At each load level, the vertical load held for 5 minutes to observe and record the testing phenomenon.

When the test load reduced to below 80% of the ultimate load, and the mid-span deflection was more than 1/50 of the span, the test was terminated.

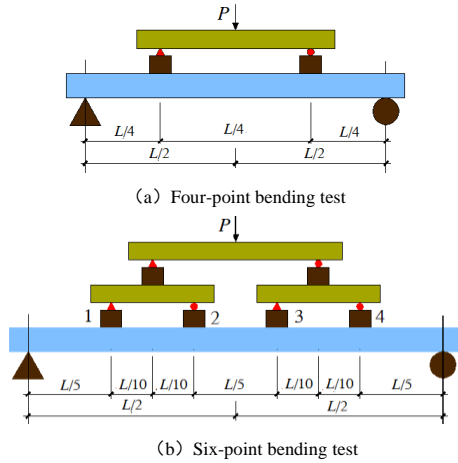


Fig. 2 Schematic view of the experimental setup

The external load was measured using load sensors placed in front of the jacks. The strains of profiled steel sheet and concrete were measured using strain gauges. The displacement and slip at the steel sheet–concrete interface were measured using linear variable differential transformer (LVDT) sensors. Fig. 3 shows the configuration of the LVDT sensors.

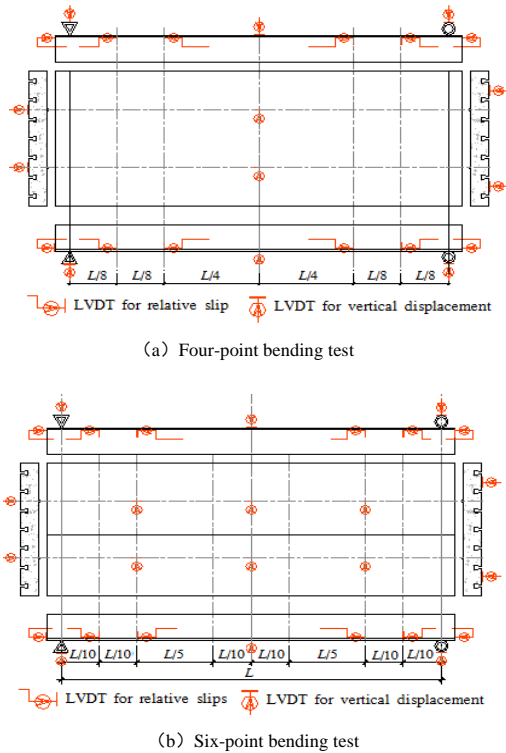


Fig. 3 Arrangement of the LVDTs

3. Test Procedures and Failure Modes

For a clear presentation of the tests, the specimens with spans of 2.0 and 3.4 m are referred to as short-span specimens, whereas those with spans of 4.8 and 6.0 m are referred to as long-span specimens.

3.1. Composite slab specimens without end anchorage

In this study, six specimens without an end anchorage were tested: three had trapezoidal profiles with different spans, and another three had dovetail profiles with different spans.

3.1.1. Trapezoidal-profiled specimens

The load bearing capacity of the trapezoidal-profile specimens decreased abruptly after reaching the ultimate load. At this point, the outer edges of the steel sheet and concrete at the mid-span developed large longitudinal cracks

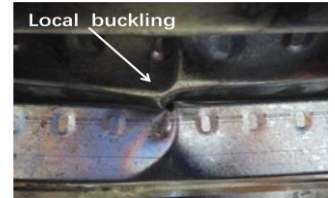
(Fig. 4(a)), the specimens exhibited significant slip at the anchoring end (Fig. 4(b)), and there were shear cracks running through the length of the specimens. Moreover, the upper and bottom flanges and troughs of the profiled steel sheet at the mid-span underwent significant buckling (Fig. 4c), leading finally to brittle longitudinal shear failures.



(a) Longitudinal crack



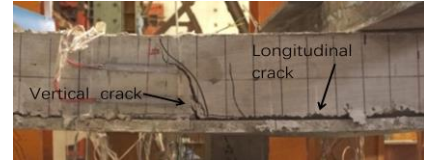
(b) End slip



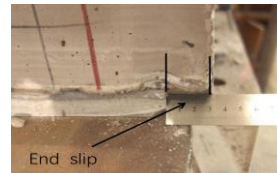
(c) Local buckling of steel sheet

Fig. 4 Failure mode of OBI-3

Two long-span specimens, OBIII-1 and OBIV-2, had the same shear span-depth ratio and were loaded similarly. The long-span specimens exhibited similar behavior to those of the short-span ones during the initial stage of the loading but developed longitudinal cracks and end-slip at a load of approximately $0.45 P_u$. After the onset of slipping, the load increased slowly, whereas the mid-span deflection increased more rapidly, resulting in longitudinal shear failure. At the point of failure, the bond between the steel sheet and concrete interface at the mid-span of the specimens failed (Fig. 5(a)) and the supporting ends of the specimens exhibited significant slip (Fig. 5(b)). In addition, the troughs of the steel sheet appeared local buckling near mid-span loading point 4 (Fig. 5(c)).



(a) Longitudinal crack



(b) End slip



(c) Local buckling of steel sheet

Fig. 5 Failure mode of OBIII-1 and OBIV-2

3.1.2. Dovetail-profiled specimens



(a) Crack load



(b) Failure load



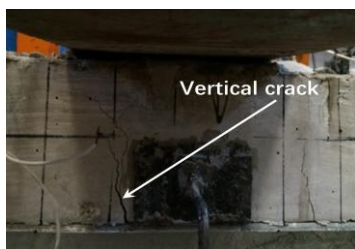
(c) End slip

Fig. 6 Failure behaviors of NBI-1

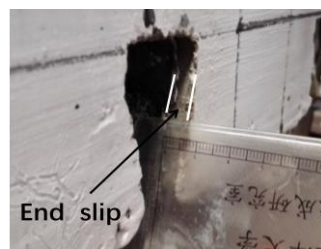
At a load of approximately 98 kN ($0.52 P_u$), NBI-1, a short-span specimen, exhibited an abrupt increase in the mid-span deflection and bond slip at the steel-sheet – concrete interface. At a load of 141 kN ($0.75 P_u$), the specimen developed vertical cracks at the mid-span (Fig. 6(a)). At a load of 189 kN (P_u), the major cracks near the mid-span loading points became wider (Fig. 6(b)) and the edges of the steel sheet at the two sides of the specimen separated from the concrete and bloated outward. In addition, the mid-span deflection increased rapidly, the bond at the profiled steel-sheet–concrete interface started slipping at the ends of the specimen (Fig. 6(c)), and the test load rapidly decreased, resulting in a longitudinal shear failure.



(a) Longitudinal crack



(b) Vertical cracks



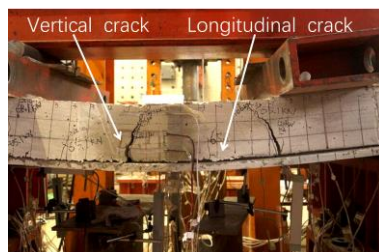
(c) End slip

Fig. 7 Failure mode of NBIII-4

Long-span specimens NBIII-4 and NBIV-4 exhibited similar behavior during the initial stage of loading. At a load of approximately $0.4 P_u$, the specimens exhibited slipping at the steel sheet – concrete interface and longitudinal cracks at both sides of mid-span loading points 2 and 3 (Fig. 2(b)). At a load of approximately $0.65 P_u$, the specimens exhibited vertical cracks at the mid-span side of loading point 3. At a load of approximately $0.8 P_u$, the steel sheet at the two sides of the specimens exhibited longitudinal cracks and bloated outward near loading points 1 and 4 (Fig. 7(a)), which was accompanied by a temporary load decrease. As the load stabilized, the load bearing capacity of the specimens increased continuously. At the ultimate load, P_u , the width of the vertical cracks rapidly increased (Fig. 7(b)), and the specimens experienced rapid slipping at the steel-sheet–concrete interface (Fig. 7(c)), resulting in a longitudinal shear failure.

3.2. Composite slab specimens with end –anchorage studs

3.2.1. Trapezoidal-profiled specimens



(a) Longitudinal and vertical crack



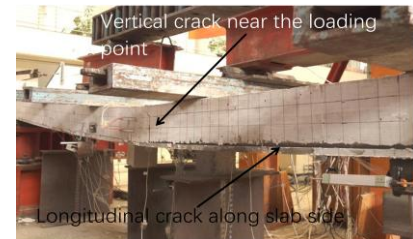
(b) End slip



(c) Local buckling of the steel sheet

Fig. 8 Failure mode of short-span trapezoidal-profile specimen

Short-span specimens OBI-1 and OBI-2 exhibited the following behavior during the loading: At a load of approximately $0.3 P_u$, the first vertical crack developed in the concrete near the loading point. At a load of approximately $0.5 P_u$, the specimens exhibited slight slipping at the ends and longitudinal cracks in the steel sheet–concrete interface near the loading points. As the test load increased, the longitudinal cracks extended to the ends of the specimens. At the ultimate load, P_u , the mid-span deflection rapidly increased, the bond between the steel sheet and concrete at the two sides failed (Fig. 8(a)), and tearing finally occurred in the steel sheet around the studs. The slipping at the end of the specimens rapidly increased (Fig. 8(b)), local buckling deformation developed in the steel sheet below the loading point (Fig. 8(c)), and the specimens lost their bearing capacity, resulting in longitudinal shear failures.



(a) Longitudinal crack



(b) End slip

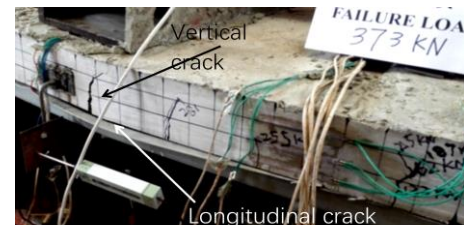


(c) Local tearing of the steel sheet

Fig. 9 Failure mode of long-span trapezoidal-profile specimen

At a load of approximately $0.2 P_u$, the long-span composite slab specimens having anchoring studs developed vertical cracks near mid-span loading point 3. At a load of approximately $0.3 P_u$, first, longitudinal cracks developed near mid-span loading points 2 and 3, and as the load increased, they extended toward the supports. Moreover, the specimens underwent slipping at the steel sheet–concrete interface. During the latter stage of loading, the mid-span deflection increased more rapidly, the longitudinal cracks at the steel-sheet–concrete interface extended to the ends of the specimens, and the specimens lost their bearing capacity, resulting in longitudinal shear failures. At the point of failure, the bond of the steel sheet–concrete interface at the mid-span failed (Fig. 9(a)), the slipping at the ends of the specimens became significant (Fig. 9(b)), and the profiled steel sheet experienced local tearing at the ends, but no buckling (Fig. 9(c)).

3.2.2. Dovetail-profiled specimens



(a) Longitudinal crack



(b) End slip



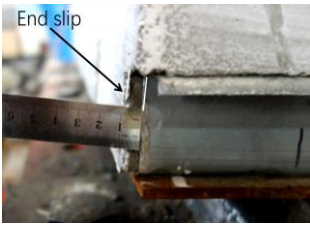
(c) Local tearing of the steel sheet

Fig. 10 Failure mode of short-span dovetail-profile specimen

At a load of 130 kN ($0.35 P_u$), NBI-3, a short-span specimen, developed vertical cracks near the loading points. As the load increased, longitudinal cracks developed at the steel sheet–concrete interface at the two sides of the specimen at the mid-span. At a load of 240 kN ($0.64 P_u$), significant slipping developed at the steel sheet–concrete interface at the ends of the specimen. As the load increased, the steel sheet at the two sides at the mid-span bloated outward (Fig. 10(a)), and the mid-span deflection increased rapidly. At a load of 373 kN (P_u), tearing developed in the troughs of the steel sheet at the ends of the specimen (Fig. 10(b) and Fig. 10(c)), the slipping rapidly increased, and the specimen was no longer appropriate for load bearing, resulting in a longitudinal shear failure.



(a) Longitudinal crack



(b) End slip



(c) Crack of concrete beneath loading point

Fig. 11 Failure mode of long-span dovetail-profile specimen

The failure behavior of the long-span specimens was described using the most typical specimen, NBII-2. At a load of 76 kN ($0.48 P_u$), vertical cracks developed at the mid-span and longitudinal cracks developed at the steel sheet–concrete interface at the two sides of the specimen in the regions of mid-span loading points 3 and 4. Moreover, as the load increased, the cracks extended toward the supports. At a load of 128 kN ($0.82 P_u$), the specimen underwent significant slipping at the steel sheet–concrete interface (Fig. 11(b)). As the load continued to increase, the steel sheet at the two sides of the specimen bloated outward, the width of the major cracks near loading point 3 increased, the mid-span deflection exceeded $L/50$, and the ultimate load, P_u , was 157 kN. The other long-span specimens exhibited failure behavior similar to that of specimen NBII-2.

The cracking load P_{cr} , slipping load P_s , and ultimate load P_u of dovetail-profiled composite slab specimens increase with the increasing of thickness of steel sheets, depths of cross-sectional, and arrangement of additional reinforcement.

4. Test Results and Discussion

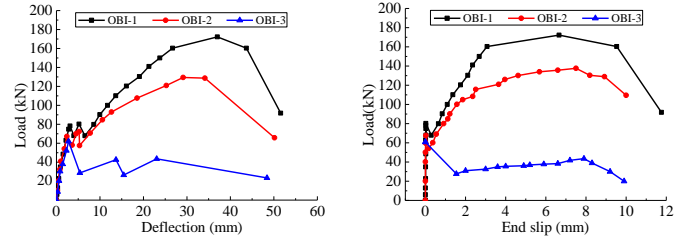
A comparative analysis of the different specimens based on the depth of slabs was conducted to study the performance and failure behavior of the short and long-span specimens.

4.1. Trapezoidal-profiled specimens

4.1.1. Short-span specimens

Fig. 12 shows the load–mid-span deflection curves and load–end slip curves of the specimens with a span of 2.0 m. Fig. 12(a) shows that during the initial stage of loading, the specimens have similar stiffness and behavior. Furthermore, the bearing capacity of the specimens with an end anchorage (OBI-1 and OBI-2) is higher than that of those without it (OBI-3) by 174% and 129%, respectively. Fig. 12(b) shows that as the load increases, the bond at the steel sheet–concrete interface of the specimens without an end anchorage fails after the onset of slipping. In addition, the load bearing capacity significantly decreases, the slipping continues to increase, and the specimens are no longer suitable for load bearing and fail. Contrastingly, the specimens with an end anchorage have a higher bearing capacity because the anchoring studs serve to restrain the slipping and increase the interaction at the profiled steel sheet–concrete interface. The composite slab specimens without an end anchorage exhibit more evident longitudinal shear failures than those with it. Contrastingly, the latter exhibit an extremely good ductility and

a significantly higher bearing capacity than the former specimens.



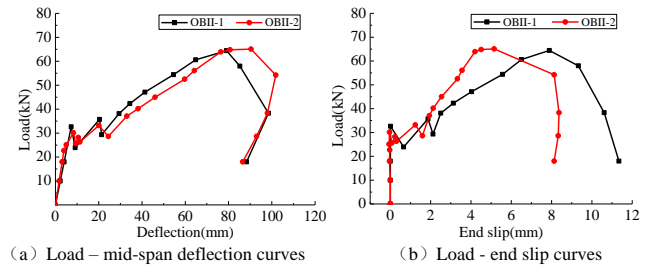
(a) Load-mid-span deflection curves

(b) Load-end slip curves

Fig. 12 Load-deflection and Load-slip curves of the specimens with a span of 2.0 m

4.1.2. Long-span specimens

All the thin slab specimens with a span of 3.4 m had an end anchorage and exhibited the same failure behavior. Compared with thick slab specimens with a span of 2.0 m having a similar end anchorage, they experienced similar longitudinal shear failures, but had a good loading bearing capacity and much better ductility, as shown in Fig. 13(a) and Fig. 13(b). Please, do not alter the title page header and make sure that you comply with the headers of the other pages.

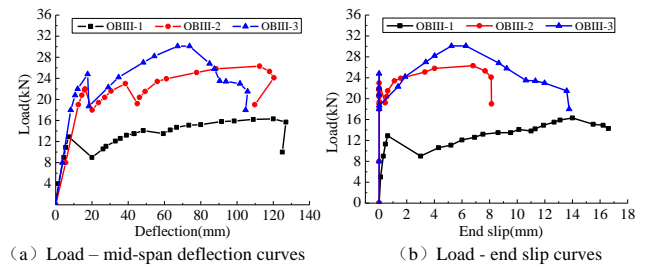


(a) Load-mid-span deflection curves

(b) Load-end slip curves

Fig. 13 Load-deflection and Load-slip curves of the specimens with a span of 3.4 m

At spans of 4.8 m and 6.0 m, all the specimens without an end anchorage and those with it exhibited similar failure behavior within their separate groups, but with the two groups of specimens displaying different failure behavior compared to each other.



(a) Load-mid-span deflection curves

(b) Load-end slip curves

Fig. 14 Load-deflection and Load-slip curves of the specimens with a span of 4.8 m

The load-mid-span deflection curves shown in Fig. 14(a) and Fig. 15(a) and the load-end slip curves shown in Fig. 14(b) and Fig. 15(b) reveal that the specimens with and without an end anchorage exhibit similar behavior during the initial stage of the loading. However, as the bond at the steel sheet–concrete interface fails, the specimens without an end anchorage experience longitudinal shear failure owing to the large end slip. Contrastingly, the specimens with an end anchorage have a significantly high bearing capacity and ductility and undergo ductile longitudinal shear failure because the studs serve to restrain the slip at the profiled steel sheet–concrete interface and the end slip is affected by the external loading. At a span of 4.8 m, the specimen with an end anchorage, OBI-2, has a higher bearing capacity than the specimen without it, OBI-1, by 41.7%. At a span of 6.0 m, the specimen with an end anchorage, OBI-2, has a higher bearing capacity than the specimen without it, OBI-1, by 31.3%. The high-depth specimens possess significantly strong cross-sectional flexural stiffness and longitudinal shear strengths. More specifically, at a span of 4.8 m, specimen OBI-3 has a higher bearing capacity than specimen OBI-2 by 32%. Furthermore, at span of 6.0 m, specimen OBI-3 has a higher bearing capacity than OBI-2 by 16.4%.

Table 4

Test result for load carrying capacity and failure mode of trapezoidal-profile specimens

No	Specimens	P_{cr} (kN)	P_s (kN)	$P_{1/250}$ (kN)	P_u (kN)	M_u (kN.m)	M_p (kN.m)	M_u/M_p	Δ_u (mm)	s (mm)	Failure mode
1	OBI-1	50.0	74.8	84.6	171.8	44.3	52.8	0.84	32.2	3.6	ductile
2	OBI-2	41.2	62.1	72.5	142.5	36.9	52.8	0.7	31.62	7.5	ductile
3	OBI-3	38.3	57.5	30.6	62.2	16.9	52.8	0.32	3.52	12	brittle
4	OBII-1	14	17.1	19.1	56.4	31.7	40.4	0.78	75.60	7.5	ductile
5	OBII-2	13	19	17.6	56.1	31.5	40.4	0.78	77.1	7.6	ductile
6	OBIII-1	12	15	9.5	16.3	18.0	44.5	0.4	119.0	14.0	brittle
7	OBIII-2	9	18	13.2	23.1	22.9	44.5	0.51	103.6	7.2	ductile
8	OBIII-3	10	22	16.5	30.5	30.1	61.1	0.49	66.79	6.9	ductile
9	OBIV-1	12	27.5	21.9	35.2	44.3	74.7	0.59	100.5	6.8	ductile
10	OBIV-2	11	19.5	19.5	26.8	36.7	74.7	0.49	145.2	17.6	brittle
11	OBIV-3	15	19	27.6	41	53.6	100.7	0.53	70.62	6.3	ductile

Note: P_{cr} is the cracking load of concrete; P_s is the slipping load; $P_{1/250}$ is the load about mid-span deflection reaches 1/250 span; P_u is the ultimate load; M_u is the test ultimate moment; M_p is the plastic moment; Δ_u is the mid-span deflection corresponding to the ultimate load; s is the end slip corresponding to the ultimate load

Table 4 lists the characteristic loads, failure behavior, measured bearing capacity, and theoretical plastic bearing capacity of the trapezoidal-profiled specimens. Table 4 shows that the specimens with an end anchorage have a remarkably larger M_u/M_p ratio than those without it. The increase in the ratio is more at short spans than that at long spans. The increase in the ratio of the long-span specimens indicates that they have a larger bonding interface between the profiled steel sheet and concrete and a higher capacity to resist the slip at the interface. These characteristics indirectly improve the bonding at the profiled steel-sheet-concrete interface.

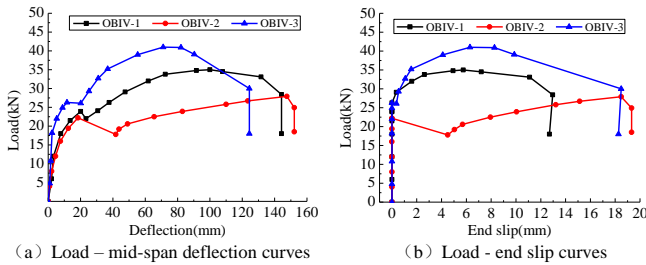


Fig. 15 Load-deflection and Load-slip curves of the specimens with a span of 6.0 m

4.2. Dovetail-profiled specimens

4.2.1. Short-span specimens

Fig. 16 shows the load-deflection curves and load-slip curves of 2.0-m span dovetail-profiled specimens. It suggests that during the initial loading stage, the specimens exhibit similar behavior. As the load increases and the bond at the profiled steel sheet-concrete interface gradually fails, the specimens without an end anchorage undergo slipping at the interface and an abrupt decrease in the bearing capacity. However, owing to the better interaction between the dovetail-profiled steel sheet and concrete, which serves to better restrain the slip at the profiled steel sheet-concrete interface, the bearing capacity can be recovered. The specimens without an end anchorage experience longitudinal shear failure only after the interaction at the profiled steel sheet-concrete interface is insufficient to resist the longitudinal shear stress at the interface. The specimens with an end anchorage have a significantly better bearing capacity than those without because the studs serve to restrain the slip at the profiled steel sheet-concrete interface, thereby improving the interaction between the profiled steel sheet and concrete. All the specimens with and without the end-anchorage studs undergo evident ductile longitudinal shear failure. The bearing capacity of the specimens with an end anchorage (NBI-2 and NBI-3) is higher than that of the specimen without it (NBI-1) by 90% and 97%, respectively.

At spans of 3.4 and 4.8 m, thin-slab specimens with end anchorages exhibit similar flexural failures, though they experience certain degrees of slip

at the steel sheet-concrete interface at the anchoring end. This is mainly because the small-depth specimens have a low cross-sectional bending bearing capacity and low longitudinal shear stress at the steel sheet-concrete interface. Fig. 17 shows the load versus deflection curves and load versus slip curves of the specimens at failure.

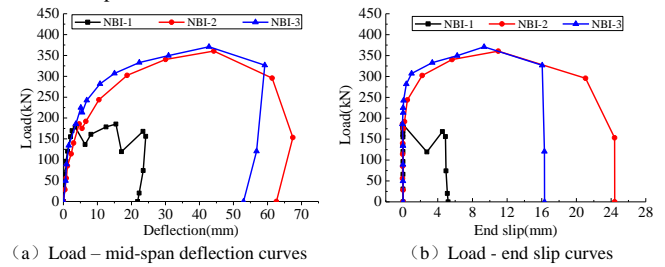


Fig. 16 Load-deflection and Load-slip curves of the specimens with a span of 2.0 m

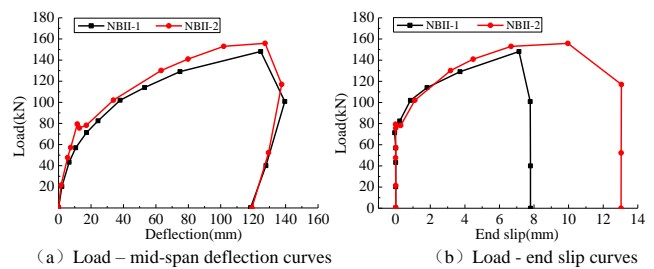


Fig. 17 Load-deflection and Load-slip curves of the specimens with a span of 3.4 m

4.2.2. Long-span specimens

Fig. 18 shows the load-deflection curves and load-slip curves of the specimens with a span of 4.8 m. It reveals that the specimens of thin slabs experience similar stresses during the initial stage of loading. As the load increases, the specimen without end anchorage (NBIII-4) experiences end slip firstly. It also undergoes local failure of the bond at the steel sheet-concrete interface. As the stress at the interface redistributes, the slip is restrained, and the cross-sectional bearing capacity recovers at a certain degree. When the external load exceeds the bond at the profiled steel sheet-concrete interface, the specimen experiences a ductile longitudinal shear failure. The specimens with an end anchorage exhibit different behavior, mainly in that they experience significantly bigger slipping loads than the specimens without an end anchorage and exhibited flexural failure. The ultimate load of specimen NBIII-3 (with an end anchorage) is 56% higher than that of specimen NBIII-4 (without an end anchorage).

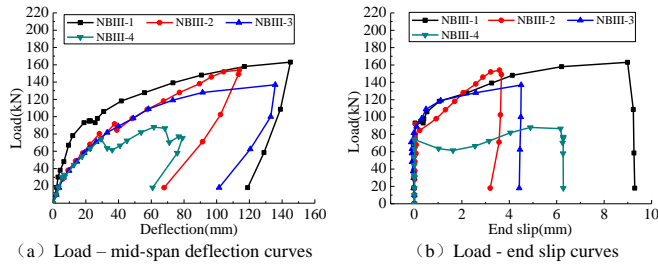


Fig. 18 Load-deflection and Load-slip curves of the specimens with a span of 4.8 m

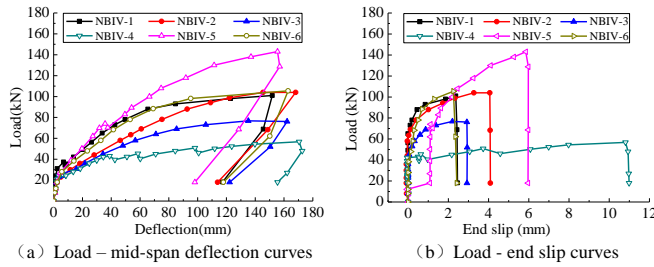


Fig. 19 Load-deflection and Load-slip curves of the specimens with a span of 6.0 m

Fig. 19 presents the load-deflection curves and load-slip curves of the specimens with a span of 6.0 m. It shows that the specimens of thin slabs with spans of 6.0 m and 4.8 m exhibit similar failure behavior, except the end-anchored specimens with a span of 6.0 m, which experienced ductile longitudinal shear failure. In comparison, the specimens with a span of 4.8 m experienced flexural failure. At a span of 6.0 m, the bearing capacity of the specimen with an end anchorage (NBIV-3) is 36.8% higher than that of the specimen without it (NBIV-4). The additional reinforcement contributed to an improved cross-sectional bearing capacity but had a little effect on the stiffness of the specimen. They served to restrain the end slip; however, at high loads, the end slip increased with an increase in the flexural deformation, with the magnitude of slip depending on the strength of the end anchorage.

Fig. 18 and fig. 19 show that the bearing capacity of the composite slabs can be improved by increasing their cross-sectional depth or decking them with thick steel sheets. Increasing the cross-sectional depth can significantly

improve the initial cross-sectional rigidity but has an insignificant effect on the cross-sectional rigidity and slip-resistance at high loads. In comparison, increasing the thickness of the profiled steel sheet can improve the interaction at the profiled steel sheet-concrete interface and, thereby, significantly reduce the slip at the steel sheet-concrete interface and cross-sectional rigidity at high loads.

Table 5 lists the characteristic loads, failure behavior, measured bearing capacity, and theoretical plastic bearing capacity of the dovetail-profiled composite slabs. It shows that the M_u/M_p ratio of the dovetail-profiled composite slabs can be effectively improved by strengthening their end anchorage, increasing the thickness of the profiled steel sheet, and implementing additional reinforcement at the troughs of the profiled steel sheet. This effectively improves the bond and longitudinal shear strength at the profiled steel sheet-concrete interface.

5. Parametric Analysis of Composite Slabs

To better reveal the failure behavior and performance of the composite slabs, specimens with different spans of 2.0, 3.4, and 6.0 m and a width of 1 m each were comparatively analyzed in terms of their load bearing capacity. The specimens in the same group had the same cross-sectional depth, span-depth ratio, and thickness of the steel sheet and were subjected to similar loading.

5.1. Short-span specimens

Fig. 20 shows the load-deflection curves and load-slip curves of without end-anchored specimens with a 2.0-m span. The small-span specimens without an end anchorage, OBI-3 and NBI-1, experience similar longitudinal shear failure, except specimen OBI-3 (with a trapezoidal-profile), which experiences a brittle failure. Contrastingly, specimen NBI-1 (with a dovetail-profile) undergoes a ductile failure. The dovetail-profiled specimen performs much better than the trapezoidal-profiled specimen because the latter has a smaller end slip during the initial stage of loading, and the end slip has a direct impact on the bearing capacity of composite slabs. After the onset of the end slip, the dovetail-profiled composite slab specimens can recover their bearing capacity, whereas the trapezoidal-profile specimens experience a remarkable decrease in their bearing capacity. The load-deflection curves show that the dovetail-profiled specimens have slightly higher cross-sectional rigidities than the trapezoidal-profiled specimens, mainly owing to the different cross-sectional geometries.

Fig. 21 shows the load-deflection curves and load-slip curves of the end-anchored specimens with a 2.0-m span. It reveals that the specimens of

Table 5
Test result for load carrying capacity and failure mode of dovetail-profile specimens

No.	Specimens	P_{cr} (kN)	P_s (kN)	$P_{1/250}$ (kN)	P_u (kN)	M_u kN.m	M_p kN.m	M_u/M_p	Δ_u (mm)	s (mm)	Failure mode
1	NB I -1	141	178.3	---	189	49.5	105.9	0.47	25.45	5.57	ductile
2	NB I -2	155	185	243.6	360	92.2	105.9	0.87	65.96	12.62	ductile
3	NB I -3	127	187.3	264.7	373	95.5	105.9	0.9	59.2	15.43	ductile
4	NB II -1	50	71	71.4	149	83.4	83.7	1	137.1	7.79	flexural
5	NB II -2	76	78	82.6	157	87.5	83.7	1.05	135.9	13.05	flexural
6	NBIII-1	50	90.1	96.1	163	127.3	120.6	1.06	142.9	9.23	flexural
7	NBIII-2	63	89.4	76	155	119.5	113.3	1.05	109.6	3.59	flexural
8	NBIII-3	48	70.2	76.6	137	106.5	91.1	1.17	116.0	2.59	flexural
9	NBIII-4	58	68.1	71.4	88	71.3	91.1	0.78	75.7	6.28	ductile
10	NBIV-1	35	73.1	60.3	100	102.4	157.5	0.65	151.8	2.37	ductile
11	NBIV-2	30	52.1	40.2	108	107.1	151.8	0.71	162.7	2.25	ductile
12	NBIV-3	28	49.7	42.8	78	80.1	120.6	0.66	161.6	2.92	ductile
13	NBIV-4	25.6	41.6	35.5	57	61.2	120.6	0.51	172.6	12.1	ductile
14	NBIV-5	38	82.1	66.5	152	146.7	186.0	0.79	154.6	1.11	ductile
15	NBIV-6	33	75.7	55.8	106	105.3	149.6	0.7	167.9	3.17	ductile

thick slab with the end anchorage have a remarkably high ductility. This is because the end-anchorage studs serve to restrain the slip at the profiled steel sheet–concrete interface, thereby indirectly improving the interaction at the steel sheet–concrete interface and significantly improving the bearing capacity. In addition, the maximum end slip is strongly correlated to the external load. Furthermore, from the onset of the interfacial slip to the ultimate bearing capacity, the end slip gradually increases with an increase in the external load, and the specimen exhibits good ductility.

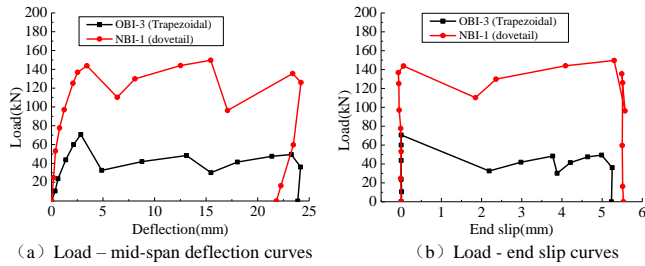


Fig. 20 Load–deflection and Load–slip curves of 2.0 m span specimen without anchorage slabs

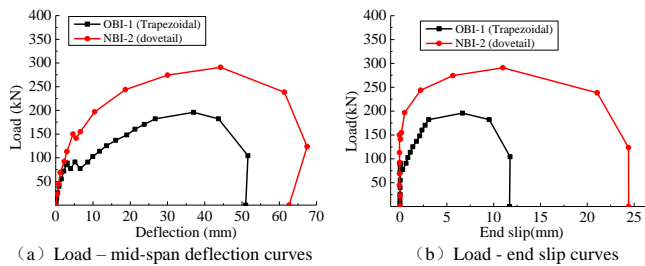


Fig. 21 Load–deflection and Load–slip curves of 2.0 m span specimen with anchorage slabs

Fig. 21 shows the load–deflection curves and load–slip curves of the end-anchored specimens with a 2.0-m span. It reveals that the specimens of thick slab with the end anchorage have a remarkably high ductility. This is because the end-anchorage studs serve to restrain the slip at the profiled steel sheet–concrete interface, thereby indirectly improving the interaction at the steel sheet–concrete interface and significantly improving the bearing capacity. In addition, the maximum end slip is strongly correlated to the external load. Furthermore, from the onset of the interfacial slip to the ultimate bearing capacity, the end slip gradually increases with an increase in the external load, and the specimen exhibits good ductility.

Fig. 22 shows the load–deflection curves and load–slip curves of the specimens with a span of 3.4 m. These specimens have much larger span–depth ratios than the specimens with a span of 2.0 m. Fig. 22 also reveals that the mid-span deflections and end slips of the two kinds of composite slabs gradually increase with an increase in the external load and exhibit evident ductile behavior during the loading. The only difference is that the trapezoidal-profiled specimens undergo longitudinal shear failure, whereas the dove-tail specimens experience flexural failure.

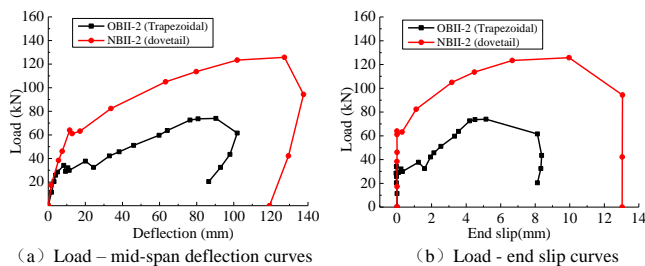


Fig. 22 Load–deflection and Load–slip curves of 3.4 m span specimen with anchorage slabs

5.2. Long-span specimens

The long-span composite slab specimens with both the cross-sectional geometries were analyzed using the specimens with a span of 6.0 m. Fig. 23 shows the load–deflection curves and load–end slip curves of the specimens

of thin slab without an end anchorage and with a 6.0 m span. It exhibits that the specimens with both the cross-sectional geometries experience ductile longitudinal shear failure. The dovetail-profiled specimens have a much better ductility than the trapezoidal-profiled specimens, and after the onset of the end slip, the former has a more evident increase in the bearing capacity than the latter. Furthermore, the end slip of the dovetail specimens changes with the variation in the load, whereas that of the trapezoidal-profiled specimens is accompanied by their failure.

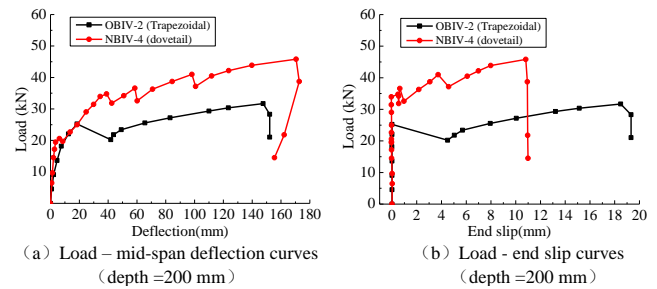


Fig. 23 Load–deflection and Load–slip curves of 6.0 m span specimen without anchorage slabs

Fig. 24 shows the load–deflection curves and load–end slip curves of the end-anchored specimens of thin slab with a 6.0-m span. Fig. 24(a) shows that the trapezoidal-profiled specimens exhibit a more evident increase in the mid-span deflection and end slip during the loading than the dovetail-profiled specimens. The effect of the end anchorage on the bearing capacity improvement is less significant for the trapezoidal-profiled specimens than that for the dovetail-profiled specimens. The bearing capacity of the dovetail-profiled specimens is significantly improved, with the end slip restrained to a larger extent, whereas that of the trapezoidal-profile specimens improves only insignificantly. All the specimens with both the cross-sectional geometries undergo ductile failure, but the dovetail-profiled specimens have a significantly better ductility than the trapezoidal-profile specimens.

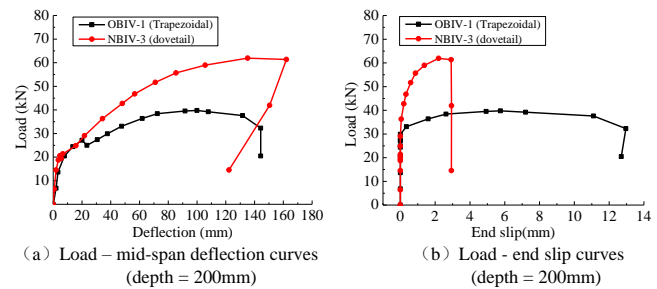


Fig. 24 Load–deflection and Load–slip curves of 6.0 m span specimen with anchorage thin slabs

Fig. 25 shows the load–deflection curves and load–end slip curves of the end-anchored specimens of thick slab with a 6.0 m span.

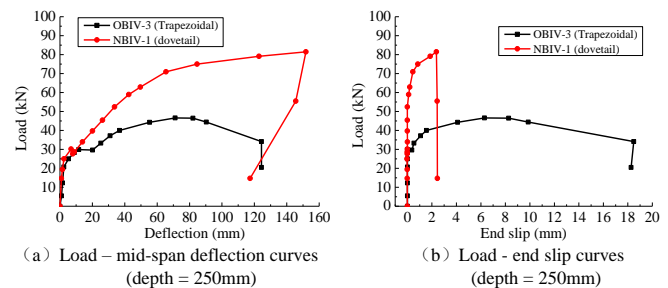


Fig. 25 Load–deflection and Load–slip curves of 6.0 m span specimen with anchorage thick slabs

It shows that the end-anchorage studs contribute to a more significant improvement in the end slip and load bearing capacity of the dovetail-profiled specimens. In terms of the failure behavior, the end-anchorage studs contribute to only an insignificant improvement in the slip-resistance of the steel sheet–concrete interface of the trapezoidal-profiled specimens. All the

specimens with both the cross-sectional geometries experience ductile longitudinal shear failures, but the dovetail-profile specimens have a better ductility and slip-resistance. In comparison, the trapezoidal-profile specimens have an evident insufficient slip-resistance and a less safety buffer than the dovetail-profiled specimens.

Table 6 compares the measured load bearing capacity, M_u , and cross-sectional plastic bearing capacity, M_p , of the specimens with both the cross-sectional geometries. The composite slab specimens with an end anchorage have much larger M_u/M_p ratios than the specimens without it. It indicates that the end anchorage contributes to a significant improvement in the bond at the steel-sheet–concrete interface. At long spans, the specimens both with and without an end anchorage have similar M_u/M_p ratios. It indicates that the profiled steel sheet–concrete interface increases in area, and is more capable of restraining the slip at the interface at long spans, thereby indirectly improving the bond at the profiled steel-sheet–concrete interface.

Table 6

Comparison of bearing capacity between the trapezoidal-profile and dovetail-profile specimens

Span (m)	Depth (mm)	Anchorage	Trapezoidal profile				Dovetail profile			
			P_u	M_u	M_p	M_u/M_p	P_u	M_u	M_p	M_u/M_p
2.0	180	No	70.7	19.2	60.0	0.32	152.4	37.0	85.4	0.43
2.0	180	Yes	161.9	41.9	60.0	0.7	290.3	74.4	85.4	0.87
2.0	180	Yes	195.2	50.3	60.0	0.84	300.8	77.0	85.4	0.9
3.4	150	Yes	64.1	36.0	45.9	0.78	126.6	67.3	67.5	1
3.4	150	Yes	63.75	36.0	45.9	0.78	131.5	70.6	67.5	1.05
6.0	200	No	30.5	41.7	69.4	0.6	46.0	49.4	97.3	0.51
6.0	200	Yes	40.0	50.3	69.4	0.72	62.9	64.6	97.3	0.66
6.0	250	Yes	46.6	60.9	93.1	0.65	80.6	82.6	127.0	0.65

6. Conclusions

In this paper, the load bearing capacity and failure modes of composite slabs with different means of end anchorage were investigated through the test of 26 composite slab specimens with two cross-sectional profiles considering different details of the end anchorage. The effects of the parameters such as the end anchorage, span-to-depth ratio, and steel sheeting profile on the load bearing capacity and failure mode of the composite slabs both with and without an end anchorage were experimentally studied. The following conclusions can be drawn from this paper:

1. The end anchorage contributes to a significant improvement in the load bearing capacity and failure mode of the composite slabs. The contribution of the end anchorage to the bearing capacity improvement decreases with an increase in the span of composite slabs. Moreover, the degree of bearing capacity improvement varies with the cross-sectional geometry of the composite slabs.

2. Composite slabs without an end anchorage and subjected to external loading experience longitudinal shear failure in most cases, and the failure behavior of the composite slabs with the different cross-sectional geometries are related to the span-depth ratio. The composite slabs with an end anchorage subjected to external loading may experience ductile longitudinal shear failure or flexural failure.

3. The bearing capacity and slip-resistance of the composite slabs can be increased with the increasing of the profiled steel sheet. Additional reinforcement at the troughs of the profiled steel sheet can improve the load bearing capacity of the composite slabs but can only slightly improve their rigidity and slip-resistance.

4. Under the same conditions, the dovetail-profiled long-span composite slabs exhibit a better performance than the trapezoidal-profiled composite slabs.

Acknowledgements

This project was supported by the National Key R & D Program of China (2017YFC0703805), Key Research and Development Program of Liaoning Province (2017229006).

References

- [1] Porter, M.L. and Greimann, L.F., “Shear-bond strength of studed steel deck slabs”, Proceedings of Sevenths International Specialty Conference on Cold-Formed Steel Structures, St. Louis, MO, USA., University of Missouri at Rolla, 285–306, 1984.
- [2] Schuster, R. M. and Ling, W. C., “Mechanical Interlocking Capacity of Composite Slabs”, 5th International Specialty Conference on Cold-Formed Steel Structures, St. Louis, USA., 387–407, 1980.
- [3] European Standard, “Eurocode 4: design of composite steel and concrete structures – part 1-1: general rules and rules for buildings”, (EN 1994-1-1:2004), European Committee for Standardization, Brussels, 2004.
- [4] Abdullah, R. and Samuel, E. W., “New modeling and evaluation procedures for horizontal shear bond in composite slabs”, Journal of Constructional Steel Research, 65(4), 891–899, 2009.
- [5] Chen S., Shi X. and Qiu Z., “Shear bond failure in composite slabs-detailed experimental studies”, Journal of Steel and Composite Structures, 11(3), 233–250, 2011.
- [6] Abdullah R., Kueh A.B.H., Izni S.I. and Samuel E.W., “Characterization of shear bond stress for design of composite slabs using an improved partial shear connection method”, Journal of Civil Engineering and Management, 21(6), 720–732, 2015.
- [7] Valivonis J., “Analysis of behaviour of contact between the profiled steel sheeting and the concrete”, Journal of Civil Engineering And Management, 7(3), 187–194, 2006.
- [8] Tsalkatidis T. and Avdelas A., “The unilateral contact problem in composite slabs: experimental study and numerical treatment”, Journal of Steel Construction, 66(3), 480–486, 2010.
- [9] Chen S., Shi X. and Zhou Y., “Strength of composite slabs with end-anchorage studs”, Proceedings of the Institution of Civil Engineers-Structures and Buildings, 168(2), 127–140, 2014.
- [10] Daniels B.J. and Crisinel M., “Composite slab behavior and strength analysis. Part I: calculation procedure”, Journal of Structural Engineering, ASCE, 119(1), 16–35, 1993.
- [11] Rana M.M., Uy B. and Mirza O., “Experimental and numerical study of end anchorage in composite slabs”, Journal of Constructional Steel Research, 115, 372–386, 2015.
- [12] Degtyarev V.V., “Strength of composite slabs with end anchorages. Part II: Parametric studies”, Journal of Constructional Steel Research, 94, 163–175, 2014.
- [13] Patrick M., “Long-spanning composite members with steel decking”, Proc. Tenth Inter. Specialty Conf. on Cold-Formed Steel Structures, St. Louis, MO, USA, 81–102, 1990.
- [14] Widjaja B.R., and Samuel E.W., “Developments in long span composite slabs”, Engineering Journal (New York), 37(2), 73–82, 2000.
- [15] Jolly C.K. and Lawson R.M., “End anchorage in composite slabs: an increased load carrying capacity”, Journal of The Structural Engineer, 70(11), 202–205, 1992.
- [16] Chen S., “Load carrying capacity of composite slabs with various end constraints”, Journal of Constructional Steel Research, 59(3), 385–403, 2003.
- [17] Bode H. and Minas F., “Composite Slabs With and Without End Anchorage Under Static And Dynamic Loading”, Composite construction-conventional and innovative. International conference, 265–270, 1997.
- [18] Gholamhoseini A., Gilbert R.L., Bradford M.A. and Chang Z.T., “Longitudinal shear stress and bond-slip relationships in composite concrete slabs”, Journal of Engineering structures, 69, 37–48, 2014.
- [19] Johnson R.P. and Shepherd A.J., “Resistance to longitudinal shear of composite slabs with longitudinal reinforcement”, Journal of Constructional Steel Research, 82, 190–194, 2013.
- [20] British Standard, Structural Use of Steelwork in Building-Part 4: Code of Practice for Design of Composite Slabs with Profiled Steel Sheeting, (BS-5950:1994), British Standard Institution, London, 1994.
- [21] Ríos J.D., Cifuentes H., Martínez-De L.C.A. and Medina-Reguera F., “Numerical modelling of the shear-bond behaviour of composite slabs in four and six-point bending tests”, Journal of Engineering Structures, 133, 91–104, 2017.
- [22] Abdullah R. and Samuel E.W., “Determination of composite slab strength using a new elemental test method”, Journal of Structural Engineering, 133(9), 1268–1277, 2007.
- [23] Brekelmans J.W.P.M., Daniels B.J., Van Hove D.B.W.E.M. and Koukkari H., “Design Recommendations for Long Span Composite Slabs with Deep Profiled Steel Sheets”, Proceedings of the 1996 Engineering Foundation Conference on Composite Construction in Steel and Concrete III, Irsee, Germany. Workshop Composite Slabs, ASCE, 660–671, 1997.
- [24] Johnson, R. P., “Composite Structures of Steel and Concrete: Beams, Slabs, Columns, and Frames for Buildings”, Third Edition, Blackwell Scientific, London 2008.

DEVELOPMENT AND APPLICATION OF A MECHANICAL MODEL OF BEAM-TO-COLUMN CONNECTIONS OF STEEL STORAGE RACKS

Nattawut Asawasongkram ^{1,*}, Prakit Chomchuen ¹ and Prakit Premthamkorn ¹

¹ Department of Civil Engineering, Faculty of Engineering, Mahanakorn University of Technology,
Nong Chok, Bangkok, 10530, Thailand

* (Corresponding author: E-mail: nattawutcivil@gmail.com)

ABSTRACT

This paper focuses on the development of a mechanical model of beam-to-column connections of steel storage racks for predicting the initial rotational stiffness and flexural strength of the connection. An application of the proposed mechanical model for predicting the lateral behavior of steel storage racks is also evaluated. The connection model is developed based on the concept of component method suggested by Eurocode 3. A new practical methodology for evaluation of the flexural strength based on the actual failure mode is introduced. To validate the proposed mechanical model, extensive studies on experimental testing by cantilever and the portal tests specified in steel storage rack design specification are conducted. The validation shows that the performance of the proposed mechanical model is satisfactory for predicting the response of connection. Moreover, it reveals that a modification factor of initial rotational stiffness and initial looseness should be incorporated into a rack's connection model to improve the accuracy in predicting lateral behavior of steel storage frames.

ARTICLE HISTORY

Received: 7 January 2018
Revised: 3 February 2019
Accepted: 1 May 2019

KEYWORDS

Beam-to-column connections;
Component method;
Experimental testing;
Mechanical model;
Semi-rigid connections;
Steel storage racks

Copyright © 2019 by The Hong Kong Institute of Steel Construction. All rights reserved.

1. Introduction

In recent years, steel storage racks are extensively utilized in industries and large warehouses for storing products. Storage racks are simple structures consisting of open-section columns and horizontal beams. The column is punched with slotted holes along its length, and the beam is prefabricated with the so-called beam-end connectors on both ends. Assembly of the racks can be achieved by simply inserting the tabs on the beam-end connectors and sliding the connectors down into the slotted holes on the column. Fig. 1 illustrates a typical beam-to-column connection of steel storage racks.

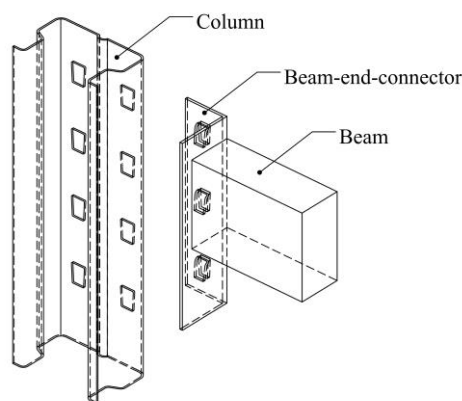


Fig. 1 Typical beam-to-column connection of steel storage racks

Despite being a simple structure, steel storage rack belies its complex connection's mechanical behavior. Accurate design and strength evaluation of the steel storage frame rely on the modeling of the moment-to-rotation ($M-\phi$) behavior of the beam-to-column connections. For estimating the connection behavior, three modelling options are available. These are empirical models based on experimental testing, finite element models, and mechanical models. Previously, most research on the estimation of connection response for the rack structures had been concentrated only on experimental testing models [1-8] and finite element models [5-6] [8]. The development of the mechanical model for this type of connection is very limited.

While experimental testing and finite element modelling yield satisfactory results, they can be costly, and time-consuming. The major drawback of these two methods is that the results are only applicable to the specific connection typologies, geometries, and material strength that undergo the testing and analysis. The mechanical models derive the connection's behavior directly from its geometries and material strength and hence adaptable to geometry and

material-strength variations of the connections. Recently, a theoretical approach for a mechanical model of storage rack connections has been proposed [9] by the concept of component method suggested by Eurocode 3 [10].

In this study, further development of the mechanical model of the beam-to-column connection of steel storage racks formulated by Kozłowski [9] has been conducted. Improvements of the model based on experimental findings from the authors [11] are proposed for a more simplistic moment-resistance calculation. Moreover, the mechanical models are developed for both increasing moment (hogging moment) and reversal moment (sagging moment) to emulate behavior under the two distinct loading conditions. Finally, the proposed model has been validated by comparing it to the results obtained from our testing. An application of the proposed model to predict lateral behavior of steel storage frames is also a highlight of this paper. In addition to the customary cantilever tests called for in design specifications, the portal tests is also conducted in this study in order to evaluate the performance for predicting lateral behavior of steel storage frames under various vertical loads.

2. Experimental study

This section presents extensive testing of the beam-to-column connections of steel storage racks. Two experimental testing methods in compliance with the international standards for design of steel storage racks are conducted for evaluation of the performance of the proposed mechanical model. Complete information of the experimental work is presented in previous research published by the authors [11].

The first experimental method is the cantilever test. This method provides a simple methodology for establishing the stiffness and strength of the connections. Moreover, the behavior of the connection under increasing moment and reversal moment, which may have different characteristics, can be distinguished by this testing method. Many researchers have conducted this test as shown the literature [1-2] [5-7]. The connection properties, which are the initial rotational stiffness and flexural strength from the cantilever test, will be used for evaluation of the proposed mechanical model in section 4.

The cantilever test cannot characterize the influences of the vertical service loading under real usage conditions, though it offers a simple approach for identifying the stiffness and strength of the connections. Thus, the portal test is conducted based on the international storage rack design specifications in this study. Beam-to-column connections are exposed to shear force, bending moment, and axial force in a portal test, which can represent the actual behavior of the connections. The results of the portal test are used to evaluate an application in which the proposed mechanical model is used to predict lateral behavior of steel storage racks. From literature, only a small number of portal tests have been reported [12-13] due to difficulty of the experiment setup. In this study, the portal testing is conducted on 6 testing frames, with varying

vertical loading in 2 levels. Each portal test involves 4 beam-to-column connections, resulting in 24 testing connections. In addition, the cantilever tests are carried out for 10 beam-to-column connections. Thus, the test specimens comprised 34 beam-to-column connections in total.

2.1. Specimen details

The test specimens of selected racks are chosen from a commercial manufacture where their configurations are commonly used. In particular, each specimen consists of a beam-end-connector welded to the end of a box beam. The beam-end connector comprised a 3 mm thickness of hot rolled angle section. The column and beam are fabricated from cold formed steel. The thickness of the column and beam is 2.5 mm and 2.0 mm respectively. Fig. 2 gives the detail for the beam-to-column connection and the column cross section.

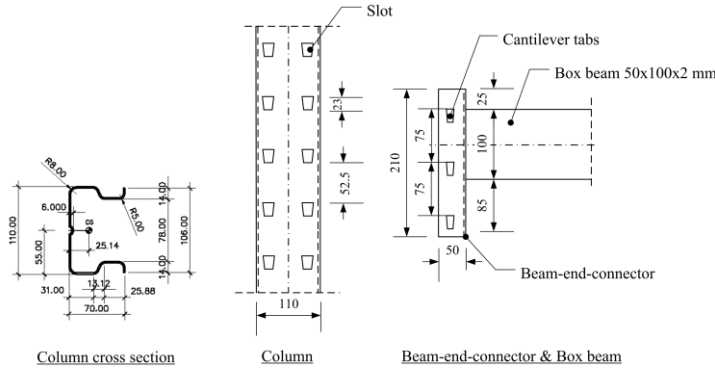


Fig. 2 Dimension of the specimen (Unit: mm)

Tensile tests on coupons extracted from the column, beam, and beam-end-connector are conducted for the purpose of indicating the actual mechanical properties of steel. The tensile tests are performed according to JIS [14] yielding the results shown in Table 1. Steel Material properties for the connection can be classified using the following ASTM standard: A611 [15], A283 [16] and A36 [17] for column, beam-end-connector, and beam, respectively.

Table 1
Steel mechanical properties

Part of the connection	Yield stress (Mpa)	Ultimate stress (Mpa)
Column	383	422
Beam-end-connector	296	374
Beam	381	419

2.2. The cantilever tests

For evaluation of the proposed mechanical model, the cantilever test setups are performed according to the international design standard for steel storage racks [18–20]. A cantilever of pallet beam joined to the midpoint of a short length of a column comprises the test setup. The column is firmly fixed at its top and bottom ends. Using a hydraulic jack placed on a load cell, the applied load is operated monotonically. To prevent any unwanted out-of-plane beam movement, the free end of the beam is restrained by a vertical guide made from a channel section. The applied loads, as well as beam and column deflections, are recorded at each increment of loading until failure takes place at the connection. Measurement of beam and column deflections is done using displacement transducers, LVDT1–LVDT9. The deflections for each load step are used to calculate the rotation of the connection. The overall layout of the experimental setups and the layout of the transducers are shown in Fig. 3. Utilizing ten connection samples comprising five hogging moment tests and five sagging moment tests, the cantilever tests are completed.

Fig. 4 shows the experimental results of the moment-rotation curve. The results show that the moment-rotation curve under hogging and sagging moments testing are quite different due to asymmetry of the connection configuration. The experimental curve expresses nonlinearity due to yielding of the connection parts, specifically steel tab and column perforation. The connection is considered to have failed when the steel tab in the tension side located farthest from the center of rotation is cut by the column perforation. At this point, the load carrying capacity drops suddenly. During the test, it was found that some of the tested connections exhibited looseness, indicated by a

short line at the beginning of the curve. This looseness occurred due to the steel tabs not fitting snugly in the column holes. When the rotation reaches about 0.002–0.006 rad, looseness is eliminated. In prior experimental studies, looseness of the connection was also uncovered [2] [5–6]. After the looseness ceases, the initial rotational stiffness of the connections is calculated [11]. Some of the tested connections do not show looseness because those connections are preloaded to prevent unwanted infirm effects at the beginning of the test setup. The averages of the initial rotational stiffness and flexural strength of the connections from the cantilever tests are shown in Table 2.

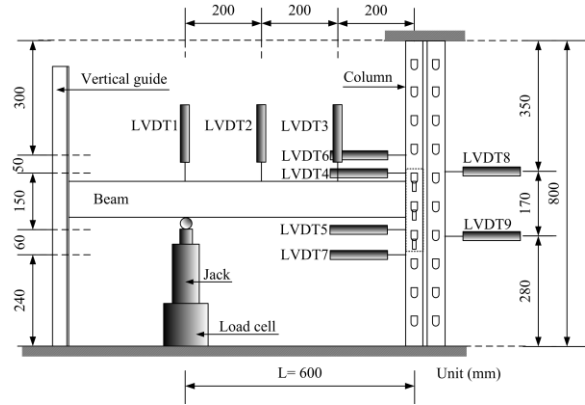
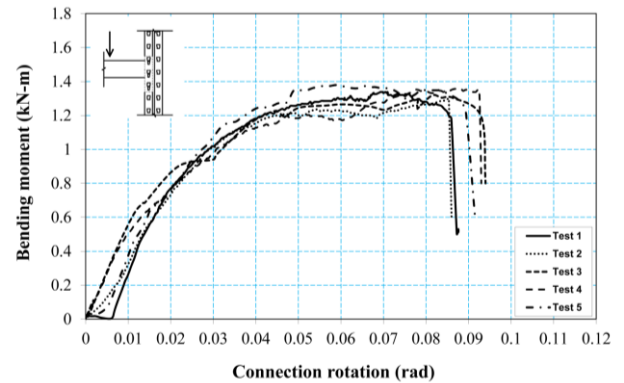


Fig. 3 Details of cantilever test setup

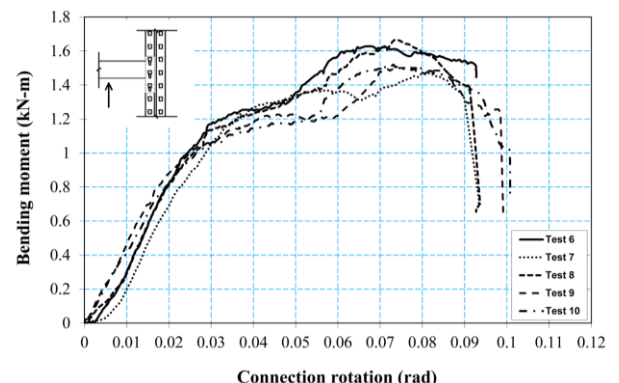
Table 2

Average value of the initial rotational stiffness and flexural strength of beam-to-column connections obtained from the cantilever tests

	Hogging moment	Sagging moment
Initial rotation stiffness (kN-m/rad)	$S_{j,ini} = 62.50$	$S_{j,ini} = 60.10$
Flexural strength (kN-m)	$M_u = 1.33$	$M_u = 1.56$



(a) Hogging moment



(b) Sagging moment

Fig. 4 Moment-rotation curves of the connections from the cantilever tests

2.3. The portal tests

In this study, the portal test [18–20] is performed according to the standard testing method to study steel storage frame behavior under lateral loads. Two portal frames fixed to hinge supports, which are fastened to a very stiff concrete floor, comprise the testing frame. Light lip channel beams are used to connect between the two portal frames in transverse directions. Fig. 5 illustrates the portal test setup. The length of portal frame is 2500 mm between column center lines. The height of portal frame is 700 mm, measured from each hinge support to the center of each horizontal beam. The space between the two portal frames is 1000 mm. For the purpose of transferring lateral loads to each portal frame equally, the horizontal rigid transfer beam is bolted to the portal frame. Lateral loads are applied to the transfer beam by a hydraulic jack mounted on a load cell fixed to a very stiff steel support connected to the concrete floor. The lateral displacement of the portal frame is measured by four displacement transducers (LVDT1–LVDT4) which are set on the columns level to the center line of the portal beam. To measure the sliding of the columns, other displacement transducers (LVDT5–LVDT8) are set at the bottom of the columns. The lateral loads and corresponding lateral displacements are recorded at each increment of loading until failure takes place at the connection.

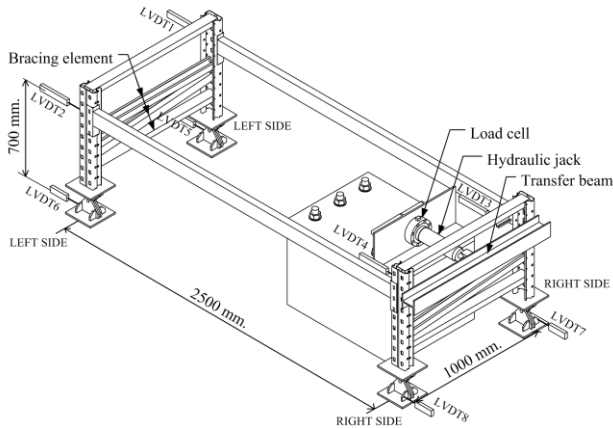


Fig. 5 Details of portal test setup



(a) No loading



(b) Normal loading (2 kN/m)

Fig. 6 Loading intensity for portal test setup

The loading intensity on steel storage racks may change frequently under service conditions. Thus, two distinctive levels of vertical loading were chosen in order to investigate the connection behavior under actual usage conditions. In this study, the two vertical loading levels are “no loading” and “normal

loading”. The normal loading level has a total load of 2.00 kN/m. This loading level corresponds to 40% of the allowable moment of the beam, which is assumed to represent the normal service loading condition on the structure. As shown in Fig. 6, sand bags resting on ordinary wood pallets are used to simulate the vertical loads. Portal tests are carried out on six frames, comprised of three testing frames for each loading level.

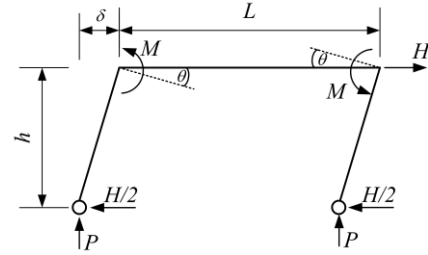


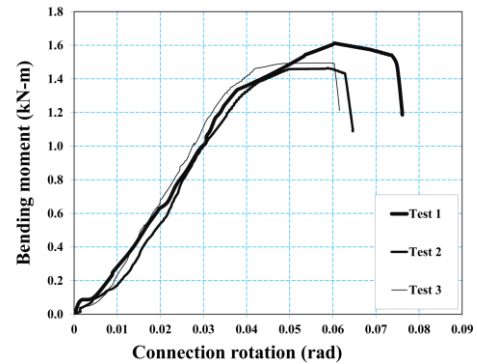
Fig. 7 Deformation of portal frame under lateral loading

The moments (M) and rotation (θ) of the beam-to-column connection in the portal frame are given as Eq. 1 and Eq. 2, respectively, illustrated in Fig. 7 [12].

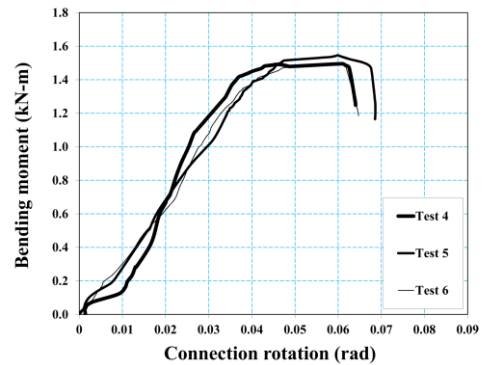
$$M = \frac{H}{2}h + P\delta \quad (1)$$

$$\theta = \frac{\delta}{h} - \left(\frac{Mh}{3EI_c} + \frac{ML}{6EI_b} \right) \quad (2)$$

where H is the lateral load applied to one portal frame, h is the height of portal frames, P is the axial force in a column due to a vertical load, and δ is the lateral displacement of the portal frame. δ is taken as the average recorded displacement obtained from displacement transducers LVDT1 to LVDT4, E is a Young's modulus, I_c and I_b are moment of inertia of the column and the portal beam respectively, and L is the horizontal distance between the centerlines of the columns. Fig. 8 shows the test results for the portal tests with two distinct vertical loading levels.



(a) Hogging moment



(b) Sagging moment

Fig. 8 Moment-rotation curves for the portal tests with two distinct vertical loading levels

The following observations can be made based on the portal test results. A failure occurs with the connection at the right side of the portal frame when the steel tab in the tension side placed farthest from the center of rotation is cut by the column perforation, like the cantilever test results. This can be explained by the force transferring mechanism of the connection as follows. At the initial stage, before the lateral load is applied to the portal frame, both sides of the beam-to-column connections have an initial hogging moment and vertical shear force (M_1 , V_1) due to vertical load, as can be seen in Fig. 9 (a). The vertical load comes from sand bags, wood pallets and the weight of the horizontal beam itself. Subsequently, when the lateral load is applied, the connection at the left side of the portal frame is subjected to a sagging moment, whereas the connection at the right side undergoes a hogging moment, as shown in Fig. 9 (b). This hogging moment and the shear force caused by the lateral load (M_2 , V_2) at the right side connection will combine with the initial hogging moment and shear force caused by the vertical load (M_1 , V_1). This force combination makes the connection at the right side of the portal frame reach its moment capacity before that on the left side. Another observation from the experimental results is that the moment-rotation curves exhibit looseness at the initial stage of both vertical load levels because the steel tabs do not fit with the column perforation. As shown in Fig. 8, the looseness is represented by a short line with a low slope value at the beginning of the curve.

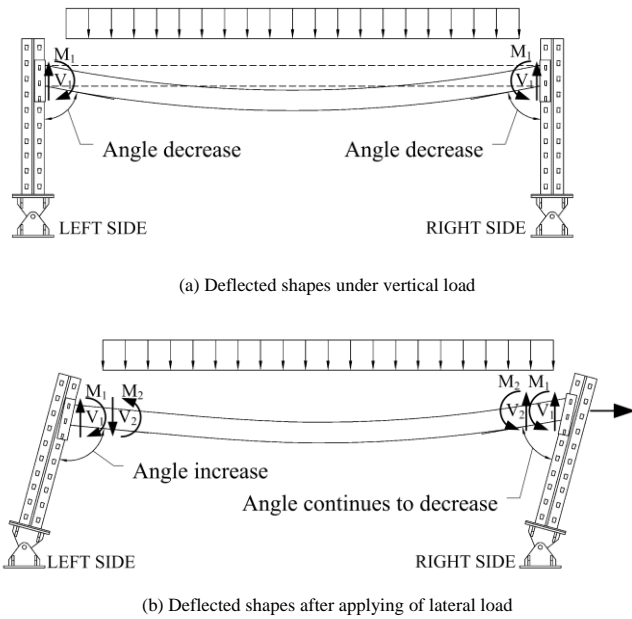


Fig. 9 Illustration of portal frame deflected shapes

3. Mechanical model of beam-to-column connections by component method

Eurocode 3 [10] outlines an analytical procedure so-called component method for determination of the design characteristics of semi-rigid beam-to-column connections. The code suggests that non-linear characteristics of the connection can be represented by linearized approximations such as bi-linear and tri-linear relationships. The design characteristics shall determine two main properties of the connections: moment resistance and rotational stiffness. Fig. 10 illustrates the concept of the analytical procedure outlined in Eurocode 3 for an unstiffened welded beam-to-column connection. The main properties depend on resistance of the components in three critical zones: tension zone, compression zone, and shear zone of the connection.

The component method consists of three main steps: dividing the connection into its basic components in which each one is represented by an elastic spring, evaluation of both stiffness and strength of each component, and finally all components being assembled into one mechanical model to determine the strength and stiffness capacity of the whole connection.

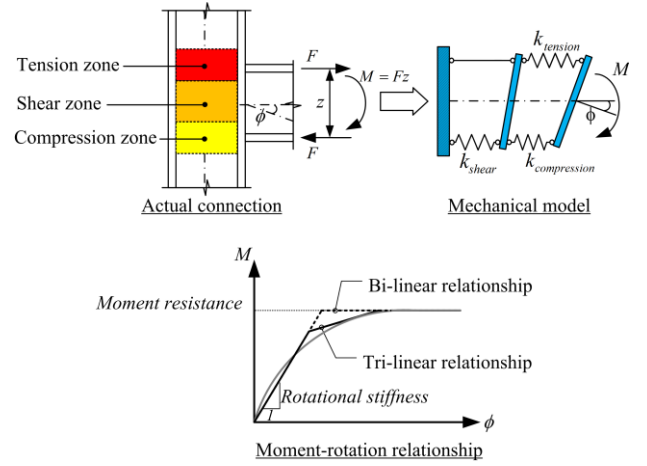


Fig. 10 Systematic model of beam-to-column connection according to Eurocode 3

In accordance with Eurocode 3, the initial rotational stiffness of the connection can be computed as:

$$S_{jmi} = \frac{M}{\phi} = \frac{Ez^2}{\sum \frac{1}{K_i}} \quad (3)$$

where E is elastic modulus, z is the lever arm between tension and compression springs, and K_i is the stiffness of each component. The connection moment resistance $M_{j,Rd}$ is governed by the weakest component as given by:

$$F_{Rd} = \min[F_{Rd,i}] \quad (4)$$

$$M_{j,Rd} = F_{Rd}z \quad (5)$$

where $F_{Rd,i}$ is the strength of component i .

Various mechanical models have been proposed in the past for several connection typologies using the component method [21-25]. However, there is no specific provision for the evaluation of beam-to-column connections for steel storage racks in those contexts. The lack of code specification means that there is considerable scope for development of an analytical procedure for predicting the behavior of beam-to-column connections of steel storage racks. This section provides procedure for determination of the initial stiffness and moment resistance of the rack's connections.

The following components are considered to be the basic components for evaluating stiffness of the beam-to-column connections in steel storage racks as illustrated in Fig. 11.

- Column web in tearing ($k_{cw,tear}$)
- Column web in bearing ($k_{cw,b}$)
- Column web in tension or compression ($k_{cw,t}$ or $k_{cw,c}$)
- Column web in shear ($k_{cw,s}$)
- Tabs in shear ($k_{t,s}$)
- Connector in bending and shear (k_{co})
- Connector web in tension or compression (k_{cwo})
- Beam flange in tension or compression (k_{bf})

The column web in shear component is not a major contributor to the initial rotational stiffness, according to the study of Zhao [26]. Moreover, the shear deformation of the column webs cancels each other out for the internal connection, upon which a two-sided bending moment is acted from the beam. Therefore, in this study, the column web in shear is neglected. The last component is only considered in the determination of the connection flexural strength. The full derivation of the basic components contributing to the mechanical model is outside the scope of this study, however available methodologies can be found in the companion paper [27]. Table 3 provides a summary of the initial stiffness and strength of each basic component.

A mechanical model adopted to predict the initial rotational stiffness of beam-to-column connections in steel storage racks is shown in Fig. 12. Each spring component in a mechanical model would be assembled in parallel or series, depending on the relevant geometries.

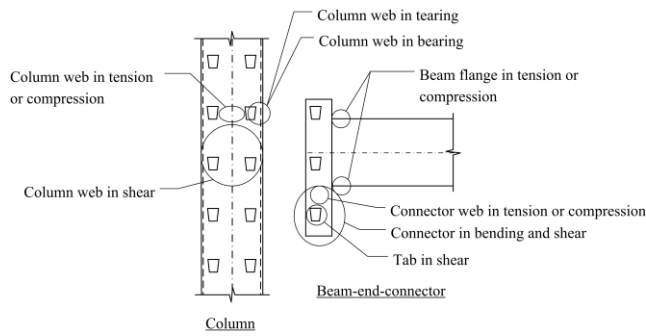


Fig. 11 Basic components of beam-to-column connections in steel storage racks

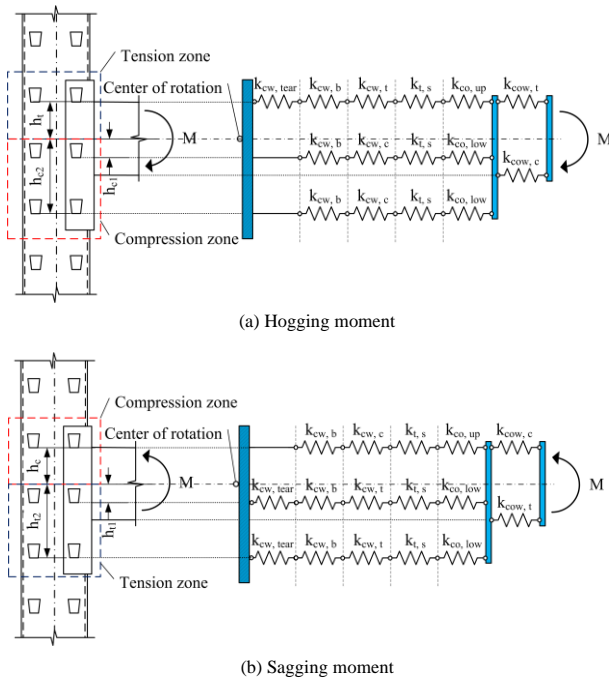


Fig. 12 Mechanical model for determination of the initial rotational stiffness

For determining the initial rotational stiffness, the center of rotation is assumed to be the center of the beam, due to the simplicity of the method, and this assumption agrees with the connection behavior during the initial stage of the experimental testing performed in this study. The initial rotational stiffness of the connection $S_{j,ini}$ can be computed by combining the stiffness of the components given by:

$$\frac{1}{S_{j,ini}} = \frac{1}{h_t^2 K_{eqt}} + \frac{1}{h_c^2 K_{eqc}} \quad (6)$$

where K_{eqt} and K_{eqc} are the stiffness of the equivalent spring in tension zone and compression zone respectively. h_t and h_c are distance from the center of rotation to the location of the tension or compression spring.

For evaluation of the flexural strength, it is assumed that the failure of the connection initially occurs at the outermost row of tabs on the tension side. This assumption is valid in case of connections with a low ratio of beam height to beam-end-connector height; it has been confirmed by many experimental investigations [2] [5-7] and by the author's experimental testing [11]. The strength of the outermost tab is calculated from the minimum value of the strength of the basic components in a row. Then, the linear distribution of force inside the connection is applied. Finally the strength of the connection is calculated from the equilibrium equation. This procedure is rather simple and gives a more conservative flexural strength than the study of Kozłowski [9]. The center of rotation is assumed to be located at the bottom surface of the beam for the connection subjected to a hogging moment. For the connection subjected to a sagging moment, it is assumed that the center of rotation is located at the top surface of the beam. Mechanical models for evaluation of flexural strength are shown on Fig. 13.

Table 3
Initial stiffness and strength of each basic component [9-10] [22]

Component	Strength	Initial stiffness
Column web in tearing	$F_{c w, t e a r} = \frac{f_{y, c w} A_{v, c w}}{\sqrt{3}}$	$k_{c w, t e a r} = \frac{F_{c w, t e a r}}{\delta_{c w, t e a r}}$
Column web in bearing	$F_{c w, b} = 2.5 \alpha f_{u, c w} d t_{c w}$	$k_{c w, b} = 24 k_b k_t d f_{u, c w}$
Column web in tension	$F_{c w, t} = \omega b_{e f f, c w, t} t_{c w} f_{y, c w}$	$k_{c w, t} = E_{c w} \frac{b'_{e f f, c w, t} t_{c w}}{d_{w c}}$
Column web in compression	$F_{c w, c} = 107661 \frac{t_{c w}^3}{d_{w c}} \sqrt{f_{y, c w}}$	$k_{c w, c} = E_{c w} \frac{b'_{e f f, c w, c} t_{c w}}{d_{w c}}$
Tabs in shear	$F_{t, s} = \frac{f_{u, c o} A_{v, t}}{\sqrt{3}}$	$k_{t, s} = \frac{1}{\left(\frac{l_t^3}{3 E_t I_t} + \frac{1.2 l_t}{G_t A_{v, t}} \right)}$
Connector in bending and shear	$F_{c o} = \frac{f_{y, c o} A_{v, c o}}{\sqrt{3}}$	$k_{c o} = \frac{1}{\left(\frac{l_{c o}^3}{3 E_{c o} I_{c o}} + \frac{1.2 l_{c o}}{G_{c o} A_{v, c o}} \right)}$
Connector web in tension and compression	$F_{c o w} = \omega b_{e f f, c o} t_{c o} f_{y, c o}$	$k_{c o w} = E_{c o} \frac{b'_{e f f, c o} t_{c o}}{d_{w c, c o}}$
Beam flange in tension or compression	$F_{b f} = b_{e f f, b f} t_{b f} f_{y, b f}$	$k_{b f} = \infty$

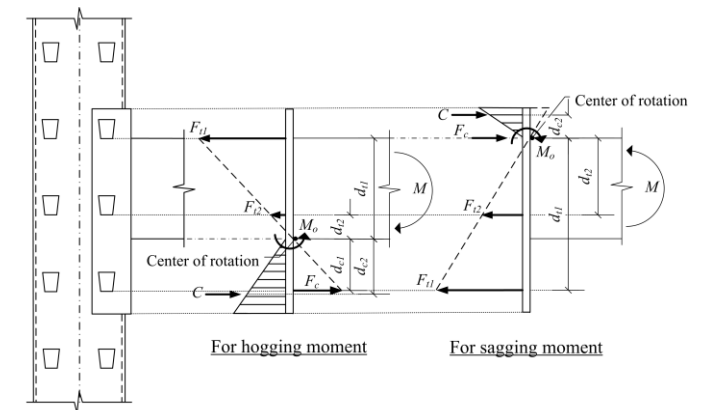


Fig. 13 Mechanical model for flexural strength evaluation

The flexural strength of the connection M_u is given by using the equilibrium equation as follow:

$$M_u = F_{ti} \sum_{i=1}^2 d_{ti} + M_o \quad (7)$$

where F_{ri} is tension force in the steel tab of i component from the center of rotation, and d_{ri} is the distance of i component from the center of rotation. M_o is the internal moment of the connector at the center of rotation, which can be obtained by using the following expression.

$$M_o = F_c d_{c1} + C d_{c2} \leq M_{co,p} \quad (8)$$

where d_{c1} is the distance from the center of rotation to a compression force F_c , d_{c2} is the distance from the center of rotation to compression force C , and $M_{c0.9}$ is a plastic moment of the connector. C is the compression force due to the

bearing stress between the connector and the column.

The bearing stress is assumed to be a triangle distribution. Using the equilibrium condition, the compression force can be obtained as follows:

$$F_{t1} + F_{t2} = C + F_c \quad (9)$$

where F_{t1} is tension force in the steel tab on the tension side at the outer most point from the center of rotation. F_{t2} is tension force in the steel tab at the second row on the tension side. F_c is compression force in the steel tab on the compression side. F_{t1} is taken as the minimum value of the strength of the basic components in a row as follows:

$$F_{t1} = \min(F_{cw,tear}, F_{cw,b}, F_{cw,t}, F_{t,s}, F_{co}) \quad (10)$$

For simplicity, elastic force distribution of internal forces inside the connection is applied. The following equation can be obtained to calculate F_{t2} and F_c .

$$\frac{F_{t1}}{d_{t1}} = \frac{F_{t2}}{d_{t2}} = \frac{F_c}{d_{c1}} \quad (11)$$

where d_{t1} is the distance from the center of rotation to the tension force F_{t1} , and d_{t2} is the distance from the center of rotation to the tension force F_{t2} .

4. Evaluation of mechanical model through experimental testing

In this section, the initial rotational stiffness $S_{j,ini}$ and the flexural strength of the connection M_u are obtained from the proposed mechanical model, and are compared with the experimental testing data to evaluate the proposed mechanical model. Geometrical data and material properties of beam-to-column connections given in section 2.1 are used as the input data for calculation of initial rotational stiffness and flexural strength of the connection by using the proposed mechanical model as described in section 3. Table 4 shows numerical values of the initial stiffness and strength of each basic component for the studied beam-to-column connection. The comparisons of the initial rotational stiffness and flexural strength of the connection from the proposed mechanical model and the cantilever test are shown in Table 5.

It can be seen that the mechanical model closely predicts the flexural strength, and that the difference is on the conservative side, while giving a moderate overestimation of the initial rotational stiffness. In particular, the flexural strength is found to be 5-11 % lower than the experimental values. This may be due to the impact of lack of fit between steel tab and column perforation, and residual stress that usually affects experimental setup [28].

The experimental testing shows that the moment-rotation relation for rack connections exhibits a non-linear behavior, which comes from many factors, such as the yielding of the steel tabs, beam-end connector, or perforated column, which the mechanical model does not take into account in the formulation. This causes the mechanical model to overestimate the initial rotational stiffness by 15-19 %.

Table 4

Characterization of component of the studied beam-to-column connection evaluated by the component method

Component	Strength (kN)	Initial stiffness (kN/cm)
Column web in tearing	$F_{cw,tear} = 8.66$	$k_{cw,tear} = 11123$
Column web in bearing	$F_{cw,b} = 7.91$	$k_{cw,b} = 79.11$
Column web in tension	$F_{cw,t} = 35.19$	$k_{cw,t} = 790.32$
Column web in compression	$F_{cw,c} = 88.98$	$k_{cw,c} = 675.68$
Tabs in shear	$F_{t,s} = 6.8$	$k_{t,s} = 1838$
Connector in bending and shear	$F_{co} = 18.29$	$k_{co,up} = 1967$ $k_{co,low} = 350$
Connector web in tension and compression	$F_{cow} = 16.87$	$k_{cow} = 1794$
Beam flange in tension or compression	$F_{bf} = 16.15$	$k_{bf} = \infty$

Table 5

Comparisons of the initial rotational stiffness and flexural strength of beam-to-column connections obtained from the mechanical model and the cantilever tests

		Hogging moment	Sagging moment
Initial rotational stiffness	Experimental result		
	(Average value)	62.50	60.10
	(kN-m/rad)		
	Mechanical model	71.71	71.98
Flexural strength	(kN-m/rad)		
	Mechanical model/Experiment	1.15	1.19
	Experimental result		
	(Average value)	1.33	1.56
(kN-m)	(kN-m)		
	Mechanical model	1.18	1.48
	(kN-m)		
	Mechanical model/Experiment	0.89	0.95

5. An application of the proposed mechanical model to predict lateral behavior of steel storage frames

5.1. Analysis of lateral behavior of steel storage frames

The proposed mechanical model discussed in section 4 is used in this section to predict lateral behavior of a single story steel storage frame. The predictions are compared with the experimental results from the portal test in terms of base shear-top displacement relation. The portal test results give the mean values of the initial stiffness and flexural strength, whereas the proposed mechanical model distinguishes both connection properties between the hogging and the sagging moment. To indirectly compare the results, a nonlinear static analysis [29], so-called pushover analysis, is applied for this study. Under the pushover analysis, a structure is subjected to gravity loadings as an initial condition. Then the lateral load is applied monotonically in a step-by-step nonlinear static analysis. From the analysis, the numerical results can be present in the form of base-shear top displacement relation that will be referred to as a “pushover curve” in this paper.

The pushover curve of a single story frame using beam-to-column connection properties obtained from the proposed mechanical model is compared with the experimental results from the portal tests. The finite element computer program SAP2000 [30] is used to carry out the pushover analysis in this study. The structural configuration and section properties of the finite element model are calibrated against the portal frame tests. The base plate is modelled as a pinned support. Uniformly distributed vertical forces are applied on the beam element to simulate the pallet load. Non-linear behavior of the beam-to-column connection is modelled by a non-linear rotational link element connected between the ends of beams and the ends of columns. The geometric nonlinearities and material nonlinearities are also considered in the finite element model.

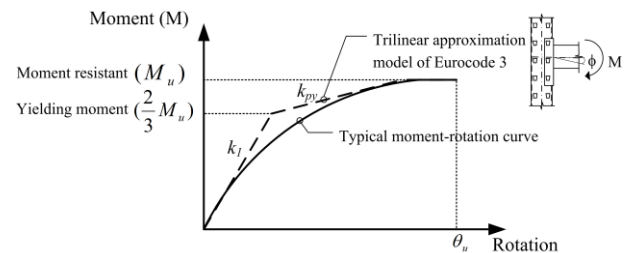


Fig. 14 Typical moment-rotation curve for rack connections and approximation of Eurocode 3

A typical moment-rotation curve for a rack connection is shown in Fig. 14. The moment-rotation relation exhibits non-linear behavior as shown in the section of experimental testing. In order to represent the non-linear behavior of the connection and simplify the analysis, a tri-linear approximation model, in accordance with Eurocode 3, is used in this study. This approximation is widely used for the development of mechanical models for hot roll section. A first yielding moment is assumed to be $2M_u/3$ [11] [22] where M_u is flexural strength; k_i is initial rotational stiffness; k_{py} is post-yielding stiffness; θ_u is plastic rotation capacity. It should be noted that the value of θ_u and k_{py} are chosen to give the best-fit to the experimental results from the cantilever test. The prediction of steel storage frame behavior under lateral loads by using an application of the proposed mechanical model is shown in Fig. 15 (a) -15 (b) for no loading and normal loading respectively. The figures present the comparison between base shear-top displacement relation from the portal test and pushover curves of portal frame with a trilinear approximation of moment-rotation relation for the proposed mechanical model.

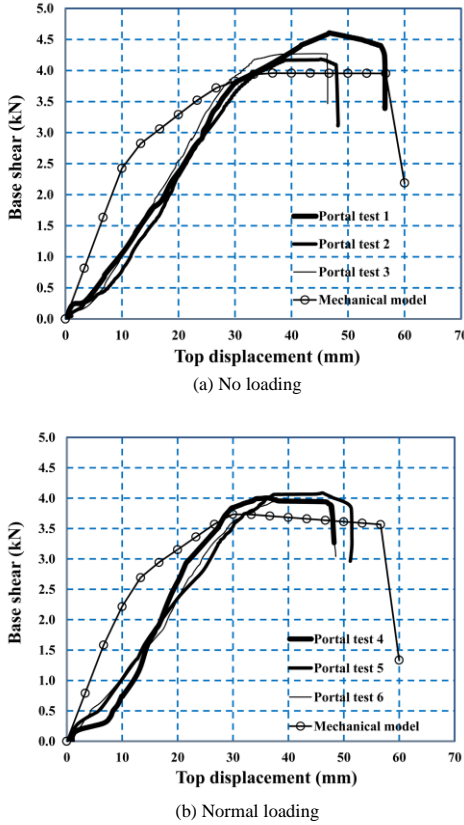


Fig. 15 Comparison of the portal test results and pushover analysis of portal frame with approximation of rack connections

From the resulting curves, it can be seen that the mechanical model give a conservative prediction of maximum base shear for all testing frames. On the other hand, the predicted displacements of the proposed mechanical model underestimate the displacement compared with the portal test results. The predicted displacement of the frame is greatly influenced by the initial rotational stiffness of the connection. It can be seen from the cantilever test in section 2.2 that the stiffness of rack connections start to deviate from the initial rotational stiffness at low value of moment. The stiffness is increasingly softened at moments approaching the ultimate moment. Therefore using the initial rotational stiffness for the rack connection model may underestimate the displacement response of the steel storage frame.

5.2. Improvement of rack's connection model

It has been shown in the previous section that the lateral behavior of steel storage frames is significantly influenced by the rack connection model. This section presents the further improvement of the rack connection model for a better prediction of the lateral behavior.

It is evident from the comparison of the portal test and the pushover analysis that the mechanical models were slightly too stiff in comparison to the actual frame, thus resulting in too low a prediction of the lateral displacement. The two sources of the problem that were addressed are the accuracy of initial

stiffness to represent the stiffness of the connections as the loading increased, and the presence of the initial looseness of the actual connections.

The linear idealization of the moment-rotation characteristic of the beam-to-column connections based on the use of the secant stiffness is applied for improvement, as shown in Fig. 16. This approach is recommended by Eurocode 3 [10]. The secant stiffness is defined as $S_{j,ini}/n$. The stiffness modification factor (n) results from the non-linearity of the connection. Generally, a stiffness modification factor of 2.0-3.5 is suggested by Eurocode 3, depending on connection types. Based on a comprehensive experimental study of beam-to-column connections under bending moment in this study, a numerical value of 1.5-2.0 is proposed for the stiffness modification factor.

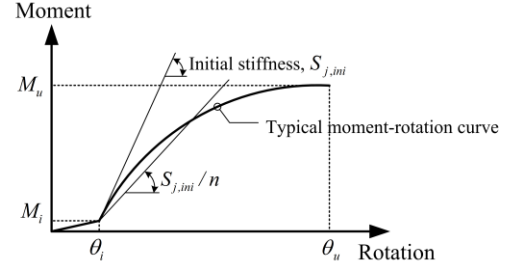


Fig. 16 Improvement of rack connection model

It is also shown in the experimental testing of rack connections that some of the moment-rotation curves show a looseness of the connection at the initial stage. The looseness contributes to the overall deformation of the portal frame; hence, it needs to be incorporated into the connection model. A flat slope of linear line is introduced in the connection model to represent looseness of the connection, as shown in Fig. 16. It should be noted that M_i and θ_i are moment and rotation, where the initial looseness is terminated. θ_i can be calculated from the gap between steel tabs and the column perforation, or can be determined by the conventional cantilever test. In this study, M_i and θ_i are taken from the cantilever test as 0.05 kN-m and 0.006 radian respectively. These numerical values, M_i and θ_i , produce a low value of stiffness in the initial looseness stage, which is about 10% of the initial rotational stiffness. The numerical values of the connection model for hogging moment and sagging moment of the connection for frame analysis are shown in Fig. 17 (a)-17 (b). In Fig. 17, the initial stiffness ($S_{j,ini}$) and flexural strength (M_u) of the connection are calculated from the proposed mechanical model. θ_u is rotation, where the steel tab is cut by the column perforation, which is taken from cantilever test. The pushover analysis is conducted for the portal frame with the connection model presented in Fig. 17. The comparison between the frame analysis results and the experimental results of the portal test are shown in Fig. 18 (a)-18 (b).

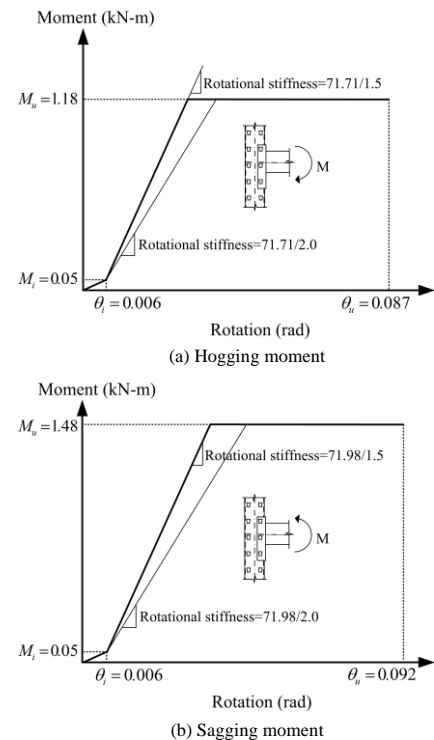


Fig. 17 Linearization of moment-rotation characteristic of rack connections

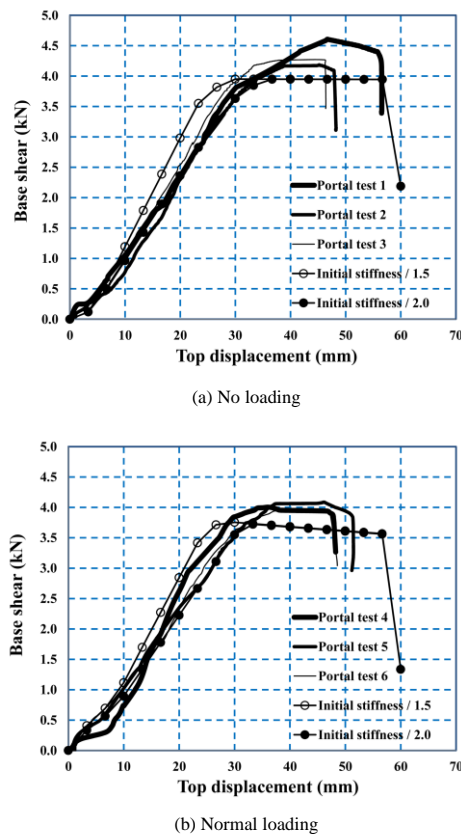


Fig. 18 Comparison of the portal test results and pushover analysis of portal frame with modification of rack connection model

As expected, introducing the stiffness modification factor (n) and the initial looseness to the mechanical model improves the accuracy of the lateral-displacement prediction from frame analysis, and the improved pushover curves agree well with the portal frame testing results, as shown in Fig. 18. To this end, modification of initial rotational stiffness and inclusion of the initial looseness to the modeling are deemed necessary for a better prediction of lateral behavior of steel storage frames.

6. Summary and conclusions

This research presents the development of a mechanical model for beam-to-column connections of steel storage racks using a component method recommended in Eurocode 3. A proposed mechanical model of the rack's connections is derived from the combination of the characteristics of the basic structural components of the connections. Initial rotational stiffness and flexural strength yielded from the mechanical model, along with simple linearized moment-rotation relationship, can be used as the estimated characteristics of any steel rack connection under both hogging and sagging moments. The study proposes a simple methodology for evaluation of the flexural strength based on the actual failure mode.

The initial mechanical model adequately predicts the flexural strength with acceptable degree of accuracy. However, the simple linearized moment-rotation relationship based on the initial stiffness and moment resistance underestimates the lateral displacement when it is applied to the pushover analysis. Consequently, the study proposes further refinement of the moment-rotation relationship by introducing initial looseness and replacing the initial stiffness with secant stiffness. It is recommended that the modification factor for the initial stiffness to secant stiffness be in the range between 1.5 and 2.

The proposed mechanical model can be used to predict the response of a connection, as well as the structural response, subjected to both vertical loads, and horizontal loads, with a fraction of testing costs and time. Also, the proposed model can be easily modified to predict the connection behavior for other geometry of connections for these types of structures.

References

- [1] Markazi F.D., Beale R.G. and Godley M.H.R., "Experimental analysis of semi-rigid boltless connectors", *Journal of Constructional Steel Research*, 28(1), 57-87, 1997.
- [2] Bernuzzi C. and Castiglioni C.A., "Experimental analysis on the cyclic behaviour of

- beam-to-column joints in steel storage pallet racks", *Thin-Walled Structures*, 39(10), 841-859, 2001.
- [3] Aguirre C., "Seismic behavior of rack structures", *Journal of Constructional Steel Research*, 61(5), 607-624, 2005.
- [4] Abdel-Jaber M., Beale R.G. and Godley M.H.R., "A theoretical and experimental investigation of pallet rack structures under sway", *Journal of Constructional Steel Research*, 62(1), 68-80, 2006.
- [5] Bajoria K.M. and Talikoti R.S., "Determination of flexibility of beam-to-column connectors used in thin walled cold-formed steel pallet racking systems", *Thin-Walled Structures*, 44(3), 372-380, 2006.
- [6] Prabha P., Marimuthu V., Saravanan M. and Jayachandran A.S., "Evaluation of connection flexibility in cold formed steel racks", *Journal of Constructional Steel Research*, 66(7), 863-872, 2010.
- [7] Zhao X., Wang T., Chen Y. and Sivakumaran K.S., "Flexural behavior of steel storage rack beam-to-upright connections", *Journal of Constructional Steel Research*, 99(8), 161-175, 2014.
- [8] Shah S.N.R., Sulong N.H.R., Khan R. and Jumaat M.Z., "Structural performance of boltless beam end connectors", *Advanced Steel Construction*, 13(2), 144-159, 2017.
- [9] Kozłowski A., Rzeszow and Słeczka L., "Preliminary component method model of storage rack joint", *Proceeding of the fifth international workshop on connections in steel structures*, Delft University of Technology, Netherlands, June, 253-262, 2004.
- [10] CEN, "Eurocode 3 - Design of steel structures Part 1-8: Design of joints", CEN European Committee for Standardization, Brussels, Belgium, 2005.
- [11] Asawasongkram N., Chomchuen P. and Premthamkorn P., "Experimental analysis of beam-to-column connection in steel storage racks using cantilever test and portal test method", *Proceeding of the 13th East Asia-Pacific Conference on Structural Engineering and Construction*, Sapporo, Japan, Paper No.268, 2013.
- [12] Krawinkler H., Cofie N.G., Astiz M.A. and Kircher C.A., "Experimental study on the seismic behavior of industrial storage racks (Report no. 41)", *The John A. Blume Earthquake Engineering Center*, Department of Civil Engineering, Stanford University, Stanford, 1979.
- [13] Harris E., "Sway behavior of high rise steel storage racks", Ph. D. Thesis, University of Sydney, Sydney, Australia, 2006.
- [14] JIS, "JIS Z2241: Method of tensile test for metallic materials", Japanese Industrial Standards Committee, Tokyo, Japan, 1998.
- [15] ASTM, "A611: Standard Specification for Structural Steel (SS), Sheet, Carbon, Cold-Rolled", ASTM American Society for Testing and Materials, PA, USA, 1997.
- [16] ASTM, "A283: Standard Specification for Low and Intermediate Tensile Strength Carbon Steel Plates", ASTM American Society for Testing and Materials, PA, USA, 2003.
- [17] ASTM, "A36: Standard Specification for Carbon Structural Steel", ASTM American Society for Testing and Materials, PA, USA, 2014.
- [18] AS, "AS 4084: Steel storage racking", Australian Standards, Sydney, Australia, 1993.
- [19] FEM, "FEM 10.2.02: Recommendation for the design of steel pallet racking and shelving", European Racking Federation, Birmingham, UK, 1998.
- [20] RMI, "MH 16.1 - Specification for the design, testing and utilization of industrial steel storage rack", RMI - Rack Manufacturers Institute, Charlotte, USA, 2008.
- [21] Huber G. and Tschemmernegg F., "Modeling of beam-to-column joints - Test evaluation and practical", *Journal of Constructional Steel Research*, 45(2), 199-216, 1998.
- [22] Faella C., Piluso V. and Rizzano G., "Structural steel semi-rigid connections - Theory, design and software", CRC Press LLC, Boca Raton, Florida, USA, 2000.
- [23] Pucinotti R., "Top-and-seat and web angle connections: prediction via mechanical model", *Journal of Constructional Steel Research*, 57(6), 661-694, 2001.
- [24] Silva L.S. and Coelho A.G., "A ductility model for steel connections", *Journal of Constructional Steel Research*, 57(1), 45-70, 2001.
- [25] Beg D., Zupancic E. and Vayas I., "On the rotation capacity of moment connections", *Journal of Constructional Steel Research*, 60(3-5), 601-620, 2004.
- [26] Zhao X., Dai L., Wang T., Sivakumaran K.S. and Chen Y., "A theoretical model for the rotational stiffness of storage rack beam-to-upright connections", *Journal of Constructional Steel Research*, 133(6), 269-281, 2017.
- [27] Asawasongkram N., Chomchuen P. and Premthamkorn P., "Mechanical modelling of beam-to-column connections of steel storage racks", *Journal of Constructional Steel Research*, (to be submitted).
- [28] Bursi O.S. and Jaspart J.P., "Calibration of a finite element model for isolated bolted end-plate steel connections", *Journal of Construction Steel Research*, 44(3), 225-262, 1997.
- [29] Applied Technology Council, "ATC-40 Seismic evaluation and retrofit of concrete buildings", Redwood City, 1996.
- [30] CSI, "SAP2000 - Linear and nonlinear static and dynamic analysis of three-dimensional structures", Computer & Structures Inc., Berkeley, CA, USA, 2009.

List of notation

$b_{eff,bf}$	Effective width of beam flange
$b_{eff,co}$	Effective width of connector web
$b'_{eff,co}$	Effective width of connector web for stiffness calculation
$b_{eff,cw,t}$	Effective width of column web in tension zone
$b'_{eff,cw,c}$	Effective width of column web in compression zone for stiffness calculation
$b'_{eff,cw,t}$	Effective width of column web in tension zone for stiffness calculation
d	Thickness of steel tab
d_{wc}	Depth of column web
$d_{wc,co}$	Depth of connector web
$f_{y,bf}$	Yield stress of beam flanges
$f_{y,co}$	Yield stress of connector web
$f_{u,co}$	Ultimate tensile strength of connector web
$f_{y,cw}$	Yield stress of column web
$f_{u,cw}$	Ultimate tensile strength of column web
l_t	The distance between the concentrated shear force and fixed end of the tab
l_{co}	The distance between the concentrated shear force and

	fixed end of the connector web
t_{bf}	Thickness of beam flanges
t_{co}	Thickness of connector web
t_{cw}	Thickness of column web
$A_{v,co}$	Shear area of the connector web
$A_{v,cw}$	Shear area of column web
$A_{v,t}$	Shear area of the tab
E_{co}	Modulus of elasticity of connector web
E_{cw}	Modulus of elasticity of column web
E_t	Modulus of elasticity of the tab
G_{co}	Tangential modulus of elasticity of connector web
G_t	Tangential modulus of elasticity of the tab
I_{co}	Moment of inertia of connector web
I_t	Moment of inertia of the tab
α	Ratio between ultimate tensile strength of connector web and ultimate tensile strength of column web
$\delta_{cw,tear}$	Deformation of column web under strength of column web in tearing
ω	Reduction factor to allow for the possible effects of shear in the column web panel